TECHNISCHE UNIVERSITÄT MÜNCHEN
Fakultät für Maschinenwesen

Thermal Design of Resistively Heated Tools for Composite Manufacturing

Jakob Sylvester Weiland

Vollständiger Abdruck der von der Fakultät für Maschinenwesen der Technischen Universität München zur Erlangung des akademischen Grades eines

Doktor-Ingenieurs

genehmigten Dissertation.

Vorsitzender:	Prof. Dr.-Ing. Hartmut Spliethoff
Prüfer der Dissertation:	Prof. Dr.-Ing. Klaus Drechsler
	Prof. Dr. Pascal Hubert

Die Dissertation wurde am 23.01.2017 bei der Technischen Universität München eingereicht und durch die Fakultät für Maschinenwesen am 08.06.2017 angenommen.

Technische Universität München
Fakultät für Maschinenwesen
Lehrstuhl für Carbon Composites
Boltzmannstraße 15
D-85748 Garching bei München

Tel.:+ 49 (0) 89 / 289 - 15092
Fax: + 49 (0) 89 / 289 - 15097
Email: info@lcc.mw.tum.de
Web: www.lcc.mw.tum.de

Für meinen Bruder und besten Freund Daniel.

Declaration

Ich erkläre hiermit ehrenwörtlich, dass ich die vorliegende Arbeit selbstständig und ohne Benutzung anderer als der angegebenen Hilfsmittel angefertigt habe; die aus fremden Quellen (einschließlich elektronischer Quellen) direkt oder indirekt übernommenen Gedanken sind ausnahmslos als solche kenntlich gemacht.

Die Arbeit wurde in gleicher oder ähnlicher Form noch keiner anderen Prüfungsbehörde vorgelegt.

....

Ort, Datum Unterschrift

Acknowledgement

This thesis would not have been possible without the outstanding support of many people in my professional as well as in my private environment. I would like to thank my supervisor Prof. Dr.-Ing. Klaus Drechsler, head of the Chair of Carbon Composites, and the administrative staff for the opportunity to work in this highly interesting research field and to grow as a researcher. I was also guided by Dr. Roland Hinterhölzl who managed the institute's Simulation Group and whom I would like to thank deeply for his technical guidance as well as his support in various matters.

I would like to express my deepest gratitude to Prof. Pascal Hubert, for the invitation to work and experience the Composite Materials and Structures Laboratory during a three-month stay at McGill University Montreal. The constructive and friendly discussions gave me advice, confidence, and motivation in a very important stage of my work.

I was very fortunate to work with great colleagues and valued friends at the Chair of Carbon Composites. Thank you Max Lipcan, Philipp Kammerhofer, Mathias Hartmann, Rhena Helmus, Thorsten Hans and many others for your great technical advice and encouraging discussions.

Furthermore, I would like to express my deep gratitude to Jordy Balvers whose sense for detail and structure greatly helped in the final stages of this thesis.

I would like to acknowledge on the one hand the financial funding which was provided partly by the European Union in the Cleansky framework and partly by the Bundesministerium für Bildung und Forschung (BMBF), and on the other hand the industrial partners in my research projects, namely Airbus Helicopters, BMW AG, the Fraunhofer Gesellschaft, Premium Aerotec, and Qpoint Composites GmbH. I also would like to acknowledge Convergent Manufacturing Technologies Inc. for the academic license of the cure simulation platform COMPRO/CCA.

Last but not least, this achievement would not have been possible without my family's and friend's love and support. Thank you mum and dad for always believing in me. Thank you Martina for being there for me, your smile and positive attitude encouraged me on countless occasions. Finally, I would like to say thank you to my close friends from Karlsruhe, you are superb!

Abstract

Carbon fiber reinforced polymer (CFRP) molds, which are applied in carbon composite processing, offer the benefit of a similar thermal expansion in tool and part, low weight and low energy consumption. However, thermal sensitivity of CFRP tools are one of the main reasons hindering their widespread application in the industry to date. The utilization of a multi-zonal electrical heating system enables a direct heat introduction with low thermal lag and the possibility to overcome potential thermal gradients during cure, originating from the tool material, thanks to a locally adjustable heat introduction. In order to support the industry in making use of the benefits of CFRP tools, this work investigates the potential of a homogeneously curing of parts induced by resistively heated CFRP molds and provides numerical methods for its exploitation.

To enable cure simulations in the ABAQUS/COMPRO environment and gain a fundamental understanding of the laminate, a material characterization of Cytec CYCOM 823-1 neat resin was conducted in a first step. Second, a numerical control method for 3D finite element cure simulations was developed to predict the thermal tool response within one heat zone with appropriate accuracy, even in cases with large temperature gradients occurring. Third, a universally applicable numerical strategy to capitalize on the thermal flexibility of resistively heated multi-zone tools was developed in order to determine an optimal partitioning of the designated heating area, utilizing 3D finite element cure simulation. Further, a cure simulation model of an application case was set up and validated, featuring a resistively heated aluminum tool to show the general applicability of the developed numerical methods for the simulation and thermal dimensioning of resistively heated tools, independent of the tool material. Fourth, an optimization procedure, originating from the literature, was implemented and adapted to enable the determination of a thickness-robust temperature cycle for up to 30 mm thick HTS40/823-1 laminates. Variations to this robust temperature cycle were identified to be applied in a resistively heated multi-zone tool where several laminate thicknesses can be subjected to different temperature cycles in order to gain a more homogeneous cure behavior in the part. Finally, a case study of a generic rotor blade was set up, employing the previously developed material card and numerical methods. The investigation of the temperature and degree of cure evolution demonstrated the capability of resistively heated CFRP tools to reach competitive thermal and degree of cure homogeneity, even in case of large parts with industrial complexity level.

Zusammenfassung

Werkzeuge aus carbonfaserverstärktem Kunststoff (CFK) weisen bedeutende Vorteile gegenüber konventionellen Werkzeugen aus Aluminium und Stahl für die Herstellung von CFK-Bauteilen auf. Sie besitzen nicht nur ein geringes Eigengewicht und einen niedrigen Energieverbrauch, sondern zeigen auch eine ähnliche Wärmedehnung wie das zu produzierende Bauteil, was dessen prozessinduzierte Deformationen verringert. Andererseits verhalten sie sich jedoch thermal sensitiv, was zu inhomogenen Temperaturverteilungen im Bauteil während der Produktion und somit zu geringerer Laminatqualität führen kann. Dies stellt einen Hauptgrund für den zögerlichen Einsatz von CFK-Werkzeugen in industriellem Rahmen dar. Eine Kompensation potentiell auftretender lokaler Temperaturgradienten ermöglicht die Verwendung von neuartigen Heiztechnologien durch einen direkten Wärmeeintrag mittels Widerstandsheizung in mehreren unabhängigen Zonen des Werkzeugs. Die Kombination dieser Heiztechnologie mit dem Werkzeugmaterial CFK verspricht folglich eine Fertigung von qualitativ hochwertigen CFK-Bauteilen, sofern diese Werkzeuge thermal ausgelegt werden können. Im Rahmen der vorliegenden Arbeit soll dieses Potential untersucht und numerische Methoden zur thermalen Berechnung und Auslegung von CFK-Werkzeugen entwickelt werden.

Um dieses Forschungsziel zu erreichen, wird im ersten Schritt eine Materialcharakterisierung des Harzsystem Cytec CYCOM 823-1 durchgeführt, um ein detailliertes Verständnis für das aushärtende Material des Bauteils zu erarbeiten sowie die Materialmodelle für die Aushärtesimulation aufsetzen zu können. Im Anschluss wird eine numerische Methode entwickelt und validiert, die eine thermale Modellierung von wiederstandbeheizten Werkzeugen in der Aushärtesimulation mit ausreichender Genauigkeit auch beim Auftreten großer Temperaturgradienten im Werkzeug ermöglicht. Darauf aufbauend wird eine universell anwendbare numerische Strategie entwickelt, die eine Bestimmung einer optimierten Heizbereichseinteilung mithilfe der Finite Elemente Methode möglich macht. Des Weiteren wird ein Berechnungsprogramm zur Aushärtezyklusoptimierung implementiert, um robuste Aushärtezyklen für die Prozessierung von bis zu 30 mm dicken Laminaten der Zielmaterialkonfiguration zu ermitteln. Abschließend wird das Potential von selbstbeheizten CFK-Werkzeugen, eine homogene Bauteilaushärtung auch in der Produktion von großen Bauteilen mit industriellem Komplexitätsgrad zu erreichen, anhand eines Anwendungsfalls eines generischen Rotorblatts demonstriert.

Contents

Nomenclature

Symbol	**Unit**	**Explanation**
Latin symbols		
A	$\mathrm{s^{-1}}$	Arrhenius function constant
A_inf	$\mathrm{m^{2}}$	influence area of a node
CSC	-	chemical shrinkage coefficient
CTE	$\mathrm{^{\circ}C^{-1}}$	coefficient of thermal expansion
c_p	$\mathrm{J\,kg^{-1}\,^{\circ}C^{-1}}$	specific heat
D	-	damping constant
ΔE	-	activation energy
E	Pa	Young's modulus
E'	Pa	storage modulus
E''	Pa	loss modulus
F	-	multi-objective fitness function value
f_m	$\mathrm{m^{-2}}$	mesh factor
G	Pa	shear modulus
G'	Pa	shear storage modulus
G''	Pa	shear loss modulus
$\mathbf{G}$	-	heat flux gradient matrix
h	$\mathrm{W\,m^{-2}\,^{\circ}C^{-1}}$	convective heat transfer coefficient
H	$\mathrm{J\,g^{-1}}$	heat of reaction
H_r	$\mathrm{J\,g^{-1}}$	ultimate heat of reaction
$\mathbb{I}$	-	Cluster of elements
J	-	individual fitness criteria
$\mathbb{J}$	-	Cluster of elements
K	$\mathrm{s^{-1}}$	resin reaction rate constant
$\mathbb{K}$	-	Cluster of elements
k	$\mathrm{W\,m^{-1}\,^{\circ}C^{-1}}$	thermal conductivity
n	m	surface normal vector
$\mathbf{n}$	$\mathrm{N\,m^{-1}}$	resultant laminate force vector
$\mathbf{m}$	N	resultant laminate moment vector
p	$\mathrm{W\,m^{-2}}$	power introduction per area
$\dot{Q}$	W	heat flux
$\mathbf{Q}_\mathrm{xy}$	Pa	laminate stiffness matrix
$\dot{q}$	$\mathrm{W\,m^{-2}}$	heat flux density

R	$\mathrm{J\,mol^{-1}\,K^{-1}}$	universal gas constant
RFL	W	reaction flux
$\mathbf{r}$	m	position vector
T	°C	temperature
T_g	°C	glass transition temperature
T_∞	°C	ambient temperature
$\mathbf{T}$	-	rotary matrix
t	s	time
V	$\mathrm{m^3}$	volume
V_f	-	fiber volume content
V_r^s	-	volumetric cure shrinkage strain
w	m	conductor gap width

Greek symbols

α	-	degree of cure
$\dot{\alpha}$	$\mathrm{s}^{-}1$	cure rate
ϵ	-	strain vector in Voigt notation
$\epsilon_\mathrm{r}^\mathrm{s}$	-	linear cure shrinkage strain
θ	rad	angle
λ	-	DiBenedetto constant
ν	-	Poisson's ratio
ρ	$\mathrm{kg\,m^{-3}}$	density
σ	Pa	stress vector in Voigt notation
σ_α	-	mean weighted standard deviation of the degree of cure
Φ	-	potential function
ω	-	weighing factor of the individual fitness criteria

Subscripts

0	property of uncured resin
1,2,3	property in the direction of the 1,2,3-axis of the coordination system
∞	property of fully cured resin
conv	property as a result of convection
f	property of fiber
gel	property at the point of gelation
glass	property in the glassy resin state

in-plane	property acting in-plane
r	property of resin
rub	property in rubbery resin state
trans	property acting out-of-plane
$\parallel$	parallel to fiber direction
$\perp$	transverse to fiber direction

Abbreviations

Abbreviation	Meaning
1D	one-dimensional
2D	two-dimensional
3D	three-dimensional
AGP	after gelation point
CCA	COMPRO Component Architecture
CFD	computational fluid dynamics
CFRP	carbon fiber reinforced polymer
CLT	classical laminate theory
CSC	chemical shrinkage coefficient
CTE	coefficient of thermal expansion
DKC	Direct Kmeans Clustering
DMA	dynamic mechanical analysis
DSC	dynamic scanning calorimetry
FDM	finite difference method
FE	finite elements
FEA	finite element analysis
FEP	fluorinated ethylene propylene
FRP	fiber reinforced polymer
GFRP	glass fiber reinforced polymer
LGM	Least Gradient Merge
LTI	linear time invariant
LVR	linear viscoelastic region
MDSC	modulated dynamic scanning calorimetry
MPC	multi-point constraint
PID	proportional-integral-derivative
RFL	reaction flux
ROM	rule of mixtures
RTM	resin transfer molding
RVE	representative volume element
SLE	system of linear equations
TGA	thermo-gravimetric analyzer
TTT	time-temperature-transformation
UD	uni-directional

-

List of Figures

List of Tables

1 Introduction

1.1 Background and Problem Statement

In industries where lightweight design is of importance, such as the aerospace and the automotive industry, fiber reinforced polymers (FRP) are employed due to their high stiffness and strength in combination with low weight. Mostly glass and carbon fibers are chosen to provide the stiffness and strength in the final compound, resulting in glass fiber reinforced polymer (GFRP) and carbon fiber reinforced polymer (CFRP) materials. A wide variety of polymer resin systems are used for the matrix material, depending on the particular specifications of the application [22]. Thermoset resin systems show a comparably low viscosity and, thus, are often selected for an enhanced impregnation of the fiber bed during part manufacture [23]. In composite processing with thermoset resin an unlinked mixture of resin and hardener is introduced in the fiber bed either prior (so called prepreg) or after the part fiber layup (injection processes) is performed. Subsequently, in most cases an exothermic cross-linking of the chemical monomers is conducted at elevated temperatures. Heat introduction is defined by the process technology chosen and either performed indirectly over the air (autoclave, oven) or directly into the tool (fluid heating or resistive heating devices). Research has also been conducted on direct heat introduction via resistive heating of the part's fiber bed [24–26] or with help of a microwave [27, 28]. However, both procedures are rarely applied in the industry to date due to the challenge to get a constant cure temperature over the part dimensions for applications with industrial complexity level.

Especially resistive heating of the tool offers the potential of reduced cycle time, reduced thermal lag between set-point and part temperature as well as reduced energy consumption in combination with moderate additional requirements for tool manufacturing [2, 13, 29].

These tools are either used as stand-alone in, for instance, resin transfer molding (RTM) [12], in Out-of-Autoclave manufacturing processes, or within an autoclave to locally support regions with low convective heat transfer in shadow zones of the air stream. Figure 1-1 shows resistively heated tools of two different tool manufacturers. The aluminum tool produced by TCX^{TM} (see Figure 1-1 (b) and (c)) depends on a conductor material, which is applied on the tool backside and isolated from the tool material itself, to introduce heat into the system [30]. In case of the CFRP tools produced by Qpoint Composites GmbH the conducting material is embedded in the tool laminate itself, if required [1]. Usually, the spacing of conducting paths is designed to gain constant power introduction in the area and a homogeneous temperature distribution on the part face of the tool.

This technology enables the division of a designated heating area into several independent heating zones. The heat introduction in each zone is controlled by a thermocouple in combination with an external control unit, enforcing the set-point temperature cycle at the location of the thermocouple. However, the resulting tool temperature field in one heating zone can be inhomogeneous and, thus, can deviate significantly from the set-point temperature at locations afar from the control thermocouple in the considered zone [31].

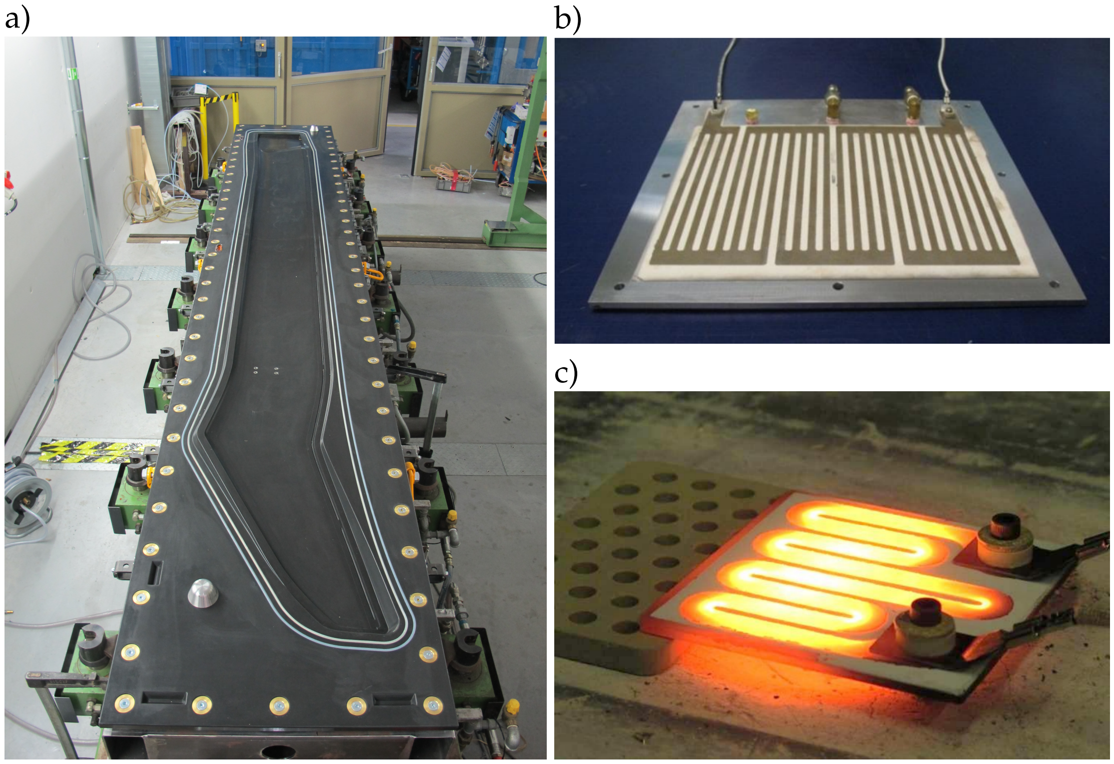

Figure 1-1 Resistively heated tools: (a) CFRP tool for a full-scale helicopter rotor blade from Qpoint Composites GmbH [1], (b) bottom side of an aluminum tool with a TCX^{TM} heating element [2], (c) TCX^{TM} heating element in service [3].

Regarding the choice of tool material, traditional options for composite manufacturing are steel and aluminum thanks to good machinability and stiff mechanical response. As the thermal expansion discrepancy between the metallic tool and the CFRP part adds to residual stress build-up and spring-in effects [32], Invar is used in some cases where dimensional fidelity during the temperature ramp is of high importance [33]. However, these metallic tooling concepts lead to high costs of the tool manufacturing, high tool weight and low energy efficiency in service life due to the high thermal tool mass. Hence, novel tooling concepts based on CFRP as tool material are subject to increasing industrial interest. However, thermal sensitivity of CFRP tools are a major concern and hinders their widespread application to date. The in-plane heat conductivity of CFRP tool material is by one magnitude lower than steel and by two magnitudes lower than aluminum [34]. This can potentially lead to large inhomogeneities in the temperature field during operation, if the thermal design is insufficient.

Given that resin cure is driven by temperature [35], a uniform temperature field in the part during the cure cycle is sought in composite processing to gain homogeneous cure within the part. Especially for thick laminates this is a significant challenge. Low thermal conductivity of the compound in combination with the exothermic reaction energy of the curing resin may lead to a local temperature overshoot in the laminate [36–38]. If this overshoot reaches a critical level, the temperature development in the part's interior is almost solely dominated by the autocatalytic reaction resulting in very high local temperatures [39], which pose the risk of material degradation [40]. On the contrary, if the temperature cycle leads to gelation of the part's surface well ahead of its interior, voids and non-uniform fiber volume fractions can occur [41, 42]. In general, thermal gradients and accompanying cure gradients increase the internal stresses in the laminate [5, 43, 44]. Hence, the thermal history of the curing part is understood to be a key parameter regarding the development of internal stresses in cross-linked polymers and, thus, potential defects such as process-induced microcracks or delamination [45–48].

Although CFRP tools in general are susceptible to temperature inhomogeneities, resistively heated CFRP tools enable an adjustment of the heat introduction to account for different part materials and thicknesses via the inclusion of multiple independent heat zones. Hence, multi-zonal resistively heated tools offer the thermal flexibility to adjust the tool heat introduction onto the local requirements of the part areas. Thus, they have the potential of providing a homogeneous tool temperature distribution while maintaining the above-stated advantages of CFRP material. In addition, the thermal flexibility of these tools provide the possibility of adjusting the temperature cycles in different part regions, potentially resulting in an overall improved cure behavior in complex parts with large discrepancies in material and thickness.

However, the thermal design of these multiple heat zones is conducted based on experience to date. Especially for complex parts the optimal allocation of heat zones is highly challenging, given that a variety of influencing factors such as the thermal behavior of tool and part, exothermic resin reaction, and environmental effects such as convection, has to be considered. In-depth process comprehension is required which, in most cases, can only be offered by process simulation. Therefore, the capability to appropriately model temperature controlled resistively heated tools in a cure simulation platform has to be developed to enable a simulation-assisted thermal dimensioning of these tools.

1.2 Dissertation Objectives

This work aims to provide an understanding for the thermal behavior of resistively heated CFRP tools and its impact on part cure. Given their thermal flexibility, these tools can be designed to overcome their drawback resulting from high thermal sensitivity and lead to homogeneous tool temperature during part cure. Moreover, they have the possibility to locally adjust the applied cure cycle onto the requirements of distinct part regions and, thus, have the potential to result in a globally improved part cure behavior. In order to contribute to their industrial application, the overall goal of this work is to investigate these potentials as well as their limits.

To pursue this target three numerical tools have to be developed, which form the technical objectives of the presented work:

- A method has to be established to appropriately model distinct heat zones in a cure simulation environment.
- A numeric approach for the thermal dimensioning of resistively heated tools has to be developed.
- A multi-objective cure cycle optimization has to be implemented, enabling the determination of an appropriate set of temperature cycles for the application in multi-zone tools.

While the focus of this work is set on CFRP tool materials, effort is undertaken to develop methods independent of the tool material to enable a general applicability in the thermal design of resistively heated tools.

1.3 Dissertation Outline

Following the problem statement and dissertation objectives in Chapter 1, the literature review in Chapter 2 outlines the state-of-the-art in modeling composite material behavior during cure. Additionally, techniques for numerical manufacturing process investigation and numerical process optimization are presented. In Chapter 3, the neat resin and tool material properties utilized in the case study are characterized. A simulation method to model one temperature controlled heat zone within a numerical cure simulation environment is developed in Chapter 4. In Chapter 5, a numerical strategy for thermal dimensioning of resistively heated tools with multiple independent heat zones is introduced. Applying the material models developed in Chapter 3, a cure cycle optimization is conducted in Chapter 6. Based on a case study of a generic rotor blade, an estimation of the potential of resistively heated tools to lead to homogeneous part cure in the manufacturing of complex parts with varying cross-sections and materials finalizes the content of this work in Chapter 7. The major conclusions and contributions as well as recommendations for future work are outlined in Chapter 8.

2 Literature Review

The assessment of the potential of resistivity heated tools for the production of high-quality CFRP parts requires an extensive use of simulation methods to predict the thermal and cure behavior of the tool as well as the part. The capability of doing so bases on the knowledge of four major fields of research, which were extensively investigated in literature and are presented briefly in this chapter:

- Composite material modeling during cure (Chapter 2.1).
- The effect of the curing process on laminate quality (Chapter 2.2).
- Process simulation to investigate different manufacturing conditions (Chapter 2.3).
- Improvement of the part quality through a correct choice of process variables (Chapter 2.4).

2.1 Composite Material Modeling During Cure

During the cure of fiber reinforced thermosets the polymeric matrix passes three distinct morphological phases: liquid, solid/rubbery and solid/glassy. These three phases are defined by the two principal transformations that may occur during cure: gelation and vitrification. Both gelation and vitrification affect the rheology, conversion rate, density, dimensional stability, and, in fact, all thermal and mechanical properties of the thermosetting material significantly [49]. In order to understand the cure phenomena time-temperature-transformation (TTT) diagrams, shown in Figure 2-1, were introduced. Herein the times required to reach gelation and vitrification under certain isothermal cure temperatures T_{cure} are plotted [4].

In the beginning of the curing process the matrix consists of unlinked monomers, which proceed to build a chemical network if the cure temperature T_{cure} is elevated above the initial glass transition temperature T_{g0}. In this state the matrix is liquid and soluble in some organic solutions [50]. At a certain degree of conversion, gelation occurs which is characterized by the incipient formation of a material of infinite molecular weight [4, 51, 52].The polymer matrix of the laminate is capable of transferring stresses from this point on, although entropy elasticity is dominant at this stage with rubbery material behavior [53]. Since cross-linking thermoset resin systems are subjected to a reduction in volume during cure, referred to as chemical shrinkage, the point of gelation also defines

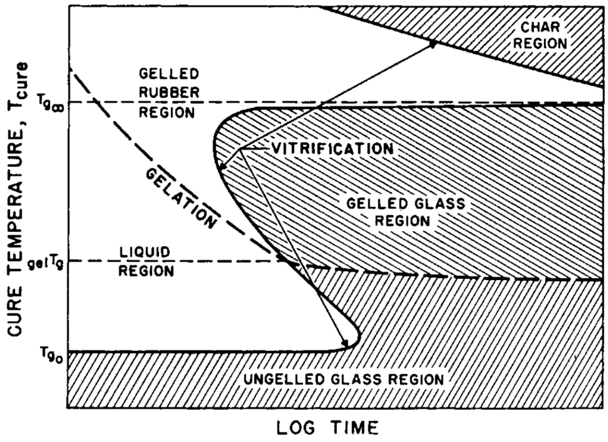

Figure 2-1 Generalized time-temperature-transformation (TTT) cure diagram. Regions showing vitrified material state are shaded. The vitrified region above T_{g0} (char region) can occur in some resin systems as a result of degradation [4].

the final shape of the part. Further resin flow to compensate apparent volume change within the part is not possible anymore [54]. The final state of the resin will either be solid/rubbery or solid/glassy, depending on the relation of the material's temperature to its glass transition temperature T_g if the gelation occurred, since the latter is irreversible.

Cross-linking of the chemical network results in an increase of the glass transition temperature from its initial value T_{g0}. Once the T_g reaches the cure temperature of the laminate T_{cure} vitrification sets in, resulting in a glassy energy elastic state [55]. Vitrification is a gradual, thermo-reversible process, leading to a restriction of the motion of the free polymer chains in the vitrified state [56]. Thus, it marks the transformation from rubber to a gelled glass (post gelation) or from a liquid to an ungelled glass (prior to gelation). If the resin temperature is below the glass transition temperature T_g, the chemical reaction proceeds diffusion-controlled, resulting in a highly decreased rate of polymerization [57]. In order to fully cure a resin system, it is thus required to expose the resin to a cure temperature close to the maximal glass transition temperature of the fully cured system $T_{g\infty}$. If the cure temperature T_{cure} is significantly lower than $T_{g\infty}$, most resin systems will not reach full polymerization in a reasonable time frame [54]. In contrast, if the cure temperature is elevated far above $T_{g\infty}$, the limit of thermal stability is reached resulting in material degradation.

In order to simulate the entire cure process of a CFRP part, the material models are required to incorporate both dependencies temperature and degree of cure. Therefore, a resin kinetics model, describing the advance of the degree of cure as a function of time and temperature, is inherently a key part of the cure simulation.

2.1.1 Cure Kinetics

Chemical cross-linking leads to a release of exothermic reaction energy during the cure of a thermoset resin system. With the assumption that the amount of released energy relates to a distinct progress state of the chemical cross-linking, the progress of the chemical reaction α can be defined as the ratio of released heat to the ultimate heat of reaction H_r [58].

$$\alpha = \frac{1}{H_\mathrm{r}} \int \dot{q}(t)dt \tag{2-1}$$

This ratio α is defined as the degree of cure, which ranges between zero (uncured) and unity (cured). Thus, the instantaneous amount of heat released $\dot{q}(t)$ is defined by the rate of reaction $\dot{\alpha}$. Two different forms of kinetic models are essentially used to describe thermoset curing reactions: phenomenological and mechanistic models [59]. As the latter require the full knowledge on the resin constituents, the former are mostly used in applied science and engineering. In general, phenomenological models define the cure rate as a function of degree of cure and temperature.

$$\dot{\alpha} = f(\alpha,T) \tag{2-2}$$

The temperature dependency in phenomenological models is mostly defined by an Arrhenius equation:

$$K = A\, \mathrm{e}^{\frac{-\Delta E}{R\,T}} \tag{2-3}$$

where ΔE denotes the activation energy, R the universal gas constant, and A the Arrhenius model constant.

An overview of the large variety of previously developed cure kinetic models is found in the literature [59, 60]. A vast majority of those models can be attributed to the following roots: Starting with the basic formula of an nth-order reaction with the reaction peak at $\alpha = 0$,

$$\dot{\alpha} = K\,(1-\alpha)^n \tag{2-4}$$

and the autocatalytic reaction with a reaction peak at 30% - 40% conversion [58],

$$\dot{\alpha} = K\,\alpha^m(1-\alpha)^n \tag{2-5}$$

Kamal and Sourour were the first to use reaction orders m and n as fitting variables and combined these two equations into a single model [61, 62]:

$$\dot{\alpha} = (K_1 + K_2\,\alpha^m)(1-\alpha)^n \tag{2-6}$$

Most recent models incorporate a linear combination of multiple independent reactions, which was first established by Lee et al., summing up an nth-order and an autocatalytic reaction [63].

$$\dot{\alpha} = \sum_{k}^{n} f_k(\alpha,T) \tag{2-7}$$

The consideration of the glass transition temperature on the cure rate requires additional enhancement of the cure kinetic models. If the glass transition temperature reaches cure temperature, the resin changes from a rubbery to a glassy state. Whereas the cure reaction is governed by chemical kinetics only prior to vitrification, the cure reaction proceeds diffusion controlled in the glassy state due to the restricted mobility of the reactive polymer groups [64, 65]. Several approaches were developed to consider diffusion behavior. Williams simply set the cure rate in the glassy state to zero [66]. Gonzales-Romero and others subtracted the degree of cure from a maximal degree of cure instead of unity in the autocatalytic formulation (see. Eq. 2-6) [35, 38, 67, 68]. Cole extended a previously developed formulation, based on free volume consideration, to determine a diffusion controlled rate constant K_d under the assumption of equal temperature dependency of K_d and the unconstrained rate constant of the chemical reaction K_c [69–72]:

$$K_\mathrm{d} = K_\mathrm{c}\, \mathrm{e}^{-C\,(\alpha-\alpha_\mathrm{c})} \tag{2-8}$$

Herein, α_c determines the diffusion control onset which Cole extended to be a linear function of temperature. Whereas in reality the onset of diffusion is gradual, this equation leads to a rather abrupt onset of the diffusion control at $\alpha = \alpha_\mathrm{c}$. An alternative to the above equation is given by Simon and Gillham [73]:

$$K_\mathrm{d} = A_\mathrm{d}\, \mathrm{e}^{-\frac{E_\mathrm{d}}{E\,T}-\frac{b}{f}} \tag{2-9}$$

where A_d resembles constants of the diffusion process, E_d is the activation energy of the diffusion process and f the equilibrium fractional free volume, given by:

$$f = a\,(T - T_\mathrm{g}) + b \tag{2-10}$$

with the model constants $a = 4.8E-4$ and $b = 2.5E-2$. The effective rate constant K_e is henceforth determined by application of the Rabinowitch equation [74]:

$$\frac{1}{K_\mathrm{e}} = \frac{1}{K_\mathrm{c}} + \frac{1}{K_\mathrm{d}} \tag{2-11}$$

In diffusion models which require the calculation of glass transition temperature T_g, such as the one presented in Equation 2-9, the DiBenedetto equation is mostly chosen to calculate T_g [75, 76]:

$$T_g(\alpha) = T_{g0} + \frac{\alpha\lambda(T_{g\infty} - T_{g0})}{1 - (1 - \lambda)\alpha} \tag{2-12}$$

The fitting constant λ is set between zero and unity. Early literature proposes the specific heat ratio between glassy and rubbery state to define the value. In recent works this approach is often dropped for superior phenomenologically determined values [77–79].

2.1.2 Thermal Properties

Three thermal properties are required to solve a heat transport problem: density, specific heat and thermal conductivity. Although it has been known that these properties depend on the degree of cure and the temperature [80], they were modeled as constant in many early cure simulation investigations resulting in reasonable fits to experimental data [37, 38, 43, 81–88], despite the fact that Shin and Hahn showed an increased simulation accuracy with temperature and degree of cure dependent property models [89]. Inclusion was proposed with a linear dependence of the thermal property ζ on the degree of cure α and the temperature T [44, 66, 90, 91]:

$$\zeta = C_0 + C_1\,T + C_2\,\alpha + C_3\,T\,\alpha \tag{2-13}$$

where C_0, C_1, C_2 and C_3 denote model constants. Although vitrification was not considered in the above mentioned publications, Johnston included a constant value for the specific heat above the glass transition temperature [17]. In order to fully capture the effect of vitrification on the specific heat, more recent models utilize sigmoid functions to describe the glass transition with linear dependencies on temperature and degree of cure in the rubbery and glass state, respectively [92, 93].

If resin and fiber data were characterized separately, the laminate properties have to be determined by means of micro-mechanic models. For specific heat, density and heat conductivity in fiber direction, Rule of Mixtures (ROM) proved to be sufficiently accurate [17, 82].

To calculate laminate transverse conductivity, a variety of models exist in literature. These models can be attributed to either an electrical resistance analogy or a potential theory approach [94]. A widely spread method, which was also applied in the author's work, is the Springer-Tsai model [95] in the corrected form of Twardowski [82]:

$$k_{2\mathrm{c}} = k_\mathrm{r} \left\{ \left(1 - 2\sqrt{\frac{V_\mathrm{f}}{\pi}} \right) + \frac{1}{B} \left[\pi - \frac{4}{\sqrt{1 - B^2 \frac{V_\mathrm{f}}{\pi}}} \cot \frac{\sqrt{1 - B^2 \frac{V_\mathrm{f}}{\pi}}}{1 + B \frac{V_\mathrm{f}}{\pi}} \right] \right\} \tag{2-14}$$

where the fiber volume fraction is denoted as V_f, the thermal conductivities of the compound as k_c, the resin and fiber transverse conductivities as k_r and $k_{2\mathrm{f}}$ and the factor B is calculated as follows:

$$B = 2 \left(\frac{k_\mathrm{r}}{k_{2\mathrm{f}} - 1} \right) \tag{2-15}$$

2.1.3 Volumetric Changes

Apparent volumetric changes in composite manufacture are attributed to two different causes: reversible thermal expansion and irreversible polymerization shrinkage [96].

$$\left(\frac{1}{V_0} \frac{dV}{dt} \right)_\mathrm{Overall} = \left(\frac{1}{V_0} \frac{dV}{dt} \right)_\mathrm{Thermal\ Expansion} - \left(\frac{1}{V_0} \frac{dV}{dt} \right)_\mathrm{Polymerization\ Shrinkage} \tag{2-16}$$

Thermal Expansion

Similar to the thermal properties, the thermal strain is modeled in literature with either two constant values above and below vitrification [43, 97, 98] or a linear dependence of the resin's coefficient of thermal expansion (CTE) on the temperature and degree of cure [99]:

$$\epsilon_\mathrm{th} = CTE_\mathrm{r}\ \Delta T = [C_0 + C_1(T - T_0) + C_2(\alpha - \alpha_0)]\ \Delta T \tag{2-17}$$

Experimental data in literature does not give evidence to a common trend of the resin thermal expansion regarding its degree of cure dependency: White and Hahn determined the thermal strains experimentally and found them to be independent of the degree of cure in longitudinal as well as transverse direction of the composite [100, 101]. On the other hand, Hill et al. proposed a degree of cure dependency in the thermal expansion model [96]. Experimental work of Khoun et al. showed a trend towards lower coefficients of thermal expansion of neat resin with increasing degree of cure above glass transition [79]. No degree of cure dependency below glass transition was experienced in this work.

Regarding temperature dependency, most of the above mentioned sources state it to be negligible, whereas other researchers highlight a significant temperature dependency of the coefficient of thermal expansion [102–105].

Once the coefficient of thermal expansion of the resin CTE_r and fiber in longitudinal and transverse direction CTE_1f and CTE_2f are determined, ply thermal expansion can be calculated with the self-consistent field micro-mechanics model, utilizing the constituents modulus E and Poisson's ratio ν [43, 106]. This results in the following expression for the longitudinal coefficient of thermal expansion of the ply CTE_1:

$$CTE_1 = \frac{CTE_\mathrm{1f}\, E_\mathrm{11f}\, V_\mathrm{f} \; + \; CTE_\mathrm{r}\, E_\mathrm{r}\, (1 - V_\mathrm{f})}{E_\mathrm{11f}\, V_\mathrm{f} \; + \; E_\mathrm{r}\, (1 - V_\mathrm{f})} \tag{2-18}$$

and the transverse thermal expansion coefficient of the ply CTE_2:

$$\begin{aligned} CTE_2 = {} & (CTE_\mathrm{2f} + \nu_\mathrm{13f}\, CTE_\mathrm{1f})\, V_\mathrm{f} + (CTE_\mathrm{r} + \nu_\mathrm{r} CTE_\mathrm{r})(1 - V_\mathrm{f}) \\ & - (\nu_\mathrm{13f} V_\mathrm{f} + \nu_\mathrm{r}(1 - V_\mathrm{f})) \left[\frac{CTE_\mathrm{1f} E_\mathrm{1f} V_\mathrm{f} + CTE_\mathrm{r} E_\mathrm{r}(1 - V_\mathrm{f})}{E_1 V_\mathrm{f} + E_\mathrm{r}(1 - V_\mathrm{f})} \right] \end{aligned} \tag{2-19}$$

where V_f denotes the fiber volume content in these equations.

Polymerization Shrinkage

Thermoset resins are subjected to a density increase and corresponding volume reduction during polymerization, referred to as chemical shrinkage [107]. Some works determined the chemical shrinkage to be a linear or bilinear function of the degree of cure [43, 97, 108–110]. Other experimental data showed that the shrinkage is nonlinear with the degree of cure and completed before the resin is fully cured [96, 101]. Later models assume a linear relationship between shrinkage and the degree of cure in-between the gel point $\alpha_\mathrm{gel} > 0$ and the final degree of cure after which no further shrinkage occurs $\alpha_\mathrm{fs} < 1$ [11]:

$$\left(\frac{1}{V_0}\frac{\Delta V}{V}\right)_\mathrm{Shrinkage} = 0 \qquad \alpha \leq \alpha_\mathrm{gel} \tag{2-20}$$

$$\left(\frac{1}{V_0}\frac{\Delta V}{V}\right)_\mathrm{Shrinkage} = \left(\frac{\alpha - \alpha_\mathrm{gel}}{\alpha_\mathrm{fs} - \alpha_\mathrm{gel}}\right)\left(\frac{1}{V_0}\frac{\Delta V}{V}\right)_\mathrm{Total} \qquad \alpha_\mathrm{gel} < \alpha < \alpha_\mathrm{fs} \tag{2-21}$$

$$\left(\frac{1}{V_0}\frac{\Delta V}{V}\right)_\mathrm{Shrinkage} = \left(\frac{1}{V_0}\frac{\Delta V}{V}\right)_\mathrm{Total} \qquad \alpha \geq \alpha_\mathrm{fs} \tag{2-22}$$

where $(\Delta V/V)_{\mathrm{Total}}$ is the total volumetric shrinkage of the resin $V_{\mathrm{r}}^{\mathrm{s}}$. The assumption of negligible cure prior to gelation in these models was introduced due to the chosen experimental technique which allowed measurements in solid state only. In a comparison of different shrinkage measurement techniques, Khoun and Hubert showed the occurrence of a significant amount of shrinkage prior to gelation [111]. The necessity of modeling shrinkage prior to gelation in a process simulation is dependent on the manufacturing process: The case study in Chapter 7 investigates an RTM process, in which volume shrinkage prior to gelation is compensated for by a post-infiltration resin flow into the part. In this case the assumption of negligible resin volume change in the part prior to gelation is valid. This assumption might become inaccurate if large degree-of-cure gradients are present in the part.

Ply volumetric change due to shrinkage can be calculated similar to thermal expansions with help of a cure shrinkage coefficient CSC and micro-mechanic models [17, 43, 106]. With the resin linear cure shrinkage strains $\epsilon_{\mathrm{r}}^{\mathrm{s}}$,

$$\epsilon_{\mathrm{r}}^{\mathrm{s}} = (1 + V_{\mathrm{r}}^{\mathrm{s}})^{1/3} - 1 \tag{2-23}$$

the strains in the principal direction i of the ply due to chemical shrinkage are determined as follows:

$$\epsilon_{i}^{\mathrm{s}} = CSC_{i}\, \epsilon_{\mathrm{r}}^{\mathrm{s}} \tag{2-24}$$

Herein, the cure shrinkage coefficients are calculated by means of micro-mechanical models similar to their thermal counterparts:

$$CSC_1 = \frac{(1 - V_{\mathrm{f}})E_{\mathrm{r}}}{V_{\mathrm{f}}E_{11\mathrm{f}} + (1 - V_{\mathrm{f}})E_{\mathrm{r}}} \tag{2-25}$$

$$CSC_2 = (1 + \nu_{\mathrm{r}})(1 - V_{\mathrm{f}}) - (\nu_{12\mathrm{f}}V_{\mathrm{f}} + \nu_{\mathrm{r}}(1 - V_{\mathrm{f}}))CSC_1 \tag{2-26}$$

Due to the high longitudinal stiffness of the carbon fiber, this yields in very small strains in the 1-direction of a unidirectional ply [43].

2.1.4 Mechanical Properties

During the cure of the laminate, the resin transforms from a liquid state to a rubbery and finally to a glassy state. The Young's modulus as well as the shear modulus increase by several magnitudes and the Poisson's ratio decreases from the initial value of 0.5, which applies in an incompressible medium [43]. The resin responds in a viscoelastic manner with a dependency on the degree of cure and temperature [46, 101, 105, 112–117]. Given that viscoelastic formulations are computational expensive [118], simplified formulations with varying complexity were developed for the simulation of process-induced stresses and deformation of composite structures [104, 119–122], if it was considered at all. Bogetti and others employed the later called Cure Hardening Instantaneous Linear Elastic (CHILE) material model to predict the modulus development [43, 68, 123] in the prediction of residual stresses in composite processing. In this model, the instantaneous isotropic resin modulus is expressed explicitly as a function of the degree of cure. Johnston extended this model by a temperature shift factor to introduce the effect of temperature. The degree of cure was converted into an expression T^* describing the deviation between glass transition temperature and resin temperature, which resulted in an excellent model fit for the resin investigated [17]:

$$\bar{E}_\mathrm{r} = E_\mathrm{r}^0 \qquad T^* < T^*_\mathrm{c1} \tag{2-27}$$

$$\bar{E}_\mathrm{r} = E_\mathrm{r}^0 + \frac{T^* - T^*_\mathrm{c1}}{T^*_\mathrm{c2} - T^*_\mathrm{c1}}(E_\mathrm{r}^\infty - E_\mathrm{r}^0) \qquad T^*_\mathrm{c1} < T^* < T^*_\mathrm{c2} \tag{2-28}$$

$$\bar{E}_\mathrm{r} = E_\mathrm{r}^\infty \qquad T^* > T^*_\mathrm{c2} \tag{2-29}$$

$$E_\mathrm{r} = \bar{E}_\mathrm{r}(1 + a_\mathrm{r}(T - T_0)) \tag{2-30}$$

where

$$T^* = (T_\mathrm{ga} - T_\mathrm{gb}\ \alpha) - T \tag{2-31}$$

$$T^*_\mathrm{c1} = T_\mathrm{c1a} + T_\mathrm{c1b}\ T \tag{2-32}$$

Herein, E_r^0 and E_r^∞ are the initial and final unrelaxed resin moduli and a_r, T_c1a, T_c1b, T^*_c2, T_ga, T_gb are model constants. A linear dependence of the glass transition temperature on the degree of cure is employed in this case (see Eq. 2-31). Recent models employed the DiBenedetto equation (Eq. 2-12) instead [8].

Given that the neat resin is isotropic, its mechanical behavior is determined with an additional independent model for the Poisson's ratio. For this purpose, several approaches are applied in literature: Bogetti assumed the Poisson's ratio of neat resin to be constant over the whole cure cycle [43]. Svanberg employed two distinct constant Poisson's ratios in glass and rubbery state [98], respectively. In contrast, Johnston used a constant bulk modulus assumption [17], thus gradually decreasing the Poisson ratio with cure:

$$\nu_\mathrm{r} = \frac{E_\mathrm{r}^\infty - E_\mathrm{r}(1 - 2\,\nu_r^\infty)}{2\,E_\mathrm{r}^\infty} \tag{2-33}$$

where E_r^∞ and ν_r^∞ define the final unrelaxed Young's modulus and the final Poisson's ratio of neat resin. The resin shear modulus is henceforth calculated by:

$$G_\mathrm{r} = \frac{E_\mathrm{r}}{2\,(1+\nu_\mathrm{r})} \tag{2-34}$$

The unidirectional mechanical behavior of the ply can be determined by the self-consistent field approach, with help of the transversely isotropic fiber properties (E_11f, E_22f, G_12f, ν_12f, ν_23f) and the isotropic resin properties (E_r, ν_r) [17, 43]. This leads to the following equation for the longitudinal Young's modulus:

$$E_{11} = E_\mathrm{11f}\,V_\mathrm{f} + E_\mathrm{r}\,(1-V_\mathrm{f}) + \left(\frac{4\,(\nu_\mathrm{r}-\nu_\mathrm{12f}^2)\,k_\mathrm{f}\,k_\mathrm{r}\,G_\mathrm{r}\,(1-V_\mathrm{f})\,V_\mathrm{f}}{(k_\mathrm{f}+G_\mathrm{r})\,k_\mathrm{r}+(k_\mathrm{f}-k_\mathrm{r})\,G_\mathrm{r}\,V_\mathrm{f}}\right) \tag{2-35}$$

The transverse Young's modulus:

$$E_{22} = \frac{1}{\frac{1}{4\,k_\mathrm{p}}+\frac{1}{4\,G_{23}}+\frac{\nu_{12}^2}{E_\mathrm{11f}}} \tag{2-36}$$

The major Poisson's ratio:

$$\nu_{12} = \nu_\mathrm{12f}\,V_\mathrm{f} + \nu_\mathrm{r}\,(1-V_\mathrm{f}) + \left(\frac{(\nu_\mathrm{r}-\nu_\mathrm{12f})\,(k_\mathrm{r}-k_\mathrm{f})\,G_\mathrm{r}\,(1-V_\mathrm{f})\,V_\mathrm{f}}{(k_\mathrm{f}+G_\mathrm{r})\,k_\mathrm{r}+(k_\mathrm{f}-k_\mathrm{r})\,G_\mathrm{r}\,V_\mathrm{f}}\right) \tag{2-37}$$

The minor Poisson's ratio:

$$\nu_{23} = \frac{2\,E_{11}\,k_\mathrm{p} - E_{11}\,E_{22} - 4\,\nu_{12}^2\,k_\mathrm{p}\,E_{22}}{2\,E_{11}\,k_\mathrm{p}} \tag{2-38}$$

And the transverse shear modulus:

$$G_{23} = \frac{G_\mathrm{r}\,[k_\mathrm{r}\,(G_\mathrm{r}+G_\mathrm{23f})+2\,G_\mathrm{23f}\,G_\mathrm{r}+k_\mathrm{r}\,(G_\mathrm{23f}-G_\mathrm{r})\,V_\mathrm{f}]}{k_\mathrm{r}\,(G_\mathrm{23f}+G_\mathrm{r})+2\,G_\mathrm{23f}\,G_\mathrm{r}-(k_\mathrm{r}+2\,G_\mathrm{r})\,(G_\mathrm{23f}-G_\mathrm{r})\,V_\mathrm{f}} \tag{2-39}$$

Whereas the isotropic plane strain bulk modulus of the resin k_r, the plane strain bulk modulus of the fiber k_f, and the effective plain strain bulk modulus of the ply k_p are defined by:

$$k_\mathrm{r} = \frac{E_\mathrm{r}}{2\,(1-\nu_\mathrm{r}-2\,\nu_\mathrm{r}^2)} \tag{2-40}$$

$$k_\mathrm{f} = \frac{E_\mathrm{11f}\,E_\mathrm{22f}}{2\,(1-\nu_\mathrm{23f})\,E_\mathrm{11f}-4\,\nu_\mathrm{12f}\,\nu_\mathrm{12f}\,E_\mathrm{22f}} \tag{2-41}$$

$$k_\mathrm{p} = \frac{(k_\mathrm{f}+G_\mathrm{r})\,k_\mathrm{r}+(k_\mathrm{f}-k_\mathrm{r})\,G_\mathrm{r}\,V_\mathrm{f}}{(k_\mathrm{f}+G_\mathrm{r})-(k_\mathrm{f}-k_\mathrm{r})\,V_\mathrm{f}} \tag{2-42}$$

2.2 Effects of the Manufacturing Process on the Laminate Quality

Spring-in and warpage of fiber reinforced laminates are the two most prominent process-induced deformation modes in CFRP part manufacturing and led to a large number of investigations in the literature, ranging from analytical expressions to fully 3D coupled thermo-chemo-viscoelastic finite element simulations (among others: [17, 32, 118, 124–141]). These deformations are a result of residual stress introduced during the laminate manufacturing process by the following sources [17, 32, 127, 142]:

- Thermal expansion of the part
- Resin cure shrinkage
- Gradients in temperature, degree of cure, and fiber volume content
- Thermal tool expansion and tool-part interaction

The influence of the thermal expansion of the part on residual stress build-up was subject of early studies that neglect the impact of temperature gradients, which is applicable for thin laminates only [143, 144]. Given that the resin gels at an elevated temperature, the part is subjected to a temperature discrepancy between its stress-free net-shape state and its actual operating state. Material anisotropy leads to CTE anisotropy, which drives a directional negative thermal expansion during cool-down, resulting in a part distortion.

Volumetric resin cure shrinkage results in a reduction of the part's dimensions. Due to directional laminate stiffness, the resulting ply strains in fiber direction are small compared to the perpendicular fiber direction of a ply. The effect of shrinkage is thus similar to the effect of decreasing part temperature [17].

In thick laminates temperature gradients and accompanying cure gradients can occur, which contribute to the development of stress and deformation due to the spatially varying material response [39]. If non-uniform cure is present, three different scenarios may occur, shown in Figure 2-2: (a) $outside-to-inside$ cure, (b) $inside-to-outside$ cure and (c) $One-sided$ cure [5]. Scenario (a) can lead to entrapped voids or volatile by-products of the curing resin and delaminations because the cured exterior region constrains the interior region [36, 44]. $inside-to-outside$ cure occurs at lower set-point temperatures than $outside-to-inside$ cure. If the part interior gels earlier than the part surface, it leads to compression stresses in the core, which is favorable over the transverse tension stresses arising in scenario (a). However, the final degree of cure can be lower in some resin systems if $inside-to-outside$ cure is chosen [5]. Finally, $one-sided$ cure (c) is induced if different mold temperatures are chosen on the top and bottom side of the laminate. Whereas this cure strategy leads to lower curing times without increasing the exothermic peak temperature, the residual stresses in thickness direction are not balanced, resulting in part distortion [5]. All of these cure strategies lead to an increase in residual stress compared to a uniform curing that causes a reduction in the laminate load carrying capability in general and may result in part distortion, delamination, microcracks, and void formation in particular [43, 145, 146].

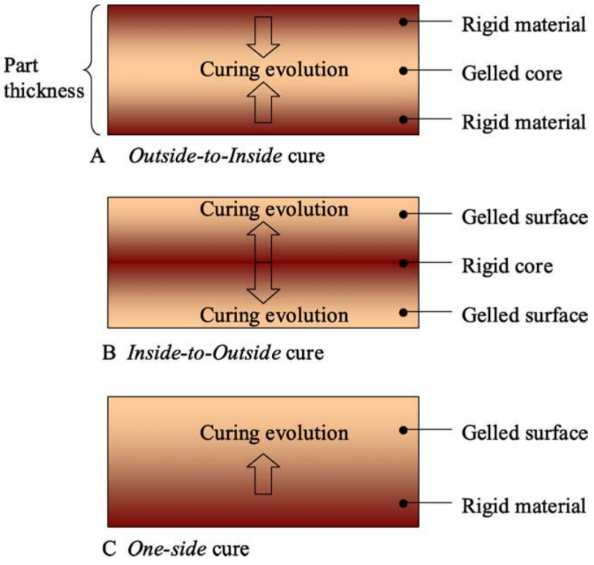

Figure 2-2 Possible non-uniform cure scenarios [5].

Fiber volume gradients in thickness direction, occurring in for example manufacturing processes using vacuum bags, can result in fiber volume content deviations by several percent as shown by Radford and others [108, 124, 126]. Hubert demonstrated that pressure gradients may induce an uneven resin flow. In an autoclave set-up this can result in local laminate thickness variations as well as fiber volume gradients, especially in the presence of resin bleed [147]. Since the laminate stiffness is defined by the fiber volume content, these gradients lead to unsymmetrical laminate layup and warpage after the cool-down. In order to improve the mechanical properties, Naji and Hoa showed that the cure cycle has an effect on the fiber volume content and developed a modified curing process to gain uniform part thickness and fiber volume content [148, 149].

If CFRP laminates are produced on a metal tool, the tool features a significantly higher thermal expansion coefficient compared to the part in most cases, depending on the tool material. Thus, fibers close to the tool part interface exhibit stress since they are pressed onto the tool surface by the autoclave pressure and both tool and part are subjected to thermal expansion (see Figure 2-3).

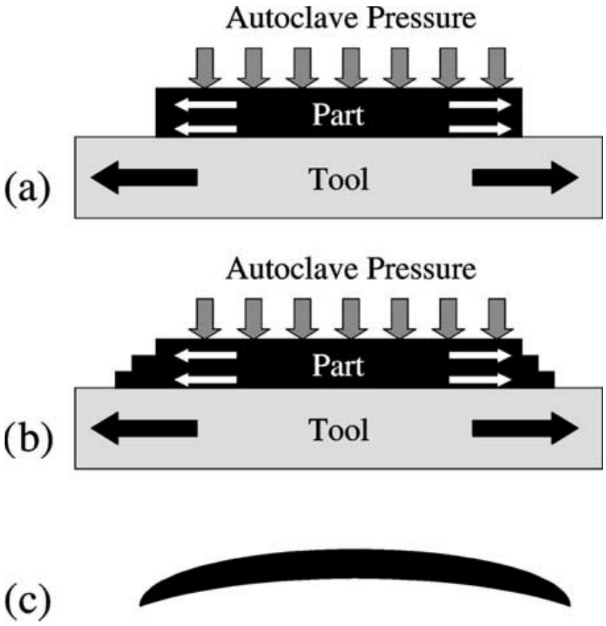

Figure 2-3 Sketch of warpage mechanism due to tool-part interaction [6].

This stress state decreases in thickness direction with increasing distance from the tool surface as the stress transfer in-between the fibers is poor [150]. Only the first layers follow the tool deformation. These stresses are "cured-in" and will be released upon demolding and, thus, result in part warpage as shown in Figure 2-3 (c) [6, 151]. To demonstrate this mechanism, Albert and Fernlund investigated the utilization of a fluorinated ethylene propylene (FEP) release sheet in-between tool and part with the result of significantly decreased spring-in of L- and C-shaped specimen [128]. If the tool material shows a similar thermal expansion as the part, this tool-part effect vanishes since the induced strain in the part due to tool-part interaction becomes very small. This is a major reason for the utilization of tools with low CTE, such as CFRP and Invar [152].

Moisture causes swelling leading to a geometrical volume change, which results in similar effects as cool-down or shrinkage. It has not been included in the description above due to its reversibility and absence in most production processes using epoxy resin systems [153]. However, if the chemical resin reaction mechanism is polycondensation, the dependency of the resin properties on moisture has to be considered, given that water is a byproduct of the resin reaction.

Overall, the residual stresses in the laminate during cure, cool-down, and after demolding are a result of the transient stress and strain build-up during the whole production process. Compensation of different mechanisms can occur. Viscoelastic resin behavior results in a reduction of the residual stress in general, but the impact depends on the resin itself as well as the applied cure cycle [117, 154]. In order to reduce residual stresses and improve laminate quality, the investigations conducted found a homogeneous temperature and degree of cure evolution to be highly beneficial. Thus, the optimization of manufacturing processes to improve part laminate quality targets the reduction of temperature and degree of cure gradients in most cases [38, 41, 146, 155, 156].

2.3 Process Simulation

Process simulation is a powerful method to understand and predict the temperature and material property development during cure. Hahn and Pagano investigated curing stresses in the seventies already, using the laminate plate theory to calculate thermal stress during cool-down [143]. Loos and Springer were the first to implement a numerical analysis to determine the temperature and degree of cure evolution as well as resin flow for a prepreg material [157]. Many researchers followed their work, utilizing various calculation techniques for the process analysis of all major CFRP manufacturing processes.

The finite difference method allows a computational efficient analysis of the thermal, mechanical, and cure behavior and, therefore, has been utilized in early numerical residual stress investigations [43, 82, 97, 101, 158, 159]. To account for more complex geometries, two-dimensional finite element formulations have been developed by Johnston to calculate thermal and mechanical laminate behavior during cure [17, 32, 160], as well as by Hubert to determine the flow and compaction behavior [161, 162]. Both were implemented in a stand-alone program called COMPRO [163]. Later, their analysis routines were transferred into commercial three-dimensional finite element programs such as Abaqus [7] and made commercially available (COMPRO Component Architecture (CCA) [163]).

2.3.1 Thermal and Cure Analysis

Two approaches are found in literature to describe the thermal transport: the two-phase model and the local equilibrium model [44, 164, 165]. The two-phase model separates the energy balance equations for fiber and resin and applies an experimentally determined heat transfer coefficient to define the interface. The local equilibrium model assumes that the fiber and resin have the same temperature locally. This assumption is valid if the heat transfer coefficient between the fiber and the resin is large or the resin flow is slow, which is characteristic for most manufacturing processes, and this assumption is thus used in the context of this work [164, 166]. The transient anisotropic Fourier equation is governing the heat transport in the laminate. It is written in Cartesian coordinates as follows [165]:

$$\rho(\mathbf{r})c_{\mathrm{p}}(\mathbf{r})\frac{\partial T(\mathbf{r},t)}{\partial t} = \nabla \cdot (k(\mathbf{r})\nabla T(\mathbf{r},t)) + \dot{q}_{\mathrm{s}}(\mathbf{r}) \tag{2-43}$$

where c_{p} is the specific heat, ρ the density, k the thermal conductivity, T the temperature and t the time. The heat source term $\dot{q}_{\mathrm{s}}(\mathbf{r})$ is defined by the exothermic resin reaction and resembles the volumetric heat flow. Utilizing Equation 2-1, the volumetric heat generation in a laminate $\dot{q}_{\mathrm{s}}(\mathbf{r})$ is calculated as follows [17]:

$$\dot{q}_{\mathrm{s}}(\mathbf{r}) = \rho_{\mathrm{r}}\, \dot{\alpha}(1 - V_{\mathrm{f}})\, H_{\mathrm{r}} \tag{2-44}$$

where ρ_{r} denotes the resin density, and H_{r} the total amount of releasable heat of the chemical reaction. The cure rate $\dot{\alpha}$ is defined by a resin kinetics model as explained in Chapter 2.1.1.

In order to model the different manufacturing technologies, tool modeling in combination with a set of appropriate boundary conditions is required for most cases, given that thermal conductance and thermal mass of the tool have a significant impact on the resulting part surface temperature field [167]. A variety of boundary conditions have been chosen in literature: Standard Dirichlet, Neumann or a combination (Cauchy) boundary condition are often used due to their simplicity and applicability for a wide range of problems. In the scalar formulation using a local coordination system with the n-axis in the normal direction of the surface this leads to [168]:

- Prescribed temperature on the boundary domain Γ:

$$T = T(t) \tag{2-45}$$

- Isolation on the boundary domain:

$$\frac{\partial T}{\partial n} = 0 \tag{2-46}$$

- Heat conduction on the boundary domain:

$$-k_{\mathrm{n}}\frac{\partial T}{\partial n} = \dot{q} \tag{2-47}$$

- Convection on the boundary domain:

$$-k_{\mathrm{n}}\frac{\partial T}{\partial n} = -h_{\Gamma}(T - T_{\infty}) \tag{2-48}$$

where h_{Γ} is the convective heat transfer coefficient. In case of a closed metal tool with a high thermal conductivity and significantly larger thermal mass compared to the part (e.g. RTM), the tool can act as a heat sink in case of exothermic resin reactions so that a prescribed temperature is sufficient during the heat-up and dwell [164, 169]. If no active cooling device is used, the cool-down is governed by convection and should be modeled with Equation 2-48 [170]. In this case, the convection coefficient h_{Γ} is dependent on the air flow around the tool. It is either determined experimentally or by means of computational fluid dynamic (CFD) simulations for applications with industrial complexity level. Autoclave processes are typically modeled with convective boundary conditions (Eq. 2-48), as well. The heat transfer coefficient h_{Γ} can deviate significantly within the autoclave, depending on the dimensions, loading, pressure, and to a lesser degree, temperature [17]. Thus, similar difficulties as in case of free convection arise in the determination of its value. The standard boundary conditions mentioned above are not applicable if energy control mechanisms are used to regulate temperature, which require additional modeling effort [171].

2.3.2 Stress and Deformation Analysis

Residual stresses can be calculated by means of the classical laminate theory (CLT) for both the thermoelastic calculation of cool-down stresses as well as the incremental approach within a process simulation [5, 43, 143]. With the temperature and the degree of cure as input from the cure analysis, the two-dimensional uni-directional (UD) ply properties given in the local ply coordinates (1, 2) are translated into the two-dimensional global laminate coordination system (x, y) as follows:

$$\mathbf{Q}_{\mathrm{xy}} = \mathbf{T}_{\mathrm{Q}}^{-1}\,\mathbf{Q}_{12}\,\mathbf{T}_{\mathrm{Q}}^{-T} \tag{2-49}$$

where $\mathbf{Q}$ denotes the ply stiffness. The transformation matrices are defined as follows [172]:

$$\mathbf{T}_{\mathrm{Q}}^{-1} = \begin{bmatrix} \cos^2(\theta) & \sin^2(\theta) & -2\sin(\theta)\cos(\theta) \\ \sin^2(\theta) & \cos^2(\theta) & 2\sin(\theta)\cos(\theta) \\ \sin(\theta)\cos(\theta) & -\sin(\theta)\cos(\theta) & \cos(\theta)^2 - \sin(\theta)^2 \end{bmatrix} \tag{2-50}$$

The coefficient of thermal expansion *CTE* and coefficient of chemical shrinkage *CSC* has to be transformed from the ply coordinates into the laminate coordinates with the following equations, as well [172]:

$$CTE_{\mathrm{x}} = \cos^2(\theta)\, CTE_1 + \sin^2(\theta)\, CTE_2 \tag{2-51}$$

$$CTE_{\mathrm{y}} = \sin^2(\theta)\, CTE_1 + \cos^2(\theta)\, CTE_2 \tag{2-52}$$

$$CTE_{\mathrm{xy}} = \sin(2\theta)\, CTE_1 - \sin(2\theta)\, CTE_2 \tag{2-53}$$

With the assumption of a uniform distribution of the in-plane strains through the laminate thickness, the summation of integrated stresses in thickness direction gives the resulting laminate forces **n** and moments **m** due to the non-mechanical strains $\epsilon_{\mathrm{nm,xy}}$:

$$\mathbf{n} = \sum_{i=1}^{n_{\mathrm{plies}}} \int_{z_i-1}^{z_k} \mathbf{Q}^i_{\mathrm{xy}}\, \epsilon^i_{\mathrm{nm,xy}}\, dz \tag{2-54}$$

$$\mathbf{m} = \sum_{i=1}^{n_{\mathrm{plies}}} \int_{z_i-1}^{z_k} \mathbf{Q}^i_{\mathrm{xy}}\, \epsilon^i_{\mathrm{nm,xy}}\, z\, dz \tag{2-55}$$

where non-mechanical ply strains in the absence of moisture are calculated as follows [17]:

$$\epsilon_{\mathrm{nm,\,xy}} = CTE_{\mathrm{xy}}\, \Delta T + CSC_{\mathrm{xy}}\, \Delta\epsilon^{\mathrm{s}}_{\mathrm{r}} \tag{2-56}$$

Here, $\Delta\epsilon^{\mathrm{s}}_{\mathrm{r}}$ is the linear cure shrinkage strain as defined in Equation 2-22. In the unconstrained case, the laminate strain can directly be calculated from the laminate forces and moments with help of the laminate compliance. Finally, the residual stress of each ply *i* is derived from the ply strain by subtraction of the non-mechanical strains:

$$\sigma^i_{\mathrm{res,xy}} = \mathbf{Q}^i_{\mathrm{xy}}\, (\epsilon^i_{\mathrm{xy}} - \epsilon^i_{\mathrm{nm,xy}}) \tag{2-57}$$

Additional to the internal stress resulting from cure shrinkage and thermal expansion, incremental process simulation approaches are capable of considering external stresses originating from the tool, as well. Thus, care in the modeling of the boundary conditions is required to appropriately incorporate the effect of the tool in the process simulation. Johnston implemented three different boundary conditions in the development of COMPRO: Fixed (prescription of zero nodal displacements), sliding (prescription of zero nodal displacement in normal direction of the surface), and free (zero nodal loads or constrains on the part boundary) boundary conditions [17]. Svanberg compared process simulations featuring these different boundary conditions with experimental determined spring-in values of L-shaped parts. He found the sliding contact condition to give the closest agreement [98]. In this case, the sliding condition was modeled as frictionless. Twigg investigated the tool-part interaction via experiment and simulation and modeled it with an elastic shear layer in-between tool and part [6, 173, 174]. The properties of the shear layer were fitted to give matching results of part warpage in simulation and experiment. However, this approach is not independent of the length of the part, which is the reason why Twigg proposed a stick-slip contact or elastic-plastic shear layer behavior as preferred solution. More recently, Khoun compared a stick-slip contact with free and fixed conditions for an RTM part and found the stick-slip tool-part interaction model to give the best agreement with experimental data [8]. If the part's boundary is not set free during the process simulation, a subsequent tool removal step is required in the analysis of process-induced deformations [17]. In this linear elastic step all constraints between tool and part are deleted. Thus, process-induced stresses are set free, resulting in part distortion.

2.3.3 COMPRO Component Architecture (CCA)

Although many other researchers implemented various two- and three-dimensional finite element cure and stress analyses [7, 68, 120, 125, 129, 175–179], the CCA package provides certain advantages thanks to its capability to include all important physical effects. Thus, it has been used for the finite element analysis conducted in this thesis, as well. The general set-up is shown in Figure 2-4 (a) and follows the modular approach, first proposed by Loos and Springer in which the complex problem of process modeling is divided into three sub-models [7, 157].

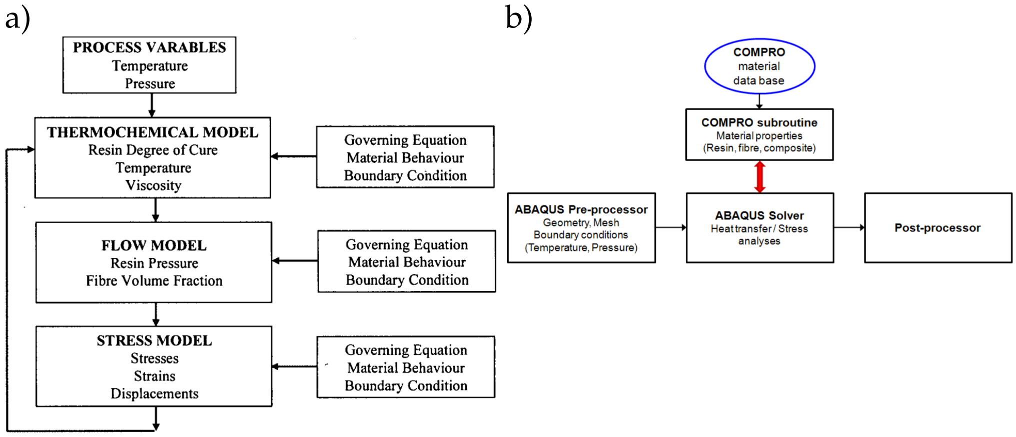

Figure 2-4 General structure of COMPRO: (a) Modular approach [7], (b) incorporation of subroutines in Abaqus [8].

To enable reasonable computational times for industrial applications, a full coupling in-between those modules is omitted and a sequential calculation is used instead: First, a thermal and cure analysis is conducted to determine the temperature and degree of cure field in the part. Second, resin flow and fiber bed compaction are calculated to determine fiber volume fractions and changes in laminate thickness. Third, a stress and deformation analysis gives results on residual stress and part distortion originating from the manufacturing process. Each of those modules are implemented in Abaqus via user-subroutines and can be run independently. The material data is included in an external database (see Fig 2-4 b). In the context of the present work fiber bed compaction was not considered as the targeted case study featured a closed mold RTM process, hence uniform fiber volume content was assumed.

2.4 Cure Cycle Optimization Techniques

In order to improve laminate quality, and reduce part distortion as well as processing time, many different process optimization tools have been developed in the past. Prior to the development of process simulation tools, cure cycle optimization involved an expensive and time-consuming experimental trial-and-error processes [180], which was conducted only on rare occasions [181, 182]. The introduction of the first numerical process analysis by Loos and Springer led to an investigation of the effects of different temperature cycles on the laminate quality [157]. Thus, the previously experimentally trial and error approach was henceforth mostly conducted by means of numerical process analysis tools [81, 183].

With help of numerical tools, Ciriscioli et al. found that the cure cycle recommended by the manufacturer is insufficient for thicker parts, and proposed reduced heating rates on the second ramp to reduce thermal gradients [184]. Kim and Lee introduced cooling and reheating steps to prevent temperature overshoots in thick autoclave laminates [185]. Chen et al. investigated the effect of moisture upon the optimal temperature path to achieve minimal residual stress [186]. These trial and error findings quickly showed that several process-related criteria have to be weighted against each other as they are contradictory: For instance, low overall temperatures result in low residual stresses but also in high processing times. Originating from this problem, several optimization strategies were investigated to find the optimal cure cycle for the processing of a given laminate. Two main approaches towards an optimal cure cycle are discussed in literature: The first approach results in a rule-based control of the manufacturing environment (e.g. autoclave) and is mostly referred to as "expert system" [187]. Here, a set of sensors is located in the most critical area of the part and the temperature and pressure is controlled according to previously determined simple rules, as shown in Figure 2-5. Thus, the final cure cycle is determined "on the fly" during the part production. The work on these "smart" cure strategies mostly includes an evaluation of process simulation to define the control rules and an initial set of process parameters [188, 189]. In contrast to this rule-based approach, others determined the cure cycle numerically a priori by means of increasingly sophisticated global optimization strategies utilizing process simulation and a multi-objective fitness function evaluation.

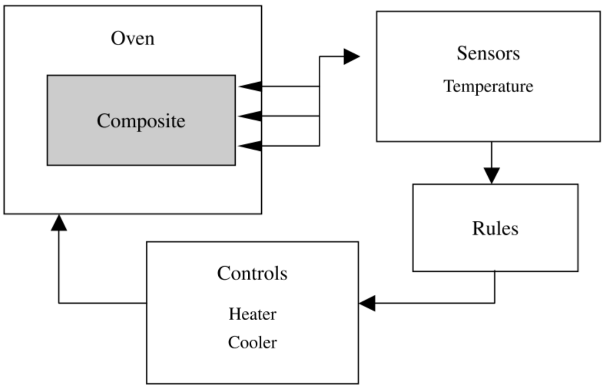

Figure 2-5 Control of the curing process in a rule-based heuristic system [9].

In an early work by Ciriscioli and Springer one of the first heuristic expert systems was set up, which takes composite temperature, compaction, residual stress and void formation in an autoclave into account [190]. In their work, the rule-based cure strategy was validated by means of cure simulations and experiments. However, they encountered difficulties in determining the viscosity and degree of cure online. Furthermore, at times different rules contradicting each other at certain cure states posed a challenge. Other researchers followed in using process simulation to set up a heuristic rule-based system to find optimal cure cycles with minimal residual stress [9, 156]. Sheen was one of the first to use numerical optimization to minimize the temperature gradients in a part by means of finite element simulation [191]. Pillai et al. developed a framework called "local criterion optimization" for the process simulation approach developed by Bogetti and Gillespie to determine an optimized cure cycle with help of a weighted optimization function considering the final degree of cure, maximum temperature, and residual stress [36, 41, 192]. Subsequent process trend analysis resulted in operating rules for the autoclave and ensured improved part quality as well as reproducibility. Thus, Pillai used numerical multi-objective process optimization to generate a rule-based framework for autoclave processing. In general, the different numerical optimization techniques employed can be divided in three categories:

- **Deterministic methods** (e.g. Nelder-Mead's or Powel's methods) calculate a local maximum or minimum of the fitness function with comparably low computational effort [40, 175, 193–195]. However, as the local extremum found might differ significantly from the global extremum, the quality of the result depends largely on the user-defined initial parameter set.
- On the contrary, **stochastic methods** (e.g. evolutionary strategy, random walk, simulated annealing, or genetic algorithms) employ random search techniques in the chosen design space [196]. They are more likely to find a global optimum but require more computational effort, which is the reason why they are often used in more recent studies [5, 197–201].
- **Neural network algorithms** [10, 202, 203] couple a set of input parameters (e.g. cure cycle time, heating rate, dwell temperature) with a set of output parameters (e.g. laminate quality and residual stress) using "hidden units", as shown in Fig. 2-6. These hidden units obtain information from the input units and proceed this information to the output units. The links in-between these units are weighted. The weight values have to be determined by training of the neural network.

Although the process simulation computational effort by means of neural networks is very small, the training of the weights needs to be extensive and typically requires at least several thousand and possibly up to millions of individual data sets, depending on the difficulty of the problem. As the amount of process simulations for teaching of the neural network alone exceeds the amount of simulations required by the other two methods to find an optimal cure cycle this method is recommended for use in special cases only where a very large number of investigations is required, such as process-interactive model-predictive monitoring and control or process investigations taking stochastic material variability into account [10, 204].

Independent of the method chosen, all numerical optimization algorithms are inherently reliant on the quality of the fitness function. The multi-objective fitness function F projects all assessment parameters J of interest for a given cure cycle, such as laminate quality and processing time, onto one value.

$$J \subset \mathbb{R}^n \land F : J \rightarrow \mathbb{R} \tag{2-58}$$

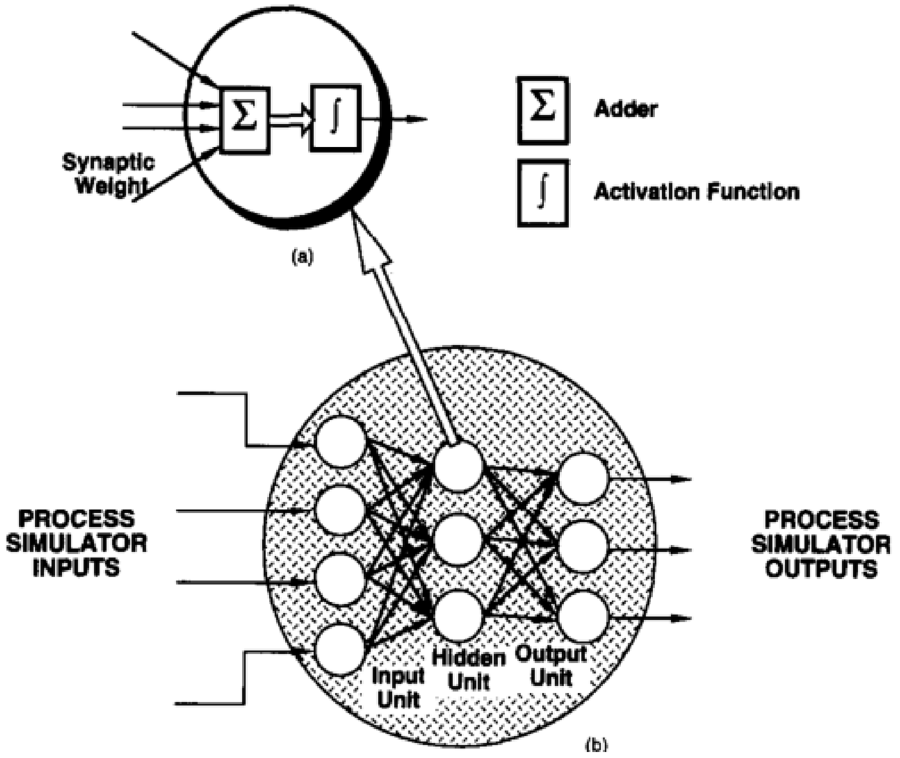

Figure 2-6 Functionality of neural networks [10].

The optimal solution is the global minimum or maximum of the fitness function, depending on the formulation of the problem. Within this work, the optimal solution is defined by the minimum of the fitness function:

$$\exists x \in \mathbb{R} : x = \min(F(J)) \tag{2-59}$$

A large variety of fitness parameters was used in the presented literature. Ruiz and Trochu developed one of the most diverse fitness functions in literature, which uses the weighted sum of seven different cure cycle assessment parameters [5, 146, 155].

$$F = \sum_{k=1}^{n} \omega_k J_\text{k} \tag{2-60}$$

The cure cycle assessment parameters used in this work were: the final extent of cure, the maximum obtained exothermic temperature, the cross-over at the after-gelation point (AGP), the degree of cure gradients, the induced curing stress, the thermal stress, and the processing time. Each individual parameter was expressed as a sigmoid function between zero and unity, with zero indicating the desired optimal state. In case of the final extent of cure the objective function is written as follows:

$$J_{\mathrm{fc}} = \frac{A_{\mathrm{fc}}}{B_{\mathrm{fc}} + \mathrm{e}^{g_{\mathrm{fc}}}} \tag{2-61}$$

$$g_{\mathrm{fc}} = -\frac{\alpha^{i}_{\mathrm{last}} - \alpha_{\mathrm{min}}}{\alpha_{\mathrm{min}}} \frac{C_{\mathrm{fc}}}{\alpha_{\mathrm{ult}} - \alpha_{\mathrm{min}}} \tag{2-62}$$

where $\alpha^{i}_{\mathrm{last}}$ is the minimal degree of cure apparent in the laminate, and α_{min} and α_{ult} the minimal required extent of cure and the ultimate degree of cure for which the resin is considered fully polymerized. A_{fc}, B_{fc} and C_{fc} are coefficients of the sigmoid function. These values are chosen dependent on the process specifications and material in question. For a given set of parameters, an exemplary objective function J_{fc} is shown in Figure 2-7.

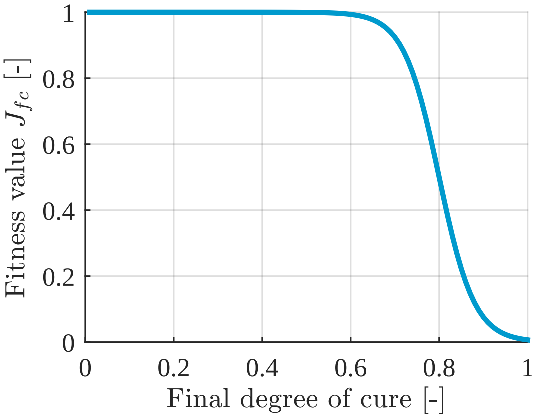

α_{min}	0.8
α_{ult}	0.95
A_{fc}	1
B_{fc}	1
C_{fc}	-3

Figure 2-7 & Table 2-1 Sigmoid function and corresponding coefficients for the final extent of cure objective.

The objective function presented in this figure leads to a preferred extent of cure between 0.9 and unity. The impact of this preference on the overall fitness function is defined by the magnitude of the weighting factor ω_{fc} in relation to all other weighting factors (see Eq. 2-60). Given that the produced parts are subjected to different requirements, the objective function coefficients as well as the weighing factors have to be set specifically for the target part: In the automobile industry the maximal cycle time restriction is set to several minutes whereas in the aerospace industry the maximal cycle time can be several hours. Thus, no overall best solution exists and the application of an optimization strategy to determine the cure cycle requires experience in the case-specific set-up of the fitness function.

Finally, the robustness of the optimized cure cycle should also be considered. As the manufacturing process as well as the material initial state are subjected to small variations, the determined cure cycle should lead to an optimal part even if these imperfections are considered. To account for batch-to-batch variation in the optimization process, Michaud investigated four different optimization techniques capable of finding the global optimum and improved an algorithm based on an evolutionary strategy [196]. In the investigation of 2.54 cm thick laminates, the resulting cure cycle led to a decrease of the amount of inferior parts by almost 80 % compared to optimization techniques neglecting batch-to-batch variation [38].

2.5 Summary

A wide variety of studies has been conducted to investigate the curing behavior of composite materials and its modeling. It was found that homogeneous part cure and, thus, homogeneous temperature distribution is critical to avoid delaminations, microcracks, void formation and contribute to reduced process-induced deformations. In order to utilize these findings and investigate part cure behavior, finite element approaches were developed, implemented, validated and, in some cases, made commercially available. Starting with these numerical investigation approaches, cure cycle optimization was conducted in literature to improve the part laminate quality. However, the literature review identified several gaps, which have to be addressed in order to fully investigate the thermal behavior of resistively heated CFRP tools and its impact on part cure in general as well as the targeted material system in particular:

1. For the targeted resin system Cytec CYCOM 823-1, which is used in the context of this work, neither sufficient characterization data nor the required material models for cure simulations are available in literature yet.
2. Most previous investigations feature traditional autoclave or RTM processes, in which the heat introduction is approximated with either direct temperature prescription or a heat transfer coefficient [8, 17, 164, 169, 205]. These traditional boundary conditions are not feasible in a simulation with temperature controlled, resistively heated CFRP tools. Since the thermal conductivity of the tool material CFRP is comparably low, significant tool temperature gradients can occur within these tools and have to be modeled accurately to investigate the cure processes. Studies on the impact of temperature controlled heat devices and their impact on part cure has not been undertaken yet in literature.
3. Few investigations were conducted to analyze and thermally dimension the thermal tool behavior for composite manufacturing [206, 207]. These stud-

ies focused on the thermal aspect and neglected exothermic resin reaction, which is applicable for thin laminates only, and prohibits investigations of the part's cure behavior. Therefore, a thermal dimensioning method is required considering the effect of resin reaction, tool and part thermal behavior as well as environmental effects such as convection.

4. Optimized temperature cycles have to be determined for the processing of thick laminates featuring the target resin system. Although a wide variety of optimization procedures is available in literature (e.g. [5, 36, 175, 193–195, 197–201]), these studies focus mostly on one overall cycle which is applied on a laminate of constant thickness. The tool technology investigated in this work can potentially apply multiple cycles in different part sections with varying thicknesses. Thus, a set of complementary optimal temperature cycles for these sections has to be determined, which has not been content of investigations available in literature to date.

3 Material Characterization

Given the lack of material models for the resin system CYCOM 823-1 RTM in literature, a material characterization had to be conducted in order to simulate the thermal and cure behavior of the case study in this thesis. The overall characterization methodology for composite processing was taken from literature [79] and slightly altered to fit to the characterization methods available and the particular resin system. To support future stress and deformation analyses of laminates featuring this resin system the mechanical properties, thermal expansion, and chemical shrinkage were characterized, as well. Since the cure analyses presented in Chapter 6 and 7 are reliant on the material models developed in this chapter, a thermal and cure validation is conducted to determine the accuracy of the material card.

The resin system CYCOM 823 is an RTM resin systems featuring low viscosity, high fracture toughness and already long shelf life at room temperature (4-5 days). The investigated derivative CYCOM 823-1 features highly increased shelf life at room temperature (>30 days) while maintaining similar mechanical properties [208]. A recommended cure temperature of 125°C for a duration of one hour is given by the manufacturer instead of a complete cure cycle for this resin system. The characterization showed, that the altered chemical formula also led to higher cure rates at the manufacturer's recommended cure temperature and increased volatile release as a byproduct of resin polymerization, which had to be investigated to determine its impact on the characterization.

3.1 Weight Loss and Thermal Stability

Traditional RTM resin systems feature little or no weight loss during cure, only in the case of material degradation at high temperatures. This has been a requirement for high-performance resin systems, given that weight loss at cure temperature is induced by the nucleation and growth of cure-induced voids as a byproduct of resin polymerization [209], which further leads to decreased laminate quality. For these traditional resin systems a dynamic temperature scan in a thermo-gravimetric analyzer (TGA) is sufficient to determine the onset of thermal instability. However, the resin system investigated showed significant out-gassing during cure which required further investigation. In some special purpose resin systems, the development of a small amount of cure-induced volatiles is tolerated to increase certain properties [209]. In general, resin polymerization is not the only source for volatiles, they can form due to residual solvents, vaporized monomers, dissolved air and moisture [210]. The initial amount of material leading to volatiles such as dissolved gases and moisture can be reduced prior to injection by vacuum-degassing. However, full elimination of micro-bubbles is difficult to realize [211]. A common method to decrease the void fraction in the final composite made by an RTM process is the increase of hydrostatic pressure, which not only decreases the bubble size but impedes volatile nucleation, as well [212].

A series of dynamic and isothermal TGA runs were conducted to investigate the weight variation during cure. Since the coefficient of variance of the weight change measurements in the TGA was rather large with 10%, at least three repetitions were conducted for each temperature and temperature rate, respectively. A temperature ramp of 10°C/min was chosen in case of the dynamic weight change runs. The isothermal measurements were conducted at 110°C, 125°C, 140°C and 160°C to cover the whole temperature range which can possibly occur during the cure of thick laminates with the investigated resin system.

A typical TGA investigation to determine the thermal stability consists of a dynamic run and the investigation of a very low threshold value for the weight loss, until which point the resin system is considered as thermally stable [8]. In the present case, this approach is not valid, since the resin system continually looses weight as soon as the resin reaction starts (see Figure 3-1 (a)). The resin weight loss behaves cure-dependent and, thus, time-dependent. Since the rising temperature of the dynamic run leads to increasing cure rates, the dynamic run shows an increase in the weight-loss change with rising temperature, which cannot be assigned to thermal stability only. Investigation of the resin kinetics (see next Section) shows, that a temperature ramp of 10°C/min leads to full cure at 200°C. However, a constant decrease in weight already suggests material degradation at this temperature.

Four isothermal temperatures runs were performed in the TGA to investigate the thermal stability of the significant temperature range as well as the behavior of resin outgassing during cure. All four temperatures reached a plateau of negligible weight change when considering reasonable curing times (see Figure 3-1 (b)). However, the amount of weight lost decreased with increasing temperature, which indicates a diffusive character of volatile transport. Higher temperatures lead to higher cure rates and thus less time for the volatiles to conglomerate and rise to the surface.

Although the measured weight loss in the TGA is significant, it should decrease in part manufacturing: The hydrostatic pressure of the RTM process might de-

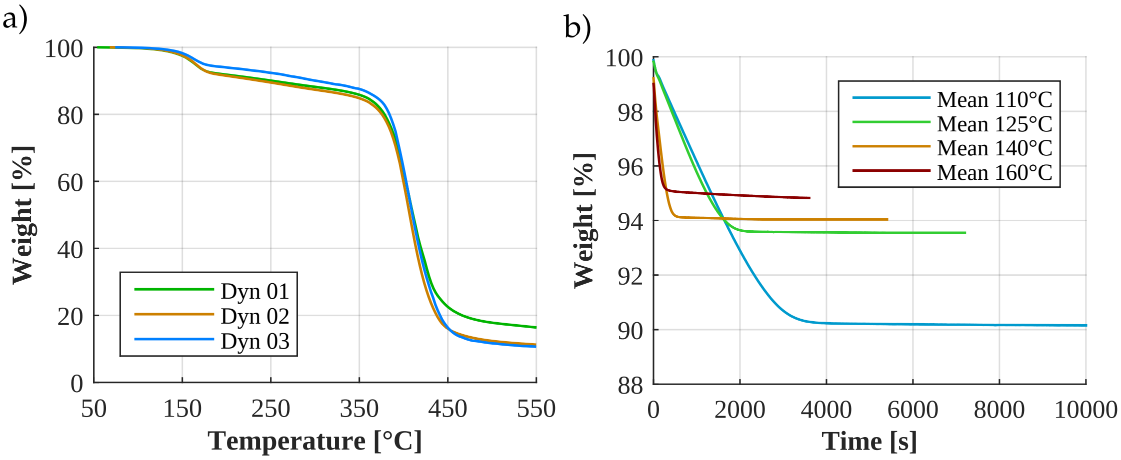

Figure 3-1 Weight variation of neat 823-1 resin: (a) dynamic runs at 10°C/min, (b) isothermal weight variation.

crease volatile generation and certainly volatile growth. A second test series was conducted to quantify the impact of hydrostatic pressure on volatile formation and growth: Specimens were fully cured under varying pressures for each of the temperatures 110°C, 125°C and 140°C and the subsequent weight loss after cure was determined with a precision scales. Approximately 30 mg neat resin was placed in small aluminum pans and cured without a lit in a pressure vessel. The resulting weight loss is given in Table 3-1. Each experiment involved six specimens to determine the standard deviations. The pressure experiments showed the expected trends: Decreasing weight loss with increasing pressure as well as increasing temperature. Thus, the processing of the resin system should aim for high curing temperatures and a high process pressure to decrease the final part's void content. Additionally, a batch of experiments were conducted at ambient pressure and temperature cycles of 1h at 160°C, 4h at 160°C and 1h at 180°C with a weight loss of -5.01 %, -4.99 % and -6.65 %, respectively. Negligible time-dependent weight change occurred at 160°C and significantly increased weight

Table 3-1 Mean pressure and temperature dependent percentage of total weight change of the resin system CYCOM 823-1.

Pressure	Temperatures 110°C	 125°C	 140°C
Ambient	-10.32 ± 0.87 %	-7.16 ± 0.66 %	-5.20 ± 0.39 %
1 bar	-7.14 ± 0.92 %	-5.79 ± 0.78 %	-4.63 ± 0.66 %
2 bar	-6.04 ± 0.65 %	-4.14 ± 0.61 %	-3.42 ± 0.40 %
3 bar	-5.12 ± 0.45 %	-4.01 ± 0.27 %	-3.99 ± 0.27 %
6 bar	-4.06 ± 0.59 %	-3.56 ± 0.37 %	-3.01 ± 0.29 %
8 bar	-3.86 ± 0.31 %	-3.05 ± 0.38 %	-3.13 ± 0.33 %

change was determined at 180°C. Therefore, the temperature limit of thermal stability was set at 160°C.

3.2 Resin Kinetics

The resin system CYCOM 823-1 from Cytec is an anhydride-based one-part epoxy resin system [208]. Thus, subsequent to the catalyzed initiation two major exothermic reactions take place: First, a free hydroxyl group reacts with the anhydrid to form a half ester and a free acid. Second, this half ester cures an epoxy to form a diester in the propagation step [213].

Characterization Method

To develop a phenomenological model for the overall energy release during cure, a series of dynamic and isothermal dynamic scanning calorimetry (DSC) runs were conducted on a Q200 from TA Instruments. Due to an enhanced risk of occurring exothermic peaks in part production with CFRP molds the cure kinetic model was required to give an accurate description of the evolution of the degree of cure over a large range of temperatures, including temperatures high above the manufacturer's recommended cure temperature of 125°C. Additionally, highly dynamic temperature evolution can arise in the processing of thick laminates. Thus, the resin kinetics model was required to be capable of predicting higher temperature rates, as well. The chosen heating rates in the dynamic cases were set at 1°C/min, 3°C/min and 5°C/min. The isothermal temperature scans were set at 100°C, 110°C, 125°C, 140°C and 160°C. Three runs were conducted at each temperature and rate to ensure repeatability of the results.

In a preliminary test, no apparent cure could be determined with the DSC at 80°C, thus all specimens were degassed for 10 min at 70°C prior to the experiment. A specimen mass between 7 and 11 mg was transferred in aluminum pans with a pierced lid (see Fig. 3-2 right) to ensure ambient pressure during the experiment. Given that the measured specific heat flow is dependent on the specimen mass, high weight loss potentially falsifies the experiments, which was a concern with the resin system investigated. All specimens were weighted immediately after the experiment. In contrast to the weight loss experiments in the previous chapter, the overall mean weight loss for the isothermal experiments was 2.0% with a standard deviation of ±0.5 %, respectively 3.1% ±0.7 % in the case of a dynamic temperature. The distribution of the weight showed the lowest weight losses at the highest isothermal temperatures.

The two different sets of experiments, weight-loss investigation and measurements straight after the respective DSC runs, showed completely different behavior with mean weight losses of $\sim 5 - 10\%$ at ambient pressure in the first case (depending on temperature) and $\sim 2\%$ in the second case. The assumed reason for the lower weight loss in comparison to specimens cured without a lid is apparent gas condensation of the generated volatiles in DSC pans itself. This theory was proven by a parallel cure of eight specimens in an oven at 120°C, of which only four specimens were covered with a pierced lit (see Figure 3-2). Whereas the measured weight loss of the specimens without a lid were in line with the results of Table 3-1 with 10.30 % ±0.85 %, the specimens with a lid showed a weight loss of only 0.75 % ±0.35 %.

Figure 3-2 Weight loss specimen without lid (left) and with lid (right). The right specimen is similar to the specimens measured in the DSC.

Concerning the heat flow of the DSC in such a case, the ultimate heat of reaction measured during an exothermic reaction in the absence of changes in the specific heat is dependent on: the specimen weight, the sum of heat flows of the heat of reaction $\dot{Q}_{\mathrm{ch}}$, the heat conversation due to emerging volatiles $\dot{Q}_{\mathrm{vol}}$ and condensation energy $\dot{Q}_{\mathrm{con}}$.

$$H_{\mathrm{r}} = \int \frac{\dot{Q}_{\mathrm{ch}}(t) + \dot{Q}_{\mathrm{vol}}(t) + \dot{Q}_{\mathrm{con}}(t)}{m(t)} dt \tag{3-1}$$

During an exothermic reaction, the reduction of specimen mass will increase the specific heat flow, whereas condensation will decrease it. Most condensation energies of organic substances are in the same order as epoxy resin reaction energies and the effect of the overall weight loss on the heat of reaction is lower than the standard deviation of the isothermal temperature scans. Hence, the effect was assumed to be negligible for the resin system investigated.

Characterization Results

Material degradation influences the specific heat flow evolution in the DSC due to the apparent mass loss. Thus, the temperature scans conducted within a DSC to determine the ultimate heat of reaction H_{r} are required to lead to full cure before the temperature limit of thermal stability is reached [58]. Only the lowest heating rate of 1°C/min showed full cure at the previously determined limit of thermal stability at 160°C. The overall heat of reaction was determined via integration of the heat flow signal using a linear baseline and showed an increase of the reaction energy with decreasing temperature rate: 319.8 ± 3.0 J/g, 338.8 ± 2.5 J/g and 361.5 ± 4.6 J/g for the heating rates 5°C/min, 3°C/min and 1°C/min, respectively. This increase can be dedicated to the increasing mass loss at higher temperatures due to material degradation. Hence, the 1°C/min heating rate experiments only were considered in the calculation of the ultimate heat of reaction H_r=361.5 J/g. The apparent change in the specific heat indicating the glass transition was determined for the uncured specimens at T_{g0}=-47.8 ± 1.2 °C. A subsequent temperature scan of the fully cured specimens led to a final glass transition temperature $T_{g\infty}$=106.7°C ±4.2°C.

The coefficient of variance for the dynamic runs was relatively low (0.9 %, 0.7% and 1.2% for 5°C/min, 3°C/min and 1°C/min), whereas the isothermal runs showed a more deviating behavior. The isothermal measurements consisted of an equilibration stage from room temperature to the target temperature and a subsequent temperature hold until a point of negligible reaction is reached. If a traditional horizontal baseline from point of negligible change at the end of the reaction to the start of the reaction is used for heat flow integration [61, 71], the integration of the heat flow resulted in 339.8 ± 4.6 J/g, 366.1 ± 13.5 J/g, 372.6 ± 4.1 J/g, 378.2 ± 9.5 J/g and 351.7 ± 3.1 J/g total isothermal heat of reaction for the temperatures 100°C, 110°C, 125°C, 140°C and 160°C.

Almost full cure was reached within all specimens at the chosen temperatures. While this behavior is not common, it has been reported for other fast curing resin systems, as well [214]. The specimens never reached the vitrified state during cure, since the cure temperatures were above the final glass transition temperatures with exception of the 100°C run. Typically, diffusive behavior is responsible for a slow-down of the chemical reaction in thermoset resin systems leading to specimens reaching negligible measurable cure rate prior to full cure [1], if the cure temperature is below vitrification temperature. Only the 100°C-specimens exhibited diffusion behavior. A subsequent dynamic temperature scan proved this explanation: A residual heat of reaction of 0 J/g and 11.2 J/g was measured at the 110°C and 100°C specimens.

The mean isothermal heat of reaction of all fully cured specimens (110°C-160°C) was thus 368.6 ±12.1 J/g. Given that the total heat of reaction measured with the dynamic temperature scans was determined at 361.5 ± 4.6 J/g, the straight

---

[1] Technically, the cure is proceeding if full cure is not reached, but the accuracy and the precision of the instrumentation or the time frame does in some cases not allow for a proper measurement of the isothermal heat of reaction above glass transition.

application of Equation 2-1 would lead to degrees of cure above unity in most cases, which is chemically not possible. This highlights the impact of the isothermal baseline and the need for a sensitive consideration in its choice, since all specimens above 106.7°C were known to be fully cured.

In literature, two alternative approaches were proposed instead of a traditional horizontal baseline: During temperature equilibration in the beginning of the isothermal dwell, the settling of the heat flow signal leads to small deviation in the early cure stages. Barton suggested a rerun of the cured specimen and utilization of this result as a baseline [215], to compensate this effect. On the other hand, Hubert et al. introduced a baseline method for partly cured resins: The residual enthalpy is determined with a dynamic temperature scan subsequently to the isothermal run. The isothermal baseline is solved for iteratively to gain a matching isothermal enthalpy according to the following equation [216]:

$$H_{\text{iso}} = H_r - H_{\text{Residual}} = \int \frac{\dot{q}_{\text{baseline}} - \dot{q}}{m} dt \tag{3-2}$$

A preliminary investigation using the traditional horizontal baseline was used to determine the influence of the initial settling stage on measurement accuracy: The 160°C run featuring the highest cure rates and longest equilibration times took 100 s between the surpassing point of apparent cure at 100°C and the point with 160°C and a stable heat flow signal, which would be the starting point of a traditional baseline. Most of this time would be spend close to 160°C until the signal is settled. The initial cure rates of the first 100 s at 160°C resulted in a "lost" specific heat flow of $\approx$ 18 J/g, which cannot be neglected. Thus, an investigation on the impact of the baseline choice on the cure rate evolution was conducted for the three highest temperatures 125°C, 140°C and 160°C and the results are shown in Figure 3-3. The resulting total enthalpy did not exactly match the determined total heat of reaction due to measurement variance for both the horizontal baseline and the choice of a second run as a baseline. However, the specimens are known to be cured after sufficient curing time. The total heat of reaction for these baseline choices were fitted that degrees of cure equal unity is reached at the end of the experiment. The two methods lead to a very similar evolution of the cure rate when encountering small total isothermal enthalpy deviations from the dynamically measured value H_r (see Fig. 3-3). However, they do differ if larger variances are encountered, which is not the case with the investigated resin system. The baseline according to Eq. 3-2 was shifted iteratively to reach total enthalpy determined and, thus, degree of cure equal unity at the experiment's end.

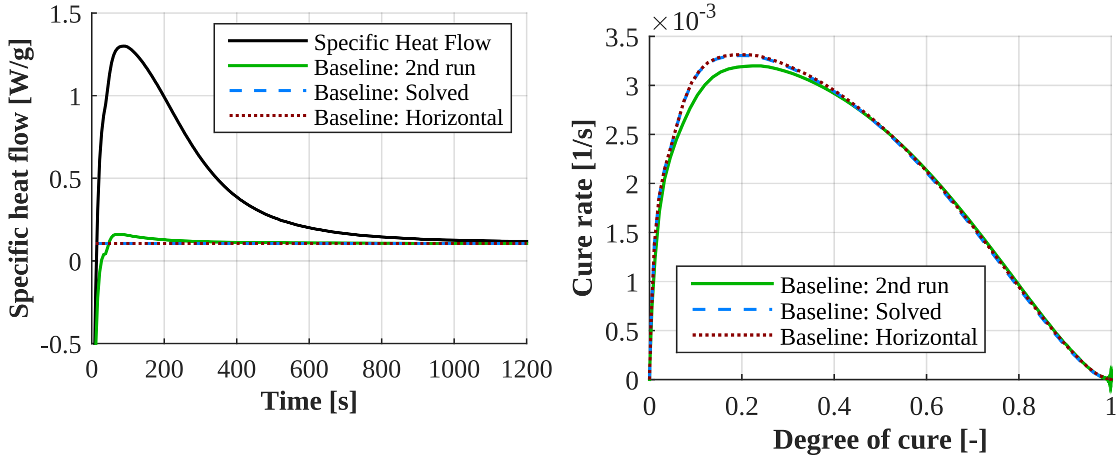

a) Specific heat flow at at 160°C:

b) Resulting cure rates at 160°C:

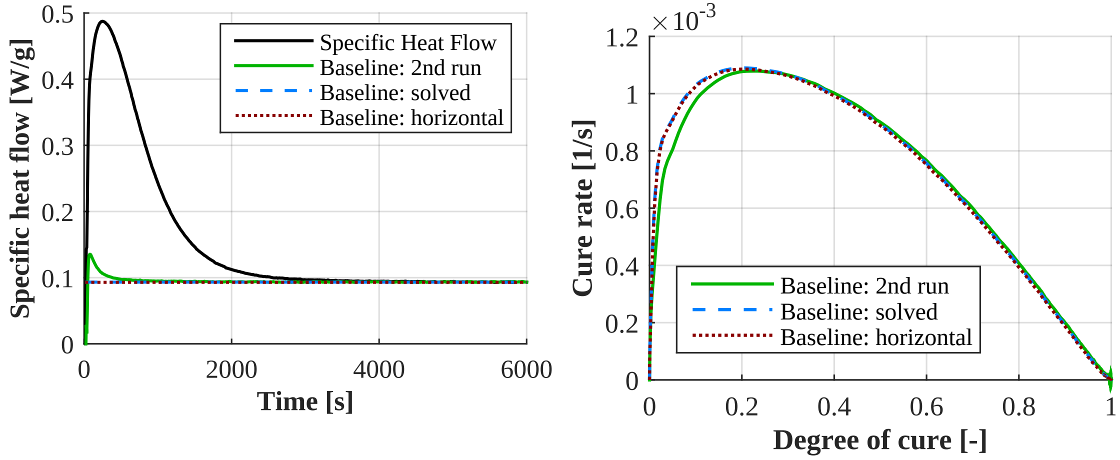

c) Specific heat flow at at 140°C:

d) Resulting cure rates at 140°C:

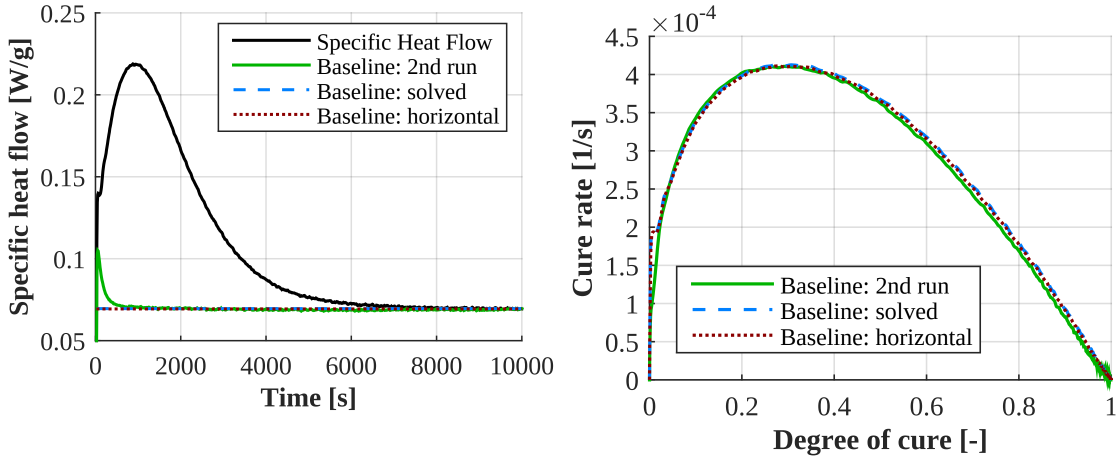

e) Specific heat flow at at 125°C:

f) Resulting cure rates at 125°C:

Figure 3-3 Comparison of different baseline choices and resulting cure rates at the temperatures 125°C, 140°C, and 160°C.

Figure 3-3 shows, that the choice of a second run as a baseline not only accounts for the initial heat lost, but also for a equilibrating heat flow originating from the instrumentation: In order to reach 160°C as quickly as possible, very high heating rates were required. The Q200 DSC did not reach thermal equilibration in the first couple of seconds at the set-point temperature. Thus, the baseline originating from the second run actually increases above the horizontal baseline (see Fig. 3-3 (a) at $\sim$ 100 s). The two effects, initial heat lost during the heating process to reach final target temperature and thermal equilibration, actually compensate each other to a large extend if overall reaction enthalpy is considered. In case of the 160°C specimen, accounting for the initial heat lost would increase the total measured isothermal enthalpy for 17.9 J/g compared to a horizontal baseline whereas the "slow" instrumental equilibration decreases the total isothermal enthalpy for -11.5 J/g, leading a total net difference of 6.4 J/g between the traditional and a second run as a baseline choice. However, given that both effects overlap only to a small extend, they do have an effect on the resulting isothermal cure rate behavior. Figure 3-3 (b), (d) and (f) show that only the highest isothermal cure rate plots are affected by these effects. At 125°C and lower, the differences in the cure rates determined by a horizontal baseline and a second run is negligible. Thus, input data for the cure kinetics model fit required a second run as a baseline for the 140°C and 160°C runs only.

It has to be noted that the second run of a DSC is not always the optimal choice for the heat flow integration: It does not take a degree of cure dependent change in the specific heat into account. However, if the specific heat can be approximated as a linear function of the degree of cure (which is valid for the present resin system), the resulting heat flow measured by the DSC due to specific heat change is a constant in the degree of cure space. Thus, the cure-dependent specific heat change is negligible in the cure rate over degree of cure plots. Hence, this offset does not change the overall cure rate characteristics and can be neglected for the cure kinetics model fit, if the model is fitted to these cure rate plots.

Phenomenological Cure Kinetics Model

Most cure cycles predominantly consists of several isothermal dwells where the majority of cure takes place. Nevertheless, it was also important to get a reasonable cure kinetics fit for the dynamic experiment's data: Within thick laminates, a dynamic temperature evolution during an isothermal temperature hold of the tool can in some cases not be avoided. If the processing time is limited and the cure rates of the resin are required to be high, the released energy cannot fully be transported towards the surface of the part. Thus, the resin

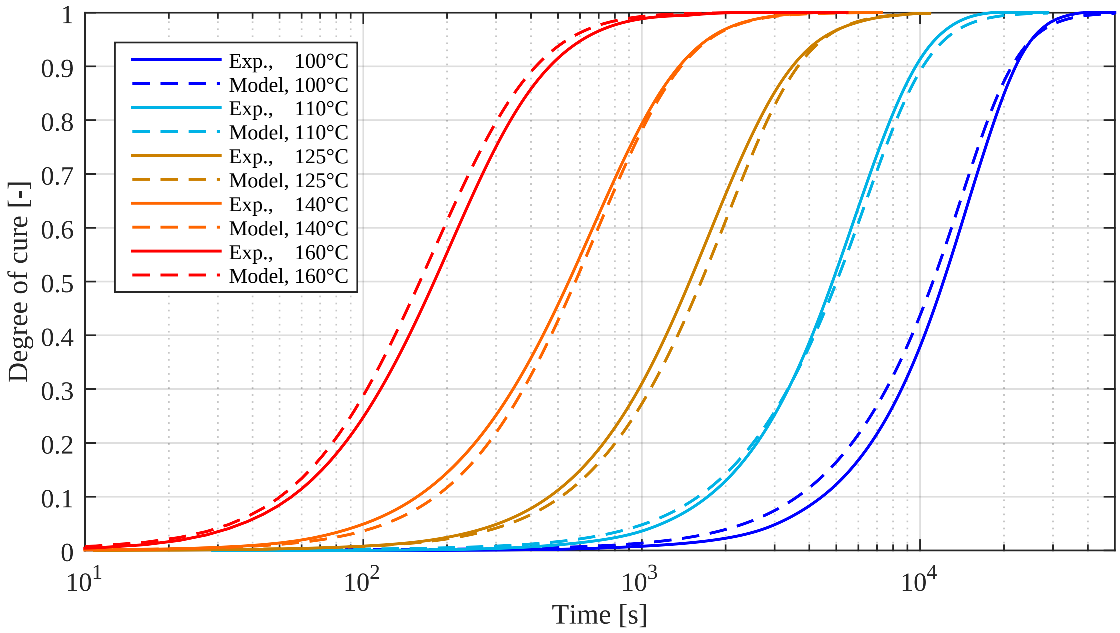

Figure 3-4 Evolution of the degree of cure at different isothermal temperatures with time; experiment and material model.

kinetics model fit was aimed towards an equally good fit for isothermal and dynamic experimental data. A linear combination of two autocatalytic reactions was chosen to model the resin kinetics:

$$\dot{\alpha} = K_1 e^{-\frac{\Delta E_1}{RT}} \alpha_1^m (1-\alpha)_1^n + K_2 e^{-\frac{\Delta E_2}{RT}} \alpha_2^m (1-\alpha)_2^n \tag{3-3}$$

With the activation energies E_i, the Arrhenius constants K_i, and the reaction orders n_i and m_i. Diffusive behavior was not modeled, given that the low glass transition temperature resulted in a lack of diffusive behavior. The standard deviations of the isothermal measurements were ~ 3.3%. The cure kinetics model was fitted by means of least-square analysis aiming at a similar accuracy. The model led to a satisfactory fit with the resulting model constants provided in Table 3-2 over the whole contemplated temperature range for both isothermal and dynamic cure behavior (see Figure 3-4 and Figure 3-5). Slightly higher model deviations than the isothermal standard deviations are encountered between 4000 s and 8000 s at 100°C and between 150 s and 200 s at 160°C only. However, these regions are not encountered in any reasonable process window for laminate manufacture.

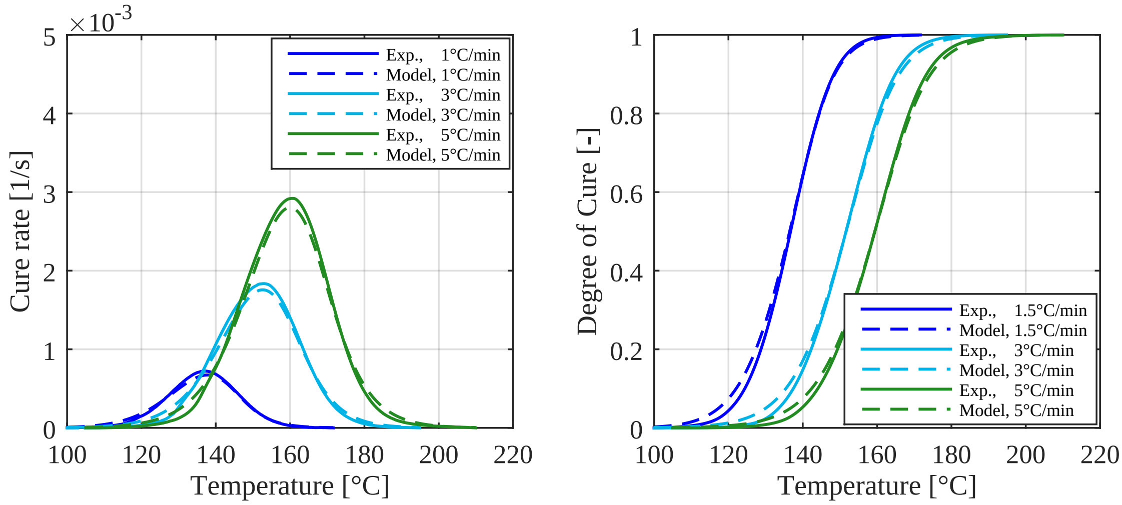

Figure 3-5 Cure rates of CYCOM 823-1 RTM at different temperature rates; experiment and material model.

Table 3-2 Cure kinetic model constants in SI units.

Cure Reaction 1			Cure Reaction 2		
ΔE_1	98397	J mol^{-1}	ΔE_2	72101	J mol^{-1}
K_1	8.2E9	s^{-1}	K_2	3.5E6	s^{-1}
m_1	1.81		m_2	1.17	
n_1	0.47		n_2	2.49	

Evolution of the Glass Transition Temperature

Vitrification leads to significant changes in the material properties. Thus, the evolution of glass transition temperature with the degree of cure needs to be characterized. The uncured glass transition temperature T_{g0} was measured at -47.8 ± 1.2 °C (mid-point value of the DSC heat flow change). The glass transition temperature $T_{g\infty}$ of the fully cured resin was determined in a similar manner via nine experiments with the resulting mean value of 106.7 ± 4.2°C. A series of eleven specimens were partially cured isothermally at 125°C within the DSC. Subsequently to the cool-down, dynamic runs were applied to measure the residual enthalpy and the corresponding glass transition temperature between T_{g0} and $T_{g\infty}$. Two specimen were prepared in a similar way at 100°C to deliver additional data points close to full cure.

The evolution of glass transition temperature was approximated with the DiBenedetto Equation 2-12. The DiBenedetto constant $\lambda = 0.46$ was fitted to the experimental data with assistance of a least square regression analysis, as shown in Figure 3-6.

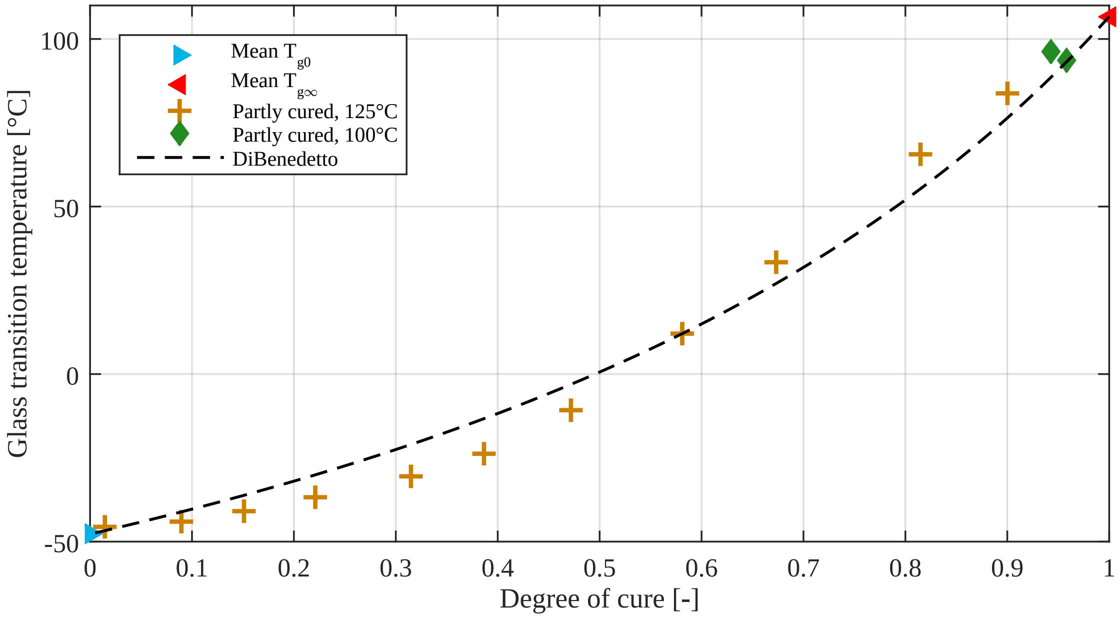

Figure 3-6 Evolution of the glass transition temperature with degree of cure; experimental values and DiBenedetto approximation.

3.3 Thermal Material Properties

The temperature evolution within the part is defined by the heat flow over the part's boundaries, the resin kinetics and the material properties density, specific heat and heat conductivity. All of these properties were determined for neat CYCOM 823-1 and are presented in the following.

Specific Heat

The specific heat of the curing resin was measured by dynamically modulated DSC (MDSC) runs at a temperature ramp of 3°C/min on a TA Q2000. Five specimen were tested with two successive MDSC runs: The first run was conducted to measure the uncured specific heat over temperature up to the start of reaction. The second run was conducted on the cured specimen to obtain data on the specific heat over temperature in the glassy and rubbery state above the glass transition temperature.

The mean progression of the specific heat with temperature for the uncured and cured state of all specimen is shown in Figure 3-7. Neglecting the initial deviations until the heat flow is stabilized, the variation in the specimens was small with maximal standard deviations of 37 J/kg/°C, 23 J/kg/°C, and 32 J/kg/°C for the regions uncured, cured glassy, and cured rubbery. A specific heat model from Convergent with linear dependencies on the degree of cure and temperature has been fitted to the data by means of least square regression analysis [58, 93]. The resulting model constants are shown in Table 3-3 in SI-units. The material model is defined by the following equations:

$$c_{\mathrm{p}} = c_{\mathrm{p_r}} + \left(\frac{c_{\mathrm{p_g}} - c_{\mathrm{p_r}}}{1 + \mathrm{e}^{k(T - T_{\mathrm{g}} - \Delta T_{\mathrm{c}})}} \right) \tag{3-4}$$

With

$$c_{\mathrm{p_r}} = (1 - \alpha)(s_{\mathrm{r0}} T + c_{\mathrm{r0}}) + \alpha(s_{\mathrm{r\infty}} T + c_{\mathrm{r\infty}}) \tag{3-5}$$

$$c_{\mathrm{p_g}} = (1 - \alpha)(s_{\mathrm{g0}} T + c_{\mathrm{g0}}) + \alpha(s_{\mathrm{g\infty}} T + c_{\mathrm{g\infty}}). \tag{3-6}$$

Almost no discrepancy between model and measurement data was identified, as shown in Figure 3-7.

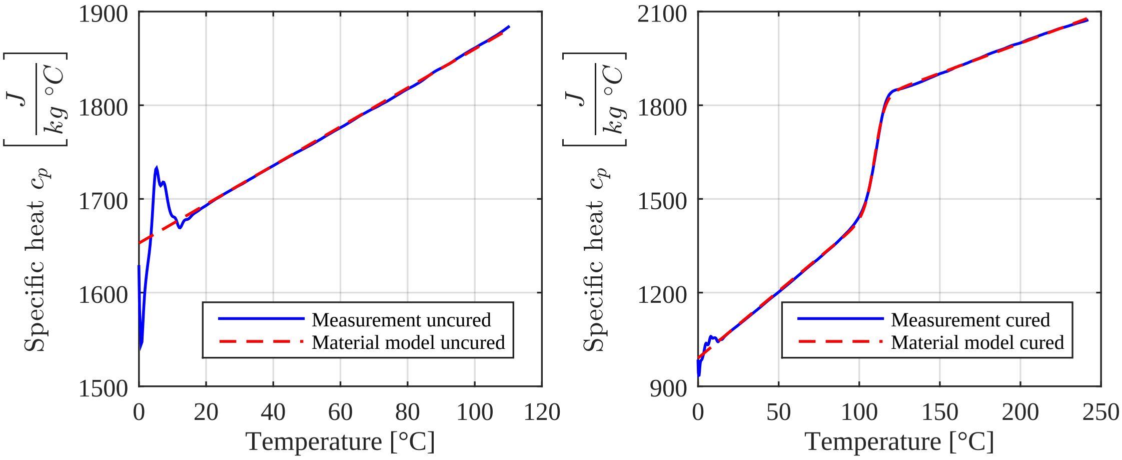

Figure 3-7 Mean specific heat over temperature and material model approximation: uncured resin (left); cured resin (right).

Table 3-3 Resin specific heat model constants of CYCOM 823-1 RTM in SI units.

Model Constant	Value	Units
s_{r0}	2.072	J/(kg °C^2)
$s_{\mathrm{r\infty}}$	1.920	J/(kg °C^2)
s_{g0}	2	J/(kg °C^2)
$s_{\mathrm{g\infty}}$	4.295	J/(kg °C^2)
c_{r0}	1652	J/(kg °C)
$c_{\mathrm{r\infty}}$	1615	J/(kg °C)
c_{g0}	1030	J/(kg °C)
$c_{\mathrm{g\infty}}$	990	J/(kg °C)
k	0.317	1/°C
ΔT_{c}	3.217	°C

Heat Conductivity

Temperature conductivity a of the cured resin was measured by means of the NanoFlash™ method at five different temperatures with three specimens each [217]. Heat conductivity is further calculated according to the following equation:

$$k = a \cdot \rho \cdot c_\mathrm{p} \tag{3-7}$$

Measurement of the resin density ρ in fully cured state at room temperature with the Archimedes' principle resulted in 1235 kg/m^3 [218]. The specific heat c_p was determined previously. The resulting heat conductivity at the measured temperatures is shown in Figure 3-8 and Table 3-4. A material model consisting of a linear dependency on both temperature and degree of cure was fitted to the experimental data via least square regression analysis [93]:

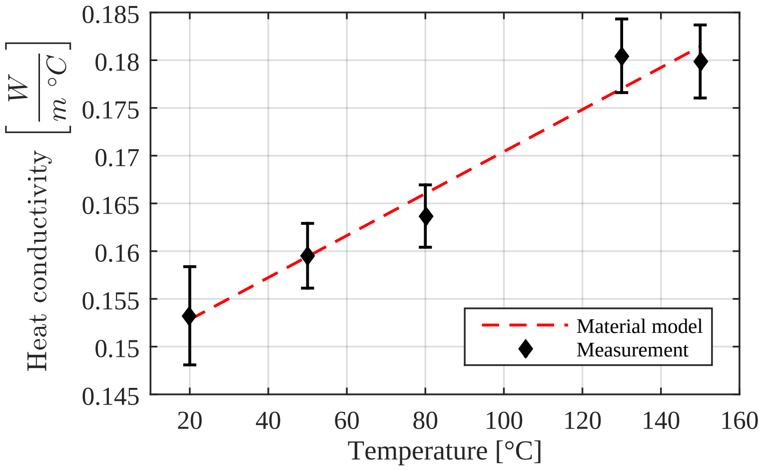

Figure 3-8 Neat resin heat conductivity as a function of temperature; measurement data and model approximation.

$$k = k_0 + f_\mathrm{T}(T - T_0) + f_\alpha(\alpha - \alpha_0) \tag{3-8}$$

k_0 is the initial conductivity at initial temperature T_0 and initial degree of cure α_0. The constants f_T and f_α define the dependence of the thermal conductivity on temperature and degree of cure, respectively. The determined model constants are given in Table 3-4 in SI units.

Table 3-4 Constants of the thermal conductivity material model of the curing resin in SI units.

Model Constant	Value	Units
k_0	0.174	W/(m °C)
f_T	2.20E-4	W/(m °C^2)
T_0	196.7	°C
f_α	1.80E-2	W/(m °C)
α_0	0	

3.4 Chemical Shrinkage

The modified rheology method developed in [11] was chosen to characterize the chemical shrinkage by means of Rheometer measurements (Anton Paar MCR-302). The measurement set-up is depicted in Figure 3-9. Isothermal measurements were conducted on a parallel plate set-up. The gap between the two hot plates was filled with liquid resin. Prior to gelation, this gap distance was fixed at 1 mm. At gelation the constant gap fixation was released. Utilizing a zero-force control of the Rheometer led to a force-free shrinkage-induced decrease in the gap distance. The resulting volumetric shrinkage V_r^s is calculated as follows [11]:

$$V_\mathrm{r}^s = \left[1 + \frac{1}{3}\left(\frac{h - h_0}{h_0}\right)\right]^3 - 1 \tag{3-9}$$

h_0 denotes the initial gap distance and h the gap measured in the experiment. This experiment can only measure the shrinkage post gelation. The resulting shrinkage model is applicable for manufacturing processes in which a post-injection resin flow can occur until the gelation of the part, similar to the RTM process investigated in the case study of Chapter 7.

An amplitude and frequency sweep test was conducted to determine the linear viscoelastic region (LVR) of the material. To characterize inside the LVR, the amplitude and frequency for the measurements was set at 0.1% strain and 10 Hz. Liquid resin was injected onto the hot bottom plate, which required the top plate to be out of position at a higher gap width. The measuring sequence started after the upper plate moved into position. It took 25 seconds from the resin injection to actual start of the measurement. Lower characterization temperatures of 100°C and 110°C were chosen for the shrinkage determination to decrease the influence of this initial sequence.

Prior to the shrinkage experiment, the point of gelation had to be determined. The point of gelation is defined as the point when the material behavior transfer from a viscoelastic liquid, where the majority of energy is dissipated, to a viscoelastic

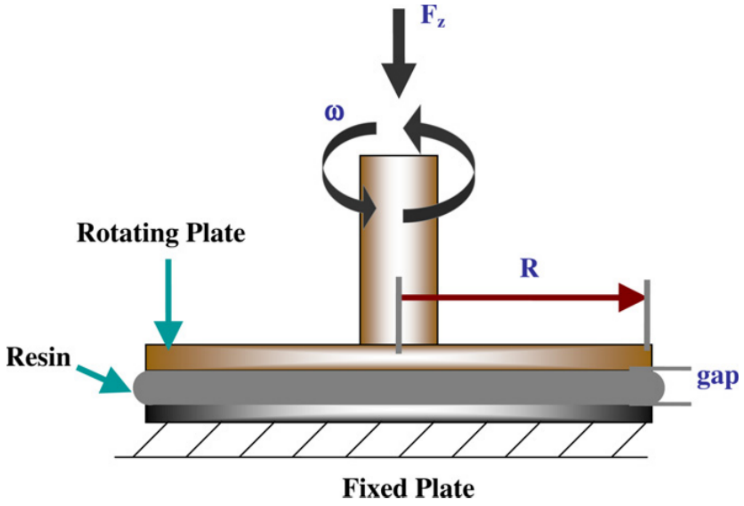

Figure 3-9 Modified shrinkage measuring set-up in the Rheometer [11].

solid, which stores the majority of energy [219, 220].Thus, it can be determined by a measurement of the crossing point of the storage modulus G' and loss modulus G'' in an isothermal Rheometer run. The experiments to determine the gelation point were conducted using a fixed gap of 1 mm set-up, and measuring procedure was aborted after gelation occurred. Six measurements for the determination of the gelation point were conducted at 125°C, resulting in $\alpha_{\mathrm{gel}} = 0.335 \pm 0.029$.

Shrinkage was measured with three experiments at each of temperatures investigated resulting in a mean final volumetric cure shrinkage of $V^{\mathrm{s}}_{\mathrm{r}\infty} = 3.8 \pm 0.26\%$ after gelation. Figure 3-10 shows the evolution of the volumetric shrinkage over the degree of cure. The corresponding model fit utilizes the "CS1" model from Convergent [93].

$$V^{s}_{\mathrm{r}} = \begin{cases} 0, & \text{for } \alpha < \alpha_{\mathrm{C1}} \\ A\,\alpha + (V^{s}_{\mathrm{r}\infty} - A)\,\alpha^{2}, & \text{for } \alpha_{\mathrm{C1}} \leq \alpha < \alpha_{\mathrm{C1}} \\ V^{s}_{\mathrm{r}\infty} & \text{for } \alpha \geq \alpha_{\mathrm{C2}} \end{cases} \tag{3-10}$$

$$\alpha_{\mathrm{s}} = \frac{\alpha - \alpha_{\mathrm{C1}}}{\alpha_{\mathrm{C2}} - \alpha_{\mathrm{C1}}} \tag{3-11}$$

A least square regression analysis was used to determine the model constants: slope of the shrinkage increase A and the degree of cure α_{C2} after which no further shrinkage occurs. $V^{s}_{\mathrm{r}\infty}$ is the final volumetric shrinkage at full cure and α_{C1} the point of gelation. The model constants are summed in Table 3-5.

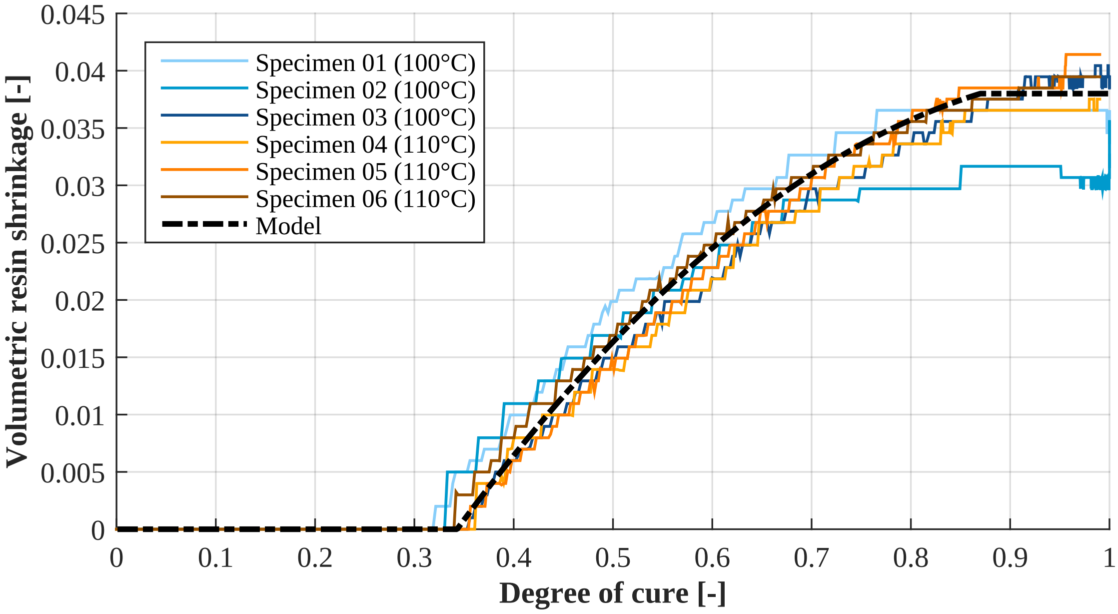

Figure 3-10 Volumetric shrinkage of CYCOM 823-1 RTM after gelation; experiments and model approximation.

Table 3-5 Shrinkage model coefficients for CYCOM 823-1 RTM.

Model Constant	Value [-]
α_{C1}	0.335
α_{C2}	0.87
A	0.062
$V^{s}_{r\infty}$	0.038

3.5 Coefficient of Thermal Expansion

The coefficient of thermal expansion (CTE) of the neat resin was measured by means of dynamic mechanical analysis (DMA) with a Q800 from TA Instruments. Fully cured neat resin plates were manufactured at 125°C. The degree of cure of these plates were controlled via dynamic DSC by means of residual enthalpy measurement. The samples were characterized in a tension set-up, where one side is clamped into a fixed position and the other side remains movable. Given that mechanical strains and creep might influence the experiment, the applied force on the movable side was very small with 0.05 N, leading to >1% deviation due to mechanical strains and creeping. A low heating rate of 2°C ensured a homogeneous temperature field in the 1.7 mm thick specimens.

Since the odometer of the DMA is not directly placed at the movable clamping itself, a thermal expansion of the clamping system has to be considered as well. Calibration runs were conducted with specimens consisting of a) 99.99 % aluminum, b) 99.99 % zinc and c) unidirectional PEEK/HTS40 with a fiber volume fraction of $V_\mathrm{f} = 33.7\%$. All three specimens had negligible temperature dependence of the CTE in the investigated temperature range. A linear calibration function for the CTE was developed with literature values for the respective CTEs [221, 222]:

$$CTE = A + B\,\frac{1}{l}\frac{dl}{dT} \tag{3-12}$$

where l is the free length of the specimen in-between both clamps and T is the temperature. The calibration constants of the DMA were determined to be $A = 20.5E - 6$ 1/°C and $B = 0.45$. The resulting mean quadratic residuum of the thermal expansion coefficient between literature value and determined value was $0.1E - 6/(°\mathrm{C})^2$, $1.2E - 6/(°\mathrm{C})^2$ and $0.7E - 6/(°\mathrm{C})^2$ for the three materials CFRP, aluminum and zinc over the contemplated temperature range after calibration.

To determine the CTE of the neat resin, four specimens were tested with a mean standard deviation of ± 1.1E-6 1/°C until vitrification. The glassy state exhibits a linear behavior of thermal expansion with temperature, as depicted in Figure 3-11. All specimens showed a large dimensional change at vitrification and occasionally occurring peaks were seen in all tests in the rubbery resin state. Here, the measurement is very sensitive to external stimulation, which is the assumed reason for these phenomena as the Young's modulus is very low. Neglecting the local peaks, the mean value of the cured rubbery thermal expansion resulted in 120E-6 1/°C without any temperature dependency. This value has to be taken with caution, since the thermal expansion of the calibration materials ranged from 6E-6 1/°C to 30E-6 1/°C. Extrapolation outside of the range of calibration material is valid, but the accuracy of the measurement decreases if the discrepancy between calibration material behavior and specimen behavior is large. Nevertheless, even the measured values for the rubbery state fit very well to thermal expansion measurements of other RTM epoxy resin systems with different measurement techniques in literature [79].

The thermal expansion model "CTE Model 2" from Convergent was fitted to the experimental data by means of least square regression analysis [93]. It is defined as follows:

$$CTE_\mathrm{r} = \begin{cases} CTE_\mathrm{rub}, & \text{for } T_\mathrm{C1} < T^* \\ C_2 + C_3\,T^* + C_4\,T^{*2}, & \text{for } T_\mathrm{C2} < T^* < T_\mathrm{C1} \\ CTE_\mathrm{glass} + a_\mathrm{CTE}(T^* - T_\mathrm{C2} & \text{for } T^* < T_\mathrm{C2} \end{cases} \tag{3-13}$$

$$T^* = T - T_\mathrm{g} \tag{3-14}$$

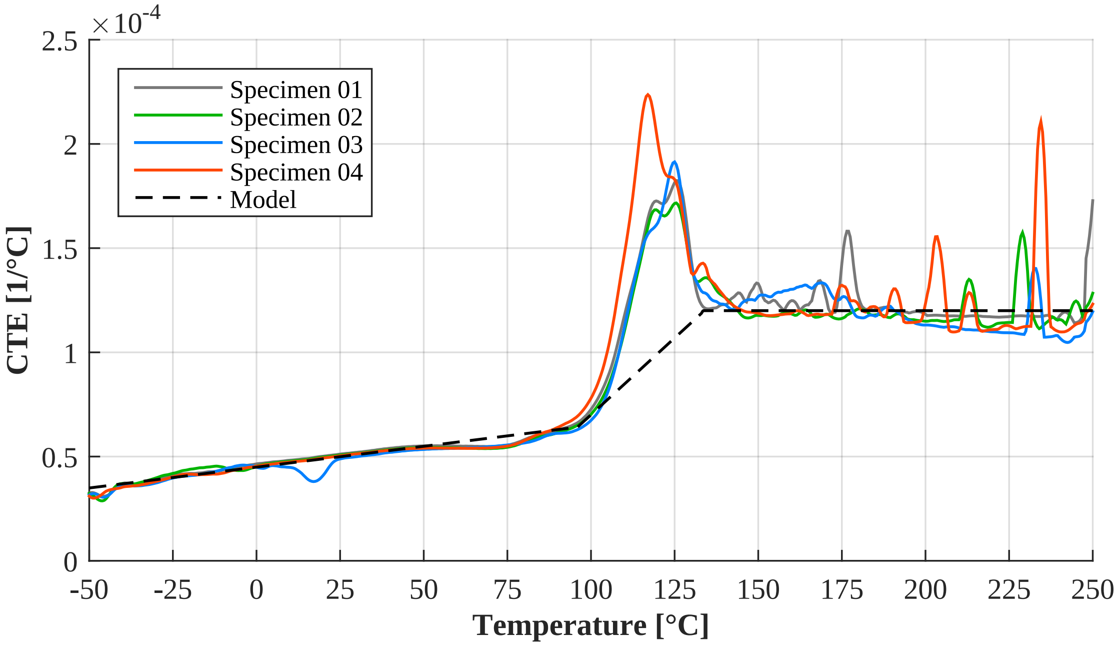

Figure 3-11 Thermal expansion of CYCOM 823-1 RTM; experimental runs and material model approximation.

where CTE_{rub} and CTE_{glass} are the thermal expansion coefficients in rubbery and glassy state prior respectively post vitrification. C_2, C_3, C_4 and a_{CTE} are model constants. T_g is the glass transition temperature calculated by the DiBenedetto Equation 2-12. Given the low glass transition temperature and in comparison high cure temperatures, the resin will stay in its rubbery state throughout the whole cure cycle until the final cool-down. With the values given in Table 3-6 a close correlation between model and experiment for the fully cured state was achieved, as shown in Figure 3-11.

Table 3-6 Constants for the thermal expansion model of CYCOM 823-1 RTM.

Model constant	Value	Unit
T_{C1}	30	°C
T_{C2}	-8	°C
CTE_{rub}	120E-6	$(°C)^{-1}$
CTE_{glass}	64E-6	$(°C)^{-1}$
C_2	75E-6	$(°C)^{-1}$
C_3	1.474E-6	$(°C)^{-2}$
C_4	0	$(°C)^{-3}$
a_{CTE}	0.2E-6	$(°C)^{-2}$

3.6 Mechanical Material Behavior

The tension mode of the DMA was used to characterize the dependence of the elastic Young's modulus with temperature. A strain and amplitude sweep was conducted prior to the modulus tests to ensure measurements in the LVR. The frequency and amplitude were set at 1 Hz and 0.1% strain for the four fully cured specimens measured. The measured temperature range was set from -50°C to 150°C, with a temperature ramp of 2°C/min. The specimen's degree of cure $\alpha = 1$ was verified with a dynamic DSC scan which also resulted in an observed glass transition due to heat capacity change at $T_g = 108°C$. The evolution of the Young's modulus with temperature as well as the model prediction is shown in Figure 3-12.

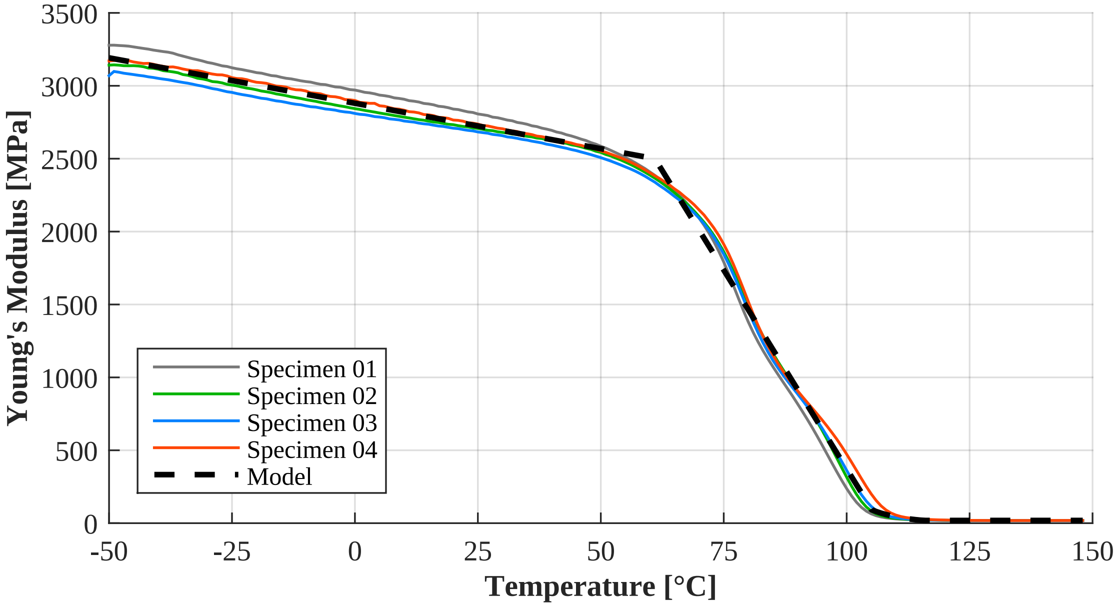

Figure 3-12 Young's modulus of CYCOM 823-1 RTM in the contemplated temperature range.

The maximum standard deviation of the modulus in the vitrified state was 86 Mpa, leading to a maximal coefficient of variation of 2.7%. The mean onset of the glass transition temperature measured with the DMA was at $T_g(onset) = 68°C$. The mean transition from elastic behavior to viscous behavior identifies the glass transition temperature as the maximal ratio of loss modulus E'' and storage modulus E' [223]:

$$T_g(tan\ \delta) = T(\max(tan\ \delta)) = T\left(\max\left(\frac{E''}{E'}\right)\right) \tag{3-15}$$

Utilizing this expression, the mean glass transition temperature was measured at $T_g(tan\ \delta) = 106.6°C$.

The moisture content of the tested specimens was determined via weight measurements during a 72 h drying spell at 120°C in an oven. A mean weight loss of 0.27 % due to moisture loss was measured with no further changes in case of a prolonged drying period.

For material models employing a temperature shift factor, similar to Johnston's model given by the Equations 2-27 to 2-32, the degree of cure dependency is expressed as a dependency on the glass transition temperature. Thus, the model can be fitted to data of cured specimens only.

The material model "RM7" was used to approximate the Young's modulus, defined as follows:

$$E_\mathrm{r} = \begin{cases} 0, & \text{for } \alpha < \alpha_\mathrm{gel} \\ E_2 + (E_1 - E_2)\left(\frac{T^* - T_2}{T_1 - T_2}\right) & \text{for } T_1 < T^* < T_2 \\ E_3 + (E_2 - E_3)\left(\frac{T^* - T_3}{T_2 - T_3}\right) & \text{for } T_2 < T^* < T_3 \\ A\ \mathrm{e}^{-kT^*} & \text{for } T_3 < T^* < T_4 \\ E_4 & \text{for } T^* > T_4 \end{cases} \tag{3-16}$$

$$T^* = T - T_\mathrm{g} \tag{3-17}$$

where E_rmin is the modulus of the liquid resin, E_1 is the initial modulus at low temperatures and E_4 the final modulus in rubbery state. E_2, E_3 and A define the magnitude and T_1 to T_4 the temperatures of the vitrification behavior. T_g is the glass transition temperature calculated by the DiBenedetto Equation 2-12 and α_gel the point of gelation. The fitted model constants are given in Table 3-7.

Table 3-7 Constants for the Young's modulus model of CYCOM 823-1 RTM.

Model constant	Value	Unit
E_1	3.19E+09	Pa
E_2	2.50E+09	Pa
E_3	1.0E+08	Pa
E_4	1.87E+07	Pa
T_1	-156	°C
T_2	-45	°C
T_3	-1	°C
T_4	10	°C
α_gel	0.33	-
A	8E+07	Pa
k	0.15	$°\mathrm{C}^{-1}$

3.7 Tool Properties

Two different material systems and their material properties are required for the cure simulation of parts produced with resistively heated tools: The material properties of the part are required as a function of the degree of cure and temperature. In contrast, the thermal material properties as a function of temperature only are relevant for the tool material. Three different tool materials were used in the simulations of this thesis:

The resistively heated tool utilizing the TCX^{TM} element shown in Figure 1-1 (b) was made of Al6061-T6. In a parameter study in Chapter 5 the properties of Invar were required to gain a more diverse estimation of the impact of different tool materials. The corresponding properties were taken from literature and are given in Table 3-8.

Table 3-8 Thermal properties of aluminum and Invar tool material [14, 15].

Property	aluminum	Invar	Units
c_p	896	515	J/kg/°C
k	167	10.5	W/m/°C
ρ	2700	8055	kg/m^3

Resistively heated CFRP tools were used for the validation experiment of the material characterization and the case study in Chapter 7. All tools featured the same laminate constituents Araldite LY86151 / TR30S and were produced with the same manufacturing technique resulting in a fiber volume fraction of $\sim$ 56%. The resin system has a significantly higher glass transition temperature than the curing temperature of the part resin to ensure shape stability of the tool at the cure temperature of the part. A thermal material characterization of the tool laminate had to be conducted, since a literature review gave only partial knowledge on the laminate thermal behavior. All relevant thermal tool properties with the exception of the in-plane heat conductivity $k_{\text{in-plane}}$ were measured by means of DSC and NanoFlash^{TM}. The specific heat c_p was measured at six equidistant temperature levels from 50°C to 150°C. The transverse thermal conductivity k_{trans} was measured at five equidistant temperature levels from 20°C to 140°C for three specimen at each temperature. Originating from literature, a longitudinal fiber conductivity of 7 W/m/°C with a temperature dependency of 1.56E-2 W/m/°C^2 and a constant resin conductivity of 0.2 W/m/°C was used to calculate longitudinal ply properties by means of rule of mixtures [17, 224, 225]. Composite properties were hereupon calculated with the classical laminate theory. The investigated temperature range was significantly lower than the glass transition temperature of the tooling resin, which is above 200°C. Specific heat and thermal conductivity showed close to linear behavior with temperature, as expected from literature [226]. The density was measured at room temperature with a value of 1470 kg/m^3. All relevant thermal material properties are shown in Table 3-9.

Table 3-9 Thermal properties of the CFRP tool.

T [°C]	$k_{\text{in-plane}}$ [W/m/°C]	k_{trans} [W/m/°C]	c_{p} [J/kg/°C]
20	2.33	0.47	875
50	2.50	0.55	1075
100	2.75	0.60	1265
150	2.98	0.64	1450

3.8 Material Model Validation

A validation of the material card was required to estimate the accuracy possible in the simulation of the sole curing laminate. Since every resin material model is directly or indirectly dependent on the degree of cure, a separate validation was conducted for the cure kinetics model prior to the validation of thermal material card.

3.8.1 Resin Kinetics Model

To validate a wide range of temperature profiles, five different DSC validation runs were set up, each consisting of an infiltration dwell at 90°C, a ramp with varying temperature rates and a second dwell. Subsequently, the specimen was cooled down with the highest cooling rates possible. A dynamic run was conducted to determine the residual enthalpy of the partially cured specimens, which could be compared to the resin kinetics model. All experimental parameters as well as comparison of experiment and resin kinetics model is given in Table 3-10.

The degree of cure deviations of the resin kinetics model according to Equation 2-1 were in the expected range, with a mean degree of cure deviation of the model prediction to experiment of $\overline{\Delta\alpha} = 0.8 \pm 2.6$ %.

Table 3-10 Resin kinetics Validation runs.

Spec.	t_1 [min]	T_1 [°C]	$\frac{d}{dt}T$ [°C/min]	t_2 [min]	T_2 [°C]	$E_{\mathrm{r,exp}}$ [J/g]	$E_{\mathrm{r,mod}}$ [J/g]	$\Delta\alpha$ [%]
1	60	90	1	10	125	174.6	184.2	2.7
2	60	90	1	10	120	226.6	240.9	4.0
3	60	90	3	5	140	146.1	147.2	0.3
4	60	90	5	2	150	147.2	146.3	- 0.2
5	60	90	5	2	160	64.6	55.0	-2.7

3.8.2 Thermal Material Card

The material characterization of the curing resin was carried out to accurately model significant exothermic reactions as well as cure below the final glass transition temperature $T_{g\infty}$. For validation purpose of the cure analysis material card, a coupon layout with a significant exothermic peak was designed. A 145x145x31 mm laminate coupon with 120 layers of ±45° non-crimp fabric (NCF), made of Toho Tenax HTS40 fibers, was manufactured with vacuum bag technique on a self-heated CFRP plate as shown in Figure 3-13.

On the top side, a second self-heated CFRP plate was positioned to introduce heat from both sides. The remaining vertical sides were insulated with a thick layer of glass wool to obtain nearly adiabatic boundaries. Given that the foil and breather material influence conductivity and neat resin regions at the inlet influence thermal behavior, considerable modeling effort was undertaken to ensure an accurate validation. A total of 18 thermocouples were placed within the laminate in three planes to enable a full measurement of the temperature profile in the stack. 12 thermocouples were placed on top and bottom of the laminate and six in the center plane. The measured temperature evolution of the laminate's

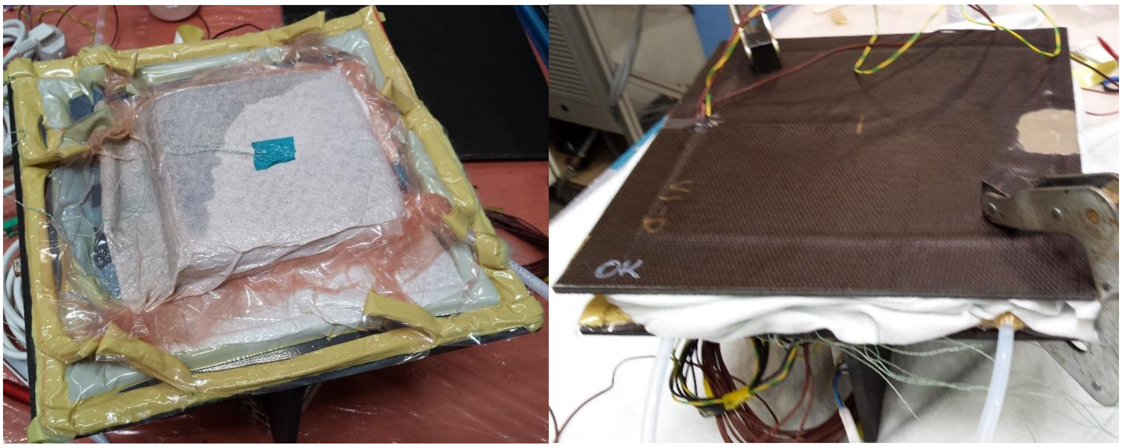

Figure 3-13 Material model validation experiment.

top and bottom surface was interpolated in space for each time step in order to enable a direct temperature boundary condition for the top and bottom nodes in the Abaqus cure simulation. The simulation model of the laminate consisted of 10 DC3D8 brick elements along each direction, resulting in a total of 1000 elements in the model. An increase in the amount of elements led to a negligible change in the simulation results. The starting temperature field was interpolated and applied in a similar way to the temperature boundary condition. Utilizing this direct prescription of temperature in the cure simulation, the impact of foil and breather materials as well as inlet/outlet were excluded from the monitored region. Finally, the initial degree of cure for the simulation was set at 1 % to account for proceeding cure during degassing and infiltration.

The validation was henceforth conducted by comparison of experiment and simulation temperatures arising in the curing laminate's middle plane only. The in-plane thermocouple positioning in this center plane implied four thermocouple locations on each side with a 10 mm distance to the laminate edges and two thermocouples next to each other in the center to accurately capture temperatures in the assumed region with the least impact of the infiltration process.

The material properties for the Toho Tenax HTS40 fiber material properties were taken from literature [16, 17, 99] and are shown in Table 3-11. A chemical determination of the fiber volume fraction as well as void content after the experiment resulted in 52.8 % and 1.3 %, respectively. Thus, void content was in line with the weight-loss measured after the DSC experiments. The initial concern of outgassing could be discarded under the chosen processing conditions. A temperature cycle incorporating a typical ramp rate applied in the industry with 1.5°C/min and a final dwell close to the manufacturer's recommended cure temperature with 120°C was chosen. Infiltration temperature was set at 80°C. The result of the simulation and experiment temperature evolution is shown in Figure 3-14.

Table 3-11 Properties of the Toho Tenax HTS40 carbon fibers [16, 17].

Mechanical properties		Thermal properties	
E_1	230 GPa	ρ	1790 [kg/m^3]
E_2	22 GPa	$k_{\parallel}$	10 [W/m/°C]+$1.56 \cdot 10^{-02}$ [W/m/°C^2] $\cdot T$
G_{12}	22 GPa	$k_{\perp}$	2.4 [W/m/°C]+$5.07 \cdot 10^{-03}$ [W/m/°C^2] $\cdot T$
ν_{12}	0.3	c_p	924.4 [J/kg/°C]+2.75 [J/kg/° C^2] $\cdot T$
ν_{23}	0.35		
$CTE_{\parallel}$	$-0.7E-06$ [1/°C]		
$CTE_{\perp}$	$8.0E-06$ [1/°C]		

The experiment did not show a 1D behavior. The resin rich area at the inlet (Pos. 5 in Figure 3-14 (a)) led to an early exothermic temperature peak and triggered further exothermic reactions in the adjacent laminate. Thus a side to side cure with a time delay of approximately 460 s in-between temperature peak at Pos. 5 and temperature peak at Pos. 4 was present. Figure 3-14 (a) shows this side to side cure at the time t=6700 s. When the peak temperature at position 5 was reached with 174.8°C, temperature at Position 4 was as low as 130.6°C and ascended with further experiment progress to a peak of 173°C at the time t=7166 s.

Overall, a close agreement between experimental and simulation results in the center plane was achieved for the whole temperature range between 80°C and 175°C. Consistently all simulation results showed a time delay in the temperature peak of approximately $\approx$ 100 s in comparison to the experiment. The maximum temperatures of simulation and experiment were deviating by +2.7°C/ +4.5°C/ -1.9°C/ +1.8°C/ +1.5°C at the positions Center/ Pos. 3/ Pos. 4/ Pos. 5/ Pos. 6. The assumed reason for the spread in the prediction accuracy might be small deviations in the fiber volume content due to the manufacturing process using a vacuum bag and in-plane location change of the thermocouples due to the debulking and infiltration process.

The thermal validation finalizes the characterization of the material card for HTS40/ CYCOM 823-1 laminates. It also highlights that caution should be exercised in the production of thick laminates. Although a slightly lower cure temperature than the manufacturer's recommended cure temperature was chosen, the center of the laminate reached up to 175°C, which is 15°C above the recommended temperature limit for thermal stability.

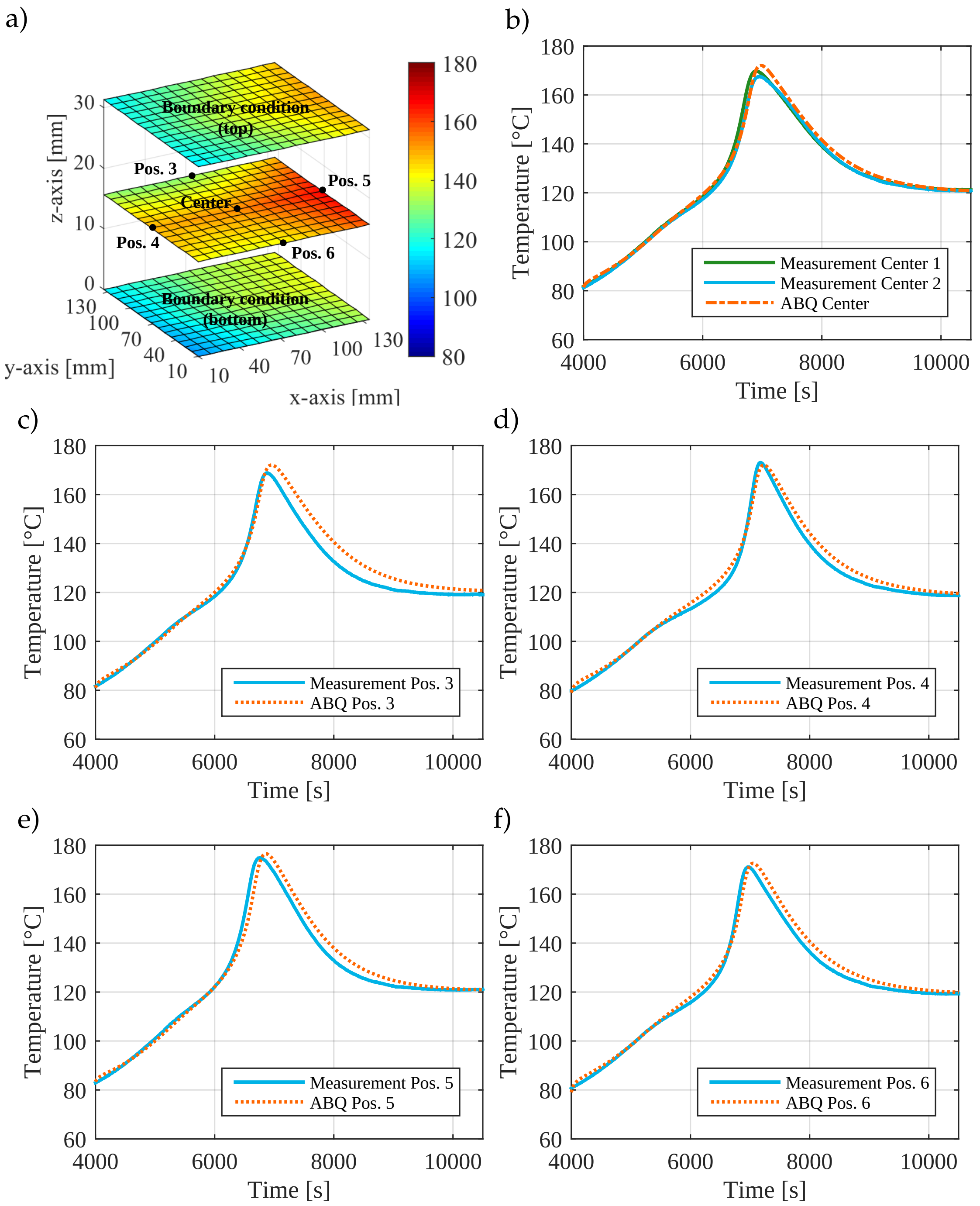

Figure 3-14 Temperature development in the validation experiment: (a) Temperature contour plot at t=6700 s showing an in-plane temperature gradient, (b) to (f) comparison of simulation and experiment at the five different positions investigated.

3.9 Summary

In this chapter, the evolution of the material properties of the neat resin Cytec CYCOM 823-1 was characterized as a function of temperature and degree of cure. Additionally, thermal tool properties were measured. Validation of the curing process of a 145 mm x 145 mm x 31 mm HTS40/ CYCOM 823-1 substructure was successfully conducted. Close agreement of the transient temperature evolution in simulation and experiment over the whole temperature range starting from negligible cure at 80°C until material degradation range above 160°C was experienced.

Specifically, the Cytec CYCOM 823-1 characterization resulted in the following findings:

1. The temperature and pressure dependent outgassing behavior of the resin was quantified. A negligible amount of mass loss was determined for DSC specimen allowing standard procedures for the enthalpy determination during the resin reaction.
2. The resin's cure temperature range exceeds the final glass transition temperature, leading to full cure without diffusion within a reasonable time frame. A cure kinetics model consisting of two separate reactions was found to lead to a close fit for the isothermal as well as dynamic temperatures. A close fit for the evolution of the glass transition temperature was achieved with the DiBenedetto equation.
3. Specific heat and thermal conductivity were modeled by means of a linear dependency on temperature and degree of cure, resulting in a close correlation to measurement data. In case of specific heat, glass transition was modeled as a sigmoid function.
4. Chemical shrinkage in the solid state exhibit a declining dependency on the degree of cure post resin gelation.
5. Thermal expansion and Young's modulus were measured for fully cured neat resin samples. A linear dependency on temperature prior to gelation and negligible dependency post gelation for both properties were ascertained.

The material characterization provided an understanding of the material behavior as well as its process window. With help of the material card, a temperature cycle optimization for various material thicknesses can be conducted and the cure behavior of the generic rotor blade can be predicted in the case study.

4 Implementation of Heat Zones

The target in the design of resistively heated zones is to enable a controlled and homogeneous temperature distribution within the zone. Since the process simulation itself already requires significant modeling effort and computing capacity, a computational efficient heat zone implementation is required. In order to support the tool manufacturing process as well as investigate the boundaries of numerically efficient homogenization strategies in the heat zone modeling, a parameter study of a representative volume element (RVE) is presented. The resulting knowledge in feasible conductor spacing also translates into the limits of a homogenization approach to model resistively heated zones within a finite element simulation. This approach is henceforth used to develop a numerical representation of temperature-controlled resistively heated zones for composite processing. The modeling procedure is verified numerically and validated by comparison of experiment and simulation temperatures of a resistively heated CFRP plate, which is subjected to convection.

4.1 Impact of a Discrete Heat Element on Temperature Homogeneity

In this thesis, two different type of tools are investigated in detail: The resistively heated tools with TCX$^{\text{TM}}$ technology have a conducting ceramic layer sprayed on the tool backside. The resistively heated CFRP tools from the tool manufacturer Qpoint use conducting carbon rovings embedded in the middle plane of the tool laminate itself [1, 30]. Thus, both investigated heating devices consist of a discrete line of conducting material with a certain width applied on either the tool backside or the tool middle plane. These conductor lines are in most cases placed equidistant, resulting in a locally highly inhomogeneous temperature distribution in the heat plane due to gaps in-between the conductor lines (see left side of Figure 4-1). The tool material between the heat plane and the tool cavity side is required to level these local temperature variances at the backside (TCX$^{\text{TM}}$ heat elements) or in the middle plane of the tool (CFRP tools) into a homogeneous temperature field in the tool-part interface. This homogenization of the tool temperatures is dependent on the tool material and thickness, width and gaps of the conductor lines, and the thermal load of the part.

Regarding the finite element model of resistively heated tools, a discrete inclusion of the conductor material would result in a very high modeling effort and high demands on the discretization and, thus, a greatly increased number of elements in a location where a coarse discretization is preferred. Hence, the thermally leveling behavior of the tool material can be utilized for a simplified model of the heating elements: Instead of a discrete path for the heat introduction the heat device representation in the model can be approximated by a heat plane with a constant power introduction. This is feasible, if a) the spacing and width of the conductor material does not change within one zone and b) the tool material and thickness compensate the localized temperature field and lead to a homogeneous temperature distribution on the tool-part interface.

To ensure a homogeneous heat-up of the tools, a parameter study on an RVE is conducted to investigate the thermal response of the self-heated tool and, thus, support tool manufacturing. Both investigated systems can be approximated with the RVE shown on the right side of Figure 4-1. The RVE is defined by the following geometric parameters: conductor width w_{h}, conductor spacing w_{c} and material thickness between conductor material and tool-part interface t. Whereas t resembles the tool thickness in case of a TCX tool, it defines half of the tool thickness in case of CFRP tools, given that the conducting rovings are located in the middle plane of the tool in this case .

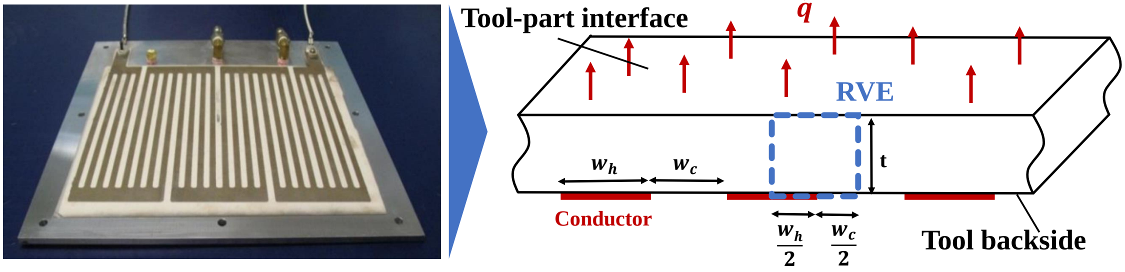

Figure 4-1 Tool backside of the TCX$^{\mathrm{TM}}$ heating element (left) [3]. Sketch of the examined RVE of the resistively heated tool (right).

The geometry is varied between the following boundaries: The width w_{h} of the conductor material is defined by the manufacturing process of the heating device and is fixed for the investigated CFRP tools at 8 mm. In case of the TCX$^{\mathrm{TM}}$ tools, the width can be adjusted in the tool manufacturing process itself and similar widths are used. The conductor gaps w_{c} are the primary design variables to ensure close to constant surface temperature in the tool-part interface and is hence varied with eight different steps ranging from the ratios $\frac{w_{\mathrm{c}}}{t} = 1$ to $\frac{w_{\mathrm{c}}}{t} = 16$. On the basis of the target tool applications, three different thicknesses $t = 4/6/8\ mm$ were investigated. Given that the self-heated technology can be applied on almost any tool material, three exemplary tool materials for different target applications were chosen in aluminum, Invar and CFRP. These materials span a wide range of conductive behavior and most other potential tool materials are within this range. The CFRP tool material properties were characterized in the previous Chapter and are shown in Table 3-9. Aluminum (Al6061-T6) and Invar (Invar 36) properties were taken from literature and are introduced in Table 3-8.

The thermal load $\dot{q}_l$ varies in the production process and a conservative upper limit was determined for the parameter study: A heat transfer simulation of a laminate with 34 mm thickness and cured CFRP properties, given in Table 3-9, was conducted with a one-sided temperature boundary condition and a 5°C/min temperature ramp from 20°C to 180°C. The maximal required surface heat flux for the set-up was determined at 1899 W/m^2 to heat up the part. To conduct a conservative investigation the thermal tool load for the parameter study was set at 2000 W/m^2, which is also the upper limit of heat introduction for the investigated resistively heated CFRP tools to date.

A quasi two-dimensional simulation model was set up consisting of linear, three-dimensional heat transfer element DC3D8 with one element in conductor direction, resembling a cross-section of the RVE, shown in Figure 4-2 (a). The thermal load of $\dot{q}_\mathrm{l} = -2000\ W/m^2$ was applied between the Positions A and B in this Figure. At the location of the conductor at the bottom material an equivalent amount of heat $\dot{q}_\mathrm{h}$ was introduced, leading to a steady state temperature field in the RVE given that all other sides were modeled as adiabatic. The temperature difference ΔT_BA of the two location A and B shown in Figure 4-2 (a) defines the capability of the tool to lead to a homogenized surface temperature at the tool-part interface in a worst case scenario.

The parameter variation with a full factorial design led to a total of 216 simulations. The temperature differences ΔT_BA at the tool-surface at the location of the potential part was examined to investigate the capability of the conductor spacing to reach a homogeneous temperature distribution at the location of the load. The results are shown in Figure 4-2 (b) to (d).

As expected, large differences can be seen for the different materials. Typical tool surface temperature discrepancies allowed in the industry are 2-3°C for an open RTM tooling. The results show, that a gap to thickness ratio of $w_\mathrm{c}/t = 3$ should not be exceeded in case of Invar or CFRP tool material to fulfill this requirement. In case of aluminum tool material the allowable ratio is significantly larger with $w_\mathrm{c}/t \approx 12$ due to vastly increased tool conductivity. Interesting is the behavior of the increasing differences in the temperature discrepancies ΔT_BA for different tool thicknesses t with increasing ratio w_c/t. These results highlight the dominance of the gap distance regarding the temperature distribution at the tool-part surface.

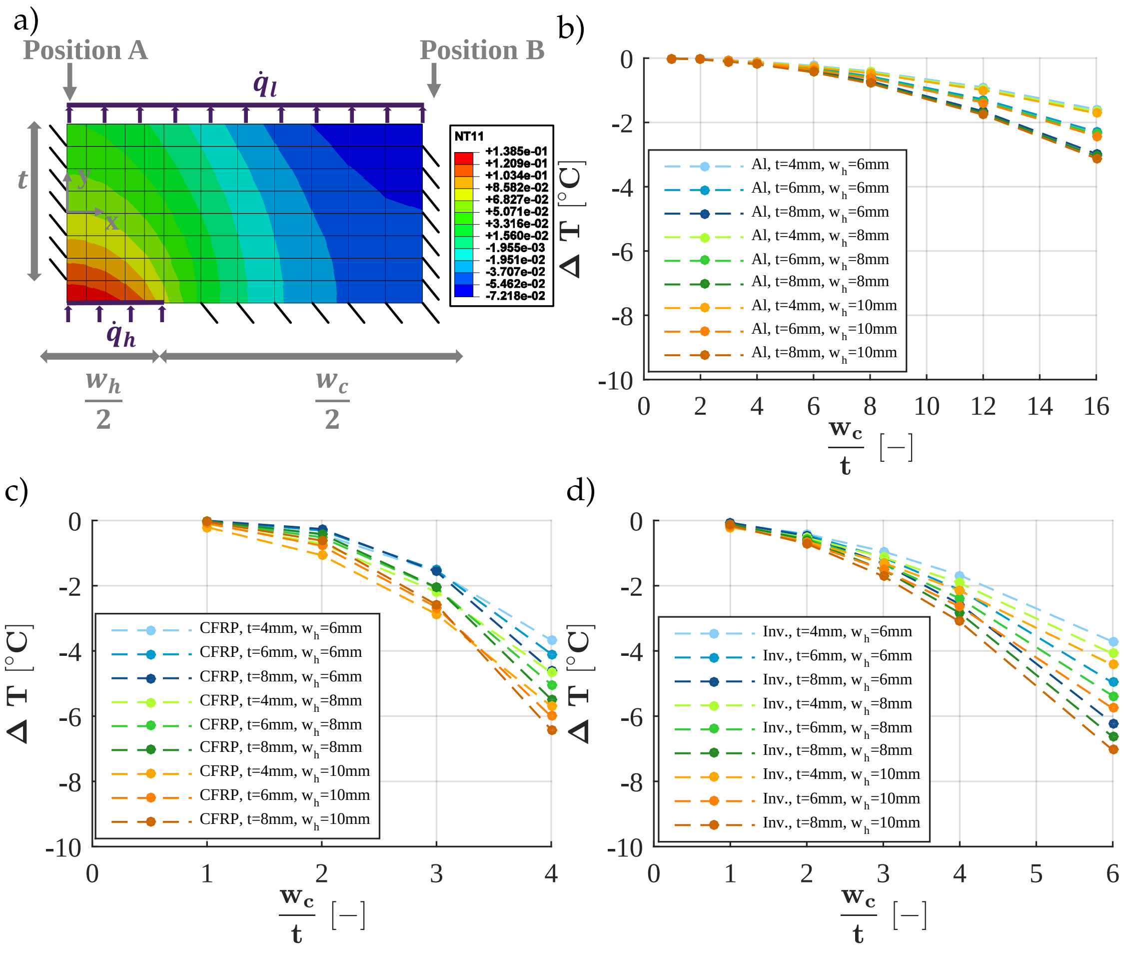

Figure 4-2 RVE study on homogenization of discrete heat introduction: (a) Finite element mesh and contour plot of a single result with CFRP material properties and results regarding gap distance allowable for the three tool materials aluminum (b), CFRP (c) and Invar (d).

Increasing tool thickness and orthotropic material behavior with higher in-plane conductivity can only partially compensate the influence of the gap distance.

In the parameter study, the heat introduced $\dot{q}_h$ was simplified as constant in the area. If the conductor material does not have a constant thickness, this simplification might not prove very accurate. Especially in case of the CFRP tools, the conducting material is a carbon roving embedded in the middle plane of the tool laminate and, thus, has an approximately elliptic cross-section instead of a constant thickness. In order to investigate the validity of the previous findings if this assumption of a constant heat introduction along the conductor width is dropped, three additional simulations were conducted to investigate the maximal temperature deviation in a worst case and, thus, the robustness of the previous findings: For the CFRP tools a maximal spacing of $w_c/t = 3$ was determined to reach sufficient temperature homogeneity. The constant load introduction of these simulations with different thickness were changed to a linear decrease of introduced energy along the conductor width from $\dot{q}_{\mathrm{h,\,left}} = 1.5\,\dot{q}_{\mathrm{h,\,mean}}$ to $\dot{q}_{\mathrm{h,\,right}} = 0.5\,\dot{q}_{\mathrm{h,\,mean}}$. Thus, the thermal load on the left side of the load introduction zone in Figure 4-2 was three times the thermal load on the right side of the load introduction zone and therefore represents a highly inhomogeneous energy introduction in the conductor area. This change in the boundary conditions led to an increase in the surface temperature discrepancy of 10.4% / 5.7% and 3.8% for the three thicknesses $t = 4/\ 6/\ 8\ mm$ and the tool material CFRP. Hence, reasonable changes in the energy introduction originating from conducting material and its thickness influence the overall temperature field only by a small amount and the results of the previous parameter study still apply if a non-constant power introduction along the conductor width is present.

4.2 Modeling an In-Situ Heated Tool

Adequate modeling of the self-heated tool temperature distribution is required to accurately capture degree of cure distribution, cure rate, and transient temperature response of the set-up. With the previous feasibility study showing the applicability of homogenization techniques, a computationally inexpensive formulation is targeted.

4.2.1 Model Requirements

In the investigated class of resistively heated tools, the amount of energy introduced is controlled by a control loop consisting of a thermocouple located within the heat plane and an exterior feedback system. The system controls the power introduction in such a way that the target temperature at the thermocouple location is enforced. The control tolerance is dependent on the quality of the control unit, but is typically within thermocouple accuracy. In Figure 4-3, a 2D sketch of an in-situ heated CFRP tool is given.

Neglecting in-plane effects, the 1D stationary energy balance at the thermocouple results in:

$$\dot{Q}_{\mathrm{h}} = \dot{Q}_{\mathrm{conv}} + \dot{Q}_{\mathrm{p}} \tag{4-1}$$

With $\dot{Q}_{\mathrm{conv}}$ and $\dot{Q}_{\mathrm{p}}$ describing the convective heat flow and heat flow into the part. Given that resistive heating elements are utilized, the control loop is required to reduce the introduced energy to zero if the right hand side of Equation 4-1 is negative.

$$\dot{Q}_{\mathrm{h}} < 0 \Rightarrow \dot{Q}_{\mathrm{h}} = 0 \tag{4-2}$$

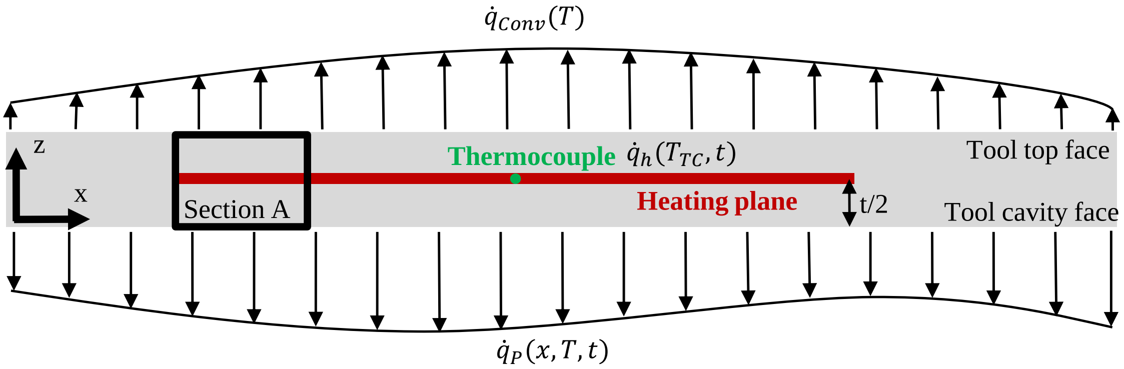

Figure 4-3 Sketch of an in-situ heated CFRP tool

In case of apparent exothermic reactions, the heat flow $\dot{Q}_{\mathrm{p}}$ may further be elaborated into its reversible fraction $\dot{Q}_{\mathrm{th}}$, accounting for temperature changes of the thermal mass, and irreversible fraction $\dot{Q}_{\mathrm{ch}}$ accounting for the chemical cure reaction.

$$\dot{Q}_{\mathrm{p}} = \dot{Q}_{\mathrm{th}} + \dot{Q}_{\mathrm{ch}} \tag{4-3}$$

A stationary investigation of Section A in Figure 4-3 shows that, although this heating system is highly adaptable if many heat patches are used, a uniform in-plane temperature distribution is not necessarily given within one heat patch: Even if the part heat flow $\dot{q}_{\mathrm{p}}$ is independent of the location, a temperature gradient towards the left side of Section A is expected, given that the heat patch ends at Section A. The left side of Section A is also subjected to the heat flows $\dot{q}_{\mathrm{conv}}$ and/or $\dot{q}_{\mathrm{p}}$, but is not imposed to internal energy introduction. Thus, it will reach lower temperatures than Section A. Furthermore, due to in-plane heat conduction, Section A will reach a lower temperature than the thermocouple placed more centrally. As demonstrated with this simplified example, the introduced energy flow $\dot{q}_{\mathrm{h}}$ enforces the target temperature at the thermocouple, but not in the whole heating area due to in-plane heat conduction and non-uniform heat flow into the part $\dot{q}_{\mathrm{p}}$. Low in-plane conductivity of CFRP emphasizes this effect. Consequently, the requirements on the curing domain boundary conditions are:

1) Modeling of the tool laminate is required since low CFRP conductivities are suspected to have a significant effect on the part surface temperatures.
2) The sole heat sink is convection.
3) The heat introduction in one patch is constant within the heating area, but transient.
4) The amount of introduced heat in time is controlled in such a way that the location of the thermocouple reaches target temperature.

5) If the temperature at the location of the thermocouple exceeds the target temperature the heat introduction is set to zero.

In general, the implementation of the first three conditions is straight forward in finite element analysis (FEA). For the remaining requirements individual solutions have to be found, depending on the application [171, 227]. However, the joint implementation of these requirements in a cure simulation environment pose a challenge in FEA, especially if aiming for general applicability. Linear combinations of Dirichlet and Neumann boundary conditions are typically used to apply a temperature-dependent heat flow such as convection. Those heat flow boundary conditions are calculated by weighting a temperature difference between the considered element and a defined ambient temperature. However, in the present case this approach cannot be utilized for tool heat introduction within the simulation as the heat flow introduced in the whole heating area is dependent on the temperature of only one point in the domain, irrespective of the element considered. Hence, a specifically designed control mechanism is implemented to address these requirements.

4.2.2 Utilization of the Reaction Flux to Control Heat Patch Temperature

Typical controlling options for modeling the heat flow boundary condition according to the third and fourth requirement stated in the previous section are linear time Invariant (LTI) control loop feedback mechanisms, such as a proportional-integral-derivative controller (PID controller). They have been used previously for temperature controlling purposes within FEA, albeit with a large amount of required time increments to settle, and could be introduced to calculate the heat flow boundary condition [171]. In the present case, the control system would be defined by the geometry and the assigned material properties. However, in cure simulation the material properties change, hence the control system changes over time. The prerequisite of the application of LTI control mechanisms is not given as the system response is time variant. The system will respond differently precure, during cure, and postcure. Thus, another solution was developed which is able to cope with the time variant system.

The general idea of the method developed was the utilization of a reaction heat flux, similar to the reaction force in a mechanical analysis, in the application of a temperature boundary condition on a single node: To satisfy the law of conservation of energy, an application of a temperature boundary condition requires an addition or subtraction of energy in the system, which is represented by the system of linear equations (SLE) to be solved within FEA. A node with an applied boundary condition can therefore be seen as a heat source or sink, dependent on the surrounding nodal temperatures. For a more convenient handling, a power is calculated to gain independence of the time increment length within FEA. This power is given as the reaction flux (RFL) within Abaqus thermal analysis and resembles the amount of thermal energy needed to reach the target temperature at the node in question. By reapplication of the RFL onto the whole heating area a transient heat introduction, which is constant in the area, is enforced. The application of the temperature boundary condition on a singular node ensures the desired temperatures on this sole location according to the targeted temperature cycle within the simulation. Given that the heat patch is controlled by one thermocouple at a distinct location, the simulation is in accordance to its physical counterpart if the respective nodal and thermocouple position are equivalent.

To reapply the RFL onto the heat patch domain, two main steps are required: The RFL is mesh-dependent as each node of a mesh with non-equal element sizes has a different attributed thermal mass due to a different attributed volume, which drives the nodal heat flux balances. It has to be transformed into a mesh-independent volumetric or an areal heat flux and subsequently applied on the heating domain in such a way that no stability issues arise and convergence of the nodal temperature and the target temperature is reached. Additional measures should be taken to ensure that the control mechanism is applicable on the time steps required by the curing simulation to prevent an increase in computational time.

According to these steps the RFL of a specific node, henceforth called sensor node n_{sens}, is tracked within FE cure analysis containing the implemented control method. In order to gain a mesh-independent power introduction, the nodal RFL value is divided by the nodal influence volume V_{inf} accounting for the thermal mass attributed to the node. Figure 4-4 shows this nodal influence volume for a symbolic distorted brick element e.

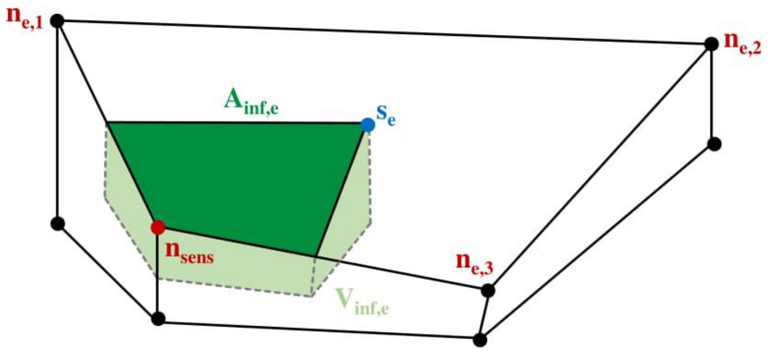

Figure 4-4 Sketch of the influence area of the sensor node of the adjacent element surface.

If the geometrical element changes in thickness direction are small compared to the element thickness z_e, a heat flux per area may be derived which is constant over the influence area A_inf of the node n_sens. Given that typical CFRP tools have a shell-type shape with a constant thickness, discretization of the contemplated tool with brick elements lead to small variations in thickness direction. A heat flux per area may be derived as in the following:

$$\frac{1}{z_\mathrm{e}}\frac{\partial A_\mathrm{inf}}{\partial z} << 1 \Rightarrow \dot{q}_\mathrm{h} = \frac{RFL_\mathrm{nsens}}{A_\mathrm{inf}} \tag{4-4}$$

The resulting power per area is calculated by a division of the reaction flux RFL_nsens by the sum of influence areas of all adjacent elements e, which are constant for the considered node in the thermo-chemical cure simulation and may be expressed by a constant mesh dependency factor f_m, accounting for the inverse of the sum over all adjacent influence areas $A_\mathrm{inf,e}$:

$$\dot{q}_\mathrm{h} = \frac{RFL_\mathrm{nsens}}{\sum_{e=1}^{n_\mathrm{a}} A_\mathrm{inf,e}} = f_\mathrm{m} \cdot RFL_\mathrm{nsens} \tag{4-5}$$

Figure 4-4 shows the influence area of one element, which is defined as the area in-between the four points sensor node $\mathbf{n}_\mathrm{sens}$, the center of the element surface area $\mathbf{s}_\mathrm{e}$, and both points bisecting the sensor node and its adjacent element nodes of the considered element $\mathbf{n}_\mathrm{e,1}$, $\mathbf{n}_\mathrm{e,3}$.

$$f_m = \frac{1}{\frac{1}{2}\sum_{e=1}^{n_\mathrm{a}}\left(\left|\frac{\mathbf{n}_\mathrm{e,1}-\mathbf{n}_\mathrm{sens}}{2} \times (\mathbf{s}_\mathrm{e} - \mathbf{n}_\mathrm{sens})\right| + \left|\frac{\mathbf{n}_\mathrm{e,3}-\mathbf{n}_\mathrm{sens}}{2} \times (\mathbf{s}_\mathrm{e} - \mathbf{n}_\mathrm{sens})\right|\right)} \tag{4-6}$$

The power per area calculated from Equation 4-5 is subsequently applied on the whole surface domain of the heat patch. The RFL is only accessible at the end of a time increment as it is a product of the solved temperature field. The heat flux boundary condition within one time increment has to be defined before the SLE is solved for. Therefore, the RFL of the previous increment has to be used as an input for calculation of the power introduction per area in the next increment. Hence, the calculated heat flux boundary conditions present an approximation. However, the effect of this approximation is small if the time increments chosen are small. If the temperature boundary condition is equal to the targeted temperature cycle, the introduced power equals the amount of power needed to reach the target temperature at the position of the considered sensor node. According to Equation 4-5, the resulting power introduction per area Δp^i, which is required in the heat patch domain to reach the target temperature in time step i at the sensor node n_{sens}, is described by

$$\Delta p^{i} = f_{\mathrm{m}} \cdot RFL^{i} \approx f_{\mathrm{m}} \cdot RFL^{i-1}. \tag{4-7}$$

Equation 4-7 gives a good prediction on the required mean power per area over many time steps. However, the delay of one time step in-between cause and control action results in high changes in the energy introduction, which further leads to oscillating behavior around the target value in transient FEA.

Further development was made considering not only the nature of RFL but also the whole control mechanism with regard to the FEA sequence. A schematic of the algorithm procedure is shown in 4-5.

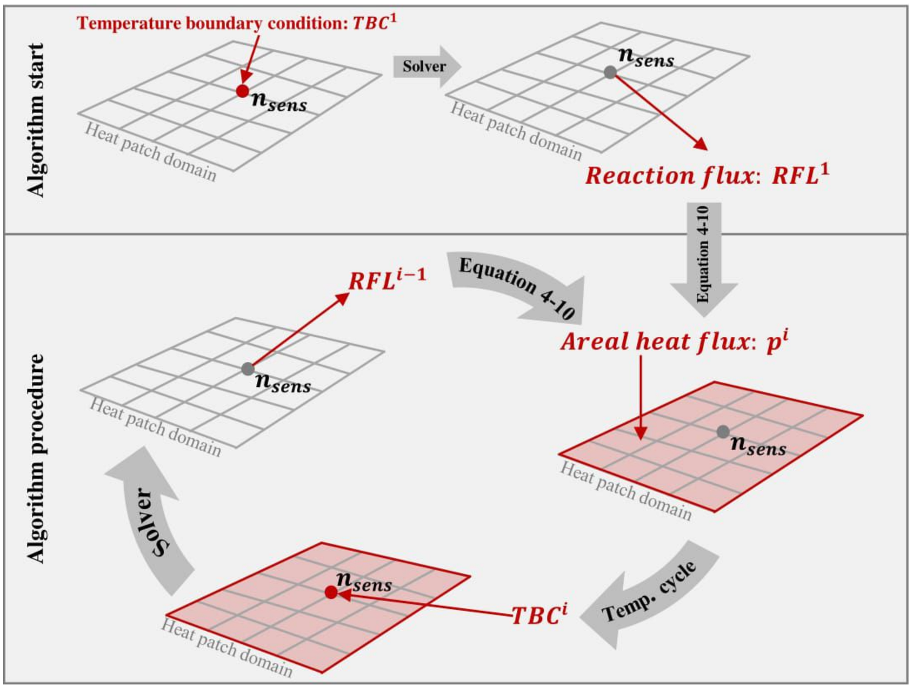

Figure 4-5 Schematic procedure of the developed control algorithm.

If a heat flux boundary condition is applied on a domain containing the sensor node, the sensor node is subjected to two sequential energy inputs. First, the heat flux boundary condition is applied, and second the RFL is iterated in such a way that the target temperature is reached. Hence, the RFL in one time step resembles the additional power required compared to the previous time step. This power discrepancy required to elevate the nodal temperature from actual value to set point value is estimated and calculated into an areal power introduction change Δp^{i}.

$$p^{i} = p^{i-1} + \Delta p^{i} \tag{4-8}$$

The starting condition is defined by:

$$p^1 = 0 \tag{4-9}$$

The total required areal power introduction to reach set point temperature is hereupon calculated with the sum over the determined energy changes of all time increments. Insertion and simplification of Equation 4-7, 4-8, and 4-9 and the introduction of an additional damping constant D results in the following description of the control algorithm:

$$p^i \approx D \cdot f_{\mathrm{m}} \cdot \sum_{j=1}^{i-1} RFL^j, \quad i > 1 \tag{4-10}$$

The damping constant D is set between 0 and 1 and influences the number of time steps required until convergence is reached. Lower values reduce the amount of immediately introduced heat flux, leading to lower convergence rate. However, they also reduce oscillating behavior if high heat fluxes are applied on low thermal masses. The damping constant has to be determined numerically by an investigation of the temperature results of the first couple of time steps. A value of 0.9 showed reasonable results for all cure simulation models investigated.

Extending Equations 4-1 and 4-3 onto a 3D application, the necessary power increment from one step to the next equals the sum of four parts:

$$\Delta p^i = \Delta p^i_{\mathrm{inplane}} + \Delta p^i_{\mathrm{conv}} + \Delta p^i_{\mathrm{th}} + \Delta p^i_{\mathrm{ch}} \tag{4-11}$$

$\Delta p^i_{\mathrm{inplane}}$ accounts for the conductive in-plane heat flow. The cure cycles predominantly applied in composite processing consist of subsequent isothermal holds and linear temperature ramps. For reasonably small time increments the temperature increments are therefore also small leading to small changes in the power increments subsequent to the initial settling time in the beginning of the simulation:

$$\frac{1}{p_{\mathrm{conv}}} \frac{\partial p_{\mathrm{conv}}}{\partial T} dT \approx \frac{\Delta p^i_{\mathrm{conv}}}{p^i_{\mathrm{conv}}} << 1 \tag{4-12}$$

$$\frac{1}{p_{\mathrm{inplane}}} \frac{\partial p_{\mathrm{inplane}}}{\partial T} dT \approx \frac{\Delta p^i_{\mathrm{inplane}}}{p^i_{\mathrm{inplane}}} << 1 \tag{4-13}$$

$$\frac{1}{p_{\mathrm{th}}} \frac{\partial p_{\mathrm{th}}}{\partial T} dT \approx \frac{\Delta p^i_{\mathrm{th}}}{p^i_{\mathrm{th}}} << 1 \tag{4-14}$$

Thus, in the case of no significant apparent exothermic reactions, the resulting power introduction through Equation 4-11 from one time step to the next is low compared to the overall power introduced after an initial settling time.

$$\frac{\Delta p^i}{p^i} << 1 \tag{4-15}$$

The majority of the required energy input change caused by heat-up and convection is accounted for in the initial time steps. Equation 4-15 shows that after these initial steps, the necessary changes in the heat introduction from one step to the next are small compared to the total introduced power and, thus, lead to a non-problematic asymptotic behavior of the temperature control.

During cure, the necessary power introduction change may be high if high cure rates are reached. However, in this case, the time steps required are very small in order to achieve high numerical accuracy and convergence of the curing simulation itself. Those smaller time steps again lead to smaller necessary changes in the power introduction and the applicability of Equation 4-11. Thus, Equation 4-10 resembles a time variant control method, which is applicable on the whole curing simulation with very limited impact on overall calculation time as only in the beginning of the cure simulation a small amount of additional numerical iterations are necessary.

These correlations are also shown in the second graph of Figure 4-11, in which the energy input changes during the cure of a 30 mm laminate coupon within self-heated CFRP tools are depicted. Here, significant relative energy change $\Delta p^i/p^i$ are apparent in the initial time steps, until the energy introduction due to heat-up and convection is settled. If discontinuous heat introduction is required, such as in case of a heat patch switch-on, Equation 4-15 does not apply for a very small amount of time steps leading to small over- or under-prediction in the required energy input (see the light green curve in the second graph of Figure 4-11 at 5412 s). The low amount of time-steps required to settle after these discontinuous heat requirements origin in the integrative behavior of the implemented control mechanism.

Finally, the fifth requirement stated in the previous section, the inability of resistive heating elements to act as heat sinks, has to be satisfied for a successful implementation of the developed control algorithm. If the sensor node is located within the middle plane of the tool and a temperature boundary condition is applied, the node may act as a heat sink if an exothermic reaction occurs. However, the self-heated CFRP tools are only able to cool down via convection, thus heat sinks within the heat plane are not acceptable. In the specific time step, when the sensor node temperature exceeds the target temperature, the temperature boundary condition has to be eliminated and the additional degree of freedom has to be solved for. Aiming for general applicability, an adaptive solution was sought. However, temperature boundary conditions cannot be switched-off adaptively in commercial FEA codes as the number of degrees of freedom and, hence, the size of the solved SLE, would change from one time increment to the next.

If the FE solver cannot be influenced directly, the option remaining is a change in the FE simulation model: The temperature boundary condition was applied on a reference node outside the tool domain and an adaptive multi-point constraint (MPC) was established to connect the reference node and the sensor node at the location of the thermocouple. The MPC was set up to enforce temperature equality between the reference node and the sensor node. If the introduced heat flux over the area resembles cooling and becomes negative, the MPC is switched off and the introduced heat flux is set to zero. Thus the temperature degree of freedom of the sensor node in the heating domain can be solved for. If the sensor node temperature is lower than the target temperature, the MPC and, thus, the control mechanism is switched on again. The numerical solutions presented for

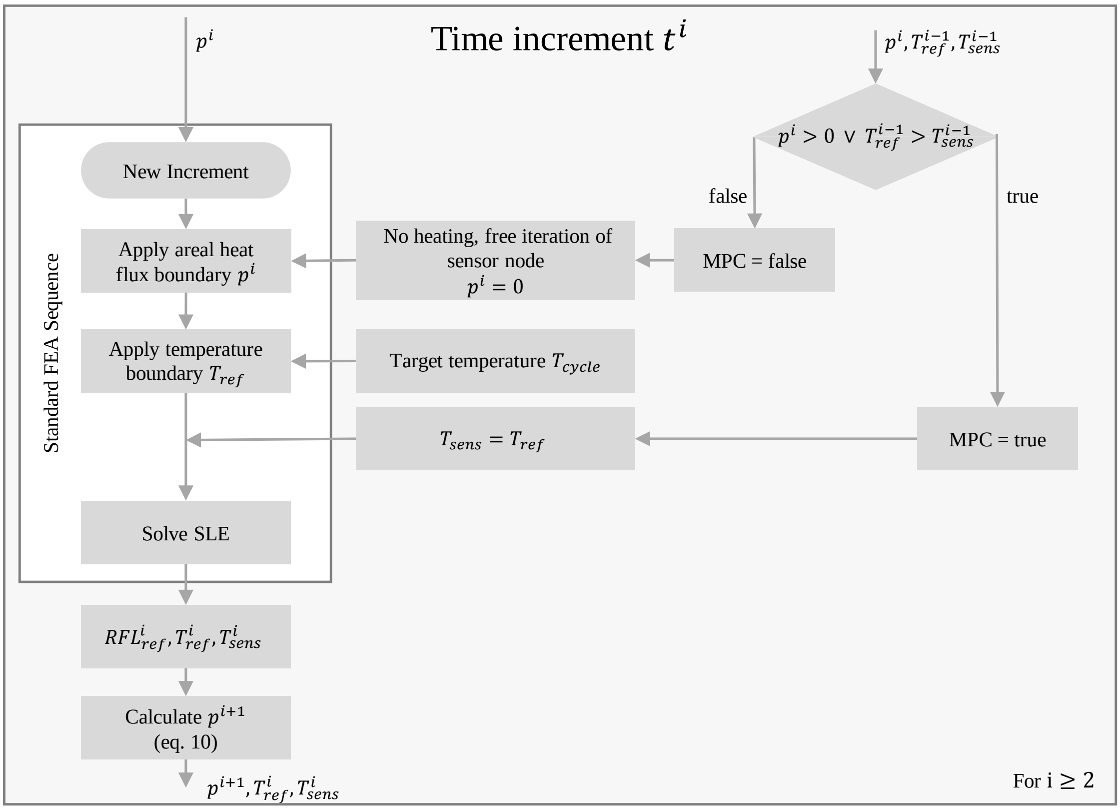

Figure 4-6 Flow chart of the calculation sequence of the implemented algorithm.

the previously established five requirements lead to a temperature controlled heat introduction, applicable in a time variant cure simulation. They were implemented in an Abaqus/COMPRO simulation platform with the Subroutines URDFIL, MPC and DFLUX. If other solvers are chosen, they can be applied in any FEA code, which provides the possibility to calculate the imposed energy change corresponding to a temperature boundary condition herein named as the reaction heat flux RFL. The calculation sequence and interactions of different components of the algorithm is shown in a flow chart in 4-6. An assessment of the accuracy and capabilities of the solutions is conducted within the final part of the present chapter.

4.3 Validation of the Control Method

The validation of the simulation method was made by a combination of an experimental validation and a numerical verification: First, a comparison of simulation and experiment of a steady state heat conduction case was set up to determine the accuracy of the spatial tool surface temperature distribution controlled by the developed method and, thus, the capability of a close calculation of the governing boundary conditions for a cure simulation in an FE environment. Second, the numerical capability of the algorithm to control the heat introduction in time to reach the targeted process temperature cycles, including influence of possible exothermic temperature peaks originating from the part, was verified.

Three major inputs are required to model the resistively heated CFRP tool in a cure simulation and, thus, the boundary conditions for the cure of a part produced by resistively heated CFRP RTM molds: The geometric model of the tool and its thermal properties, the heat transfer coefficient due to convection and an appropriate heat introduction technique by a virtual heating system. Tool properties were characterized in Chapter 3 and the convection coefficients of a resistively heated CFRP tool had to be characterized in order to validate the numerical heat introduction technique.

4.3.1 Determination of the Convection Coefficient

The heat transfer coefficient was determined in a 1D steady state set-up, characterizing convection within a workshop environment. Figure 4-7 depicts the set-up of the experiment. A resistively heated CFRP plate of the dimensions 300x300 mm and a thickness of 8 mm was placed upon a 4 mm aluminum plate of equal in-plane dimensions. Isolation was placed on all sides except for the top surface above the heat plane in the middle of the tool laminate.

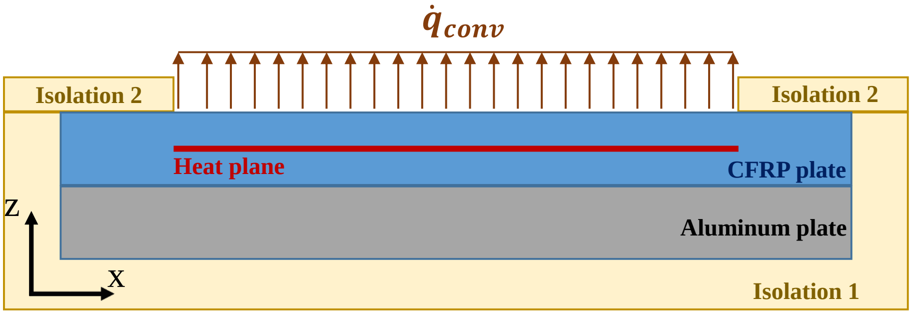

Figure 4-7 Sketch of the convection measurement set-up.

The combination of an aluminum plate with thermal insulation ensured an in-plane temperature gradient smaller than the thermocouple accuracy of ±1°C, which could thus be considered negligible.

Two steady state experiments were conducted at the isothermal set-point temperatures $T_{\mathrm{center},1} = 60°\mathrm{C}$ and $T_{\mathrm{center},2} = 80°\mathrm{C}$. Since the control thermocouple was embedded in the middle plane of the tool laminate a temperature gradient between tool middle plane and top surface was present and a convective heat transfer coefficient h_{conv} was determined by equation of convection and conduction in the z-direction:

$$h_{\mathrm{conv}} = \frac{k_{33}}{0.5\, t_{\mathrm{CFRP}}} \cdot \frac{T_{\mathrm{center}} - T_{\mathrm{surf}}}{T_{\mathrm{surf}} - T_{\mathrm{RT}}} \tag{4-16}$$

Where k_{33}, t_{CFRP}, T_{surf} and T_{RT} are denoting the laminate transverse heat conductivity, laminate thickness, laminate surface temperature and room temperature. The room temperature was determined at 22.3°C and the mean surface temperatures at $T_{\mathrm{surf},1} = 55.0°\mathrm{C}$ and $T_{\mathrm{surf},2} = 72.81°\mathrm{C}$ at the respective set-point temperatures.

With Equation 4-16, the mean heat transfer coefficients $h_{\mathrm{conv},1}$=21.2 W/m^2/°C and $h_{\mathrm{conv},2}$=20.7 W/m^2/°C were calculated. Thus, a negligible temperature dependency of the heat transfer coefficient of a flat CFRP plate was determined in negative gravity direction, and a constant heat transfer coefficient of $h_{\mathrm{conv,\ top}}$=21 W/m^2/°C was utilized in the validation simulation model at all temperatures investigated. It is important to gain an indication of directional changes in the convective heat transfer coefficient given that hot air rises in negative gravity direction and thus, hot air underneath the CFRP plate is more likely to get stuck leading to a different air flow pattern. Hence, the set-up was turned upside down and a constant heat transfer coefficient of $h_{\mathrm{conv,\ bottom}}$=12 W/m^2/°C was determined for a flat CFRP plate subjected to convection in positive gravity direction.

4.3.2 Validation of the Tool Temperature Prediction induced by the Boundary Condition Control Mechanism

The validation experiment featured a similar set-up as shown in Figure 4-7, except for a removal of the Isolation 2 and the aluminum plate. Thus, the sole CFRP plate was subjected to convection only and the presence of the unheated regions at the sides resulted in a highly inhomogeneous temperature distribution. The temperature field of the top CFRP tool surface was measured at 25 positions inside the heating area (white spots in Fig. 4-8) at the elevated tool set-point temperatures 100°C and 150°C in the middle plane of the CFRP plate.

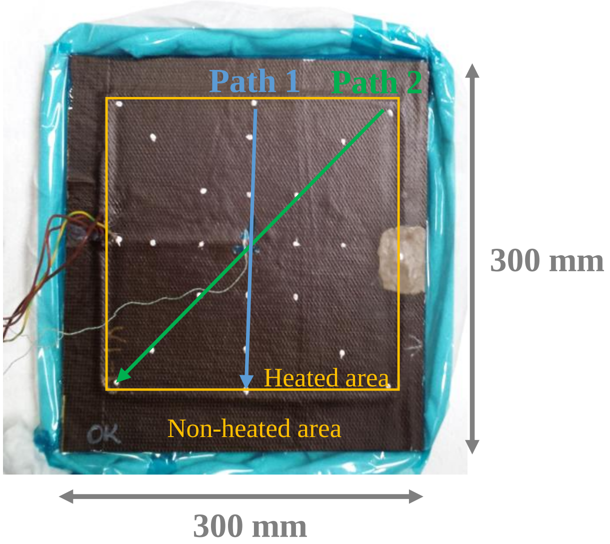

Figure 4-8 Picture of the validation experiment.

A 3D thermal simulation model, including the developed control method and the determined convection coefficient h_{conv}=21 W/m^2/°C, was set up. The tool was discretized with 8 elements in thickness direction, resulting in a total pf 5200 linear DC3D8 elements. Nodes were placed in the FE model coinciding with the thermocouple positions in the experiment. Two representative paths along different measurement locations were chosen for the validation. The comparison of the surface temperatures along Path 1 and 2 in Figure 4-8 to the 3D thermal simulation is shown in Figure 4-9. This Figure also shows the discrepancy between set-point temperature in the middle plane of the laminate (red line) and surface temperatures along path 1 and 2 (blue and green lines). The set-point temperature is not reached, independent of the location of the surface, due to low transverse heat conductivity of the CFRP laminate.

A very close agreement between simulation and experiment at both set-point temperatures was achieved. The discrepancy between measurement and simulation of Path 1 was smaller than the thermocouple accuracy at almost all locations. Only the last position in path direction at 100°C showed a deviation of 3.4°C. Similar accuracy was observed for Path 2, if the corner positions were not taken into consideration. In the corners of the heated domain the simulation was very sensitive to the exact positioning of the border of the heating area, given that the in-plane heat flux towards the unheated region was highest in the corners. Overall, this investigation showcases the capability of the developed modeling approach for a very close prediction of tool temperatures even in case of high temperature gradients apparent in one heat zone of a resistively heated CFRP tool.

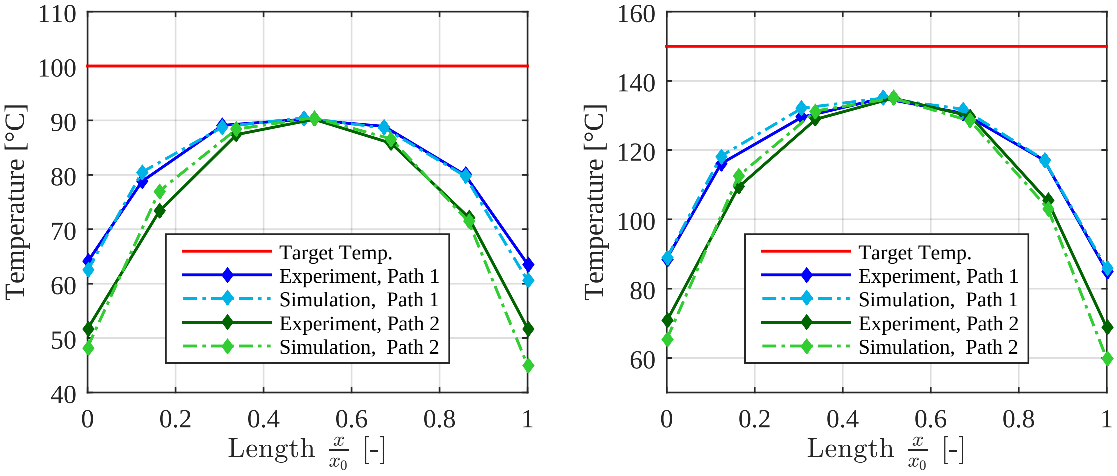

Figure 4-9 Simulation and experiment comparison of tool convection at two different target temperatures.

An in-plane temperature gradient of up to 70°C manifested within the heating area in the experiment. In a full manufacturing set-up consisting of part and tool, the thermal mass and conductivity of the part would reduce the in-plane gradient significantly and inclusion of additional heat patches would lead to a more refined heat introduction and produce significantly lower temperature gradients in the heating area. Nevertheless, the experiment highlights the need of an appropriate thermal dimensioning of the heating area in the application of resistively heated tools, given that very large temperature gradients can potentially arise.

4.3.3 Numerical Verification of the Transient Control Mechanism Response

The different scenarios of standard cure cycles in which the control algorithm is required to adjust the introduced heat in accordance to the preset temperature cycle and, thus, requires verification, are:

- Heat up of the thermal masses of tool and laminate.
- Set-ups subjected to exothermic reactions.
- Cool-down governed by convection.
- Compensation of convection during an isothermal hold.

All these scenarios are relevant during cure of a thick CFRP laminate within the CFRP-tool. Therefore this application case was chosen for the numerical verification to showcase the accuracy of the developed power introduction control method. The simulation set-up is depicted in Figure 4-10.

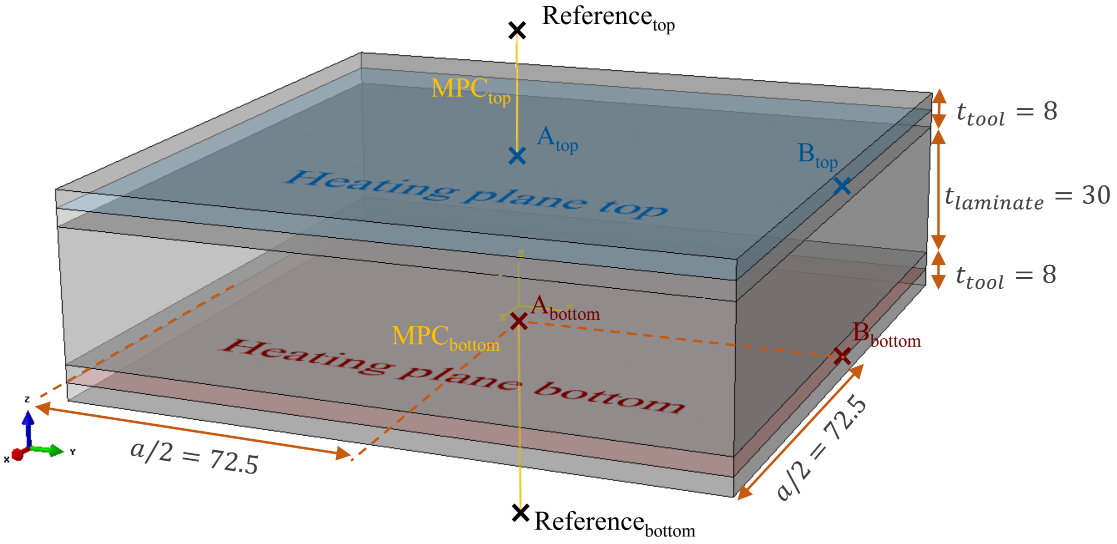

Figure 4-10 Setup of the simulation verification model [12].

The verification model consisted of 30 mm curing laminate and 8 mm cured tool CFRP laminate on the top and bottom side. Discretization was conducted utilizing linear DC3D8 elements, with either horizontal edge discretized by a total of six elements. Eight elements were used in the thickness direction of the part, the tool top plate and the tool bottom plate respectively. A heat transfer coefficient of h_1=21 W/m^2/°C and h_2=12 W/m^2/°C respectively was applied at the top and bottom side to account for two different convection coefficients. The heat plane was located in the middle plane of the tool laminate and the control method was applied including reference points outside the domain and sensor nodes located at position A such as shown in Figure 4-10. The initial temperature was set at 80°C, followed by a temperature ramp of 1.5°C/min up to 120°C and a 8400 s hold at that temperature. Graph 1 in Figure 4-11 shows the heat plane temperatures of nodes located at position B in Figure 4-10 for the bottom and top side as well as the amount of energy introduced, which was controlled by the algorithm to reach the displayed temperatures.

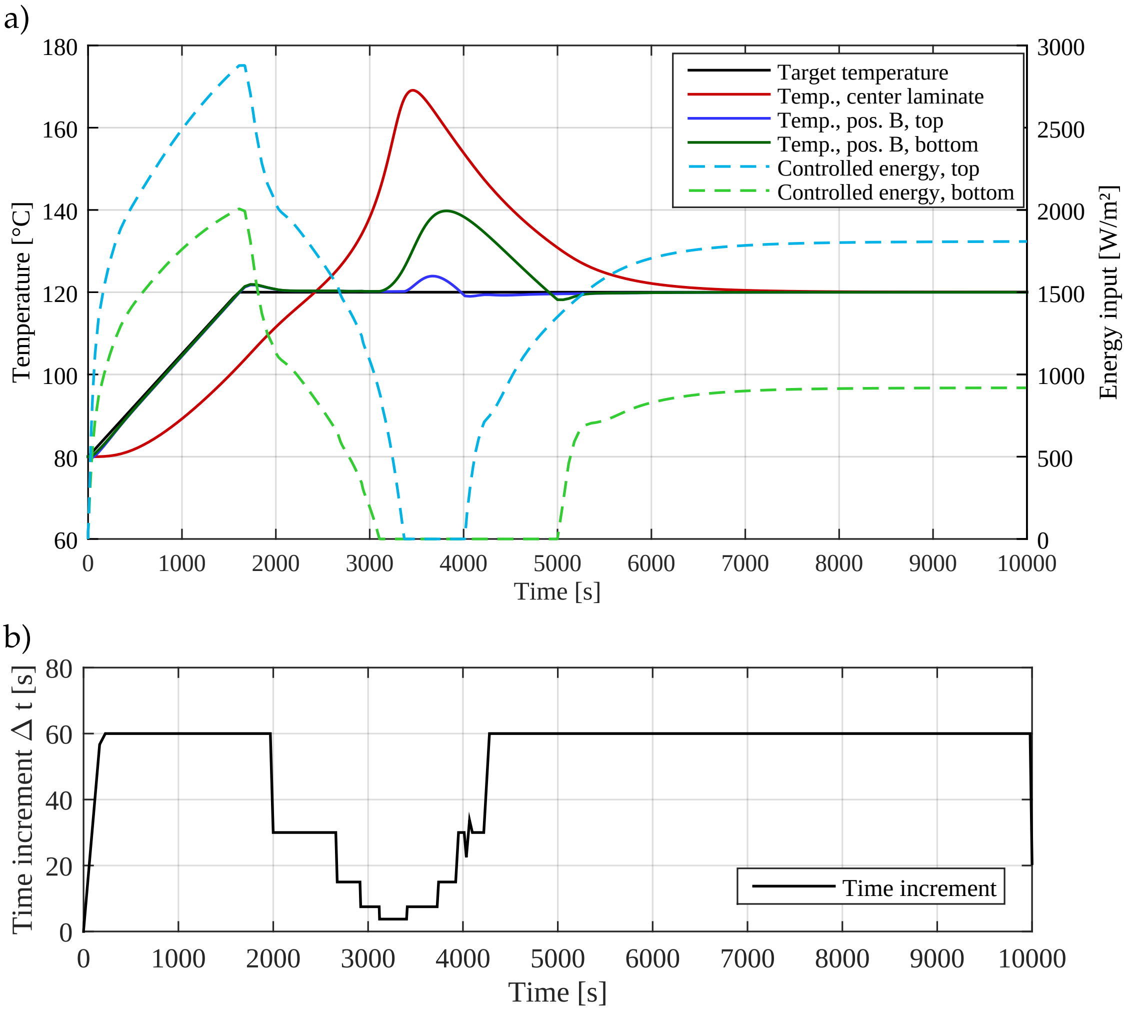

Figure 4-11 Evolution of temperatures, controlled energy input, and time step length in the verification simulation.

The heat-up phase from 80°C to 120°C showed a close match between the target temperature and the controlled heat area temperatures at both sides (see Fig. 4-11 (a)). The introduced power to follow the targeted temperature cycle in that period accumulated from the inner energy required to heat up the thermal mass and the compensation of convective heat loss. The center of the laminate was subjected to temperature change after approximately 400 s, due to thermal lag. Subsequent to the initial settling time, a constant power introduction was required to account for elevation of the tool and part temperature. The rise in the required power introduction was attributed to the convective heat loss, which is a linear function of the surface temperature.

At the transition from the heat-up to the hold stage at $t = 1600\ s$ significantly less energy was required, given that the tool reached set-point temperature and only the decreasing heat flux into the part as well as convection had to be compensated for from this point on. The algorithm controlled the introduced energy with a slight overshoot of 1.9°C resulting in a significant drop of the surface heat flux. Given that almost no decrease in the slope of the laminate's center temperature is seen at this point, the sole exothermic reaction energy is already sufficient to elevate the center temperatures and proceed the curing process. This is also illustrated by the decrease of the energy introduction on both sides until the heat flow direction is reversed from the part into the tool and the resin reaction energy cam compensate for convection at 3100 s on the bottom side and at 3400 s on the top side.

The heat convection coefficients led to the convective heat loss being lower than the heat flux from the part into the tool on both sides. The heating device is not able to apply internal cooling effects in general and Equation 4-2 took effect. The energy introduction was set to zero and the tool temperatures rose significantly above set-point temperature. Given that the convective heat loss on the top side was significantly higher than on the bottom side, the duration of zero energy introduction was shorter on the top side as the heat provided by the part's resin reaction slowly decreased.

Once the part cure approached completion and the reactive energy flux declined, the tool temperatures dropped due to convection until set-point temperature was reached at 4000 s on the top side and 4950 s on he bottom side. Since no estimation terms were introduced to obviate the time delay of one time increment in the control algorithm, a small undershoot of up to 1.8°C was observed as soon as the heat plane temperature of the bottom side reached the target temperature again. With the selected damping constant D=0.9 the algorithm needed five time steps to control the introduced power in such a way that a temperature discrepancy lower than 1°C between target and heat plane temperature was reached. From this point on, the compensation of convection was enforced by the control algorithm with almost no discrepancy between the target temperature and the actual heat plane temperature.

It should be noted, that such a large exotherm in the middle plane of the laminate is not desired in composite processing and the set-point temperature cycle should be adjusted in such a case. Once the laminate surface temperature reaches 120°C, the energy introduction drops to zero (see Fig. 4-11 a) and the exothermic reaction energy alone is responsible for the steep increase in temperature. While e.g. fluid heated systems could potentially apply cooling, the utilized resistive heating technology is not able to do so. However, the impact of cooling on the laminate's center temperature is very limited in case of thick laminates due to the low transverse heat conductivity of the material. The impact of an optimized cure cycle on the temperature overshoot in the laminate's center far exceeds the impact of cooling technology and should be investigated thoroughly in such a case.

Overall, the heat plane temperatures of the whole cure process, containing all relevant application scenarios, was controlled by the algorithm successfully. In case of an instantaneous and significant drop or rise of the required heat introduction, temperature over- or undershoots lower than 2°C were detected. No influence of the different convection coefficients and, hence, the total amount of introduced energy required, on the convergence behavior of the algorithm was observed. The amount of time until the control algorithm successfully corrected the introduced power is dependent on the time step length. The time step length within this example was set adaptive with an upper limit of 60 s and is shown Figure 4-11 (b). The time step length was lowered between 2000 s and 4200 s to ensure a convergent solution during cure. In this cure period, big changes in temperature as well as material properties have to be accounted for. However, apart from the initial settling stage no reduction in the time step length originating from the control method itself was required, which shows the efficiency of the developed method.

4.4 Summary

In order to enable an appropriate cure analysis of the part manufactured with temperature controlled resistively heated tools, a universally applicable numerical method was implemented and validated in the Abaqus/CCA FEA cure simulation environment. A set of five requirements based on the physical behavior of self-heated tools was derived and the numerical method, consisting of a control algorithm and a simulation model extension, was developed to address each of these requirements. A verification of the numerical power introduction control method in a simulation model predicting the cure of a 30 mm CFRP laminate with resistively heated CFRP tools showed a close control of the heat plane temperature in time to follow the set-point temperature appropriately.

The validation of the spatial temperature distribution governed by the developed numerical method confirmed that appropriate simplifications were made in the set-up of the simulation method. Additionally, high temperature gradients of up to 70°C within the validation tool highlighted the need for the developed method in thermal and cure simulations of parts produced by resistively heated CFRP tools, since these potentially arising surface tool temperature gradients cannot be accounted for with standard boundary conditions.

The developed approach to model resistively heated tools is used to determine the capability of the thermal dimensioning technique developed in the following chapter and to investigate the generic rotor blade in the case study.

5 Thermal Dimensioning of Multi-Zone Molds

To fully realize the potential of resistively self-heated tools with several independent heating zones, a simulation method needs to be developed to determine a sound allocation of these heating zones. The effectiveness of the developed method has to be investigated via the determination of the absolute temperature accuracy reached as well as relative improvement over the experience based estimations, which are often used. Finally, the impact of different tool materials on the zone dimensions and, eventually, on the part temperature and cure needs to be determined. The content of this chapter was developed in a collaboration with the McGill University Montreal and the curing laminate's material system in this chapter is different to the material system in the other chapters of this work. However, the methods developed are independent of the part and tool material.

5.1 Set-Up of a Validated Application Case

In order to ensure feasibility on a wide range of applications, the model to be developed needs to be able to consider the thermal behavior of the complete tool, the thermal and cure behavior of the part as well as the impact of environmental effects influencing the temperature field, such as convection. Thus, an application case was chosen which includes all these effects, and in which a zonal allocation can be easily defined with standard knowledge of carbon composite processing.

5.1.1 Experimental Set-Up

The validation set-up chosen consisted of a tapered Out-of-Autoclave part produced on a six-zone aluminum tool with TCX$^{\text{TM}}$ heating elements at the McGill University Montreal [13]. The allocation of the heating zones is shown in Figure 5-2. Each individual heat zone possessed its own sensing thermocouple located in the middle plane of the tool, colored green in Figure 5-1. An external PID-control device regulates the heat introduction for each zone in such a way that the respective thermocouple reaches the set-point temperature cycle. The heating elements were placed on the underside of a flat 4.8 mm thick Al6061-T6 plate with the dimensions of approximately 600 mm x 400 mm. In accordance to

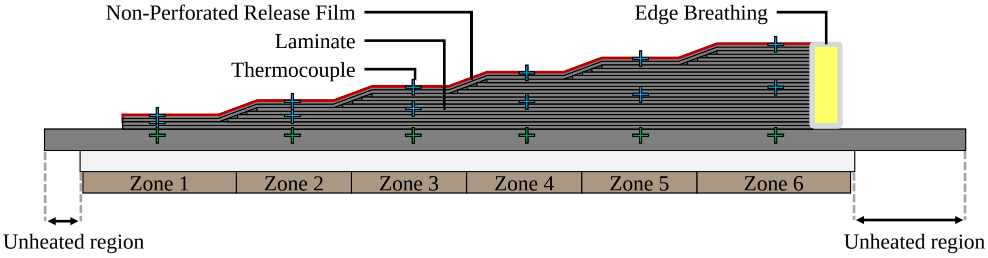

Figure 5-1 Sketch of the validation model set-up [13].

the allocation of the heat zones on the tool, the part consisted of six areas with 4/8/12/16/20/24 plies of CYCOM 5320 8HS prepreg material leading to increasing thickness along the length of the part (see Figure 5-1). The part placement ensured coincidence of the respective tool zone and the corresponding part area transitions. Part dimensions were 450 mm in the x-direction and 100 mm in the y-direction. Fiberglass isolation sheets were placed above and below the tool, covering the whole area except for a 25.4 mm boundary along the tool edge. The applied cure cycle consisted of temperature ramps of 3°C/min and two hold stages of 121°C and 177°C for the duration of 2 h and 3 h, respectively.

5.1.2 Material Models of the Curing Laminate

Kratz et al. investigated the material Cycom 5320 with a Thornel T650-35 carbon fiber experimentally [18]. In this work, the thermal properties of the resin system were determined and a resin kinetics model was set up. Additionally, a validation experiment was conducted and showed a close correlation between simulation and experiment. These material models and properties were used in this Chapter.

The utilized model for the prediction of the evolution of the degree of cure features a combination of the Kamal and Sourour cure kinetics model and a diffusion factor developed by Cole et al. [18, 61, 71]:

$$\frac{d\alpha}{dt} = K_1\alpha^{m_1}(1-\alpha)^{n_1} + \frac{K_2\alpha^{m_2}(1-\alpha)^{n_2}}{1+\mathrm{e}^{D(\alpha-(\alpha_{\mathrm{C0}}+\alpha_{\mathrm{CT}}T))}}\ , \tag{5-1}$$

where K is the Arrhenius temperature dependency

$$K = A\mathrm{e}^{\frac{-\Delta E}{RT}}\ . \tag{5-2}$$

Within these equations ΔE represents the activation energy, R the universal gas constant, and A the Arrhenius constant required to describe the temperature dependency. The constants m and n govern the autocatalytic behavior, C resembles the diffusion constant, α_{C0} is the critical degree of cure at 0 K temperature, and α_{CT} accounts for the increase in the critical resin temperature at which point the reaction becomes diffusion controlled. All values are presented in Table 5-1. The thermal properties of the constituents of the curing part are presented in SI units in Table 5-2 [18]. Three different tool materials were used within this study to show the influence of tool properties on the thermal dimensioning. The information on the corresponding thermal properties are given in the Tables 3-8 and 3-9.

Table 5-1 Resin cure kinetics model constants Cycom 5320 [18].

Model constant	Value	Units
E_1	82375	[J/mol]
A_1	8.23E7	[1/s]
m_1	0.75	[-]
n_1	12.46	[-]
E_2	62355	[J/mol]
A_2	1.04E5	[1/s]
m_2	0.9	[-]
n_2	2.07	[-]
C	40.4	[-]
α_{C0}	-1.12	[-]
α_{CT}	4.53E-3	[1/°C]

Table 5-2 Thermal properties of the constituents of the curing CFRP material [18, 19].

Property	Cycom 5320 (resin)	T650-35 (fiber)	Units
c_{p}	1260	712	[J/kg/°C]
k_{l}	0.167	14	[W/m°C]
k_{t}	-	5	[W/m°C]
ρ	1310	1770	[kg/m^3]

5.1.3 Simulation Model and Validation

A simulation model was set up according to the validation experiment using the Convergent/COMPRO cure simulation platform and the Abaqus FE solver. Discretization was undertaken using linear DC3D8 elements, as shown in Figure 5-2. Four elements were used in the tool thickness direction, leading to a total of 11496 elements for the tool. Two plies in the thickness direction were homogenized in one element layer within the part, leading to a total of 3080 elements. In

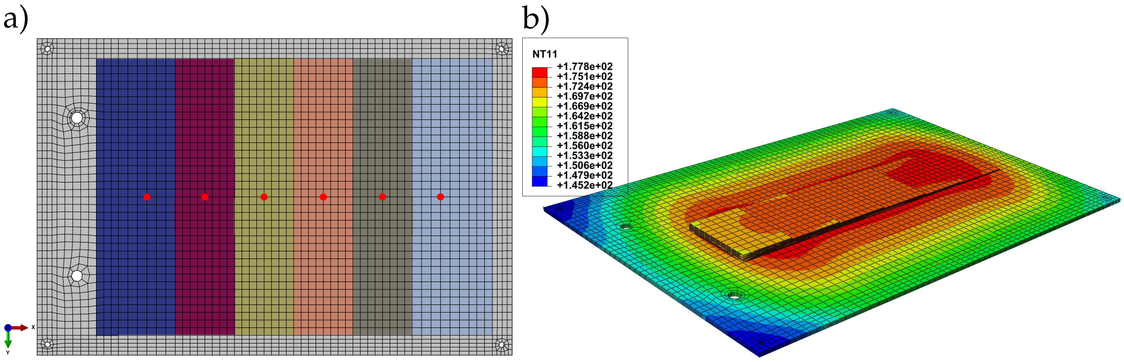

Figure 5-2 (a) Heat zone allocation on the bottom side of the validation tool. The zones are distinguished by element colors; bright red spots mark the locations of the control thermocouples. (b) FE-model with temperature contour plot in the second hold stage (at approx. 17000 s).

the non-insulated areas along the edge of the tool, a convection coefficient of 21 W/m/°C was applied on the tool top side and a value of 12 W/m/°C was applied on the bottom side in accordance with the values measured in Chapter 4.

The experiment showed a temperature gradient in the steady state stages in the thickness direction, indicating a non-perfect isolation of the top side. With the assumption of a 1D steady state heat flow and a negligible temperature gradient between the location of the tool thermocouple and the tool surface T_{Tool}, the heat transfer coefficient h_{iso} was determined by equation of convection and conduction.

$$h_{\mathrm{iso}} = \frac{k_{33}}{t_{\mathrm{l}}} \cdot \frac{T_{\mathrm{tool}} - T_{\mathrm{p,b}}}{T_{\mathrm{p,b}} - T_{\mathrm{RT}}} \tag{5-3}$$

With the laminate thickness t_{l}, the part bag-side temperature $T_{\mathrm{p,b}}$ and the room temperature T_{RT}, the heat transfer coefficient for the isolated region on the top side was determined at 1.4 W/m/°C. The temperatures at three different locations were compared and are shown in Figure 5-3: the thermocouple embedded in the tool, the middle plane of the laminate and the bag-side of the laminate. Whereas the tool temperature was controlled at the measured location to match the temperature cycle in simulation and experiment, the mentioned offset appeared in the middle of the laminate and the bag-side location in the two dwell stages indicating the natural convection influence. With the determined convection coefficient, the simulation showed a close correlation within thermocouple accuracy with the experimental results in both dwell stages. Significant deviation between the simulation and the experiment occurred solely during the first ramp until 121°C, which was to be expected due to the negligence of the prepreg compaction behavior in the simulation. It has been shown for the same part material experimentally, that the initial ratio of area in contact between tool and part in relation to the whole interface area ranges from 80% to 90%, depending

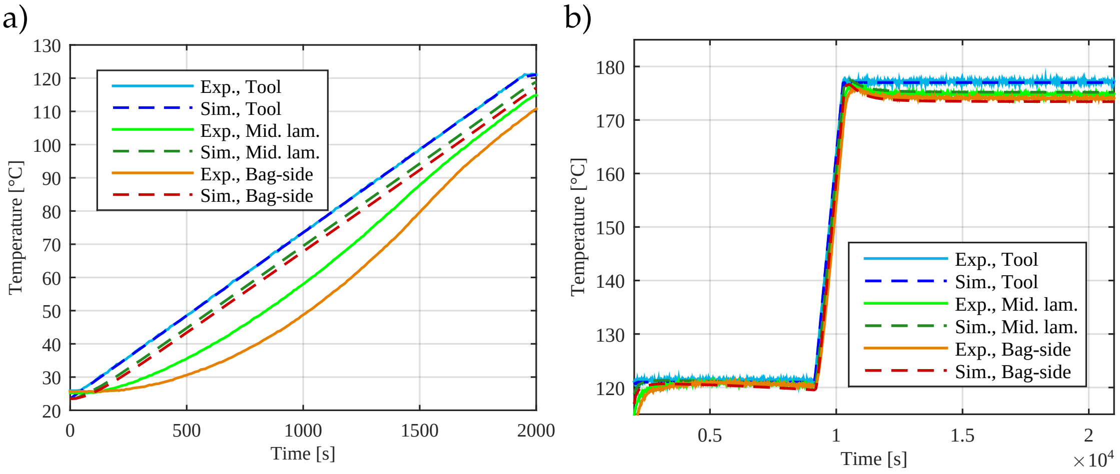

Figure 5-3 Temperature validation of the simulation model at three different locations in zone 5: (a) Compaction temperature range and (b) temperature range of interest for the validation.

on the set-up and debulk duration, and reaches full contact at ~60°C [228]. Thus, small gaps in-between tool and part lead to a higher thermal gap resistance in the initial stages of the experiment compared to the simulation, in which the effect of gap resistance is neglected. Additionally, during the first ramp up to 121°C, a significant laminate thickness change was measured experimentally [229]. In the initial stages of the temperature ramp, macro voids and dry fiber bundles are present in the material and increasing viscosity leads to resin flow into those tows, which are used as air evacuation channels. Therefore, given that air is apparent in the laminate until ~100°C, laminate thermal conductivity and density is decreased initially and gradually increases with compaction progress. Finally, the geometric change cannot be modeled in a sole thermal/cure simulation. Consideration of the geometric change would require a fully coupled thermal-mechanical analysis.

The first temperature ramp is not critical for the cure simulation as resin temperature is too low for significant cure. Starting with the first dwell, in the remaining temperature range the mean deviation of the simulation in Zone 5 was determined at 0.2°C for the tool thermocouple, -0.6°C for the thermocouple embedded in the middle of the laminate and 0.0°C for the bag-side thermocouple. Standard deviations for the tool, middle and bag-side thermocouples were 0.1°C, 0.7°C and 1.4°C, respectively. Similar accuracy was determined in the other zones. Hence, the validation showed high accuracy in the important time frame from 2000 s until the end and the simulation model is used as a template for the subsequent evaluation of the thermal dimensioning method.

5.2 Thermal Dimensioning of the Heating Area

5.2.1 Approach

The partitioning of the designated heating area should be conducted in such a way that the temperature field is as homogeneous as possible during the part manufacture. Each partition, called heating zone within this work, has its own control unit of sensing thermocouple and external PID control modulating the applied surface heat flux $\dot{q}_{\mathrm{h}}$ in the zone to reach the set-point temperature $T_{\mathrm{set-point}}$. If the control thermocouple is placed within the heating zone and the control mechanism is accurate, it is an intrinsic prerequisite that the temperature at the location of the thermocouple T_{TC} meets the set-point temperature.

$$\forall\ \dot{q}_{\mathrm{h}} : T_{\mathrm{TC}}(\dot{q}_{\mathrm{h}}) = T_{\mathrm{set-point}} \tag{5-4}$$

Due to heat transport (see Eq. 2-43), a heat flow between heating zone and surrounding material is present if temperature gradients are apparent. This heat flow is dependent on the material, geometry, environment and it varies in the whole heating zone in most application cases. With the assumption of a constant heat flux in the area,

$$\dot{q}(x,y) = \dot{q}_{\mathrm{h}} \tag{5-5}$$

this leads to a nonuniform temperature in the heating zone. If the size of a small zone decreases, the difference in temperature between the control location and its periphery decreases too, leading to a more homogeneous temperature allocation in the zone. An infinite small heating zone will naturally reach set-point temperature. Thus, perfect temperature equality in a heating area is reached, if an infinite amount of zones are spread within the area. In the presented approach, this concept is transferred into a FEM cure simulation. First, a simulation with the largest number of heat zones possible is conducted and the resulting surface heat flux is tracked leading to a time- and location-dependent surface heat flux, which is required to reach set-point temperature in the designated heating area. In a second step, the surface heat fluxes of each zone is investigated and a sound partitioning of the designated heating area is made by merging the small zones with similar thermal behavior.

Given that elements are the smallest units, they define the smallest possible zones in an FE analysis with nodes resembling the control points. Thus, by application of a temperature boundary condition in the designated heating area in the first step, all nodes n_i within this area will act as controlling units and the respective zone areas can be determined by the inverse of the mesh factor f_m introduced in Chapter 4 in Equation 4-6:

$$A_{\mathrm{inf},i} = \frac{1}{2}\sum_{e=1}^{n_\mathrm{a}}\left(\left|\frac{\mathbf{n}_{\mathrm{e},1} - \mathbf{n}_i}{2} \times (\mathbf{s}_\mathrm{e} - \mathbf{n}_i)\right| + \left|\frac{\mathbf{n}_{\mathrm{e},3} - \mathbf{n}_i}{2} \times (\mathbf{s}_\mathrm{e} - \mathbf{n}_i)\right|\right) \tag{5-6}$$

Further, the application of Equation 4-16 on the cure simulation results lead to a time- and location-dependent surface heat flux. It contains the information of the impact of convection, thermal mass and transport effects as well as the resin cure on the temperature field in the designated heating area of the tool. Figure 5-4 shows the derived surface heat flux during both temperature ramps and dwells of the simulation model.

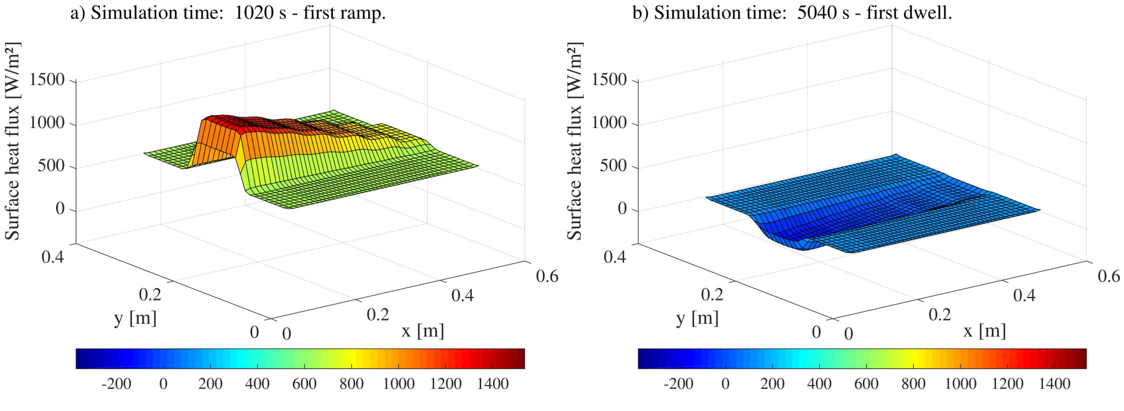
a) Simulation time: 1020 s - first ramp.

b) Simulation time: 5040 s - first dwell.

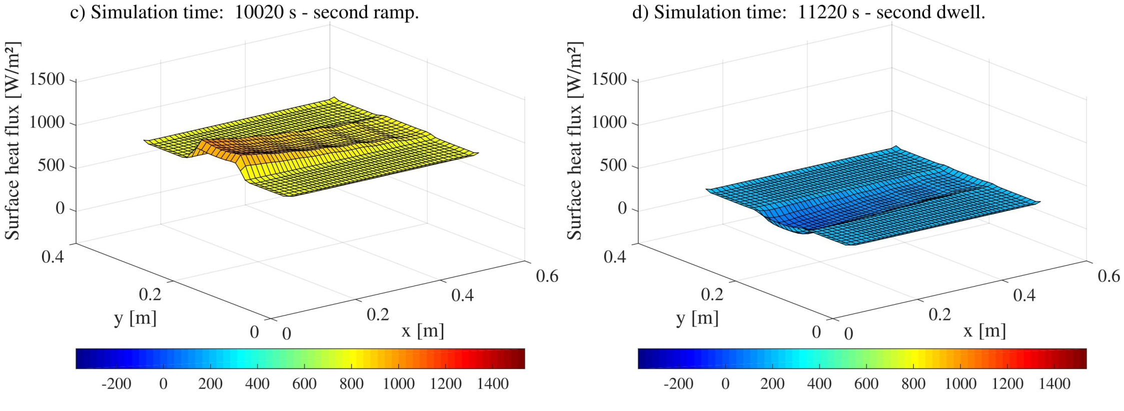
c) Simulation time: 10020 s - second ramp.

d) Simulation time: 11220 s - second dwell.

Figure 5-4 Calculated surface heat flux $\dot{q}_\mathrm{h}(x,y)$ at different time steps in the inner heating area of the tapered laminate.

As demonstrated with help of this Figure, all major thermal phenomena during the cure are present: The heat-up of thermal mass is apparent in Figure 5-4 (a) and (c), in which the overall surface heat flux of the set-up is higher compared to the dwells. In contrast, resin cure during the dwells releases exothermic reaction energy. Thus, nodes closely located to the part will need to provide less heat, leading to a lower heat flux of those elements compared to their surroundings (see Figure 5-4 (b) and (d)). Convection is seen in the difference in the overall energy level apparent in the isothermal dwells of Figure 5-4 (b) and (d). Convective heat loss increases with temperature, hence it leads to an increased offset of the total surface heat flux at 177°C compared to 121°C. Overall, all major effects for thermal tool behavior can be derived from the surface heat flux progress in the area. An exception occurs in case of exothermic resin reaction during temperature ramps in which the heat fluxes for resin cure and the heat-up of thermal mass compensate each other. However, given that the tool is required to control temperature only, it can be dimensioned according to the sum of heat fluxes. Hence, compensatory effects do not have to be accounted for in the thermal tool dimensioning. To obtain a constant heat patch allocation from the calculated time-dependent surface heat flux two different algorithms were developed, implemented, and evaluated: the Least Gradient Merge (LGM) algorithm and the Direct Kmeans Clusterung (DKC) algorithm. Both algorithms were designed to identify an optimal numerical solution for a partitioning of the designated heating area, independent of tool materials, restrictions of a specific tool manufacturer, or costs. Introduction of these considerations is straightforward in most cases but not in the scope of the presented work.

5.2.2 Least Gradient Merge Algorithm

The general idea of this algorithm bases on the assumption that a neighboring element pair is similar and should be considered in the same cluster if the difference in the surface heat flux behavior between those elements is small. Considering that many elements might have small differences in their heat flux behavior, the impact on the overall heat flux in the designated area is assumed to be the lowest if the element pair with the overall lowest difference in the surface heat fluxes is merged into one cluster. In the implementation of this concept, each element forms its own cluster at the start of the merge operation. For each cluster pair in contact $\mathbb{I}$ and $\mathbb{J}$, the sum of all heat flux differences in time $G_{\mathbb{I}\mathbb{J}}$ is calculated

$$G_{\mathbb{I}\mathbb{J}} = \int |\dot{q}_{\mathbb{I}}(t) - \dot{q}_{\mathbb{J}}(t)| dt \tag{5-7}$$

and the cluster pair with the minimal difference will be merged into a new cluster $\mathbb{K}$.

$$G_{\mathbb{I}\mathbb{J}} = \min(\mathbf{G}) \Rightarrow \mathbb{K} = \mathbb{I} \cup \mathbb{J} \tag{5-8}$$

Finally, the surface heat fluxes of the two clusters are averaged with consideration of their heat surface areas A.

$$\dot{q}_{\mathbb{K}}(t) = \frac{\dot{q}_{\mathbb{I}}(t)\, A_{\mathbb{I}} + \dot{q}_{\mathbb{J}}(t)\, A_{\mathbb{J}}}{A_{\mathbb{I}} + A_{\mathbb{J}}} \tag{5-9}$$

The next iteration will commence with the calculation of the new **G**-matrix. With each iteration one cluster pair is merged. Thus, for a problem with n elements and the desired number of clusters m, the algorithm requires $l = n - m$ iterations.

This approach considers time-dependency of the cluster surface heat fluxes to a full extend but it is also susceptible to local singularities. Occasionally, in element locations close to a corner or in case of poor mesh quality leading to inaccuracy of the Approximation 4-16, local singularities will occur leading to one element having larger gradients to its neighbors than all other gradients apparent in the model. Since the algorithm proceeds to merge until a predefined number of remaining clusters, these local singularities and edge effects might resemble most of the final number of clusters in industrial parts. Data smoothing was investigated but could not fully negate these effects. To circumvent this problem and investigate the capability of the algorithm an additional step was included in the merging process: First 90 % of the total possible amount of merging operations were conducted. Subsequently, an allocation step was added in which all clusters with the size of less than five elements were merged with their neighbor with the least difference in the surface heat flux to the cluster in question. Finally, the standard merging process is commenced until the final amount of desired element clusters is reached. With this adjustment, the proposed algorithm is robust enough to be applied.

Given that the Least Gradient Merge (LGM) algorithm determines the zone allocation along the biggest gradient lines in the time-dependent surface heat flux, the resulting zone allocation in the simulation model reflects this behavior. As shown in Figure 5-5, it leads to the introduction of several transition zones on the part edge, whereas the main heat area located directly under the part is sectioned into two groups only.

5.2.3 Direct Kmeans Clustering Algorithm

The second approach uses the well-known clustering technique kmeans++ and is thus called Direct Kmeans++ Clustering (DKC) algorithm [230]. For a set of

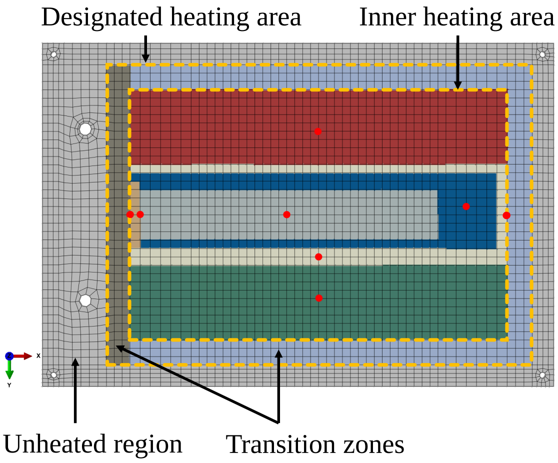

Figure 5-5 Heat zone allocation of the LGM algorithm in the heat zone design area. The zones are distinguished by element colors; bright red spots mark the locations of the control thermocouples.

n data points $\chi \subset \mathbb{R}^d$ a defined number of k centroid points C are spread to minimize the potential function,

$$\Phi = \sum_{x \in \chi} \min_{c \in C} \|x - c\|^2 . \tag{5-10}$$

The data points are assigned to the closest centroid and, thus, form a cluster. As this clustering technique uses one value per data point, the time-dependent information of each element in the heating area needs to be mapped to one value. A straight forward approach to do so is to integrate the absolute heat fluxes for every element i and calculate the total absolute energy balance.

$$q_{\mathrm{tot,i}} = \int |\dot{q}_i(t)| dt \tag{5-11}$$

Although this gives a reasonable estimation of the total energy required in certain areas of the tool, it is not fully sufficient to make a proper heat patch allocation as local time-dependency is neglected. The application of Equation 5-11 will lead to a compensation of high and low peaks in the surface heat flux in time. Hence, a region with oscillating behavior in time will be combined with a region with constant surface heat flux if the mean values are similar. To take this compensatory effect into consideration the kmeans++ clustering technique is applied to the integral of surface heat flux deviations from the mean value instead.

$$\Delta q_{\mathrm{dev,i}} = \int |\dot{q}_i(t) - \dot{q}_{\mathrm{mean}}(t)| dt \tag{5-12}$$

If the presented approach is employed in the application case of this work, it leads to the clustered mean heat deviation shown in Figure 5-6 (a). Within this figure, the red dots represent elements located in the inner design area with high deviations from the mean heat flow, whereas the blue dots refer to elements with low deviations. The elements located closest to the 24-ply side of the tapered laminate reach the highest values, whereas the elements located close to the 4-ply side reach the lowest values. The heat zone allocation was transferred to zonal allocation within the finite element cure simulation (see Figure 5-6 (b)) and an evaluation was made, presented in Chapter 5.3.

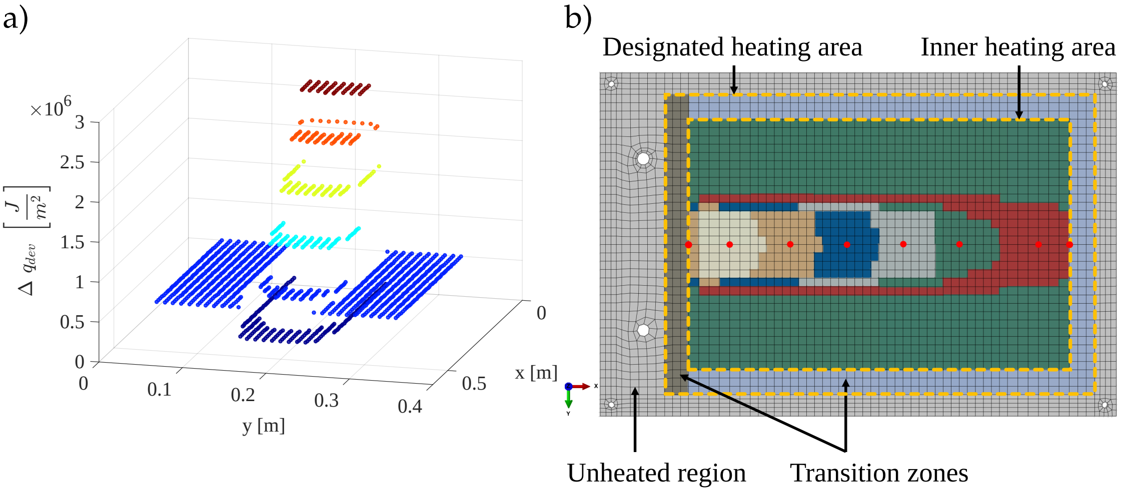

Figure 5-6 Result of the DKC algorithm: (a) Final Δq_{dev} allocation for the simulation model with aluminum tool material and (b) resulting heat zone allocation. The zones are distinguished by element colors; bright red spots mark the locations of the control thermocouples.

5.2.4 The Effect of Unheated Regions

In almost all concepts for self-heated tools, unheated regions similar to the ones depicted in Figure 5-1 are present outside of the part cavity region . It has been shown experimentally that unheated regions can have a significant impact on the tool temperature field in the previous Chapter. Since they are subjected to convection and have an own thermal mass, a heat flow towards these unheated regions arises during the manufacturing process. In the presented application case, this effect leads to surface heat fluxes at the edge elements, which are at least one magnitude higher than in the inner area and, therefore, needs to be taken into consideration in the thermal tool dimensioning. Within the proposed dimensioning method, this heat flow is compensated for in the first couple of element rows of the designated heating area. Due to the large heat flows apparent along the edges of the heating area, the application of a clustering technique will result in edge effects dominating the procedure. Hence, a two-stage approach is taken to cluster the heating zone: First, the clustering technique is only used to allocate the required number of transition heating zones. Second, the inner heating area excluding the transition zones is investigated and the partitioning of the undisturbed inner heating area is made.

The introduction of transition zones has to be made irrespective of the partitioning algorithm chosen. In the application case, it led to two transition zones: the unheated region facing the thick side of the laminate, which has a greater width than the unheated regions on the three other tool sides and a separate zone is proposed by the algorithm for this side, as indicated in Figure 5-6 (b). The remaining other three tool sides are clustered into one transitional heating zone. The spread of these transition zones was estimated at three element rows, given that only in these first element rows an influence could be determined in the surface heat flux. Thus, the final width of the transition zones was $\sim$ 0.03 m for the presented application case.

5.2.5 Control Thermocouple Placement in a Multi-Zone Tool

The placement of the control thermocouple for each heat zone is crucial for the overall temperature accuracy in the considered zone given that it directly influences the amount of energy introduced in the zone. Due to heat transport, the temperature of one specific zone is not only dependent on its zone dimensions and the location of its own thermocouple but also on the neighboring zones and their thermocouple placements. Thus, the sensitivity of the temperature field of one zone regarding thermocouple placement depends on the dimensions of the zone in question as well as the heat flux over its borders and needs to be considered individually. If a neighboring zone is subjected to a large temperature gradient leading to a large heat flux from the considered zone to the neighboring zone, the control unit will introduce more heat the closer the control thermocouple is placed towards this border. Given that the power introduction in one zone is constant in the area, the overall energy introduced in the considered zone and, thus, the overall temperature of the zone will rise. A sensitivity study was conducted to showcase this behavior, the results are shown in Figure 5-7. Three sensitivity simulations were conducted, and the temperature profile along the x-direction in the middle of the tool-part interface was investigated in the middle of the second dwell stage, at t=15000 s. The cases in the sensitivity study differ in the placement of the control thermocouple of zone six: Whereas in the standard validation simulation model, acting as a template, the control thermocouple is placed in the middle of zone six, in the other simulations the control thermocou-

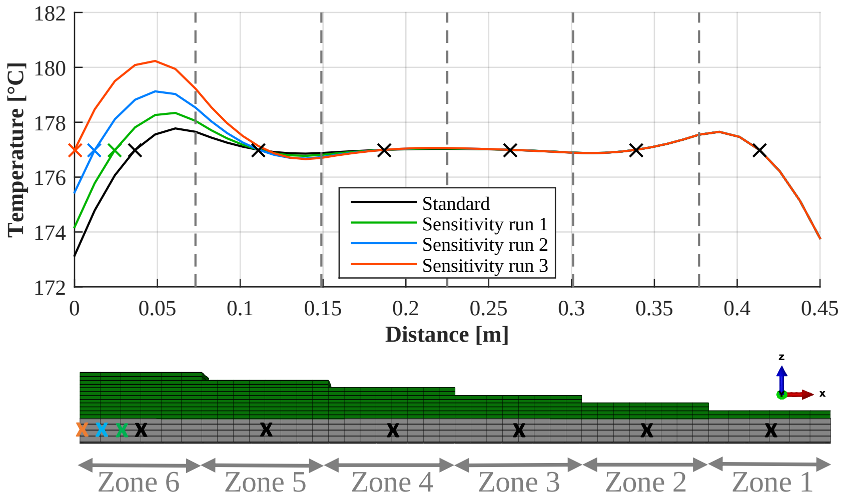

Figure 5-7 Tool-part interface temperature along the x-direction of the standard validation run and several sensitivity runs in the middle of the second dwell time at t=15000 s. Control thermocouple positions are marked with an X. Different plot and marker colors indicate the different sensitivity runs and their respective thermocouple positions in zone 6.

ple was moved further towards the colder border of the zone on the left side (see Figure 5-7).

Due to the control mechanism, the set-point temperature is enforced at the location of the thermocouple by the modulation of the introduced energy in the whole zone. The set-point temperature in the second dwell stage is 177°C, which is reached at all thermocouple positions. The further the control thermocouple is moved towards the border of zone six, the more energy has to be introduced by the control unit to ensure target temperature at the location of this control thermocouple. Thus, the further the control thermocouple is moved towards the border, the higher the temperatures in the whole zone becomes.

Overall, it can be stated that the temperature fields of larger zones are less sensitive to thermocouple placement than in the case of smaller zones and the sensitivity of the zonal temperature field with respect to thermocouple placement increases towards the zone borders. Additionally, a reduced thermal gradient in the designated heating area leads to a significantly reduced sensitivity. Given that the thermal dimensioning strategy of the designated heating area presented has the target to reduce these thermal gradients, the application of the strategy reduces the sensitivity of the thermocouple placement in the inner heating area, as well.

Due to the interacting behavior of different control zones, no deterministic way of finding an optimal thermocouple positioning could be determined. However, two justified guidelines were set up, which led to satisfactory results in all case studies discussed in the current work:

1) The position of the control thermocouple in the transition zones should be as close as possible to the inner heating area.
2) The position of the control thermocouple in the inner heating zones should be placed centrally, for instance at the location with the largest distance to all surrounding zones in the area of interest.

Transition zones are subjected to large heat flows and temperature gradients. By placing their control thermocouple closest to the inner heating area the control method will assure that the temperature at the border to the inner heating area matches the set-point value. Hence, only small temperature gradients are present at the border of the inner heating area, leading to small in-plane heat fluxes towards them. Therefore, the inner heating area is almost undisturbed from the unheated regions.

The guideline for the placement of the thermocouples in the inner heating zones is based on the assumption that smaller temperature differences are apparent if the control thermocouple possesses the smallest influence of surrounding heat zones. A central placement ensures a maximal distance to the surrounding heat zones and, hence, the least impact of their respective thermal behavior on the considered zone control through thermal conduction. Additionally, the central placement reduces the sensitivity of the temperature field with regard to thermocouple placement.

5.3 Evaluation

While the input for both algorithms is the same, the surface heat flux in the designated heated area resulting from a temperature boundary condition, the calculated heat zone distribution differs considerably. The DKC algorithm evaluates the total heat difference in comparison to a mean value and is thus not capable of considering the full time-dependent behavior of the required surface energy flux. On the other hand, the LGM algorithm is capable of considering this time-dependent behavior but is less robust and requires increased computational effort. In theory, both algorithm have their advantages and disadvantages:

Direct Kmeans Clustering	**Least Gradient Merge**
• Low computational effort.	• High computational effort (many neighbor search operations).
• Robust evaluation of the surface heat flux.	• More sensitive to local singularities in the surface heat flux.
• Number of final zones is not directly defined.	• Number of final zones is directly defined.
• Evaluation of total heat flow balance; neglection of time-dependent heat flux deviations in-between elements.	• Consideration of time-dependent local heat flow deviations in-between elements.

In general, the LGM algorithm favors transitional zones more than the DKC algorithm. A quantitative comparison is required to assess the capability of both partitioning algorithms.

5.3.1 Assessment of the Developed Partitioning Approach

Given that the heat area in the present application case is located at the bottom side of the tool, whereas the part is located at the top side of the tool, a distinction between two evaluation surfaces needs to be made: the area of dimensioning and the area of interest. The area of dimensioning is the inner heating area located at the bottom side of the tool where the heat flows were investigated to build the zonal allocations. In contrast, the area of interest is the contact area between the tool and the part, where temperature homogeneity is desired. Due to tool thickness and the resulting through-thickness conduction, the outcome is not necessarily similar. However, as the present application case features an aluminum plate with 4.8 mm thickness, this effect is very small. The impact increases with decreasing thermal tool conductivity as will be demonstrated in the following chapter. To evaluate the quality of the heat zone allocation made the mean temperature residual $\overline{T}_\mathrm{r}$ over the equidistant time-steps t between actual heat area temperature T_sim and set-point temperature T_SP is calculated for each element e.

$$\overline{T}_{\mathrm{r,e}} = \frac{1}{n_\mathrm{t}} \sum_{k=1}^{n_\mathrm{t}} \left(T_{\mathrm{sim,e}}(t_\mathrm{k}) - T_\mathrm{SP}(t_\mathrm{k})\right) \tag{5-13}$$

The proposed dimensioning strategy was applied to the presented application case: First, a cure simulation was conducted with temperature boundary conditions in the designated heating area according to the desired temperature cycle. The resulting RFL was used to calculate an areal surface heat flux and the clustering/merging algorithms presented were applied. Finally, the determined heat zone allocation were incorporated in a second cure simulation with the appropriate representation of temperature-controlled heat zones defined by Equation 4-10. These cure analyses were compared with the cure simulation of the validation case and the quality of the heat zone dimensioning method was estimated by investigating the resulting temperature distribution apparent in the tool. A small change to the simulation model presented previously was made to prohibit that tool thickness conductivity generates a general offset in the derived temperature residual: The location of the control thermocouples were placed on the bottom side of the tool. Hence, perfect zonal allocation is able to reach a temperature residual of zero in the area of dimensioning.

In Figure 5-8, the mean temperature residua of the validation model and the models defined by the developed algorithms are compared for the tool-part contact surface $\overline{T}_{\mathrm{r,cs}}$ and the inner dimensioning area $\overline{T}_{\mathrm{r,iha}}$ at the bottom side of the tool. The dashed white lines represent the location of the part and the areas of constant amount of plies with the 24-ply side located at low x-values.

Both mean temperature residua $\overline{T}_{\mathrm{r,iha}}$ and $\overline{T}_{\mathrm{r,cs}}$ in the validation set-up show the absence of transition zones leading to lower temperatures and, thus, higher temperature residua towards the border of the heating area (see Fig. 5-8 (a), (b)) . Hence, the temperatures at the edge of the laminate in x-direction are up to ~ -4.8°C lower than set-point temperature due to their location close to unheated regions. The laminate edges in the y-direction are subjected to a mean temperature decrease of ~ -1.7°C compared to the set-point value.

Compared to the validation simulation, the zonal allocation determined by the LGM algorithm leads to a significant upgrade in temperature homogeneity in both considered areas $\overline{T}_{\mathrm{r,iha}}$ and $\overline{T}_{\mathrm{r,cs}}$. The mean temperature in the contact surface between tool and part deviates between −0.5°C and −1.7°C from the set-point value. Within the heating area on the bottom side of the tool, the biggest temperature deviations are located at the edges with a value of −5.6°C from set-point temperature.

The zonal allocation calculated with the DKC algorithm showed a further increase in temperature accuracy over the whole heating area (see Fig. 5-8 (e), (f)). The mean temperature in the contact surface between tool and part deviates only between −0.5°C and −1°C from the set-point value, which fulfills typical temperature accuracy requirements currently applied in composite processing. Within the inner heating area on the bottom side of the tool only regions close

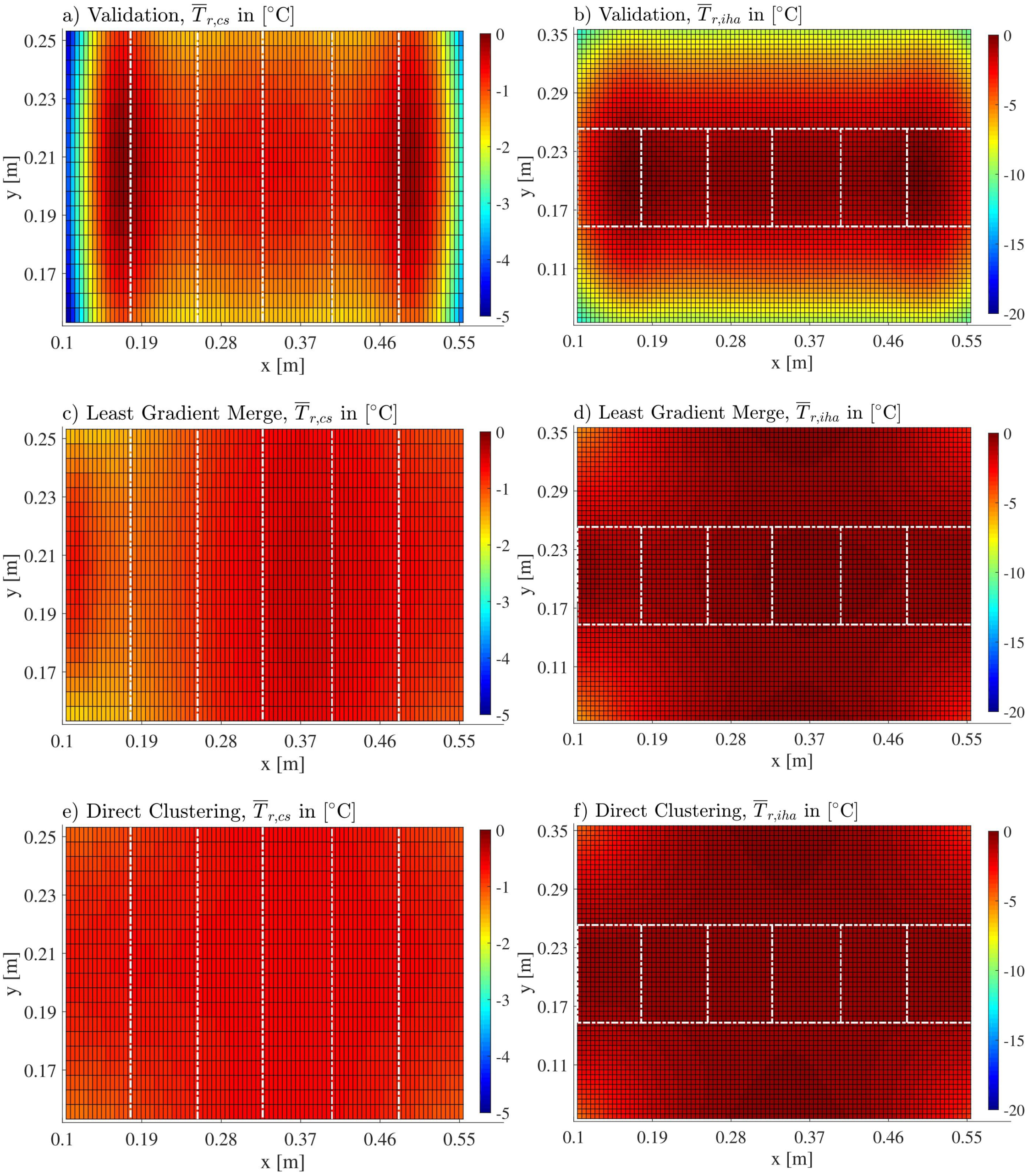

Figure 5-8 Residual mean temperature in the contact surface $\overline{T}_{\mathrm{r,cs}}$ and the inner heating area $\overline{T}_{\mathrm{r,iha}}$ in the validation model and the results of application of both developed algorithms.

to the four corners of the heating area deviate up to −4.8°C from the set-point temperature.

The in-plane temperature difference in the contact surface between the tool and the part is reflected in the in-plane degree of cure gradient, depicted in Figure 5-9. A through-thickness degree of cure gradient cannot completely be avoided in the current manufacturing set-up as the heat source and the heat sink are located on opposite sides of the part. However, with a sound zonal allocation of the heating patches, an in-plane degree of cure gradient can be prevented. In Figure 5-9 the in-plane degree of cure evolution and the resulting in-plane difference for the 24-ply zone is shown. The consulted nodes were chosen to represent the maximal in-plane deviation apparent on the tool-part contact surface. The in-plane temperature deviation in the validation model resulted in a maximum degree of cure deviation of 7.9 %. On the contrary, improved temperature accuracy of the models with the numerical zone allocation showed a maximum deviation of 1.5 % in case of the LGM algorithm and 0.8 % in case of the DKC algorithm.

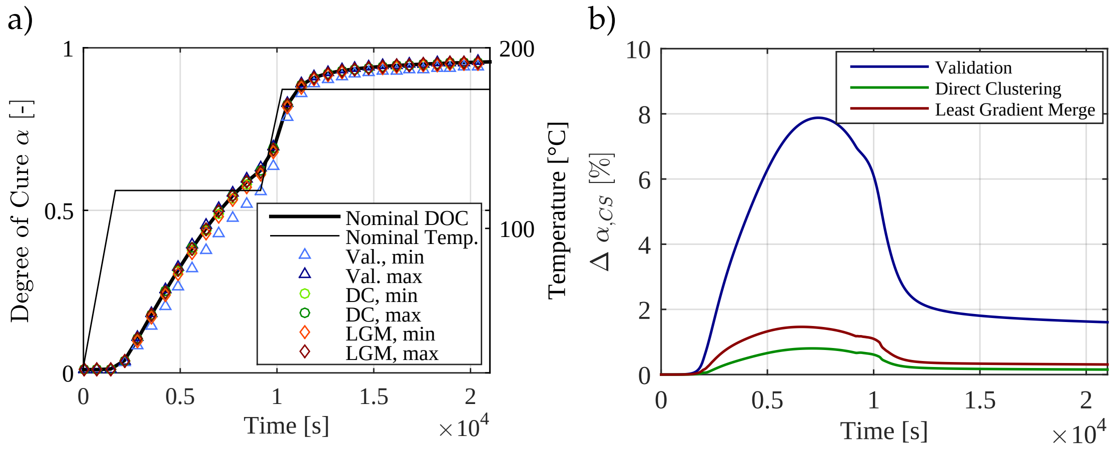

Figure 5-9 Maximal degree of cure differences in the 24-ply Zone 6 within the validation model in comparison with the results utilizing the numerical zone allocation: (a) Evolution of the degree of cure α and (b) maximal in-plane degree of cure $\Delta\alpha$ deviation in the contact surface area.

Combining all three case studies above, two major findings can be stated: First, the presented thermal tool dimensioning strategy for composite processing is very well-suited to ensure temperature and degree of cure homogeneity in the tool-part interface. Negligible deviations from the set-point temperature are observed on the present application case if the zonal allocation, determined by the introduced method, is applied. Therefore, between the two proposed partitioning algorithms, the DKC technique proved to lead to temperatures closer to the set-point value and is recommended for further use based on the presented study. Second, transition zones in thermal tool dimensioning have a major impact on the resulting temperature field in the whole heating area and should be designed very carefully. In some applications, where the part does not have a significant thickness or material changes along its dimensions, the appropriate allocation of transition zones is more important than the allocation of the heating zones in the inner heating area.

5.3.2 Influence of the Tool Material on Thermal Management

The tool material for resistively self-heated tools can be various. Given the different technologies present in the industry, resistively self-heated tools for composite processing can be manufactured of all commonly used tool materials. Two additional investigations were conducted to study the influence of the tool material on the heat zone allocation and temperature accuracy. The materials chosen, CFRP in quasi-isotropic layup and Invar, have significantly reduced thermal conductivity in comparison to aluminum as shown in Table 3-9.

The developed simulation strategy with a DKC algorithm was applied on simulation models featuring these tool materials and heat zone modifications have been made in the inner heating area accordingly. The heat zone allocations determined are shown in Figure 5-10.

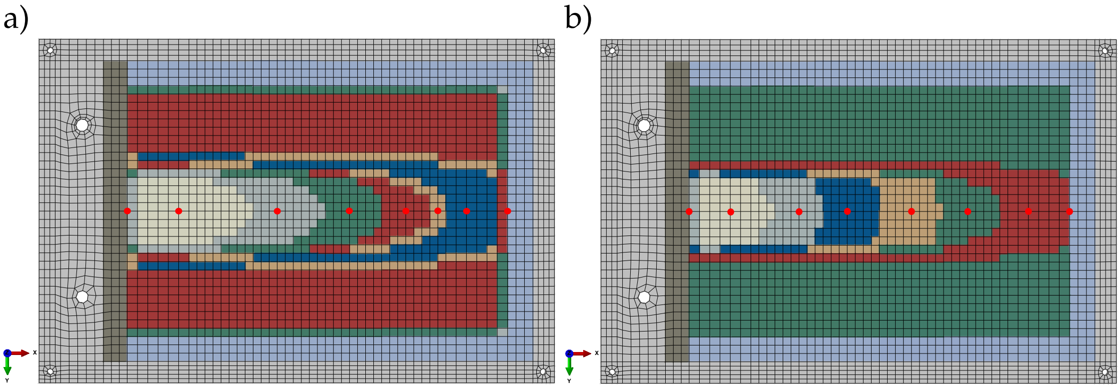

Figure 5-10 Heat zone allocation of the DKC algorithm applied on (a) a CFRP tool and (b) an Invar tool. The zones are distinguished by element colors; bright red spots mark the locations of the control thermocouples.

The placement of the thermocouples was conducted according to the two guidelines presented in Chapter 5.2. Whereas the heat zone allocation in case of Invar as tool material is almost identical to the aluminum case shown in Figure 5-6, CFRP leads to a slightly different allocation: The first element row in the inner heating area bordering to the transition zone was clustered differently than its neighboring inner area elements. This is an indicator that CFRP tool material requires a greater width of the transition zones. The cause of this is assumed to be the orthotropic material behavior of CFRP, causing a significantly higher in-plane thermal conductivity than in transverse direction. A local heat sink opposite to a heating area in thickness direction will induce a heat transport within the medium. In orthotropic materials with increased in-plane conductivity, a larger amount of heat will flow in-plane compared to isotropic materials. This results in a temperature drop over a larger radius. Hence, discontinuities in the required heat flux on the tool top side are spread over a larger area on the tool bottom side where the heat is provided. The same effect can be seen in the zone allocation below the part. The larger spread of heat flux discontinuities on the tool bottom side lead to the introduction of an own "part transition zone", colored in beige in Figure 5-10 (a). Given that the DKC technique resulted in one Δq_{dev}-level for this "part transition zone" and the number of overall Δq_{dev}-levels was predefined as six for the inner area in all studies in the present work, the remaining area in the CFRP case held one less Δq_{dev}-level to cluster the surface heat flux. This let the zones gain in size compared to the Invar and aluminum cases.

The mean temperature residuals with the tool materials CFRP and Invar are shown in Figure 5-11.

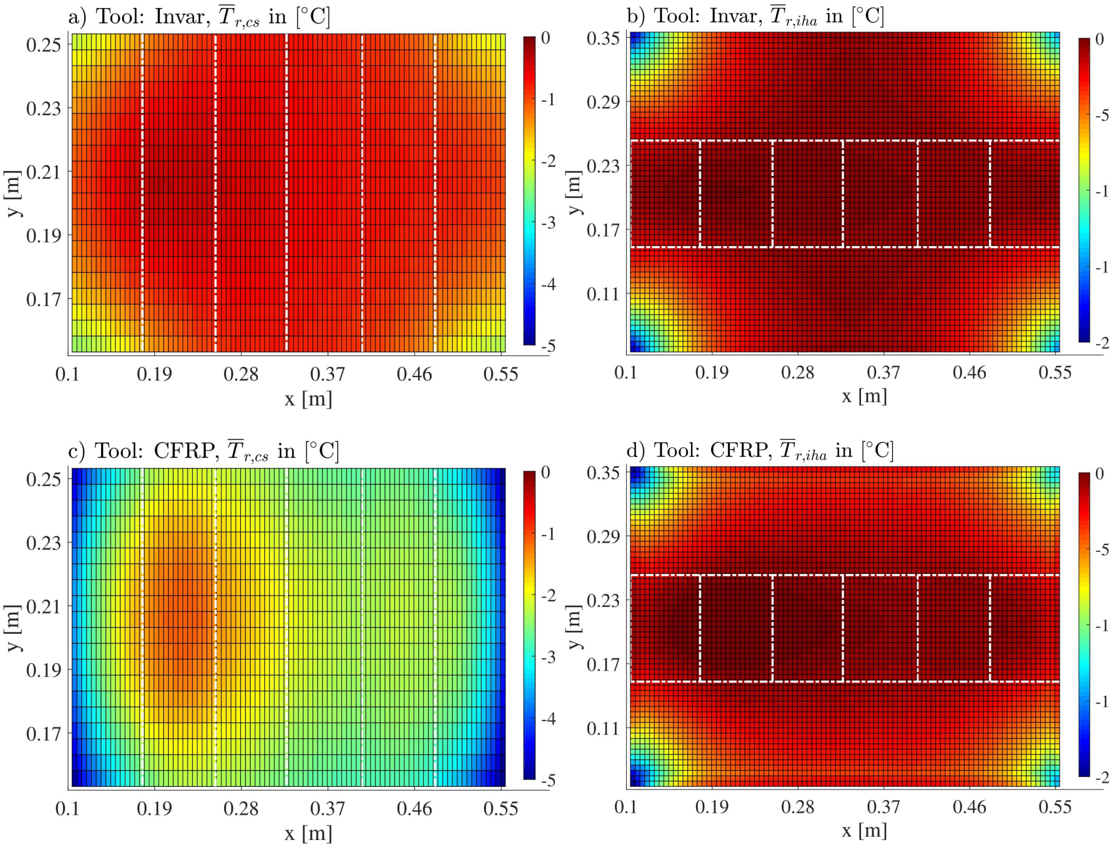

Figure 5-11 Residual mean temperature in the contact surface $\overline{T}_{\mathrm{r,cs}}$ and the inner heating area $\overline{T}_{\mathrm{r,iha}}$ utilizing tool material properties of Invar and quasi-isotropic CFRP.

For both cases an increase in the mean temperature gradient towards the edges of the inner heating area was observed. However, if only the heating area located on the bottom side below the part is considered the biggest mean temperature discrepancy is -2°C for Invar and -3°C for CFRP. The vast majority of elements feature a mean temperature residual smaller than -1°C in both cases. Whereas a similar in-plane temperature homogeneity could be determined in the tool-part contact surface, the lower through-thickness conductivity of CFRP resulted in a general temperature offset. In the undisturbed regions where through-thickness heat flow is dominating, the offset was determined to be -1.6°C for the CFRP tool. In case of a CFRP tool application, this could be compensated for with help of an adjustment of the set-point temperature by that margin. Taking this possibility into account, the CFRP case with numerically determined heat zones featured a better temperature accuracy than the validation case with an aluminum tool, although high thermal conductivity of aluminum proves to be very beneficial for temperature homogeneity.

5.4 Summary and Discussion

In this chapter, a numerical method for the thermal dimensioning of temperature controlled tools with multiple resistively heated zones was developed. This numerical method takes the specific thermal behavior of tool and part as well as the part resin cure and environmental effects, such as convection, into account.

In order to demonstrate the method, an application case consisting of a tapered laminate manufactured on a self-heated aluminum tool was set up. The thermal dimensioning of the heat zones was conducted utilizing two different developed algorithms to derive the final heat zones. Additionally, the impact of the tool material on the final optimal heat zone distribution was studied. The following conclusions were made based on the application case:

1. Whereas a conventional thermal dimensioning of the heat zones based on experience led to a significant deviation in the zone temperatures, the developed numerical approach shows an almost uniform temperature distribution in the heated area of the tool. The reduced thermal gradients led to a significant reduction in the in-plane degree of cure gradient of the application case.
2. The application of this thermal dimensioning strategy showed the necessity of transitioning heat zones, which thermally decouple the unheated region from the heated region in the tool. Within these transition zones, large temperature gradients are present.
3. The positioning of the control thermocouples of the heat zones has a strong impact on the overall temperature field of resistively heated tools. However, the increased temperature homogeneity achieved by the developed thermal dimensioning strategy results in a reduced sensitivity of the heat zone temperature field to thermocouple placement variation. Two justified

guidelines for thermocouple placement were set up, which led to satisfactory temperature homogeneity in the application case.

4. Comparing the three tool materials investigated, aluminum and Invar led to similar final heat zones distribution of the thermal dimensioning strategy with similar thermal results. Both materials feature an isotropic behavior but possess vastly differing thermal conductivity. In case of a CFRP tool, orthotropic reduced thermal conductivity led to a slightly different heat zone distribution.

The evaluation of the application case demonstrates the applicability of the developed method onto resistively heated tools featuring a simple geometry. In Chapter 7, the method is applied on a case study with a more complex problem featuring double-curved geometries and varying laminate thicknesses and materials.

6 Multi-Zone Cure Cycle Optimization

Heat transfer in composite manufacture is a transient process and highly dependent on the part's thickness and cure behavior. To improve part quality and reduce residual stress and risk of defects such as microcracks, delamination, void formation etc. great effort has been undertaken in research and industry alike to ensure a homogeneous cure in the part (see Chapter 2). However, for a complex part with significant disparity in its thickness and/or material, it is not enough to ensure a homogeneous tool temperature. In fact, homogeneous tool temperature might lead to significant inhomogeneity in the part's curing profile due to the apparent thermal lag and exothermic temperature overshoot in thicker laminates. With resistively heated multi-zone tools the temperature cycle of each zone can be tailored onto the part section heated by this very zone. Thus, it has a great potential to improve part cure behavior of complex parts with multiple thicknesses and/or materials. In order to do so, the applicant requires the information on the optimal temperature cycles in dependence of part material and thicknesses to appropriately control each zone. Since a single-zone optimization might not prove to lead to the best overall result, additional optimization steps based on those single zone-optimizations were conducted to gain the optimal temperature cycles in each zone for parts with different thicknesses manufactured by self-heated multi-zonal CFRP tools.

6.1 Optimization Via Finite Difference Method

The one-dimensional finite difference method offers the potential of a computationally inexpensive analysis of the cure behavior of a laminate. Most laminates have a very small thickness compared to its other dimensions leading to a good overall accuracy of these 1D investigations in thickness direction. In order to optimize the temperature cycle several hundreds of cure analysis have to be conducted, which is currently only applicable with 1D FDM analysis in a reasonable amount of time. Thus, a finite difference optimization scheme was implemented in MATLAB® consisting of a thermal and cure analysis and a multi-objective optimization framework.

6.1.1 Finite Difference Analysis

A central difference formulation of the discretization in space was used in the analysis of the domain [231]:

$$u'(x) \approx \frac{u(x + \Delta x) - u(x - \Delta x)}{2\Delta x} \tag{6-1}$$

Where u is the considered variable and x the coordinate. The application of this discretization scheme on the heat transfer equation (Eq. 2-43) under consideration of location-dependent material properties yields in:

$$\rho_i c_{\mathrm{p},i} \frac{T_i^{j+1} - T_i^j}{\Delta t} \approx \frac{1}{4}\frac{(k_{i+1} - k_{i-1})T_{i+1}^{j+1}}{\Delta x^2} + \frac{1}{4}\frac{(k_{i-1} - k_{i+1})T_{i-1}^{j+1}}{\Delta x^2} + k_i \frac{T_{i+1}^{j+1} - 2T_i^{j+1} + T_{i-1}^{j+1}}{\Delta x^2} + \dot{q}(x) \tag{6-2}$$

With the nodal temperature T, the conductivity k, the specific heat c_p, the density ρ, the time step length Δt and the discretization spacing Δx. The index i denotes the considered node and j the time step. The heat generation term $\dot{q}$ is calculated according to Equation 2-44. To form an implicit problem statement, Equation 6-2 is rearranged into the following equation in tensor notation:

$$\begin{pmatrix} \vdots \\ T_i^{j+1} \\ \vdots \end{pmatrix} = \underbrace{\begin{pmatrix} \cdots & 0 & \ddots & \ddots & \ddots & 0 & 0 & 0 & \cdots \\ \cdots & 0 & 0 & \frac{\Delta t}{\Delta x^2}\frac{k_i + \frac{1}{4}k_{i+1} - \frac{1}{4}k_{i-1}}{\rho_i c_{\mathrm{p},i}} & 1 + 2\frac{\Delta t}{\Delta x^2}\frac{k_i}{\rho_i c_{\mathrm{p},i}} & \frac{\Delta t}{\Delta x^2}\frac{k_i + \frac{1}{4}k_{i-1} - \frac{1}{4}k_{i+1}}{\rho_i c_{\mathrm{p},i}} & 0 & 0 & \cdots \\ \cdots & 0 & 0 & 0 & \ddots & \ddots & \ddots & 0 & \cdots \end{pmatrix}}_{\mathbf{M}}^{-1} \begin{pmatrix} \vdots \\ T_{i-1}^j \\ T_i^j \\ T_{i+1}^j \\ \vdots \end{pmatrix} \tag{6-3}$$

The inverse of the tridiagonal matrix **M** incorporates the full relation between the temperatures in the next time step T_i^{j+1} and the current temperatures T_i^j. The first and last line of **M** defines the type of boundary condition. In case of temperature boundary conditions, the entries $M(1,1)$ and $M(n,n)$ are set to unity. An explicit scheme for the calculation of the cure rate of the next time increment $\dot{\alpha}^{j+1}$ was chosen. Thus, Equation 2-7 becomes:

$$\dot{\alpha}^{j+1} = \sum_{k=1}^{n} f_k(\alpha^j, T^j) \tag{6-4}$$

Where n is the number of independent reactions in the formulation of the cure kinetics.

In literature, a wide variety of FDM cure analysis codes were developed and validated via experiment, as shown in Chapter 2. Thus, experimental validation of the approach itself has been done on numerous occasions and was not pursuit again in this work. To show the accuracy of the implemented code, it was successfully verified against the state-of-the art cure simulation programs RAVEN from Convergent Manufacturing Technologies, Inc. [163]. In the prediction of the temperature and degree of cure evolution of a 30 mm AS4/8552 laminate subjected to temperature boundary conditions a maximum temperature deviation of <1°C was experienced between the FDM code and RAVEN, while the mean temperature deviation as well as the mean degree of cure deviation over all time-steps was negligible.

6.1.2 Optimization Framework

A MATLAB® framework was set up to enable an optimization of the temperature cycle within the design space limits set by the applicant utilizing a genetic algorithm and a subsequent gradient-driven direct search technique. These limits are mandatory to decrease the design space and enable optimization with a finite amount of simulation runs. Typical limits originate from the manufacturing process itself, such as maximum/minimum tool temperatures and realistic boundaries on the heating rates.

Restrictions on the Design Space

The more variable the temperature cycle optimization is, the more design variables have to be considered leading to higher calculation times. In order to compromise between reasonable calculation times and flexibility in the temperature cycle choice, a general cycle was chosen consisting of three subsequent sequences of heating ramps and dwells. Similar number of variables were chosen in cure cycle optimizations in literature [146, 155]. With the infiltration temperature T_0, the lower limit of the design space of each sequence is defined by three variables leading to a total of nine design variables in the optimization (see Fig. 6-1).

The limits for the design variables originating from the resistively heated CFRP tools were set with maximum heating rate and maximum tool temperature in accordance to the tool resin mechanical behavior. Regarding the lower limit of the heating rate, a very small value close to zero was set given that controlled cooling of the tool is not possible with this tool technology. All other limits were chosen to keep the design space within reasonable values and not restricting the different temperature cycles at the same time. The utilized limits for the optimization work conducted in the context of this thesis is given in Table 6-1.

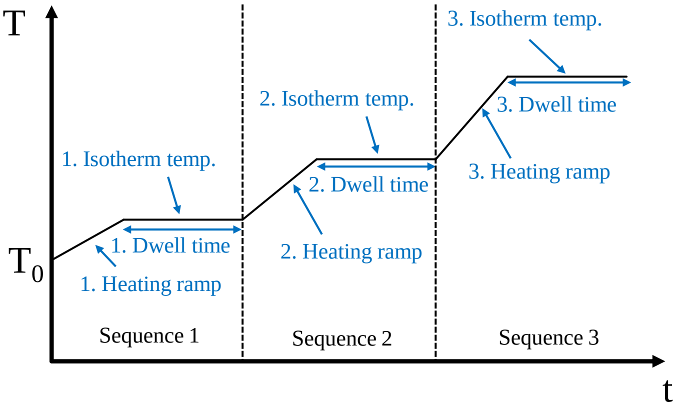

Figure 6-1 Design variables of a generic three-dwell temperature cycle.

Table 6-1 Design space limits for the nine design variables of the cure cycle.

Sequence no.	Heating Rate [° C/min]	Dwell Temperature [°C]	Dwell time [min]
1	[0.01; 8]	[90; 160]	[1; 330]
2	[0.01; 8]	[90; 160]	[1; 330]
3	[0.01; 8]	[90; 160]	[1; 330]

It has to be noted that the optimization algorithm can effectively drop (by changing the duration of the dwell to a very small value) a dwell in favor of a prolonged heating or dwell sequence. Hence, the schematic sequence shown in Figure 6-1 can lead to a wide variety of different temperature cycles and one- or two-dwell temperature cycles or sole slowly increasing temperature ramps were included in the design space.

Evaluation Function

The multi-objective evaluation function developed by Ruiz and Trochu, explained in Chapter 2.4, was implemented and adapted to fit the purpose of this work [5, 146, 155]. Six different objectives were combined into one fitness value according to Equation 2-60 and are shown in Figure 6-2:

- Final degree of cure,
- maximum cure temperature,
- degree of cure deviation at the point of gelation,
- thickness degree of cure gradients,
- thickness temperature gradient,
- and total processing time.

The evaluation of each individual objective was made by a modulation between the two extremes "desired" (objective function value approaching zero) and "not desired " (objective function value approaching one) via a sigmoid function.

The evaluation of the final degree of cure J_{fc} according to Equation 2-61 and 2-62 were implemented in the context of this thesis:

$$J_{\mathrm{fc}} = \frac{A_{\mathrm{fc}}}{B_{\mathrm{fc}} + \mathrm{e}^{g_{\mathrm{fc}}}} \tag{6-5}$$

$$g_{\mathrm{fc}} = -\frac{\alpha_{\mathrm{lam}} - \alpha_{\mathrm{min}}}{\alpha_{\mathrm{min}}} \frac{C_{\mathrm{fc}}}{\alpha_{\mathrm{ult}} - \alpha_{\mathrm{min}}} \tag{6-6}$$

α_{lam} denotes the minimal final degree of cure in thickness direction, α_{min} and α_{ult} the minimal required degree of cure and the ultimate degree of cure for which the resin is considered fully polymerized. The constants A_{fc}, B_{fc} and C_{fc} define the sigmoid shape and value. Similar shape constants are apparent in all following objective functions as well.

The evaluation of the maximum cure temperature J_{T} is modeled as follows:

$$J_{\mathrm{T}} = \frac{A_{\mathrm{T}}}{B_{\mathrm{T}} + \mathrm{e}^{-C_{\mathrm{T}} \frac{T - T_{\mathrm{min}}}{T_{\mathrm{max}} - T_{\mathrm{min}}}}} \tag{6-7}$$

Where T is the maximum laminate temperature occurring. T_{min} and T_{max} are temperatures defining the onset and width of the slope of the sigmoid function. The point at which the resin modulus begins to develop was identified as an important point for cure cycle optimization, given that it has a significant impact on the residual stress state [155]. To decrease the residual stress state, the point of gelation should occur at the same time on the surface and in the middle of the laminate. The corresponding objective function is defined by:

$$J_{\mathrm{gel}} = \frac{A_{\mathrm{gel}}}{B_{\mathrm{gel}} + \mathrm{e}^{-C_{\mathrm{gel}} \left(\frac{\alpha_{\mathrm{s}} - \alpha_{\mathrm{gel}}}{\alpha_{\mathrm{gel}}} \right)^2}} + D_{\mathrm{gel}} \tag{6-8}$$

The point of gelation is denoted as α_{gel}. α_{s} resembles the degree of cure at the laminate surface when the center gels. Additionally to the consideration of the point of gelation, the mean degree of cure gradient between surface and center is minimized with the following objective:

$$J_{\Delta\alpha} = \frac{1}{n} \sum_{k=1}^{n} \frac{A_{\Delta\alpha}}{B_{\Delta\alpha} + \mathrm{e}^{-C_{\Delta\alpha} \frac{|\alpha_{\mathrm{s}} - \alpha_{\mathrm{c}}|_k - D_{\Delta\alpha}}{D_{\Delta\alpha}}}} \tag{6-9}$$

Herein, the degree of cure of the surface and the center of the laminate is denoted as α_s and α_c for each time increment k. Technically, the point of gelation condition in Equation 6-8 is included in the mean degree of cure gradient objective, but a separate formulation offers the possibility to emphasize the degree of cure gradient at the point of gelation in the fitness function formulation. The maximum thermal gradient ΔT_max in thickness direction is considered with the following equation:

$$J_{\Delta\mathrm{T}} = \frac{A_{\Delta\mathrm{T}}}{B_{\Delta\mathrm{T}} + \mathrm{e}^{-C_{\Delta\mathrm{T}} \frac{\Delta T_\mathrm{max} - D_{\Delta\mathrm{T}}}{D_{\Delta\mathrm{T}}}}} + C_{\Delta\mathrm{T}} \tag{6-10}$$

Where ΔT_max is the maximum thermal gradient occurring in the whole process cycle between the middle of the curing laminate and it's surface.

Finally, the total processing time t_end is evaluated by a similar sigmoid function as the maximum allowable temperature. The objective function reaches one at a defined time t_max. The turning point of the sigmoid curve is defined by the time t_turn. This results in the following objective function:

$$J_\mathrm{t} = \frac{A_\mathrm{t}}{B_\mathrm{t} + \mathrm{e}^{-C_\mathrm{t} \frac{t_\mathrm{end} - t_\mathrm{turn}}{t_\mathrm{max} - t_\mathrm{turn}}}} \tag{6-11}$$

Where t denotes the total time of the temperature cycle.

The overall fitness value of the investigated temperature cycle in this work is thus determined as follows:

$$F = \omega_\mathrm{fc} J_\mathrm{fc} + \omega_\mathrm{T} J_\mathrm{T} + \omega_\mathrm{gel} J_\mathrm{gel} + \omega_{\Delta\alpha} J_{\Delta\alpha} + \omega_{\Delta\mathrm{T}} J_{\Delta\mathrm{T}} + \omega_\mathrm{t} J_\mathrm{t} \tag{6-12}$$

The weighting factors ω_i of the individual objective function i have to be chosen similar to the objective function constants A_i, B_i, C_i and D_i with consideration of the respective material, manufacturing technology and application.

Optimum Search Technique

The design space for multi-objective cure cycle optimization has a large number of local extremal values. Thus, a random search technique was employed by utilization of a genetic algorithm to localize the global optimum in the design space with a subsequent gradient-driven direct search technique employing the MATLAB® interior-point algorithm, which is applicable on large-scale, sparse problems [232].

In the beginning of an optimization employing the genetic algorithm, an initial amount of random temperature cycles ("population") are set up. In the itera-

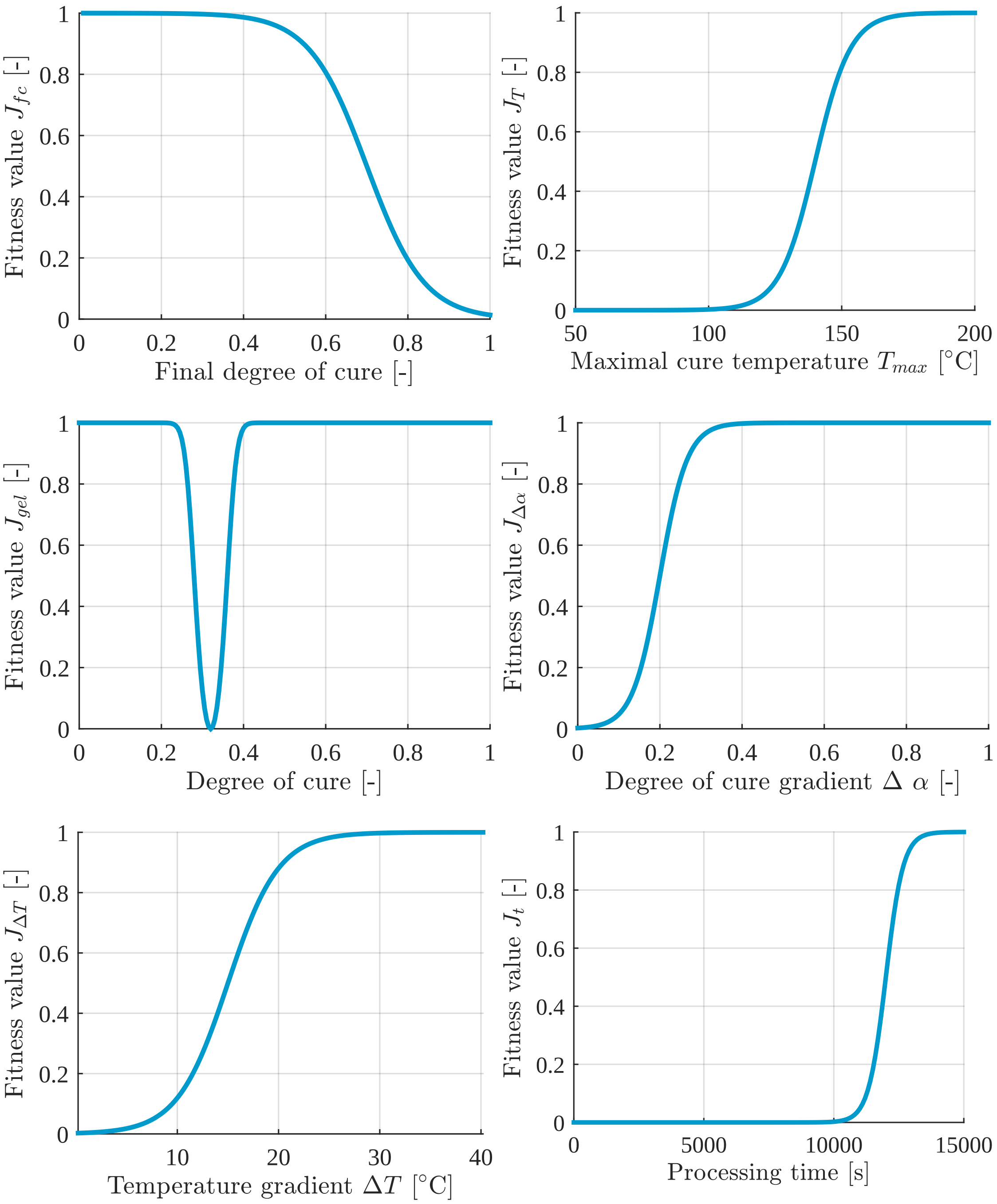

Figure 6-2 Individual fitness functions for the 1D FDM temperature cycle optimization.

tion loop, the fitness values of the temperature cycles are evaluated and a small amount of the fittest cycles are kept ("elite"). The other temperature cycles are discarded and a new set of cycles are set up by either an arbitrary parameter change ("mutation") or by merging parameters of two previous cycles ("crossover"). This procedure is continued until a stopping criterion is reached, such as maximal number of iterations or negligible change in the resulting fitness value. With the appropriate choice of optimization parameters a temperature cycle close to the optimum is found. Due to the random behavior of the algorithm the design space around this optimal value is not searched systematically. The subsequent employment of a gradient-driven direct search technique enables the systematical investigation of the design space around the values provided by the genetic algorithm to find the optimum. This way, a further slight improvement of the fitness value provided by the genetic algorithm can be achieved in some cases.

The search parameters of the genetic algorithm determine the computational effort and time as well as the fitness value of the final optimized cycle. If the number of initial generations is too low in comparison to the design space, it is less likely that the global optimum is found instead of a local extremum. Thus, the optimization search parameters need to be defined in accordance with the design space. To determine the search behavior of the genetic algorithm for problems investigated in this thesis, a parameter study of a FDM optimization featuring a 30 mm HTS40/ 823-1 laminate was conducted with the varied search parameters: population size, number of generations, number of elite and crossover ratio. Due to the random behavior of the optimization technique, each parameter combination was repeated three times leading to a total number of 2160 optimization cycles and the resulting fitness values of the optimization runs were evaluated.

The number of generations was varied between 20 and 200, with 120 being the critical number of generations at which no further increase in the final fitness function value could be determined. The number of elite has a minor effect on the overall fitness values found, with a minimal increase in fitness if four elite cycles are considered. The crossover ratio of 0.4 gave the best results, although the impact on the overall mean fitness values found is rather small again. Similar low impact has the number of elites in the optimum search algorithm, with 4 elites providing a slight improvement in the overall average fitness values found. Regarding the size of the population, a slight improvement in the fitness values found were seen until 200 independent temperature cycle parameter sets.

In accordance with this study, the genetic algorithm optimizations in this thesis were conducted featuring a population size of 200 for 120 generations with 4 elites and a crossover ratio of 0.8. In order to estimate how reliable the local optimum was found with the optimization procedure, these parameters were applied to 25 optimization runs of a 30 mm laminate featuring HTS40/823-1 material. The coefficient of variation of the final fitness value determined in these 25 optimization runs was 10.7 %. Hence, the optimization procedure did not find the global optimum in every run. In the subsequent optimization studies, a number of optimization runs were conducted in each case to gain an optimization result close to the global optimum of the fitness function.

6.2 Cure Cycle Optimization of 823-1 Laminates

The target application of a generic rotor blade, presented in the case study in Chapter 7, features CFRP laminate thicknesses ranging from 1 mm to 30 mm. Due to low through thickness conductivity in combination with exothermic resin reaction, increasing laminate thickness leads to increasing risk of temperature overshoot. This is especially a concern, if the cure rate is particularly sensitive to temperature: Figure 6-3 shows the cure rates of the investigated resin system 823-1 at different temperature on the left side, and the resulting temperature overshoot $\Delta T_{\text{center}} = T_{\text{center}} - T_{\text{surface}} = T_{\text{center}} - T_{\text{setpoint}}$ during the cure of a 30 mm laminate with 50 % fiber volume content on the right side. The depicted temperatures were calculated with the implemented FDM code and isothermal surface temperature boundary conditions.

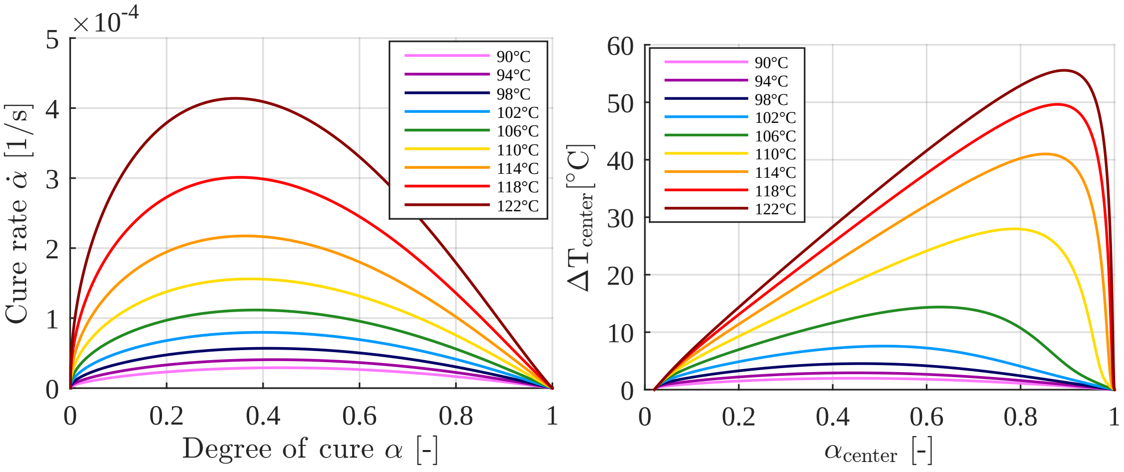

Figure 6-3 Cure rates at different cure temperatures for the 823-1 resin system (left). FDM result of the exothermic temperature overshoot of a 30 mm laminate with HTS40/823-1 material configuration and 50 % fiber volume content (right).

A temperature increase of 8°C in this resin system leads to an increase in the cure rate by a factor of two, which further translates to an increase of released heat by a factor of two (see. Eq. 2-1). As the heat transport from the center of the laminate towards the surface by conduction is approximately linear with temperature and increases only by a small amount in a temperature increases of 8°C, it is clear that the system quickly becomes unstable and results in uncontrolled temperature increase in the center of the laminate (see Fig 6-3 right). Thus, the temperature cycle for the cure of thick laminates has to be chosen very carefully, if controlled resin reaction and good part quality with small temperature and degree of cure gradients are desired. The manufacturer's recommended cure temperature of 125°C is applicable for thin laminates only, and temperature cycle optimization for thick laminates is required.

The introduced thermal dimensioning strategy of Chapter 5 lead to thermally independent manufacturing zones within a manufacturing set-up, which behave thermally similar. Thus, if a part has large laminate thickness variation, the advanced tool heating technology could potentially compensate for these changes in the thermal load of the part and support in a more uniform part cure. Three steps have to be conducted to accomplish this goal for the materials investigated in this thesis: The validation experiment of Chapter 3 has shown that a temperature cycle based around the manufacturer's recommended cure temperature is not applicable for laminates with up to 30 mm thickness. Thus, a temperature cycle optimization has to be conducted for critical laminate set-ups in a single zone optimization in the first place. Based on these results the temperature cycle has further to be adjusted to lead to favorable results if universally applied in one zone featuring varying part thicknesses in a second step. This step is required to gain an optimal cure behavior in case of one applied temperature cycle onto the whole part featuring varying thicknesses and/or materials. This case can further be considered as a reference for an investigation of the impact of a multi-zone heating, where a different optimal temperature cycle is applied in each zone. To do so, alterations to this temperature cycle have to be found in a final step, which lead to a more homogeneous cure if a multi-zone heating technique is used.

6.2.1 Single Zone Optimization

The choice of the weighing factors as well as the constants of the individual objective evaluation function is critical for the resulting optimal temperature cycle. In this thesis, the values were chosen with consideration of the industrial background of the case study in Chapter 7 and are shown in Table 6-2. All introduced individual criteria try to distinguish between a "better" and "worse" and compromises in-between different contradicting criteria are made in the summation to one final fitness value. However, the maximum resin temperature criterion has to be fulfilled and builds the upper limit of the temperature cycle optimization search. The weight loss investigation in Chapter 3 showed an increasing mass loss above 160 °C indicating thermal instability above that temperature and the maximum temperature criterion was set in accordance. Increasing laminate thickness lead to an increasing risk of temperature overshoot and, thus, thermal and degree of cure gradients within the curing laminate. This is especially the case for the resin system investigated with the reported high cure rate change with temperature. Each laminate can be perfectly homogeneously cured if the cure cycle time is elongated long enough. Thus, the objective of a cycle time restriction is the natural antagonist to the objective of a reduction in laminate temperature and degree of cure gradients during the production of thick laminates. Hence, the cycle time restriction completely defines the optimization and only cure cycles of similar duration should be compared. The time restriction was thus set up to lead to similar cycle times as the standard cure cycle based on the manufacturer's recommended cure temperature, which was used in the validation experiment (see Chapter 3). The chosen weighing factor ω_t represents the importance of the time criterion. Given that the part has to be close to fully cured within this time the corresponding weighing factor ω_fc was raised as well.

Table 6-2 Objective function constants and weighing factors for the optimization of 823-1 laminate manufacturing.

Constant	J_fc		J_T		J_gel	$J_{\Delta\mathrm{T}}$	$J_{\Delta\alpha}$	J_t	
A_i	1		1		1	1	1	1	
B_i	1		1		0.618	1	1	1	
C_i	-3		3		140	6	6	6	
D_i	-		-		-0.618	15	0.06	-	
Other:	α_ult	α_min	T_max	T_min	-	-	-	t_max	t_min
	0.95	0.9	175°C	165°C	-	-	-	14000 s	12000 s
ω_i	2		1		1	1	1	4	

The target application for the optimized cure cycle is a part produced by a CFRP tooling. Hence, the thermal FDM model for the cure cycle optimization study in part thickness direction is required to feature not only the part, but also the tool material until the location of heat introduction, which is the middle plane of the tooling shell. Due to the low transverse conductivity of the CFRP tool, this 5 mm tool material between heat introduction plane and curing part surface effectively acts as an additional insulation layer and, thus, has a significant impact on the temperature evolution within the part since cure cycle target temperature does not equal part surface temperature. Consequently, the FDM model for the optimization study includes 5 mm CFRP tool laminate between the temperature boundary conditions $T_\mathrm{set-point}$ and the curing part's surface at the top and bottom side, as shown in the sketch in Figure 6-4.

The target application for the optimized cure cycles features varying part laminates thicknesses of up to 30 mm in the CFRP section and up to 15 mm in the GFRP spar. Three thicknesses were investigated for both material combinations. The material models of Chapter 3 were used to model the evolution of material properties of the CYCOM 823-1 resin system. The curing laminate's fiber properties are given in Table 3-11 for the HTS40 carbon fiber and in Table 6-3 in case of the S2 glass fiber. Given the stochastic nature of the genetic algorithm as well

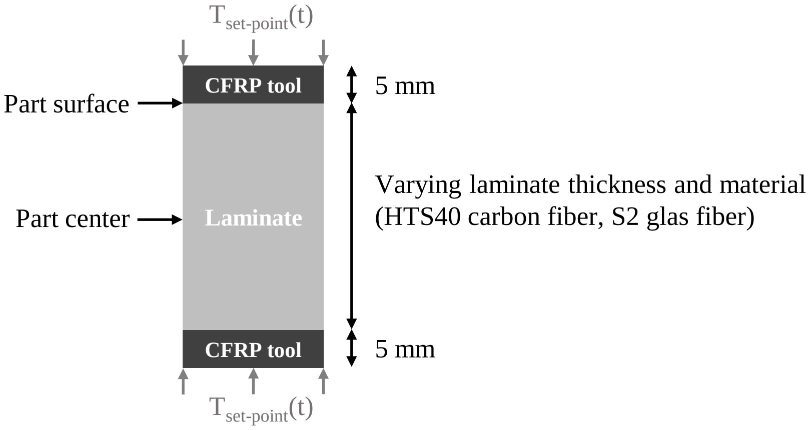

Figure 6-4 Sketch of the FDM temperature cycle optimization laminate set-up.

as the complexity of the search domain, the global optimum is not guaranteed to be found by each run. Therefore, 25 optimization runs were conducted for each thickness and material combination.

Table 6-3 Properties of the S2 glass fibers [20].

Mechanical properties		Thermal properties	
E	93.8 GPa	ρ	2488 [kg/m^3]
ν	0.23	k	1.45 [W/m/°C]
CTE	1.6E-06 [1/°C]	c_p	737 [J/kg/°C]

In Figure 6-5, the resulting laminate surface and center evolution of temperature and degree of cure for the CFRP set-ups (see Fig. 6-5 (c), (e) and (g)) and GFRP set-ups (see Fig. 6-5 (d), (f) and (h)) with optimized set-point temperature $T_{\text{set-point}}$ are shown. The results of the thickest set-ups, 30 mm in case of CFRP and 15 mm in case of GFRP, with the standard temperature cycle base on the manfucturer's recommended cure temperature applied are shown for reference in Fig. 6-5 (a) and (b).

Naturally, the thickest laminate featuring 30 mm CFRP showed the highest temperature overshoot with an optimized temperature cycle and, thus, was the most critical case regarding thermal and degree of cure gradients. The optimized cure cycle for this laminate is therefore discussed in detail in the following (see Fig. 6-5 (c)).

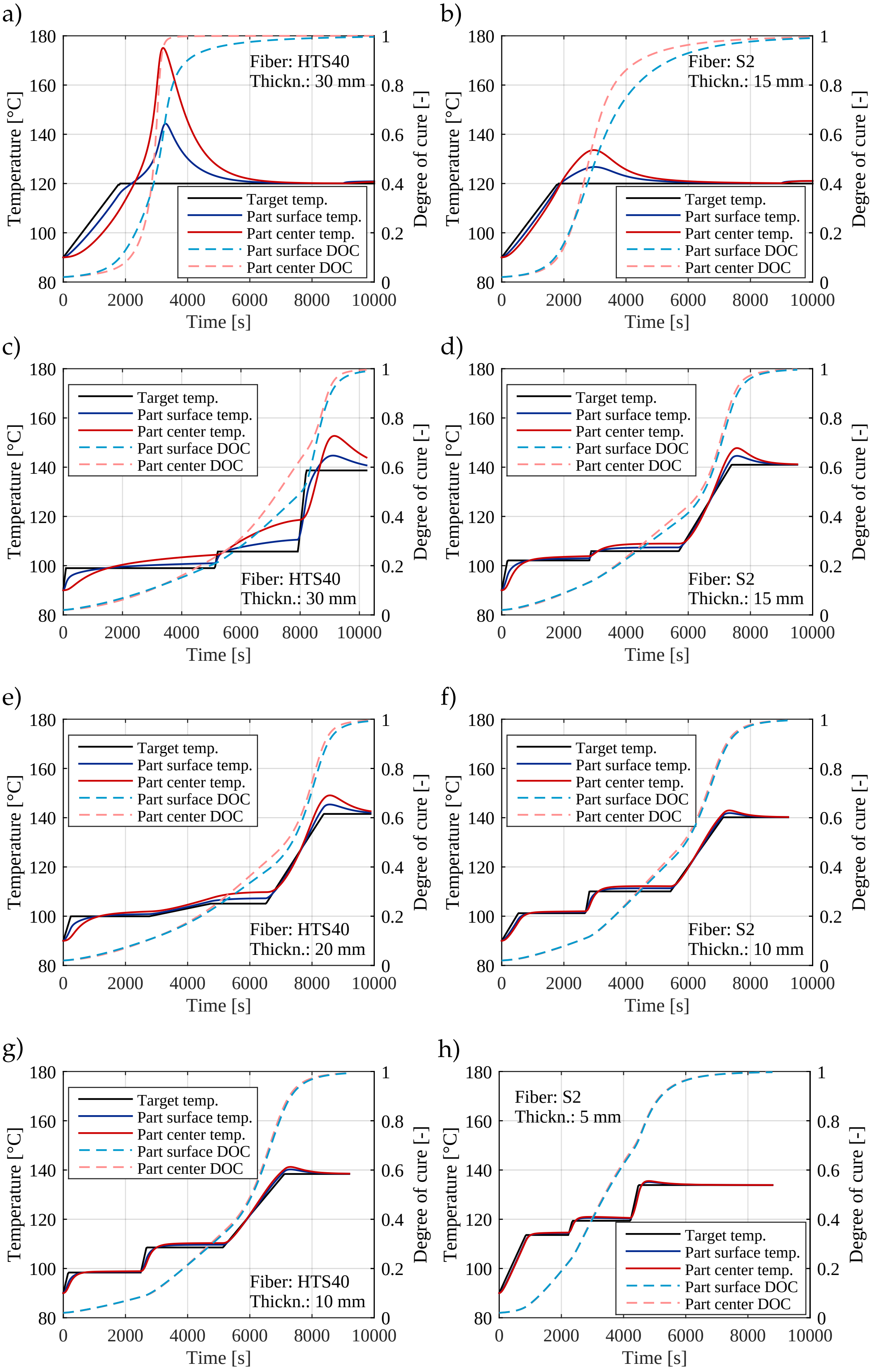

Figure 6-5 Standard (a-b) and optimized (c-h) cure cycle of the HTS40- and S2-laminate for different thicknesses.

The optimization results of the 30 mm CFRP laminate in Figure 6-5 (c) showed, that no gradient-free temperature cycle is possible for the contemplated cycle time of ~ 10000 s in combination with the material thickness. The optimal temperature cycle found is defined by several trends: an elongated dwell time at a relatively low temperature of 99°C, which lasts for half of the total cure cycle time. This temperature acts as a limit for a controlled cure reaction, in which the transport effects still dominate the temperature profile in thickness direction. Hence, the exothermic reaction energy can still be transported into the tool leading to low temperature and degree of cure gradients at this stage. Thus, the more energy is released at this temperature the more energy is taken out of the system and the lower will be the final temperature spike in the middle of the laminate at the end of the cure cycle.

At the end of the first dwell at 5100 s, the temperature deviation between surface and center is 3.4°C and the following second ramp is chosen to increase the part surface temperature to part center temperature. This enables a close to uniform cure until the point of gelation at 6200 s, where the degree of cure deviation between part laminate center and surface is ~ 3%. This time also indicates the starting point of a significant increase in center and surface temperature deviations up to ~ 8°C compared to set-point value at 7900 s. As the temperature and degree of cure deviations between center and surface at this time are getting too large, the tool surface temperature is subjected to a steep temperature ramp resulting in higher heating rates in the part's surface than in the center of the laminate. This steep heating ramp results in a decrease in the degree of cure gradient. The higher the final temperature level of the third dwell is elevated, the lower the resulting degree of cure gradients. However, higher final dwell temperature also lead to elevation of the final laminate center temperatures, which are required to stay below 160°C due to thermal stability reasons. The final dwell temperature of 139°C leads to laminate center peak temperatures of 153°C, which is well below that threshold. The maximum values for the peak temperature, thermal and degree of cure discrepancy between laminate center and surface for this optimized temperature cycle in comparison to the cure cycle based around the manufacturer's recommended cure temperature is presented in Table 6-4.

Table 6-4 Numerically determined overall improvement of optimized cure cycle for a 30 mm CFRP laminate.

	Fitness value	time [s]	$T_{\max}$ [°C]	$\Delta_{\max}T$ [°C]	$\Delta_{\max}\alpha$ [-]
Std. cure cycle	7.22	10900	175.3	33.9	0.354
Opt. cure cycle	0.445	10240	152.7	8.0	0.138

Although this optimized cure cycle does lead to gradients in temperature and degree of cure as well as a final temperature overshoot, it significantly reduces these gradients as well as the final temperature overshoot in comparison to the standard cure cycle, given in Figure 6-5 (a). The optimization shows, that for the 30 mm carbon laminate the projected cycle time is not sufficient if a close to gradient-free cure is targeted. If smaller gradients or lower final temperatures are required in the 30 mm carbon fiber laminate, the overall cycle time has to be increased.

The optimization of CFRP with lower thicknesses as well as GFRP laminates, shown in Figure 6-5 (d) to (h), follows a similar trend and general explanation to the ones presented in detail for the 30 mm laminate, albeit with more homogeneous results thanks to more prominent transport effects in thickness direction apparent in thinner laminates. Gelling occurs in all optimized cycles in the second dwell stage.

6.2.2 Consideration of Varying Material Thickness in One Zone

In the previous single-zone optimization, highly specialized optimal temperature cycles were found for specific material and thickness combinations. However, in a part with varying cross-sections such as the use-case presented in Chapter 7, a single temperature cycle has to be picked for multiple thicknesses and materials in most cases, given that one temperature cycle is applied onto the whole part in a conventional manufacturing tool. This temperature cycle choice should thus lead to the overall best results regarding temperature and degree of cure homogeneity. For such an application case a temperature cycle is sought, which results in low sensitivity of the fitness function value with regard to thickness variation while maintaining an overall low fitness function value.

In general, the laminate with the highest thickness is the most sensitive set-up regarding the target temperature cycle. However, that does not necessarily mean that the temperature cycle optimized for the thickest set-up is the best solution for overall application onto a part with varying thicknesses. The fitness function is highly non-linear in the design space and in some cases the optimum found features a steep gradient towards higher values if small set-up variations occur. If this is the case in the optimization of a temperature cycle for a thicker laminate, the overall better solution might be the application of the cure cycle of a thinner section onto the whole zone.

The comparison of the optimized cure cycles for the 20 mm and 30 mm laminate of the previous section resembles an example for this case: The optimum found in the 30 mm section featured a very steep temperature ramp onto the final dwell to elevate the surface degree of cure as fast as possible and, thus, reach a more homogeneous degree of cure profile. However, given that in the 20 mm laminate the temperature deviation in the second dwell stage and the corresponding degree of cure deviation is significantly lower, the heating rate is too high leading to an outside-to-inside cure, which should be avoided [5]. In general, in a thick part featuring varying thicknesses the heat transport in thickness direction is rather low leading to varying thermal lag. Thus, high heating ramps applied onto a thick part, which are optimized for one thickness only, are likely to lead to significant in-plane temperature gradients, as well.

In order to find a best solution for one single temperature cycle $T_{\text{set-point}}$ that leads to overall optimal results in a part featuring varying thicknesses, the three previously determined optimal single-zone temperature cycles for the thicker laminates of 15 mm upwards were applied onto the respective other set-ups: Each of the temperature cycle optimized for 15 mm GFRP, 20 mm CFRP and 30 mm CFRP was applied onto the respective laminate set-ups given in Figure 6-6.

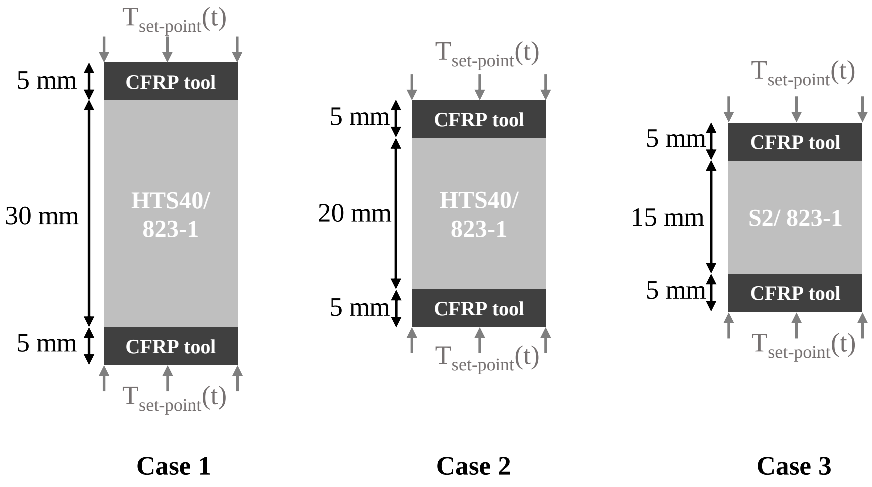

Figure 6-6 Sketch of the FDM temperature cycle optimization laminate set-up for the determination of a thickness-robust temperature cycle.

Thus, the robustness of the previously determined optimal temperature cycles with respect to thickness changes was determined. The resulting fitness function evaluations according to Equation 6-12 for these combinations are given in Table 6-5 and can be compared to derive the most thickness-robust temperature cycle.

Table 6-5 Numerically determined fitness function values for different cure cycle and laminate set-up combinations.

Laminate / Opt. cycle	Case 1	Case 2	Case 3	$\sum F_i$
30 mm CFRP (Figure 6-5 (c))	0.354	0.223	0.154	0.731
20 mm CFRP (Figure 6-5 (e))	0.376	0.069	0.044	0.489
15 mm GFRP (Figure 6-5 (d))	0.447	0.095	0.039	0.581

In order to compare the different temperature cycles, the fitness function values generated by application of one distinct temperature cycle $T_{\text{set-point}}$ on all investigated laminate set-ups were summed, enabling a comparison of the different cycles applied on varying laminate set-ups. In case of a diverse importance of the different laminate set-ups in one part, additional weighting factors for the fitness values of distinct material combinations may be applied to stress their importance. For the present case the different set-ups were equally weighted and the optimized cycle for the 20 mm HTS40 laminate generates the overall best result if applied on 823-1 laminates with varying thickness. Therefore, this temperature cycle was utilized as the baseline optimized cure cycle in the following work.

6.2.3 Consideration of Multiple Heating Zones

If the same temperature cycle is applied over the whole laminate, in-plane temperature and degree of cure gradients can occur in the laminate's center of overall thick CFRP laminates with non-constant thickness due to low heat conductivity in thickness direction. In contrast to conventional manufacturing tools, molds with multiple heating zones offer the possibility of introducing different cure cycles along the part's dimensions, which might prove beneficial to decrease these in-plane gradients in the laminate's center. On the other hand, different temperature cycles in different heating zones lead to a change of the surface temperature gradient and, thus, the degree of cure gradient at the surface. Therefore, the application of this technique often resembles a tradeoff, which lowers the highest in-plane gradients in the center of the laminate while at the same time inducing small gradients in the surface regions.

In general, in-plane heat conduction compensates for the in-plane temperature gradients to a certain extend. However, in parts with large laminate thickness variations such as helicopter rotor blades, large in-plane temperature and degree of cure gradients may occur and cannot be compensated by in-plane heat conduction only. In order to develop different cure cycles for different material thicknesses of one part, a worst case estimation can be made by neglecting the in-plane heat conduction. In this case, 1D studies of the different material set-ups can be compared and an adjusted temperature cycle for each heating zone is developed. If these solutions are henceforth applied onto a manufacturing set-up with different heating zones and part thicknesses the resulting in-plane gradient will in any case be lower than the ones predicted with the 1D studies. Thus, a separate temperature cycle $T_{\text{set-point}}$ for each of the laminates shown in Figure 6-6 is targeted, which lead to low temperature and degree of cure deviation in-between the different cases and favorable overall cure behavior at the same time.

In Figure 6-7 the temperature and degree of cure evolutions of the three previously investigated laminates 30 mm HTS40/823-1, 20 mm HTS40/823-1, 15 mm S2/823-1 with an applied temperature cycle in accordance with the previous study of an optimal robust temperature cycle are compared.

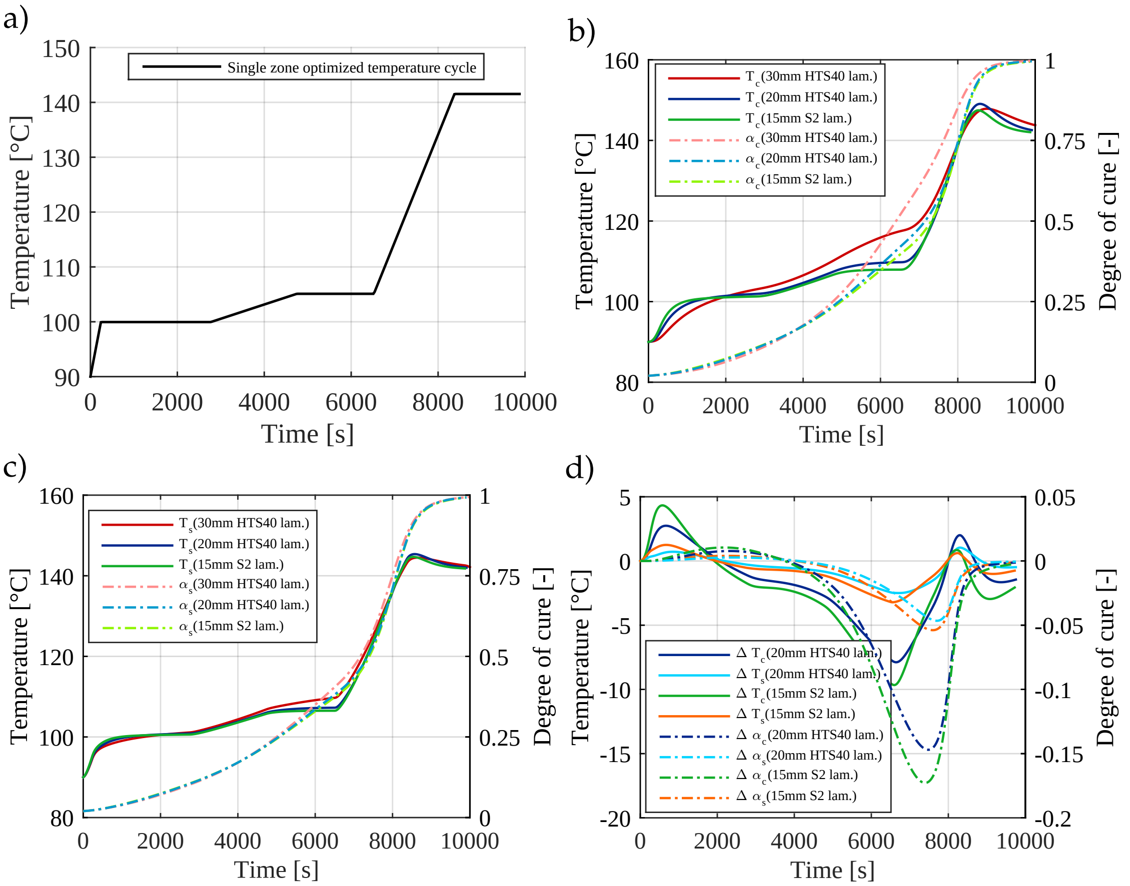

Figure 6-7 Comparison of the temperature and degree of cure evolutions of different laminates with the single-zone optimized cure cycle based on independent 1D cure analysis: (a) Optimized target temperature cycle, (b) laminate center temperatures and degrees of cure, (c) laminate surface temperatures and degrees of cure, and (d) resulting temperature and degree of cure deviation at the surface and the center of the different laminate set-ups.

Naturally, the highest temperature overshoot is seen in the laminate with the largest thickness. This is to be expected, given that the impact of heat transport on the temperature evolution during the exothermic reaction is decreasing with increasing laminate thickness, but this can potentially lead to significant in-plane gradients in terms of temperature and degree of cure. However, if different cure cycles are to be applied onto different sections due to an advanced multi-zone heating technique, better results with lower deviations in-between the different zones with different laminates might be possible. For the presented case depicted in Figure 6-7, this could potentially lead to an elevation of the second dwell temperature for the thinner laminates with the goal of overall smaller deviations in-between the different laminate set-ups.

To enable an investigation of such an approach, a second round of optimization was conducted: The previously optimized robust temperature cycle for the manufacturing of 823-1 laminates with varying thickness was utilized for the laminate set-up with maximal thickness (30 mm HTS40/823-1 laminate) and as a master temperature template for other laminate configurations. The target temperature cycles for the other two laminate set-ups were henceforth subjected to optimization utilizing a sigmoid fitness function towards minimal deviations compared to this master template.

Given that only small deviations from the original optimized cycle are required, the gradient-driven optimization algorithm only was employed. The individual fitness functions were set up to result in decreasing values the closer the match of laminate center and surface temperatures as well as center and surface degree of cures with the respective values of the 30 mm HTS40/823-1 laminate.

$$J_{\mathrm{Ts}} = \frac{A_{\mathrm{Ts}}}{B_{\mathrm{Ts}} + \mathrm{e}^{-C_{\mathrm{Ts}} \frac{\overline{\Delta T_{\mathrm{s}}} - T_{\mathrm{min,s}}}{T_{\mathrm{max,s}} - T_{\mathrm{min,s}}}}} \tag{6-13}$$

$$J_{\mathrm{Tc}} = \frac{A_{\mathrm{Tc}}}{B_{\mathrm{Tc}} + \mathrm{e}^{-C_{\mathrm{Tc}} \frac{\overline{\Delta T_{\mathrm{c}}} - T_{\mathrm{min,c}}}{T_{\mathrm{max,T}} - T_{\mathrm{min,c}}}}} \tag{6-14}$$

$$J_{\alpha\mathrm{s}} = \frac{A_{\alpha\mathrm{s}}}{B_{\alpha\mathrm{s}} + \mathrm{e}^{-C_{\alpha\mathrm{s}} \frac{\overline{\Delta\alpha_{\mathrm{s}}} - \alpha_{\mathrm{min,s}}}{\alpha_{\mathrm{max,s}} - \alpha_{\mathrm{min,s}}}}} \tag{6-15}$$

$$J_{\alpha\mathrm{c}} = \frac{A_{\alpha\mathrm{c}}}{B_{\alpha\mathrm{c}} + \mathrm{e}^{-C_{\alpha\mathrm{c}} \frac{\overline{\Delta\alpha_{\mathrm{c}}} - \alpha_{\mathrm{min,c}}}{\alpha_{\mathrm{max,c}} - \alpha_{\mathrm{min,c}}}}} \tag{6-16}$$

With the first index T or α indicating the physical variable of comparison (temperature or degree of cure) and the second index s or c indicating the location (center or surface). The mean deviation of the values obtained in the investigated temperature cycle in comparison to the 30 mm laminate are denoted as $\overline{\Delta T_\mathrm{s}}$ in case of temperature and $\overline{\Delta \alpha_\mathrm{s}}$ in case of degree of cure. The fitness value of each temperature cycle in the optimization is further calculated employing weighing factors according to:

$$F = \omega_{\mathrm{Ts}} J_{\mathrm{Ts}} + \omega_{Tc} J_{\mathrm{Tc}} + \omega_{\alpha\mathrm{s}} J_{\alpha\mathrm{s}} + \omega_{\alpha\mathrm{c}} J_{\alpha\mathrm{c}}. \tag{6-17}$$

The values for the employed optimization constants are given in Table 6-6.

Table 6-6 Function constants for the multi-zone temperature cycle optimization.

Fitness function / Constant	J_{Ts}	J_{Tc}	$J_{\alpha\mathrm{s}}$	$J_{\alpha\mathrm{c}}$
A	1	1	1	1
B	1	1	1	1
C	6	6	5	5
min	6	6	0.05	0.05
max	3	3	0.025	0.025

The results of this multi-zone optimization are shown in Figure 6-8. By a slight alteration of the set-point temperature cycle for the different set-ups, the magnitude of the maximum degree of cure deviation of the 20 mm HTS40 laminate compared to the 30 mm HTS40 laminate can be reduced from previously -14.7 % at t=7381 s to -6.5 % in the laminate's center. The deviation of the laminates surface degree of cures is decreased from previously -4.7 % to +3.2 % at the same time. In case of the 15 mm laminate featuring a S2 glass fiber overall larger deviations occur due to the increased thickness difference in-between the laminates of comparison, but the deviation reduction resulting from the multi-zone optimization follows a similar trend: A degree of cure deviation in the laminate's center of -17.3 % magnitude was decreased to -8.3 % with the multi-zone optimized cure cycle. The multi-zone optimized cure cycle for the 15 mm S2 laminate led to a decrease in the maximum surface degree of cure deviation from previously -5.3 % to 4.3 %.

Overall, the comparison of 1D studies showed the potential for a general decrease in the temperature and degree of cure deviations in the center of a 823-1 laminate with varying thickness if temperature cycles, which are optimized for multi-zone tools, are applied. While the magnitude of the surface deviations stay roughly the same, the algebraic sign changed.

It has to be noted that this method of multi-zone cure cycle optimization depends on the selection of representative laminate configurations. Since there typically exist laminate thickness transitions within a part area heated by one heating

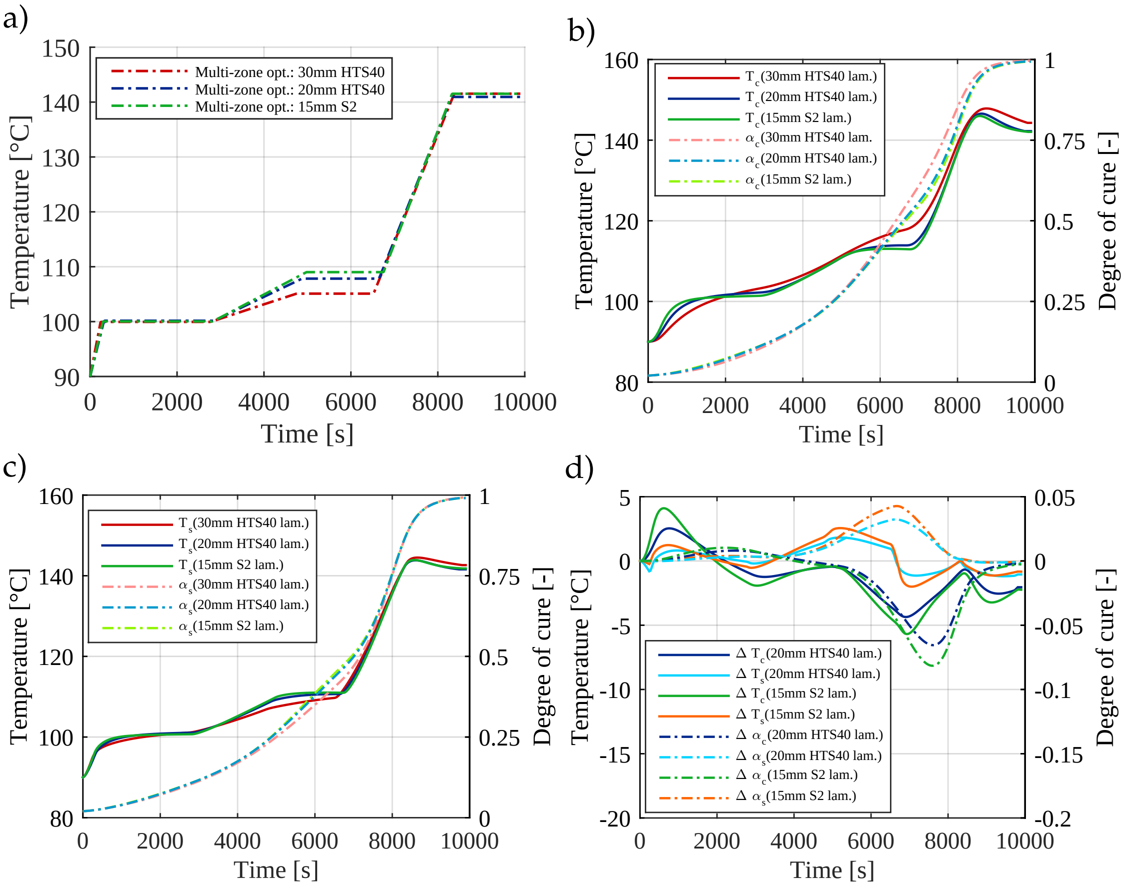

Figure 6-8 Comparison of the temperature and degree of cure evolutions of different laminates with the multi-zone optimized cure cycles based on independent 1D cure analysis: (a) Optimized target temperature cycles, (b) laminate center temperatures and degrees of cure, (c) laminate surface temperatures and degrees of cure, and (d) temperature and degree of cure deviation of the thinner laminates in comparison with the 30 mm HTS40 laminate.

zone in the tool, laminate layup deviations to the representative configuration cannot be avoided and occur in this part area. However, the impact of these deviations is low if the master temperature cycle is robust to laminate thickness variations. This precondition applies in the present case, since the identification of a thickness-robust temperature cycle was the purpose of the investigation conducted in the previous section and the result was used to set up the master configuration.

This study concludes the cure cycle optimization for 823-1 laminates manufactured by resistively heated CFRP tools with multiple independent heating zones. The final cure cycles, which will be used in the subsequent case study, are summarized in Table 6-7. The cycles are well within the capabilities of the tool technology with a maximal heating ramp of up to 3 °C/min and a maximal final temperature of up to 144.4 °C.

Table 6-7 Final numerically optimized temperature cycles for optimal resin cure of a laminate featuring the 823-1 resin system.

Application		Single-zone	Multi-zone	Multi-zone	Multi-zone
Approx. thickness	[mm]	variable	30	20	15
Infiltr. temp.	[°C]	90	90	90	90
1. Ramp	[°C/min]	2.48	2.48	2.78	3.00
1. Dwell temp.	[°C]	99.9	99.9	99.9	99.6
1. Dwell time	[min]	42.1	42.1	42.1	42.1
2. Ramp	[°C/min]	0.16	0.16	0.23	0.23
2. Dwell temp.	[°C]	105.1	105.1	108.7	107.8
2. Dwell time	[min]	29.5	29.5	29.5	29.5
3. Ramp	[°C/min]	1.18	1.18	1.31	1.17
3. Dwell temp.	[°C]	141.5	141.5	143.4	144.4
3. Dwell time	[min]	25.2	25.2	25.2	25.2

6.3 Summary and Discussion

In order to investigate and optimize the cure behavior of laminates featuring the Cytec CYCOM 823-1 resin system, a 1-D finite difference scheme was implemented in MATLAB® in this chapter. An optimization framework, utilizing a combination of genetic algorithm and direct gradient method, was set up for a numerical temperature cycle optimization. The optimization was conducted in three stages: First, the optimal temperature cycle for several laminate thicknesses was determined. Secondly, a robustness study was conducted to determine the temperature cycle that leads to the overall best results in case of a laminate featuring several thicknesses. Finally, variations to this robust temperature cycle were identified to be applied in a resistively heated multi-zonal tool where several laminate thicknesses can be subjected to different temperature cycles in order to gain an overall more homogeneous cure behavior in the part. Three conclusions can be highlighted:

1. A cure cycle based on the manufacturer's recommended cure temperature for the resin is applicable for thin laminates only. The cure rate of the resin is very sensitive to small temperature changes, leading to a significant risk of uncontrolled resin reactions if thick laminates are manufactured.
2. All cure cycles investigated showed a high temperature discrepancy between laminate surface and center during cure of a 30 mm laminate within the total cycle time restrictions. However, temperature cycles were found which restrict the temperature overshoot to a thermally stable process win-

dow while reducing the magnitude of the temperature and degree of cure gradients in thickness direction significantly.

3. 1D optimization techniques can be used to determine a set of complementary temperature cycles, applicable on the different zones in a multi-zone mold of a part with varying materials and thicknesses. A comparison of the cure profiles showed the potential for significant in-plane cure gradient reduction in the laminate's center by the application of different complementary temperature cycles.

The optimized temperature cycles will be used in the following case study of a generic rotor blade.

7 Case Study: Generic Rotor Blade

Resistively self-heated CFRP tools offer the potential to an optimized cure process specifically tailored to the part and, thus, increased part quality through a more homogeneous cure. Additionally, a direct heat introduction enables decreased thermal lag in the cure cycle as well as reduced cycle time. Given that thick parts with various cross-sections and different materials are defined by a complex thermal and cure behavior, this thermal tailoring technique has to incorporate the thermal effects of tool and part as well as the chemical resin reaction and environmental effects such as convection. In order to investigate the potential of these tools a numerical approach was developed to provide the simulation capability to appropriately predict the thermal response in the manufacturing process (see Chapter 4) and a dimensioning strategy was presented to thermally tailor the tools onto the needs of the part (see Chapter 5). A material characterization was conducted to gain input data for the simulation (see Chapter 3) and a set of optimized cure cycles has been established for the different material and thickness combinations (see Chapter 6). The content of the previous Chapters now enable an assessment of the potential of resistively heated tools. In this chapter, this assessment is exemplarily made by application of the developed methods onto a generic rotor blade part produced by a resistively heated CFRP tool.

Rotor blades are typical composite parts with varying laminate cross-sections and different material combinations. Thus, a zonal heating technique might prove beneficial for overall temperature and cure homogeneity. The generic blade was designed with typical design features apparent in helicopter rotor blades. Figure 7-1 shows the different sections of a manufactured part, with a 30 mm monolithic CFRP section next to a transition section leading into a sandwich section, which features 1 mm CFRP laminate. Within the sandwich section, a GFRP spar was embedded.

Figure 7-1 Different material sections of the generic rotor blade.

The part was produced using a low-pressure lightweight CFRP RTM tool by Qpoint Composites GmbH in the framework of the EU-funded project "Lightweight, Energy-Efficient Tooling for the Manufacturing of Rotor Blades" (LEE-ToRB) [1]. The tool consisted of a 10 mm shell laminate with an additional rib structure on the backside to provide enough stiffness. Since the rib structure was in contact with the tool shell and subjected to convection, it could potentially act as a heat sink. Thus, it was thermally isolated by the tool manufacturer with an in-house solution while maintaining the mechanical stiffness. Five independent heating elements were embedded in the middle plane of the tool laminate in each side resulting in five heat zones per side. The allocation of each zone was conducted based on composite manufacturing experience by Qpoint Composites GmbH.

7.1 Experimental Determination of the Temperature Development

To determine the simulation accuracy, a part was manufactured in the resistively self-heated CFRP tool with target fiber volume content of 50 % in all sections. A total of eight thermocouples were embedded at different locations of the part to measure the temperature evolution. Figure 7-2 and 7-3 shows the measurement set-up and the thermocouple positions.

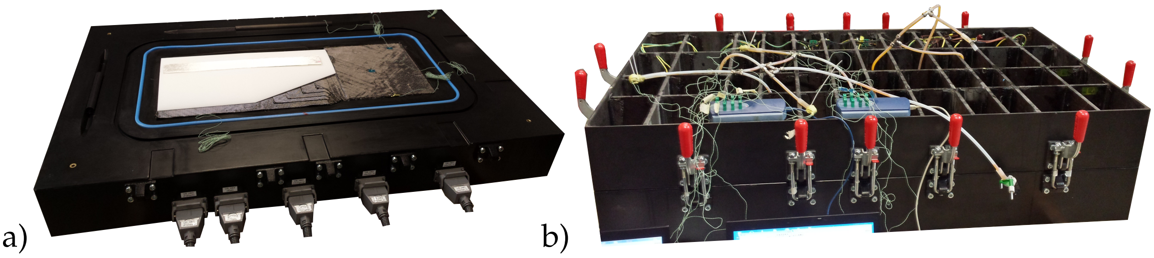

Figure 7-2 Manufacturing of the generic rotor blade: (a) Manufacturing set-up, (b) closed mold after infiltration.

Since the tool was a closed-mold RTM tool, part production with the tool typically was conducted using increased resin pressure. However, in the experiment the thermocouples had to be introduced through the resin outlets, which prevented additional resin pressure. The infiltration process was, thus, conducted using vacuum pressure only. Thanks to the low resin viscosity at the infiltration temperature of 80°C, a full infiltration was achieved. However, a slightly higher porosity content could not be avoided. The mean porosity content of the final part was determined chemically in the monolithic CFRP section to be 3.2 % and

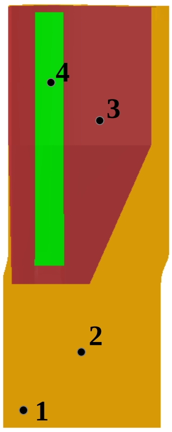

Thermocouple	Location
1.a	Laminate middle
1.b	Top part face
2.a	Bottom part face
2.b	Laminate middle
2.c	Top part face
3.a	Bottom part face
3.b	Top part face
4.a	Between sandwich core and GFRP laminate

Figure 7-3 & Table 7-1 Location of the thermocouple in the temperature evolution experiment.

via pyrolysis in the GFRP spar to be 0.9 % with standard deviations of 1.3 % and 0.1 %, respectively. An increased porosity content leads to a decreased resin volume fraction and ultimately decreased released energy during the resin polymerization, which has to be accounted for in the simulation. The temperature cycle was set in accordance with typical RTM manufacturing cycles originating from the industry and the resin manufacturer's recommended cure temperature.

Subsequent to the infiltration process at 80°C a temperature ramp of 1°C/min was applied in all heat zones followed by a 120 min dwell at 120°C. Given that the applied cure cycle was not optimized, a significant exothermic reaction occurred in the monolithic CFRP section. Simulation accuracy could therefore be determined in three laminates featuring completely different thermal behavior: In the monolithic section close to adiabatic thermal behavior is experienced during the temperature overshoot, whereas heat transport effects dominate the temperature development in the sandwich section. The thermal behavior at the thermocouple position of the GFRP spar lies in-between those two extremes.

Figure 7-4 shows the temperature development in the experiment CFRP, GFRP and Sandwich section at the locations indicated in Figure 7-3. As has already been shown by the thermal validation experiment (see Chapter 3) and in the temperature cycle optimization (see Chapter 6), this temperature cycle led to overall very high temperature overshoots. Although the control unit switched the heat zones off above 120°C, the released energy originating from the curing resin in combination with low thermal conductivity of CFRP laminate resulted in a peak temperature of 172°C in the CFRP laminate center (TC 2.b in Figure 7-4). The maximum tool-part interface temperatures above (TC 2.c) and below this location (TC 2.a) was measured to be 145°C and 156 °C respectively, which is still well below tool glass transition temperature. The temperature offset in-between those sides is explained by a difference in the convective heat transfer.

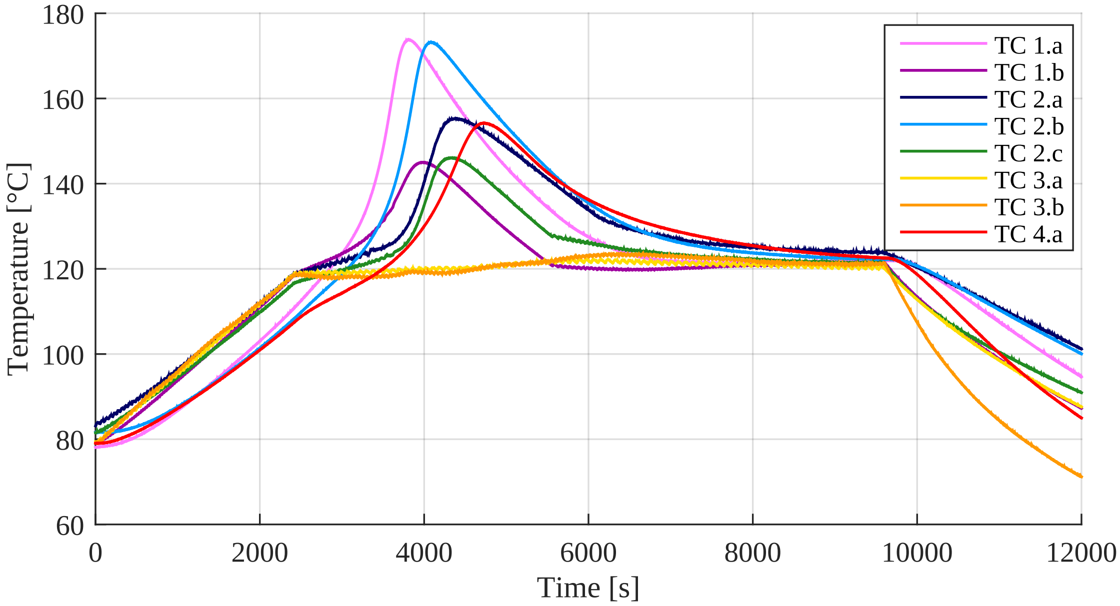

Figure 7-4 Temperature evolution in the simulation accuracy estimation experiment.

The thermocouple located at the edge of the monolithic laminate (TC 1.a) showed a temperature peak of roughly the same magnitude compared to the center of the laminate with an earlier occurrence of ∼ 300 s. This indicates the presence of an in-plane temperature and, thus, a degree of cure gradient from the edge of the monolithic laminate towards its center. The reason for this thermal behavior is the presence of the transitional heating zone, colored in yellow in Figure 7-7: at the edge of the laminate heat is introduced from an additional direction compared to the purely transverse heat conduction present in the center of the monolithic laminate. Thus, the laminate temperature increase at the edge of the laminate was higher than in the laminate's center and the critical temperature for an uncontrolled resin reaction was reached earlier. At the thermocouple located underneath the top GFRP spar (TC 4.a), a peak temperature overshoot of 154°C was measured. The occurrence was significantly postponed to 4800 s, whereas the cycle time of the peak in the monolithic CFRP center was 4200 s. As expected, the 1 mm thin skin layer enclosing the sandwich foam did not experience any significant temperature overshoot (TC 3.a and TC 3.b).

7.2 Simulation Model

A major uncertainty in the simulation of manufacturing processes with resistively heated CFRP tools such as the one shown in Fig. 7-2 is the impact of convection. The convective heat transfer is dependent on the air flow in the tools surroundings and, thus, location-dependent. Especially for large structures with mechanical stiffeners, this air flow can only be predicted by computational fluid dynamics (CFD). Given that the temperature field on the outer tool surface depends on the controlled temperature field in the tool and, thus, the exothermic resin reaction in the part, an analysis of the convective heat transfer would require a coupling of the CFD simulation predicting the air flow and the FEM simulation predicting the temperature and degree of cure field in the part. However, the computational effort for such a procedure is very large and limit its application to small scale problems only. Thus, a reverse-engineering approach was applied for the determination of a convection coefficient in order to gain an accurate simulation while maintaining reasonable calculation times.

7.2.1 Geometry and Discretization

Figure 7-5 shows the Abaqus simulation model consisting of three parts: the two molds and the generic rotor blade. An insulation layer was introduced to decouple the tool shell and mechanical stiffener thermally. Dimensions of the part were:

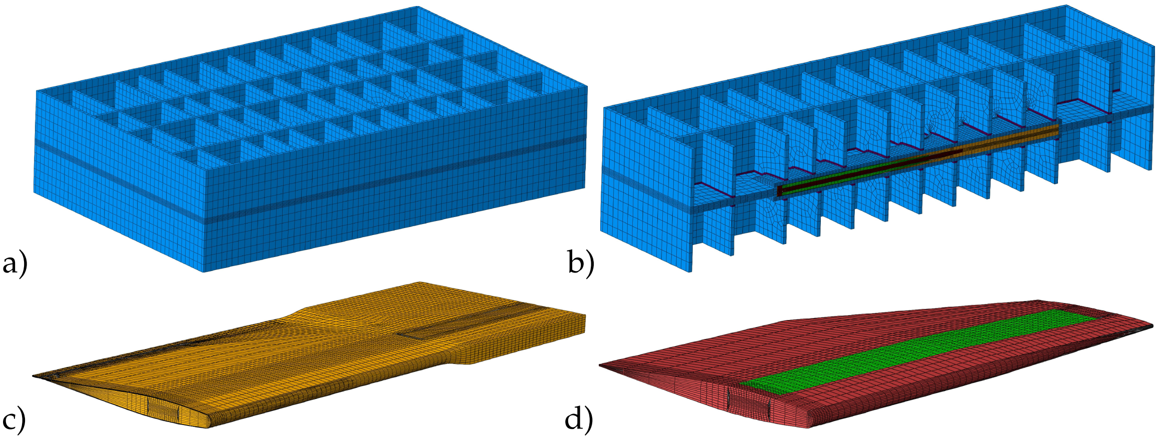

Figure 7-5 Simulation model of the generic rotor blade and the CFRP tool: (a) Finite element discretization of the tool, (b) cross-section through the tool and part, (c) FE mesh of the curing CFRP rotor blade (yellow) and (d) foam core (red) and curing GFRP spar (green) of the simulation model.

910 mm length, a 350 mm width in the sandwich section and a 340 mm width in the monolithic section. The maximum thickness was 31 mm in the monolithic CFRP section and 29 mm in the Sandwich section. Outer dimensions of one mold was 1500 mm x 900 mm x 170 mm. A total of 73070 linear heat transfer brick elements (DC3D8) were used to model the tool. The numerical representation of the part consisted of 28696 linear heat transfer brick elements. The discretization was conducted with priority on a reasonable numerical resolution in the thick laminate section with risk of exothermic temperature overshoot while maintaining

a reasonable amount of elements for computational efficiency. A discretization study did not show significant differences in the temperature field of the part with an increased amount of elements.

7.2.2 Material Card

Whereas the tool features the fully cured CFRP properties determined in Chapter 3, the part consists of curing GFRP and CFRP and a Rohacell foam core. The resin system CYCOM 823-1 was characterized in Chapter 3 and the respective COMPRO/CCA material card was set up accordingly. Remaining unknown material data was taken from literature, such as the carbon fiber data given in Table 3-11, the thermal properties of the S2 glass fiber and the Rohacell core which are given in Table 6-3 and 7-2. GFRP laminate orientation was unidirectional along the length direction of the spar. In case of the CFRP, a $[0,90]_n$ orientation was chosen leading to a thermally quasi-isotropic laminate behavior in-plane and significantly reduced thermal conductivity in transverse direction. The laminate properties were determined with the micro-mechanical models presented in Chapter 2.

Table 7-2 Properties of the Rohacell Rist51 foam core [21].

Mechanical properties		Thermal properties	
E	75 MPa	ρ	52 [kg/m^3]
G	24	k	0.0371 [W/m/°C]
CTE	3.26E-05 [1/°C]	c_p(40°C)	1250 [J/kg/°C]
		c_p(100°C)	1680 [J/kg/°C]
		c_p(120°C)	1720 [J/kg/°C]
		c_p(140°C)	1780 [J/kg/°C]
		c_p(160°C)	1860 [J/kg/°C]

7.2.3 Thermally Insulated Mechanical Stiffeners

In order to stiffen the CFRP tool structure, it was necessary to introduce a large number of ribs to prevent tool deformation at the hydrostatic operating resin pressure and to meet manufacturing tolerances. These potential heat sinks were thermally isolated by the tool manufacturer Qpoint, while still providing sufficient stiffness with an in-house solution based on a Rohacell foam core. To investigate the capability of the thermal isolation, two different exemplary self-heated rib structures were built, one with and one without the thermal isolation.

Steady-state temperature profiles of the blackened surfaces of the free standing structures only subjected to convection at the set-point temperature 140°C were determined by means of thermography. The resulting temperature fields are given in Figure 7-6.

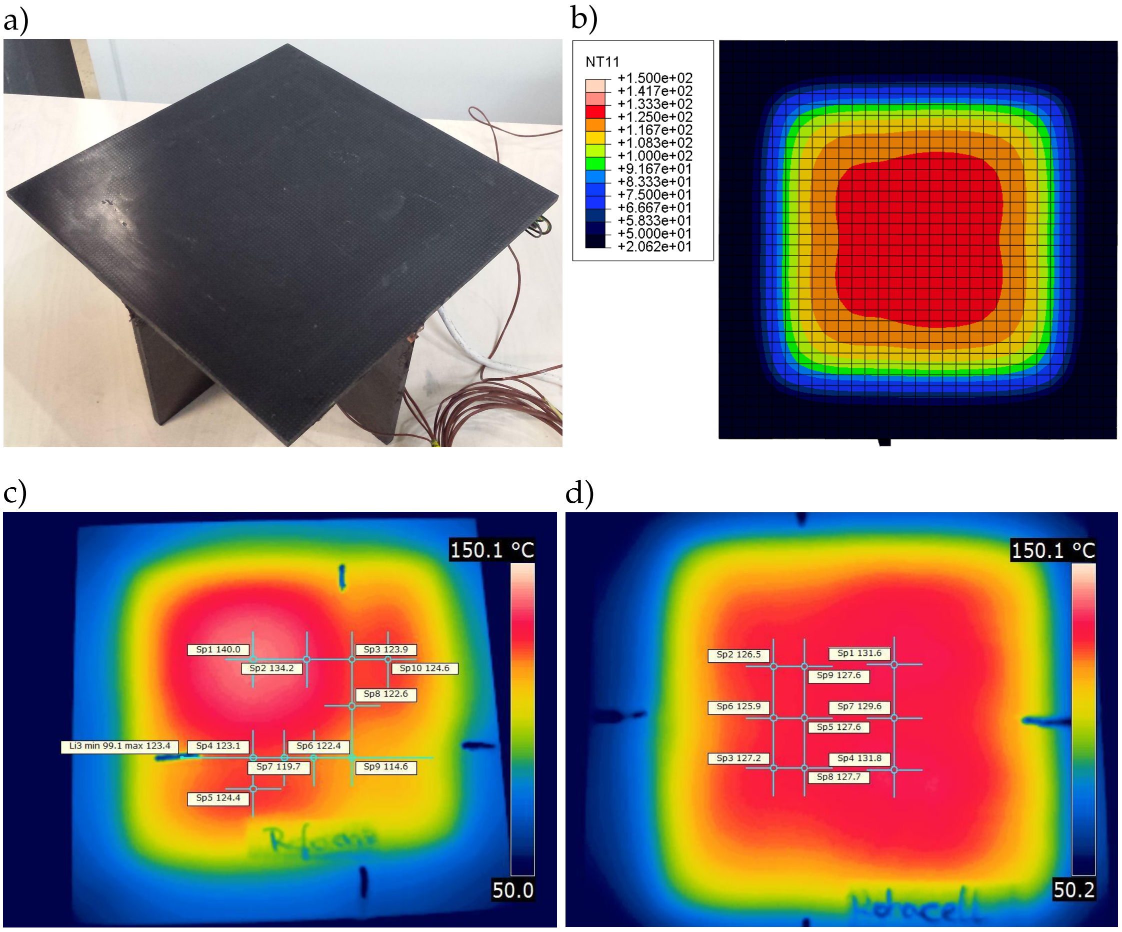

Figure 7-6 Thermography experiment: (a) Experimental rib structure, (b) Abaqus thermal simulation with isolation of the ribs, (c) tool surface profiles without isolation of the rib structure and (d) tool surface profiles with isolation of the rib structure[1].

In both experiments, the temperature dropped significantly towards the outer boarder of the top surface, similar to the validation example in Chapter 4. However, the cases differed largely in the impact of the rib structure on the backside on the surface temperature field on the topside. In both cases the control thermocouple was placed centrally and the mechanical stiffening structure slightly off-center, hence ribs did not interfere in the thermal control. In the non-isolated case in Figure 7-6 (c), the temperature drop due to the non-isolated stiffening structure was determined at ≈ 10°C. On the other hand, a significantly smaller deviation of ≈ 2°C was experienced on the overall temperature field on the opposite tool surface in case of rib isolation (see Fig. 7-6 (d)). Given that the

---

[1] These thermography pictures were provided by courtesy of Qpoint Composites GmbH.

exact constituents proportions, the geometry and thermal properties of the thermal isolation of the mechanical stiffeners is unknown, the thermal properties of the insulation layer between ribs and tool shell were reverse-engineered in an Abaqus thermal simulation of the experiment. A thermal simulation was set up with eight elements in thickness direction of the tool shell and one element in thickness direction of the ribs (see Fig. 7-6 (b)). The temperature control method of Chapter 4 was used to appropriately model the heat introduction of the resistively heated CFRP tool. The convective boundary conditions were set in accordance to the convection experiments in Chapter 4 with 21 W/m/°C for the outer surfaces on the top side and 12 W/m/°C for the outer surfaces on the bottom side. First, a homogenized estimation of the thermal properties of the insulation layer was calculated with an assumed constituent ratio and their properties by rule-of-mixtures. Fine-tuning of the homogenized thermal conductivity was conducted via reverse engineering of the in-plane temperature profile impact of the ribs according to the experiment shown in Figure 7-6 (b).

With the resulting thermal insulation properties given in Table 7-3 the mean temperature deviation between simulation and experiment at the nine points investigated in Figure 7-6 (d) was determined at 1.1°C with a standard deviation of 1.4°C. Relative temperature drops on the tool surface due to rips were ≈ 2°C in both simulation and experiment.

Table 7-3 Thermal properties of the insulation layer of the mechanical stiffeners.

ρ [kg/m^3]	c_p [W/kg/°C]	k [W/m/°C]
293	1330	0.105

7.2.4 Region Interactions and Boundary Conditions

The five different independently controlled heat zones of each tool side were incorporated with the modeling approach developed in Chapter 4 utilizing a damping constant for all zones of $D = 0.8$. Thus, the heat was introduced in the middle of the tool laminate in such a way, that the control thermocouple in the considered zone followed the targeted temperature cycle. Cooling in these heat zones was not possible with the technology at hand and was purely governed by convection. The heat zone distribution in the simulation model is shown in Figure 7-7.

The thermal contact between tool and part was modeled with tie constraints. This is a reasonable approximation for an RTM process since the liquid resin

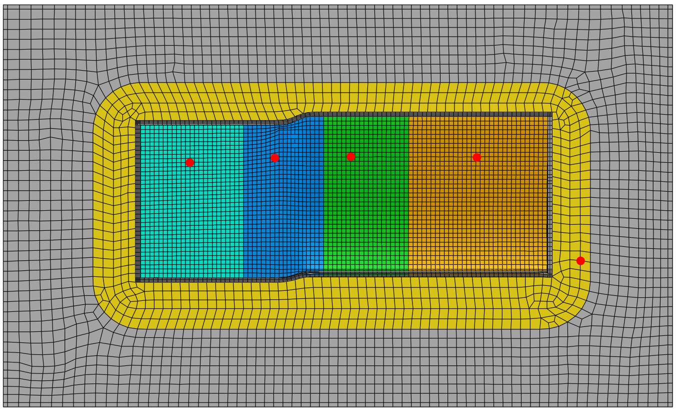

Figure 7-7 Heat zone distribution in accordance of the manufactured molds utilized in the experiment. Elements of the same heat zones are colored similar, gray elements mark unheated elements. The red dots mark the location of the control thermocouples while the gray area marks the unheated region.

enables a perfect contact in the initial stage of the manufacturing process, which is maintained with proceeding cure. Resin shrinkage could potentially lead to tool-part separation on one side, but was experienced in the latter cool-down stages with no impact on the cure behavior through thermal gap resistance.

An uncertainty in the model set-up was the introduction of convection behavior in the cure simulation model. Given the rib structure on the top and bottom side of the part, the air cannot flow freely onto the hot surfaces. Hence, the heat transfer will certainly be significantly lower than the values determined in Chapter 4, where the convection coefficient of a flat plate is measured with no geometric hindrance to the air stream. As a detailed model in a CFD analysis was not possible due to excessive calculation times, a reverse-engineered reduced smeared convection coefficient was determined for the top and bottom sides of the tool on the basis of the post-cure cool down behavior of the whole set-up, as described in the following:

In the beginning of the cool-down phase of the experiment after complete part cure, all heat zones were switched off and the manufacturing set-up were subjected to natural convection only (Switch off at t=9600 s in Figure 7-4). The cool-down behavior is given in Figure 7-8.

The simulation model was set up with two different convection coefficients for the top and bottom surfaces of the frame structure, respectively. Beginning with the experimentally determined convection coefficients of h_{top}=21 W/m^2/°C and h_{bot}=12 W/m^2/°C a set of simulations were run with decreasing heat transfer coefficients for these two surface sets. The best fit was reached with the heat transfer coefficients of h_{top}=10 W/m^2/°C and h_{bot}=3.5 W/m^2/°C. Thus, these values were employed in the following cure analysis of the generic rotor blade.

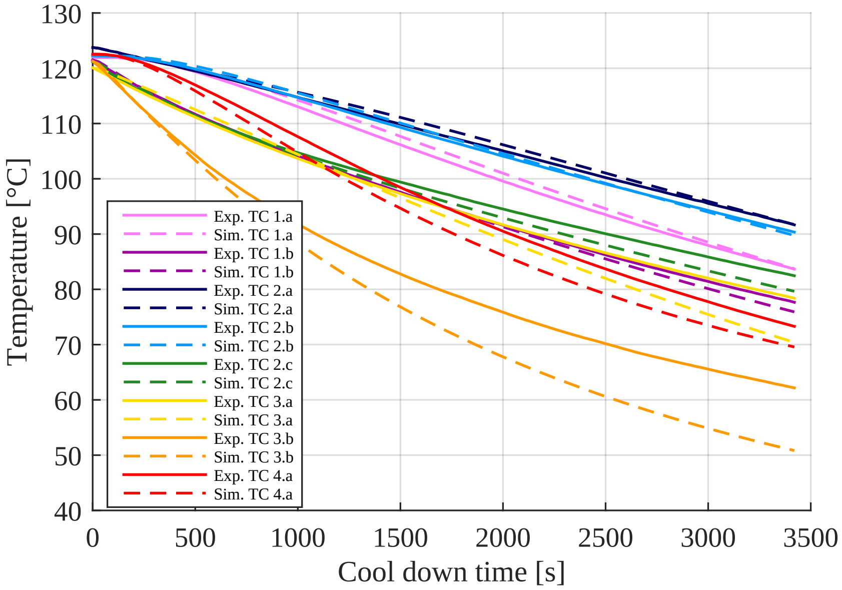

Figure 7-8 Comparison of cool down rates of simulation and experiment of the manufacturing set-up at the location of the measurement thermocouples with the adjusted convection coefficients.

It has to be noted that this procedure is only possible a posteriori to tool manufacture. It enables satisfying correlation of simulation of experiment of the impact of convection and, thus, a simulative investigation of this specific CFRP tool and thermally dimensioned variations with different zonal distribution or applied cure cycles. However, this approach cannot be pursuit if a new tool has to be designed and a priori determination of the convective heat transfer is required. In order to transfer the methods developed in this work to a industrial design process, future work should involve investigations in accurate convective boundary condition modeling with information given in the design stage of the resistively heated tool itself.

7.3 Simulation Accuracy

A cure simulation was run with the set-point temperature cycle of the experiment enabling an accuracy estimation of the simulation model. Figure 7-9 shows the comparison of experiment and simulation at the investigated locations in the monolithic section of the generic rotor blade (see Figure 7-3 for thermocouple location identification).

With the approximation of rib isolation and especially the smeared convection coefficient, the simulation showed deviations between 0.6 °C and 3.6 °C, with the exception of the GFRP spar, were larger deviations were encountered. Table 7-

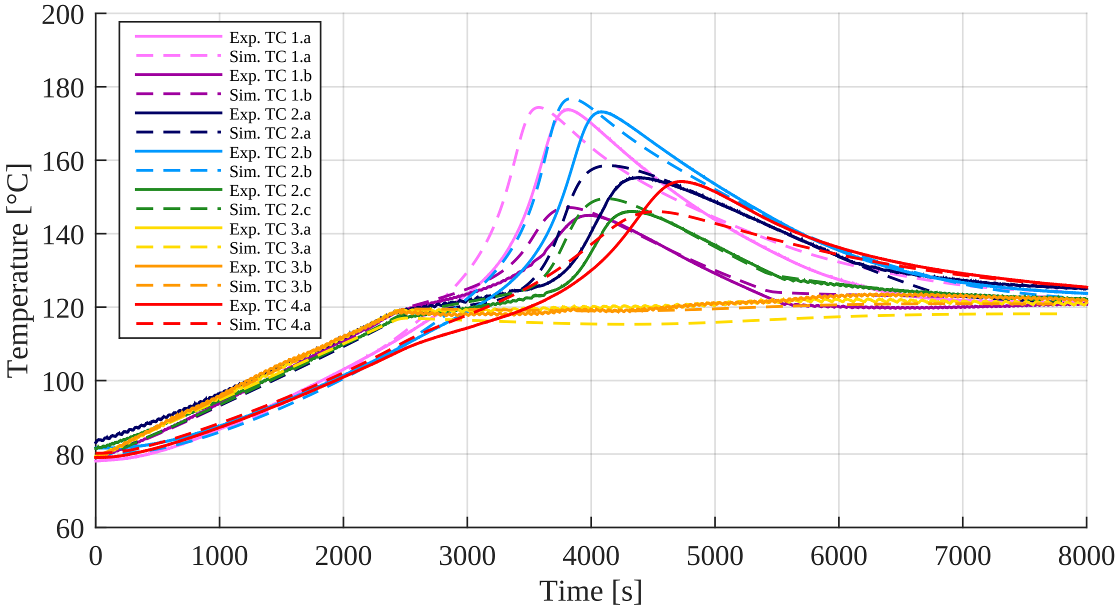

Figure 7-9 Comparison of temperature evolution in experiment and simulation in the monolithic sections.

4 shows the time and temperature deviations of all important locations at the point of maximum peak temperature. All peak temperatures were predicted 3-4 minutes too early in the simulation. The major reason of these deviations in time between simulation and experiment was the high sensitivity of the whole manufacturing set-up. As long as the heat up was purely governed by transport (until approx. 110°C), simulation and experiment showed a very close match. Above 110°C, the cure rates of the resin showed a steep increase with temperature (see Chapter 6). Once the resin reactions reached temperatures at which the heat transport between part and tool was significantly lower than the heat generated by the autocatalytic resin reaction, a close to adiabatic cure behavior in the part's laminate center was reached. In this case, even small deviations in the material models, the initial degree of cure, or local fiber volume content have a large impact on the overall temperature evolution. The initial degree of cure was set at 2 % in the simulation to account for the proceeding cure during the degassing and infiltration stage. Shrinkage in the initial stages of resin cure until gelation will lead to a proceeding resin flow into the part. Given that the infiltration was

Table 7-4 Deviation of peak temperatures and peak temperature times between simulation and experiment.

	TC 1.a	TC 1.b	TC 2.a	TC 2.b	TC 2.c	TC 4.a
ΔT [°C]	0.6	2.1	3.2	3.6	3.5	-8.2
Δt [s]	-232	-171	-243	-246	-200	-213

not simulated and this post-infiltration resin flow was neglected, the constant initial degree of cure in the simulation could prove somewhat inaccurate in the regions close to the resin inlet and outlet, and might be partly responsible for the deviations. Additionally, the accuracy of the resin kinetics model with ~ 3 % can potentially contribute to the deviations between simulation and experiment.

Nevertheless, while the overall peak timing is too early, the simulation showed a fairly accurate picture of the peak temperature magnitude and relation to each other. Thus, the simulation is very capable of predicting temperature gradients and, thus, degree of cure gradients for the investigated manufacturing set-up. The simulation model is well suited to be used for the thermal dimensioning strategy. Additionally, if an optimized cure strategy or heat zone allocation is applied in the simulation model the uncontrolled resin reaction is prohibited, which should increase simulation accuracy.

7.4 Thermal Dimensioning

Two different algorithms were developed in Chapter 5 to translate the resulting surface heat flux into a zonal distribution: the Direct Kmeans++ Clustering (DKC) algorithm and the Least Gradient Merge (LGM) algorithm. In the application on an example featuring a flat out-of-autoclave tool for the manufacturing of a stepped laminate the DKC algorithm resulted in slightly favorable results. However, through the double-curved geometry and the presence of different part materials the complexity level of the application case is significantly increased. Additionally, as a more general assessment of the capabilities of resistive heated tools is targeted, tool manufacturing restrictions on the minimal zone size and shape have to be taken into account, as well. Thus, both algorithms were applied on the problem case and the resulting numerical zone distributions were interpreted into simple zone geometries which can be manufactured, as well.

Although the investigated part has a significantly increased complexity level to the stepped laminate the algorithms were developed on (see Chapter 5), both algorithm showed reasonable results in the calculation of appropriate heating zones. However, a major problem was posed by the mechanically stiffening structure: Efforts were made by the tool manufacturer to decouple them thermally and an open surface thermography indeed showed a maximal temperature drop on the backside of a rib of ~ 2°C when subjected to convection only. However, the temperature drop at the location of the ribs can increase during a heat-up of the structure, when the thermal load is especially high. Thus, they had a significant influence and the dimensioning algorithm developed considered this impact. Due to the distinct thermal behavior of the ribs, the rib structure was emphasized by both algorithms in the calculation of the different heating zones, as shown for the DKC algorithm in Figure 7-10 (a). Simply accounting for the stiffening structure by separate thermal zones was not possible, since tool manufacturing does not allow very thin bands along the whole tool. Additionally, these thin zones would have to account for the heating of both tool and part and, thus, different thin heating zones would be required accounting for the different part thicknesses. A large number of heating zones would result to compensate for the rib structure only, with additional heating zones for the remaining tool area. Although there is not a defined limit on the total amount of heat zones, a separate power control unit is required for each heating zone contributing to the expenditure on tool purchase. In order to compare industrially feasible solutions, the number of heating zones per cavity side was set to eight with one additional transition zone around the tool cavity. With this amount of heating zones, the impact of the stiffening structure had either to be neglected or accounted for by small alterations to the undisturbed heat zone allocation. Thus, the thermal dimensioning strategy was applied onto two different simulation models, one with and one without the mechanical stiffening structure. The results are shown in Fig. 7-10.

Similar to the application case of a tapered laminate in Chapter 5, the zone distribution calculated by the LGM algorithm (Fig. 7-10 (b)) and the DKC algorithm (Fig. 7-10 (c)) differed, although a general common trend regarding the allocation of large zones is seen. The interpretation for the final feasible heat zone distribution shown in Fig. 7-10 (d) was conducted based on the DKC zone distribution, given that this algorithm reached slightly favorable results in the tapered laminate study.

The top and bottom molds are symmetrical, the only difference in the simulation model in-between both sides is a reduced convective heat transfer coefficient in case of the latter. This heat transfer acts as a temperature-dependent offset in the overall energy requirement during the cure cycle. Due to the temperature-dependency of the convective energy flux and the overall higher temperature level of the bottom side of the tool the zone allocation calculated by the algorithm can differ in theory, but the difference were marginal for the investigated case. Symmetrical heat zones were applied on the top and bottom mold. Control thermocouple positions for the cure analysis of the thermally dimensioning manufacturing mold are shown as bright red dots in Figure 7-10 (d). They were in accordance with the guidelines presented in Chapter 5.

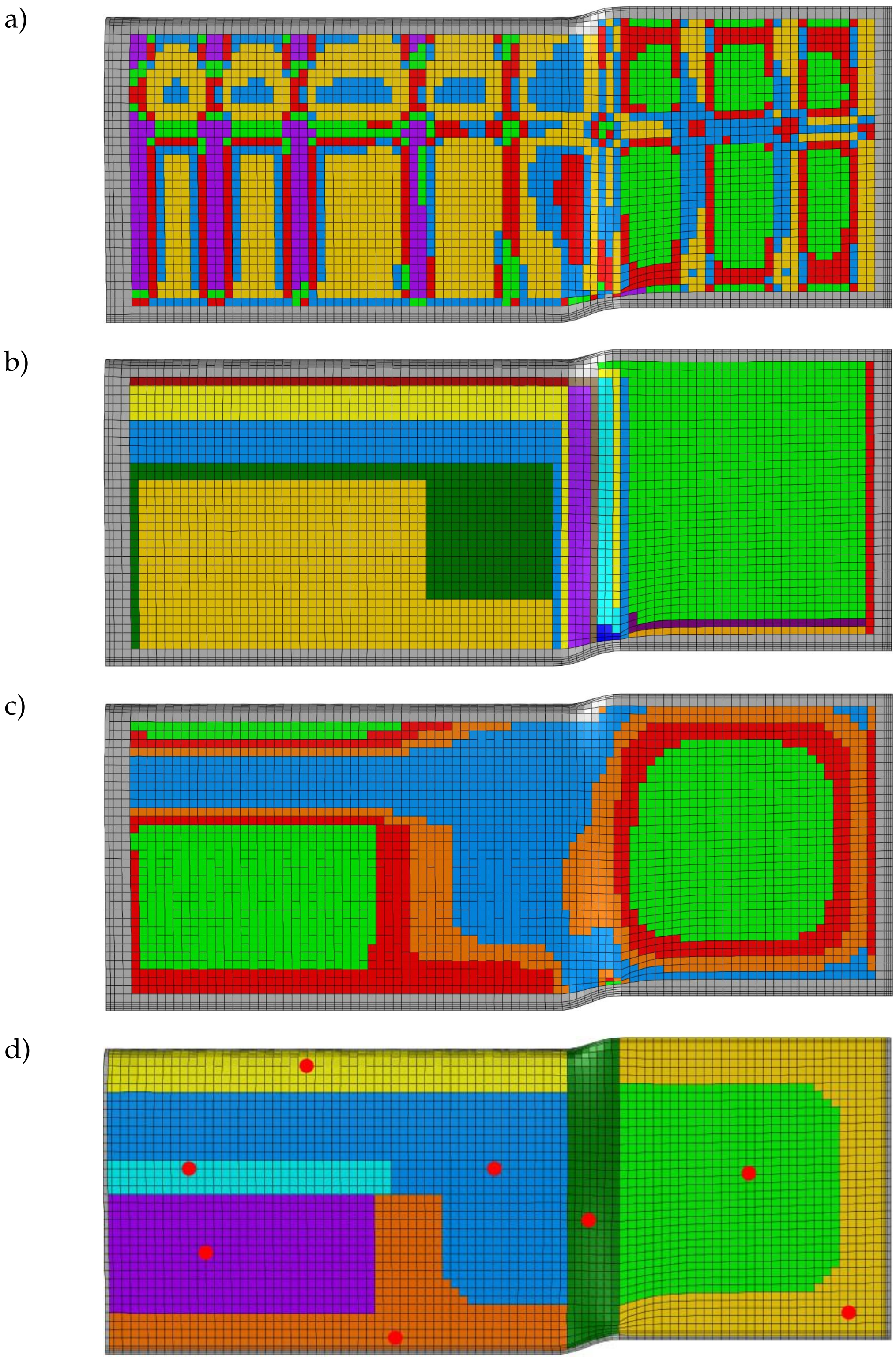

Figure 7-10 Numerically determined heat zone distributions: (a) Simulation model with ribs and DKC clustering, (b) simulation model without ribs and LGM clustering, (c) simulation model without ribs and DKC clustering, and (d) resulting interpretation for the heat zone distribution. The zones are distinguished by element colors and bright red spots mark the locations of the control thermocouples.

7.5 Estimation of the Potential of Resistively Heated Tools for Improved Part Cure

Although CFRP tools have many advantages such as direct heat introduction, light-weight design, and very small coefficient of thermal expansion, the temperature distribution during part cure is a concern in industrial applications due to their low thermal conductivity. In order to assess the thermal capabilities of resistively heated CFRP tools, the thermal and cure behavior of the thermally dimensioned simulation model of the generic rotor blade manufacturing process with a temperature cycle suited to the part's thicknesses is discussed. Further, the potential of a multi-zone heat introduction "when and where it is needed" is assessed.

7.5.1 Thermochemical Part Response to Thermally Dimensioned Resistively Heated CFRP Molds

A cure simulation was conducted to identify the impact of the thermally dimensioned, resistively heated CFRP tool on the part's curing process. The numerical heat zone control strategy developed in Chapter 4 was employed to obtain accurate temperature controlled heat introduction in the simulation model in each zone, with a set-point temperature cycle in accordance with the robust single-zone optimization results given in Table 6-7. Heat zone distribution and control temperature point placement is shown in Figure 7-10 (d). Figure 7-11 (a) and (b) shows the transient temperature and degree of cure evolution at several location within the part.

Overall, the temperature development in the part closely follows the 1D investigations conducted in the previous Chapter. The largest temperature gradients in thickness direction is apparent at the end of the second dwell in the center of the monolithic section between laminate middle plane (Loc. 2.b) and the top surface (Loc. 2.c). Whereas the simulation accuracy experiment displayed a cure progress from the sides of the monolithic laminate to its center, the temperature evolution at the edge of the monolithic section does not deviate significantly from the center of the monolithic laminate in the middle plane (Loc. 1.a) as well as at the respective surfaces (Loc. 1.b). The temperatures between the foam core and the GFRP spar (Loc. 4.a) showed a significant temperature overshoot of similar value as the monolithic CFRP in the beginning of the last dwell only.

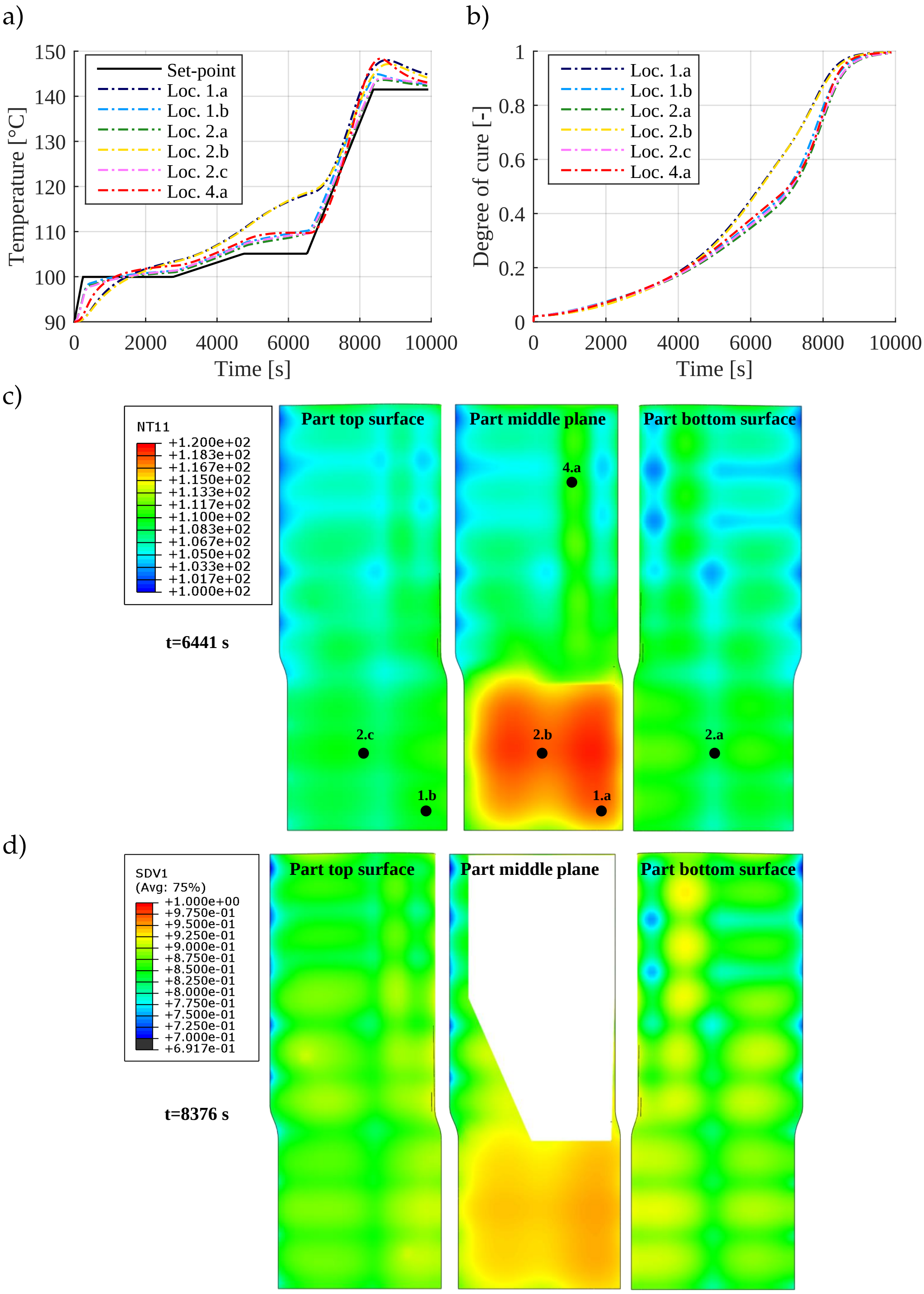

Figure 7-11 Temperature and degree of cure evolution in the thermally dimensioned model: (a) Transient temperature evolution, (b) transient degree of cure evolution, (c) temperature contour plots at the end of the second dwell, and (d) degree of cure contour plots at the beginning of the third dwell.

In Figure 7-11 (c), the temperature contour plot at the time of the largest deviations at the end of the second dwell is depicted. Given that the relative temperature overshoot of the resin at this point is the highest, the part's surface temperatures at this stage are slightly above set-point temperature with the exception of the locations close to the mechanical stiffeners. The impact of the tool stiffening structure on the part's thermal behavior can be seen at this point, with local temperature deviations of up to -3°C from set-point value at the trailing edge of the blade. An exothermic temperature overshoot in the middle plane of the monolithic section is apparent, given that the applied cure cycle cannot fully prevent this effect from occurring.

It has to be noted that the tool bottom side was subjected to a lower convection coefficient and featured a slightly more deviating behavior of the surface temperatures. Since the heating zones completely compensate the mean convection influence, the overall energy introduction in the heating zones increases significantly with increasing convection coefficient. Thus, the temperature field in heating zones subjected to a lower convection coefficient are more sensitive to local changes leading to slightly higher surface temperature deviations originating from the thermal impact of the mechanical stiffeners.

Since the degree of cure is a result of the transient local temperature history, a degree of cure gradient was seen at the beginning of the third dwell on the surfaces as well as the middle plane. While a surface degree of cure appeared between 85 and 90 % at this stage in almost all areas except the trailing edge at the top side, the bottom side featured higher degree of cure deviations at the locations of the mechanical stiffeners in the sandwich section. The surface degree of cure at the GFRP spar is slightly elevated to 93 % at the bottom side, as the exothermic reaction leads to a higher surface temperature overshoot at this stage due to low convection impact. The middle plane features a degree of cure of ~ 95% in the monolithic section. The sandwich material is not curing and the respective area remains white in the contour plot.

Overall, this study shows that manufacturing within the requirements of typical industrial applications is possible with resistively self-heated CFRP tools even for large and complex parts. The surface temperatures of all areas showed only a bigger deviation than 3 °C, if significant exothermic reaction within the thick laminate occurred. Thus, close to homogeneous surface temperature is possible with these tools for parts with large thickness variations, where a varying heat introduction in space and time is required. It also shows that for a thermally dimensioned resistively heated CFRP tool, overall surface temperature deviations in operation resulting from varying materials and thicknesses are so low, that an isolated mechanical stiffening structure has a thermal impact on the surface temperature and degree of cure field which exceeds the general deviations originating from the laminate material and thickness variations. Thus, in order to built a resistively heated manufacturing tool for large parts, development effort should be undertaken to reduce the thermal contact of a stiffening structure to an absolute minimum. If no stiffening structure is required in the tool, close to perfect temperature distribution should be possible with a thermally dimensioned resistively heated CFRP tool using a limited amount of heat zones, independent of apparent laminate variations of the part.

7.5.2 Impact of Varying Set-Point Temperature Cycles

In contrast to other tools featuring a material with high thermal conductivity, resistively heated CFRP tools are actually capable of a diverse heat introduction according to the local part material and thickness by the application of different temperature cycles in different heating zones. However, the drawback of such an approach is a potentially more inhomogeneous part surface cure behavior and an investigation is required to assess the potential.

To investigate the impact of varying set-point temperature cycles, the thermally dimensioned simulation was adjusted to feature the three previously optimized set-point temperature cycles developed for a multi-zone application. The respective temperature cycles are given in Table 6-7. The multi-zone temperature cycle for the approximate thickness of 30 mm was applied in the monolithic section (green and yellow zones on the right side in Figure 7-10 (d)), the cycle for an approximate thickness of 20 mm was applied on the transition section (dark green in Figure 7-10 (d)) and the cycle for an approximate thickness of 15 mm was applied on all remaining zones, namely the sandwich section and the GFRP spar.

Figure 7-12 (a) and (c) shows the temperature evolution at certain locations as well as the temperature distribution at the end of the second dwell.

Since different temperature cycles potentially increase the surface temperature deviations, the surface temperature evolution of Figure 7-12 had to be investigated and compared to the case with a uniform temperature cycle applied, which is given in the previous section in Figure 7-11. The overall temperature distribution was more homogeneous. The part surface temperatures in this area increased during the second dwell up to $\sim 5°C$ above set-point temperature. due to the exothermic reaction in the inner monolithic section. This was not the case in the sandwich section of the part, as the laminate in this section was very thin. Due to the different cure cycle applied in the sandwich section, the surface tem-

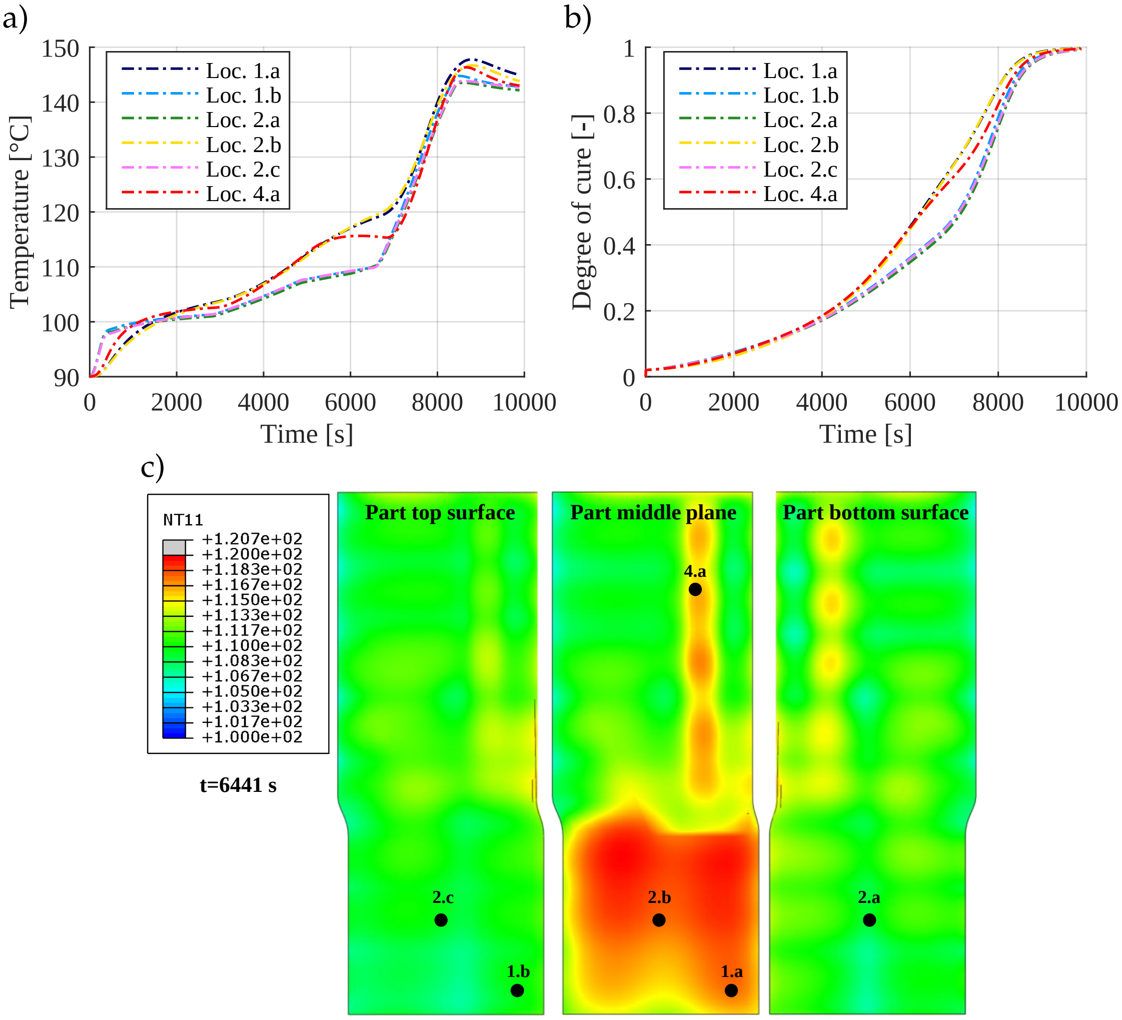

Figure 7-12 Temperature and degree of cure evolution in the thermally dimensioned model with multiple applied temperature cycles: (a) Transient temperature evolution, (b) transient degree of cure evolution, and (c) temperature contour plots for the surfaces and part middle plane.

perature was elevated to match the surface temperature of the monolithic section. The temperature deviations apparent between sandwich and monolithic section were in line with the surface temperature deviations occurring in the monolithic section itself.

The single exception was the GFRP spar featuring a ≈ 8 mm laminate thickness with a one-sided isolation by the sandwich core, which resulted in a temperature rise of ∼ 5° C above the overall surface temperature at the bottom side. The bottom side was subjected to a lower convection coefficient leading to a more inhomogeneous surface temperature as it was more sensitive to the location of heat introduction due to exothermic resin reaction or heat zones.

However, the temperature cycle of the 8 mm GFRP spar was optimized to lead to a similar overall temperature and degree of cure profile compared to the 30 mm monolithic section in general and not in the surface plane only. The comparison of the temperature evolutions at Loc. 4.a (inner surface GFRP spar) and Loc. 2.b (center monolithic laminate) in Figure 7-12 (b) shows that the two different temperature cycles led to a close match in the degree of cure evolutions in the GFRP spar and the monolithic section in the part's interior as well, despite the fact that the laminate thickness vary by a significant amount. Thus, the approach of a multiple temperature cycle application to ensure a more uniform in-plane part cure in the parts interior, which features varying laminate thicknesses, does work. The optimization procedure developed was capable of providing the appropriate temperature cycles to do so.

Figure 7-13 illustrates these findings. The degree of cure contour plot in a cutting plane through the part is given and compared to the simulation with one overall temperature cycle applied at the end of the second dwell. The cutting plane is located on the bottom side of the upper spar (see Figure 7-13), between the middle plane and the part's top surface.

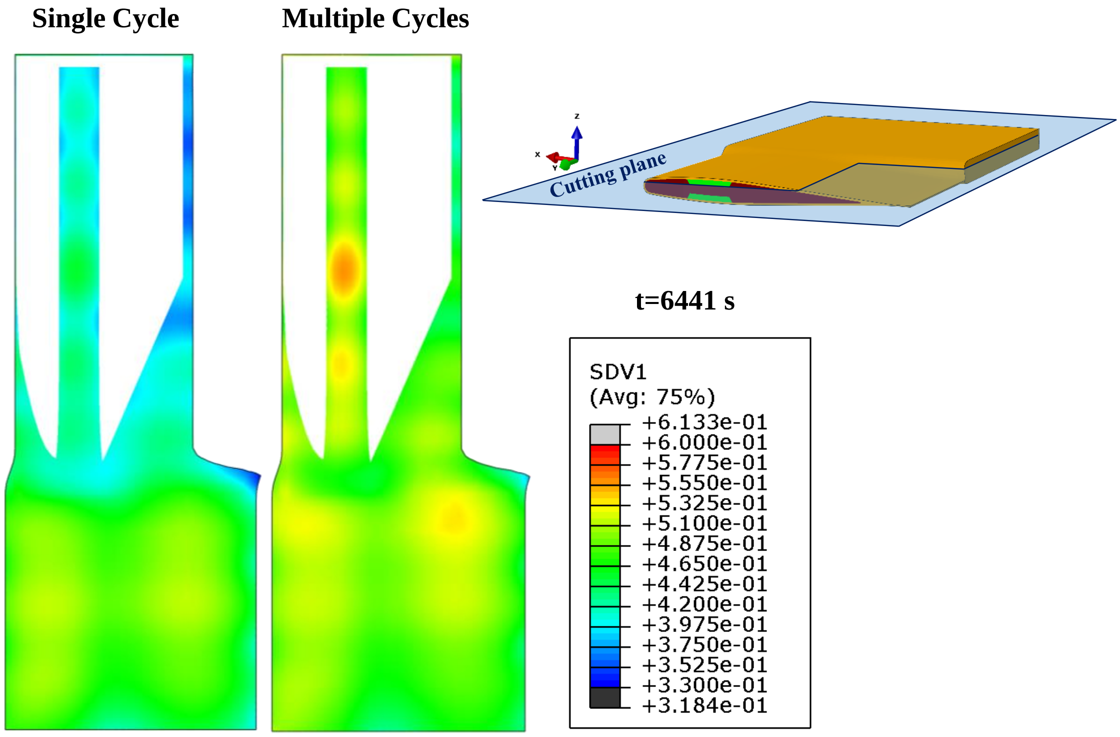

Figure 7-13 Comparison of degree of cure contour plots between the simulations with one overall temperature cycle (left) and varying temperature cycle (right) at the end of the second dwell.

Since there are some local degree of cure deviations apparent resulting from the impact of the mechanical stiffeners, the mean degree of cure level on the bottom side of the GFRP spar is similar to the degree of cure in the monolithic section in the same plane. In contrast, in the simulation with one overall temperature cycle applied, the cure of the GFRP spar is delayed, leading to a mean in-plane degree of cure offset of ~ -10 % between GFRP spar and monolithic section in the same plane.

While the improvement in the cure behavior induced by the application of the thermal dimensioning method and different cure cycles was illustrated at certain surfaces and times in this chapter, an overall comparison of the curing behavior in the simulation can be made by the evolution of the standard deviation of all curing elements in the simulation in every time step. Lower standard deviation of the degree of cure in the curing elements resembles a higher degree of homogeneity in the curing process. Given that one degree of cure is given by one element with a distinct volume v_i, a weighted standard deviation has to be used to consider the differences in element volume and gain a mesh-independent standard deviation of the degree of cure σ_α in one time step:

$$\sigma_\alpha = \sqrt{\frac{\sum_{i=1}^{n} v_i(\alpha_i - \overline{\alpha})^2}{\sum_{i=1}^{n} v_i}} \tag{7-1}$$

Where $\overline{\alpha}$ denotes the mean weighted degree of cure, which is calculated with the mean elemental volume $\overline{v_\mathrm{e}}$ according to:

$$\overline{\alpha} = \frac{1}{n}\sum_{i=1}^{n} \frac{v_i}{\overline{v_\mathrm{e}}}\alpha_i \tag{7-2}$$

It has to be noted that, although these expressions enable a general comparison of degree of cure homogeneity of different setups, local degree of cure differences are considered similar to global degree of cure differences. However, the former lead to higher degree of cure gradients and, thus, worse laminate quality. Hence, investigation of the mean weighted degree of cure can only add to a general investigation of the cure behavior and should not be the sole value of consideration in the assessment of the cure behavior of a part.

Four different variants of the simulation model introduced in this chapter were compared via the mean weighted degree of cure:

- **Case 1** is the simulation accuracy experiment, which contains of the heat-zone distribution made by the manufacturer (see Fig. 7-7) and a cure cycle based on the resin manufacturer's recommended cure temperature (see Fig. 6-5 (a)).

- **Case 2** constitutes of the heat zone distribution made by the manufacturer and the numerically optimized temperature cycle originating from a single zone examination (see Table 6-7).
- **Case 3** represents the simulation model variant investigated in the previous section, with thermally dimensioned heat-zone distribution and the numerically optimized temperature cycle originating from a single zone examination.
- **Case 4** is the simulation model variant investigated in this section, with thermally dimensioned heat-zone distribution and a set of complementary multiple temperature cycles (see Fig. 6-8 (a)).

The evolution of the mean weighted degree of cure during the manufacturing process is given in Figure 7-14 and illustrates, that the biggest increase in the degree of cure homogeneity can be achieved in the application of an optimized temperature cycle (comparison of Case 2 to Case 1) and the thermal dimensioning technique (comparison of Case 3 to Case 2).

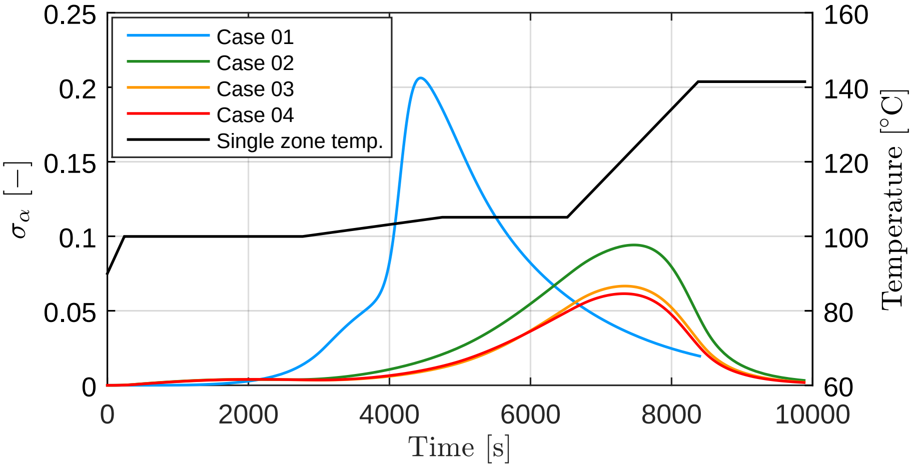

Figure 7-14 Comparison of the mean weighted standard deviation of the degree of cure in the curing elements of different simulation variants.

The application of different complementary temperature cycles led to a further decrease of the maximum σ_α by 7.7 % (comparison of Case 4 to Case 3), although the geometry and material combination of the generic rotor blade does not favor a σ_α comparison: Due to the non-curing sandwich core, a large portion of the curing volume is located in the monolithic section, which is subjected to the same temperature cycle as in Case 3. The complementary temperature cycles are applied in the sandwich section, where they do lead to overall improved cure behavior, but the corresponding curing element volume is low in comparison to the monolithic section leading to an overall moderate improvement of the σ_α value. Nevertheless, a distinct improvement in the σ_α-value is seen, indicating an overall improved cure behavior through the application of a set of complementary temperature cycles in the different heat zones.

7.6 Summary and Discussion

A case study featuring a generic rotor blade was conducted to investigate the thermal and cure behavior of a large part with industrial complexity level manufactured by a resistively heated CFRP RTM tool. A comparison of the part temperatures during the manufacturing process in experiment and simulation showed that the model is capable to predict the specific thermal characteristics apparent in the use case. The application of the thermal dimensioning strategy on this simulation model and investigation of its results led to the following conclusions:

1. Although the mechanical stiffeners were thermally isolated by the tool manufacturer to a certain extend, they still had a significant impact on the overall thermal and cure behavior of the part. Effort has to be undertaken to decouple the mechanical stiffeners as much as possible in case of resistively heated CFRP tools.
2. Manufacturing within the thermal requirements of most industrial applications is possible with resistively heated CFRP tools even for large and complex parts.
3. It is beneficial for the overall cure behavior to apply different temperature cycles onto part sections featuring different material or laminate thickness, if the respective cure cycles are carefully chosen. The temperature cycles can be optimized to lead to small in-plane degree of cure deviations in the laminate's interior instead of homogeneous degree of cure at the surface only. The procedure to derive these cure cycles, which was developed in Chapter 6, resulted in improved part cure at the surface as well as in the inner laminate.

The last-mentioned statement can, in some cases, result in an improvement of the part's cure behavior induced by a resistively heated CFRP RTM tool in comparison to the cure behavior induced by traditional RTM tools made of aluminum or steel. Application of a non-uniform surface temperature onto a curing part in cases where higher temperature gradients are required is challenging with tools made of traditional tool material due to the higher heat conductivity.

8 Conclusions, Contributions and Future Work

Although CFRP tools possess a variety of advantages, they are known for their thermal sensitivity and resulting temperature deviations during part production, which in some cases prohibit their widespread application. This work aims to provide the required knowledge and methods to achieve homogeneous part cure in composite manufacturing with resistively heated CFRP tools and, thus, contributes to their application in the industry. The following conclusions and contributions are a result of the presented work:

1. **The potentially inhomogeneous temperature field generated by resistively heated CFRP tools can be predicted computationally efficient with appropriate accuracy.**
   The temperature response within one heat zone is controlled at a distinct control point. The power introduction within the whole heat zone is controlled to result in set-point temperature at the control point. Thus, temperature gradients may occur if the heat balance is location-dependent in the zone. Variations in part thickness and material as well as environmental impacts on the heat flow, such as convection, are potentially contributing to a diverse temperature field within one zone. Since the cure behavior of the part is governed by the tool temperature field, this temperature variation can have a significant impact on part cure behavior and needs to be considered.
   Contribution: A computationally efficient numerical surface heat flux control method was developed and implemented in Abaqus utilizing the cure simulation platform provided by COMPRO/CCA. Validation results show that temperatures of resistively heated CFRP tools can be predicted within thermocouple accuracy even if large temperature gradients within one zone occur.
2. **Close to homogeneous part surface temperatures can be achieved with resistively heated CFRP tools even for large parts with industrial complexity level.**
   With a sound alignment of multiple heat zones in a designated heating area the manufacturing tool can be tailored to the requirements of the part to be produced. Thus, variations in the part, such as thickness or material changes, can be accounted for, resulting in a close to uniform surface temperature.

Contribution: A numeric approach was developed to determine the allocation of multiple zones in a resistively heated manufacturing tool. Results of its application show a significantly increased temperature homogeneity of the tool and an improved degree of cure homogeneity in the part. Additionally, the investigation of two application cases with varying complexity level indicate, that transition zones between heated and unheated regions vastly increase the temperature uniformity in a designated heating area. Finally, a justified set of guidelines for the positioning of control thermocouples was determined.

3. **The application of adjusted temperature cycles onto different part areas is feasible with resistively heated CFRP tools, potentially leading to improved part cure.**
   The cure behavior of laminates varies with its thickness since the exothermic resin reaction increases the local laminate temperature, which in turn increases the rates of chemical reaction. This can lead to slight variation in the part surface temperature, given that low thermal conductivity of the tool material results in a partially insulating behavior between set-point temperature plane and part surface temperature. Additionally, variation in the laminate thickness can amount to in-plane degree of cure gradients in the part's interior.
   Contribution: An optimization scheme was implemented and applied to gain a thickness-robust optimal temperature cycle for laminate manufacturing with the investigated resin system. An adjusted optimization technique was developed to determine a set of complementary temperature cycles to be applied in different heat zones of one tool. A comparison of results of the application of multiple complementary cycles in contrast to one overall cycle showed that further cure homogeneity improvement can be achieved. The numeric case study of a generic rotor blade showed a more homogeneous in-plane degree of cure distribution at the part's surface as well as the part interior, if multiple complementary cure cycles were employed.

The content of this thesis contributes to a simulation-based thermal design of resistively heated tools and, thus, addresses one of the major concerns regarding the widespread application of resistively heated CFRP tools. In order to generate more complementary knowledge to pursue an industrialization of these manufacturing tools the following topics should be content of future investigations:

1. While part material and thickness variations could be handled well in the thermal dimensioning of the case study, the mechanically stiffening rib structure caused local variations in the surface temperature, which were often of greater magnitude than the global variations. To support

the application of CFRP tools onto large structures, further research is required to provide a thermally decoupled stiffening technique of the tool shell laminate. At the same time, experimental investigations have to be conducted to quantify the thermal contact between tool and stiffeners, enabling more accurate simulation results.

2. The application of a reverse engineering approach to determine a convection coefficient as well as the thermal properties of the isolation of the mechanical stiffeners led to a close correlation of the simulation model with the experiment in the case study. While this is applicable if a general estimation of the capabilities of CFRP tools is conducted, industrial thermal tool design requires this information a priori. Thus, experimental work is required to improve the quantification of the thermal behavior, contact, and heat transfer between the part, tool shell, mechanical stiffener and ambient air. A potential tool-part separation in the RTM manufacturing process could not be determined in the temperature evolution of the measurement thermocouples but might occur in other cases. Through combination of this experimental work with a coupling of CFD and cure simulation, generally applicable rules or guidelines might be found to appropriately model the convection impact in a sole cure simulation without prior experiments requiring the whole manufacturing tool. Additionally, a full coupling of cure simulation with a mechanical analysis might give an indication of the occurrence as well as thermal and cure impact of tool-part separation in a closed mold.

3. The current state of development of resistively heated tools does not include controlled tool cooling, which would significantly contribute in the reduction of the risk of a temperature overshoot in case of thick laminate manufacturing. Controlled cooling of resistively heated tools would offer new possibilities in the temperature cycle choice and reduce cycle times, as well.

4. CFRP tools offer the advantage of low thermal expansion which, in general, is potentially beneficial for the reduction of process-induced deformations. However, there might be limits in the applicability of this assumption as the tool material itself features mechanically directional laminate response and is subjected to a certain temperature variation through the cure cycle. The impact of the tool material CFRP onto process-induced deformations of the part upon demolding should be content of future investigations.

5. While most researchers in literature agree that homogeneous temperature and degree of cure distribution results in improved laminate quality, quan-

tified information on the impact of temperature and degree of cure gradients on laminate load carrying capability is scarce. To gain information how restrictive the allowable for in-plane and out-of-plane temperature and degree of cure homogeneity has to be set, a variety of studies needs to be conducted. This includes an experimental determination of the resin strength as well as the interface strength as a function of temperature and degree of cure, micro-mechanical investigations on the occurrence of resin cracks and macromechanical validation of the calculated stress states in the process simulation.

Bibliography

[1] *Qpoint Composites GmbH, Dresden*, 2012.

[2] A. W. Smith, K. Goyette, C. Kazanas, and P. Hubert, "Development of a heat tooling solution to improve process flexibility for out-of-autoclave prepregs," in *SAMPE*, 2013.

[3] S. Payette, "Heated tool processing of out-of-autoclave composite materials," Master's thesis, McGill University, 2015.

[4] J. Enns and J. Gillkam, "Time-temperature-transformation (ttt) cure diagram: Modeling the cure behavior of thermosets," *Journal of applied polymer science*, vol. 28, pp. 2567–2591, 1983.

[5] E. Ruiz and F. Trochu, "Numerical analysis of cure temperature and internal stresses in thin and thick rtm parts," *Composites: Part A*, vol. 36, pp. 806–826, 2005.

[6] G. Twigg, A. Poursartip, and G. Fernlund, "Tool–part interaction in composites processing. part i: experimental investigation and analytical model," *Composites: Part A*, vol. 35, pp. 121–133, 2004.

[7] A. R. A. Arafath, "Efficient numerical techniques for predicting process induces stress and deformation in composite structures," Ph.D. dissertation, University of British Columbia, 2007.

[8] L. Khoun, "Process-induced stress and deformation in woven composites manufactured by resin transfer moulding," Ph.D. dissertation, McGill University, Montreal, 2009.

[9] D. Lee, S. Kim, W. Lee, S. Ha, and S. Tsai, "Smart cure of thick composite filament wound strctures to minimize the development of residual stresses," *Composites: Part A*, vol. 37, pp. 530–537, 2006.

[10] N. Rai and R. Pitchumani, "Rapid cure simulation using artificial neural networks," *Composites: Part A*, vol. 28, pp. 847–859, 1997.

[11] M. Haider and P. Hubert, "Cure shrinkage characterization and modeling of a polyester resin containing low profile additives," *Composites: Part A*, vol. 38, pp. 994–1009, 2006.

[12] J. Weiland, M. Hartmann, and R. Hinterhölzl, "Characterization and numerical investigation of an rtm cure process with cfrp molds and independent heat patches," in *Proceedings of the 20th International Conference on Composite Materials (ICCM20)*, 2015.

[13] S. Payette, S. Smith, K. Goyette, and P. Hubert, "Multi-zoned heated tooling for out-of-autoclave processing of variable thickness composite laminates," in *Cancom2015 - Canadian international conference on composite materials*, 2015.

[14] *Material Data Sheet of Al6061-T6*. ASM, 2015.

[15] *Material Data Sheet of Invar 36 Alloy*. Carpenter, 2015.

[16] *Material Data Sheet Toho Tenax HTS40*. Toho Tenax, 2011.

[17] A. A. Johnston, "An integrated model of the development of process-induced deformation in autoclave processing of composite structures," Ph.D. dissertation, The University of British Columbia, April 1997.

[18] J. Kratz, K. Hsiao, G. Fernlund, and P. Hubert, "Thermal models for mtm45-1 and cycom 5320 out-of-autoclave prepreg resins," *Journal of Composite Materials*, vol. 47, pp. 341–352, 2012.

[19] Cytec, "Material data sheet of thornel t-650/35 carbon fiber," 2012.

[20] AGY, *High Strength Glass Fibers - Technical Paper*, 2006.

[21] Evonik, *Material data sheet of Rohacell Rist 51*, 2008.

[22] F. Henning and E. Moeller, *Handbuch Leichtbau*. Hanser Verlag, 2011.

[23] S. G. Advani and E. M. Sozer, *Process Modeling in Composites Manufacturing*. Marcel Dekker, Inc., 2003.

[24] N. Athanasopoulos, D. Sikoutris, T. Panidis, and V. Kostopoulos, "Numerical investigation and experimental verification of the joule heating effect of polyacrylonitrile-based carbon fiber tows under high vacuum conditions," *Journal of Composite Materials*, vol. 0, pp. 1–12, 2011.

[25] N. Athanasopoulos and . Kostopoulos, "Resistive heating of multidirectional and unidirectional dry carbon fibre preforms," *Composites Science and Technology*, vol. 72, pp. 1273–1282, 2012.

[26] N. Athanasopoulos, G. Koutsoukis, D. Vlachos, and V. Kostopoulos, "Temperature uniformity analysis and development of open lightweight composite molds using carbon fibers as heating elements," *Composites: Part B*, vol. 50, pp. 279–289, 2013.

[27] A. Thostenson and T. Chou, "Microwave processing: fundamentals and applications," *Composites: Part A*, vol. 30, pp. 1055–1071, 1999.

[28] D. Papargyris, R. Day, A. Nesbitt, and D. Bakavos, "Comparison of the mechanical and physical properties of a carbon fibre epoxy composite man-

ufactured by resin transfer moulding using conventional and microwave heating," *Composites Science and*, vol. 68, pp. 1852–1861, 2008.

[29] S. Payette, A. Smith, K. Goyette, C. Kazanas, and P. Hubert, "Out-of-autoclave manufacturing: Benchmarking of an integrally heated tool-plate," in *SAMPE Journal, Vol. 51, No. 1*, 2015.

[30] *Thermoceramix, Montreal*, 2012.

[31] J. Weiland, M. Hartmann, and R. Hinterhölzl, "Cure simulation with resistively in situ heated cfrp molds: Implementation and validation," *Composites: Part A*, vol. 80, pp. 171–181, 2016.

[32] G. Fernlund, "Experimental and numerical study of the effect of cure cycle, tool surface, geometry, and lay-up on the dimensional fidelity of autoclave-processed composite parts," *Composites: Part A*, vol. 33, pp. 341–351, 2002.

[33] H. Ghiasi, M. Rahmat, P. Hubert, and L. Lessard, "Curved composite structures and compromise between process-induced deformations and structural performance," in *Proceedings on the 18th International Conference on Composite Materials*, 2009.

[34] *ASM Handbook Volume 21 - Composites*. ASM International, 2001.

[35] V. Gonzales-Romero and N. Casillas, "Isothermal and temperature programmed kinetic studies of thermosets," *Polymer Engineering and Science*, vol. 29, 1989.

[36] V. Pillai and P. Beris, A.N. nd Dhurjati, "Intelligent curing of thick composites using a knowledge-based system," *Journal of Composite Materials*, vol. 31, no. 1, pp. 22–51, 1997.

[37] D. J. Michaud, A. N. Beris, and P. S. Dhurjati, "Curing behavior of thick-sectioned rtm composites," *Journal of Composite Materials*, vol. 32, no. 14, pp. 1273–1279, 1998.

[38] D. J. Michaud, A. N. Beris, and P. S. Dhurjati, "Thick-sectioned rtm composite manufacturing, part ii. robust cure cycle optimization and control," *Journal of Composite Materials*, vol. 36, pp. 1201–1231, 2002.

[39] S. Pusatcioglu, J. Hassler, A. L. Fricke, and H. McGee, "Effect of temperature gradients on cure and stress gradients in thick thermoset castings," *Journal of applied polymer science*, vol. 25, pp. 381–393, 1980.

[40] M. Li, Q. Zhu, P. Geubelle, and C. Tucker, "Optimal curing for thermoset matrix composites: Thermochemical considerations," *Polymer Composites*, vol. 22, no. 1, pp. 118–131, 2001.

[41] V. Pillai, A. N. Beris, and P. S. Dhurjati, "Implementation of model-based optimal temperature profiles for autoclave curing of composites using a knowledge-based system," *Industrial & Engineering Chemistry Research*, vol. 33, pp. 2443–2452, 1994.

[42] C. Kim, H. Teng, C. Tucker, and S. White, "The continuous curing process for thermoset polymer composites. part 1: Modeling and demonstration," *Journal of Composite Materials*, vol. 29, no. 9, pp. 1222–1253, 1995.

[43] T. Bogetti and J. Gillespie, "Process-induced stress and deformation in thick-section thermoset composite laminates," *Composite Materials*, vol. 26, no. 5, pp. 626–660, 1992.

[44] J. Balvers, "In situ strain and cure monitoring in liquid composite moulding by fibre bragg grating sensors," Ph.D. dissertation, Technical University Delft, 2014.

[45] A. Plepys and R. Farris, "Evolution of residual stresses in three-dimensionally constrained epoxy resins," *Polymer*, vol. 31, no. 10, pp. 1932–1936, 1990.

[46] D. Adolf and J. Martind, "Calculation of stresses in crosslinking polymers," *Journal of Composite Materials*, vol. 30, no. 1, pp. 13–34, 1996.

[47] M. Harsch, J. Karger-Kocsis, F. Herzog, and M. Fejo, "Effect of cure regime on internal strain and stress development in a filled epoxy resin assessed by fiber bragg-grating optical strain and normal force measurements," *Journal of reinforced plastics & composites*, vol. 30, pp. 1417–1427, 2011.

[48] C. Brauner, T. B. Block, H. Purol, and A. S. Herrmann, "Microlevel manufacturing process simulation of carbon fiber/epoxy composites to analyze the effect of chemical and thermal induced residual stresses," *Journal of Composite Materials*, vol. 46, no. 17, pp. 2123–2143, 2012.

[49] L. Barral, J. Cano, J. Lopez, P. Nogueira, and C. Ramirez, "Isothermal cure of an epoxy/cycloaliphatic amin gelation," *Polymer International*, vol. 38, pp. 353–356, 1995.

[50] L. Nunez, F. Fraga, A. Castro, M. Nunez, and M. Villanueva, "Ttt cure diagram for an epoxy system diglycidyl ether of bisphenol a/1,2 diamine cyclohexane/calcium carbonate filler," *Polymer*, vol. 75, pp. 3581–3587, 2001.

[51] J. Lopez, C. Ramirez, A. Torres, M. Abad, L. Barral, J. Cano, and F. J. Diez, "Isothermal curing by dynamic mechanical analysis of three epoxy resin systems: Gelation and vitrification," *Journal of applied polymer science*, vol. 83, pp. 78–85, 2002.

[52] L. Nunez-Regueira, C. Gracia-Fernandez, and S. Gomez-Barreiro, "Use of rheology dielectic analysis and differential scanning calorimetry for gel time determination of a thermoset," *Polymer*, vol. 46, pp. 5979–5985, 2005.

[53] G. Ehrenstein, *Faserverbundwerkstoffe*, 2nd ed., 2006.

[54] M. Harsch, "Methoden und ansätze zur spannungsarmen vernetzung von epoxidharzen," Ph.D. dissertation, Technische Universität Kaiserslautern, 2008.

[55] G. Ehrenstein, *Polymer Werkstoffe*, 3rd ed. Hanser Verlag, 2011.

[56] J. Lange, N. Altmann, C. Kelly, and P. Halley, "Understanding vitrification during cure of epoxy resins using dynamic scanning calorimetry and rheological techniques," *Polymer*, vol. 41, pp. 5949–5955, 2000.

[57] K. Hofmann and W. Glasser, "Cure monitoring of an epoxy-amine system by dynamic mechanical thermal analysis," *Thermochimica Acta*, vol. 499, pp. 169–184, 1990.

[58] D. Dykeman, "Minimizing uncertainty in cure modeling for composite manufacturing," Ph.D. dissertation, University of British Columbia, 2008.

[59] P. Halley and M. Mackay, "Chemorheology of thermosets-an overview," *Polymer Engineering and Science*, vol. 36, no. 5, pp. 593–609, 1996.

[60] V. Calado and S. Advani, *Thermoset Resin Cure Kinetics and Rheology, Processing of Composites*, R. Dave and A. Loos, Eds. Carl Hanser Verlag, 2000.

[61] M. Kamal and S. Sourour, "Kinetics and thermal characterization of thermoset cure," *Polymer Engineering and Science*, vol. 13, no. 1, pp. 59–64, 1973.

[62] M. Kamal, "Thermoset characterization for moldability analysis," *Polymer Engineering and Science*, vol. 14, no. 3, pp. 231–239, 1974.

[63] W. Lee, A. Loos, and G. Pringer, "Heat of reaction, degree of cure, and viscosity of hercules 3501-6 resin," *Journal of Composite Materials*, vol. 16, pp. 510–520, 1982.

[64] K. Horie, I. Mita, and H. Kambe, "Calorimetric investigation of polymerization reactions. iv. curing reaction of polyester fumarate with styrene," *Journal of Polymer Science: Part A-1*, vol. 8, pp. 2839–2852, 1970.

[65] J. Schawe, "A description of chemical and diffusion control in isothermal kinetics of cure kinetics," *Thermochimica Acta*, vol. 388, pp. 299–312, 2002.

[66] R. Williams, M. Benavente, and R. Ruseckaite, "Criteria for selecting cure cycles in autoclave processing of graphite/epoxy composites," *Polymer En-*

gineering and Science, vol. 30, no. 18, pp. 1140–1145, 1990.

[67] P. Lam, H. Plaumann, and T. Tran, "An improved kinetic model for the autocatalytic curing of styrene-based thermoset resins," *Journal of Applied Polymer Science*, vol. 41, pp. 3043–3057, 1990.

[68] Huang, Bogetti, and Gillespie, "Process induced stress for woven fabric thick section composite structures," *Composite Structures*, vol. 49, pp. 303–312, 2000.

[69] C. Chern and G. Poehlein, "A kinetic model for curing reactions of epoxides with amines," *Polymer Engineering and Science*, vol. 27, no. 11, pp. 788–795, 1987.

[70] U. Khanna and M. Chanda, "Kinetics of anhydride curing of lsophthalic diglycidyl ester using differential scanning calorimetry," *Journal of applied polymer science*, vol. 49, pp. 319–329, 1993.

[71] Cole, "A new approach to modeling the cure kinetics of epoxy amine thermosetting resins," *Macromolecules*, vol. 24, pp. 3093–3097, 1991.

[72] K. Cole, J. Hechler, and D. Noel, "A new approach to modeling the cure kinetics of epoxy amine thermosetting resins. 2. application to a typical system based on bis[4-(diglycidylamino)phenyl]methane and bis(4-aminophenyl) sulfone," *Macromolecules*, vol. 24, pp. 3098–3110, 1991.

[73] Simon and Gillham, "Reaction kinetics and ttt cure diagrams for offstoichiometric ratios of a high-tg epoxy-amine system," *Journal of Applied Polymer Science*, vol. 46, pp. 1245–1270, 1992.

[74] E. Rabinowitch, "Collision, co-ordination, diffusion and reaction velocity in condensed systems," *Transactions of the Faraday Society*, vol. 33, pp. 1225–1233, 1937.

[75] A. DiBenedetto, "Prediction of the glass transition temperature of polymers: A model based on the principle of corresponding states," *Journal of Polymer Science: Part B: Polymer Physics*, vol. 25, pp. 1949–1969, 1987.

[76] H. Stutz, "A generalized theory for the glass transition temperature of crosslinked and uncrosslinked polymers," *Polymer Physics*, vol. 28, pp. 1483–1498, 1990.

[77] J. Pascault and R. Williams, "Glass transition temperature versus conversion relationships for thermosetting polymers," *Journal of Polymer Science: Part B: Polymer Physics*, vol. 28, pp. 85–95, 1990.

[78] P. Karkanas, "Modelling the cure of a commercial epoxy resin for applications inresind transfer moulding," *Polymer International*, vol. 41, pp. 183–191, 1996.

[79] L. Khoun, T. Centea, and P. Hubert, "Characterization methodology of thermoset resins for the processing of composite materials - case study: Cycom 890rtm epoxy resin," *Journal of Composite Materials*, vol. 44, pp. 1397–1415, 2010.

[80] E. Scott and J. Beck, "Estimation of thermal properties in carbon/epoxy composite materials during curing," *Journal of Composite Materials*, vol. 26, no. 1, pp. 20–36, 1992.

[81] L. Hjellming and J. Walker, "Thermal curing cycles for composite cylinders with thick walls and thermoset resins," *Journal of Composite Materials*, vol. 23, p. 10481064, 1989.

[82] T. Twardowski, S. Lin, and P. Geil, "Curing in thick composite laminates: Experiment and simulation," *Journal of Composite Materials*, vol. 27, no. 3, pp. 216–249, 1993.

[83] T. Corden, I. Jones, D. Hones, and V. Middleton, "The mechanisms of interlaminar cracking in thick resin transfer moulded composite cylinders," *Composites: Part A*, vol. 29, pp. 455–464, 1998.

[84] D. C. Blest, B. R. Duffy, S. McKee, and A. K. Zulkifle, "Curing simulation of thermoset composites," *Composites: Part A*, vol. 30, pp. 1289–1309, 1999.

[85] V. Antonucci, M. Giordano, K. Hsiao, and S. Advani, "A methodology to reduce thermal gradients due to the exothermic reactions in composites processing," *International Journal of Heat and Mass Transfer*, vol. 45, pp. 1675–1684, 2002.

[86] A. Cheung, Y. Yu, and K. Pochiraju, "Three-dimensional !nite element simulation of curing of polymer composites," *Finite Elements in Analysis and Design*, vol. 40, pp. 895–912, 2004.

[87] Z.-S. Guo, S. Du, and B. Zhang, "Temperature field of thick thermoset composite laminates during cure process," *Composites Science and Technology*, vol. 65, pp. 517–523, 2005.

[88] Rouison, "Resin transfer molding of hemp fiber composites: optimizationof the process and mechanical properties of the materials," *Composite Science and Technology*, vol. 66, pp. 895–906, 2006.

[89] D. Shin and H. T. Hahn, "Compaction of thick composites: Simulation and experiment," *Polymer Composites*, vol. 25, no. 1, pp. 49–59, 2004.

[90] K. Olofsson, "Temperature predictions in thick composite laminates at low cure temperatures," *Applied Composites Materials*, vol. 4, pp. 1–11, 1997.

[91] S. Yi, H. Hilton, and M. Ahmad, "A finite element approach for cure simulation of thermosetting matrix composites," *Computers & Structures*, vol. 64, pp. 383–388, 1997.

[92] J. Balvers, H. Bersee, A. Beukers, and J. Jansen, "Determination of cure dependent properties for curing simulation of thick-walled composites," in *49th AIAA/ASME/ASCE/AHS/ASC Structures, Structural Dynamics, and Materials Conference*, 2008.

[93] C. M. T. Inc., *COMPRO Model Documentation, Release 1.3*, 2014.

[94] R. Rolfes and U. Hammerschmidt, "Transverse thermal conductivity of cfrp laminates: A numerical and experimental validation of approximation formulae," *Composite Science and Technology*, vol. 54, p. 4554, 1995.

[95] Springer and Tsai, "Thermal conductivities of unidirectional materials," *Composite Materials*, vol. 1, pp. 166–173, 1967.

[96] R. Hill, , S. Muzumdar, and L. Lee, "Analysis of volumetric changes of unsaturated polyester resins during curing," *Polymer Engineering and Science*, vol. 35, no. 10, pp. 852–359, 1995.

[97] T. A. Bogetti and J. W. Gillespie, "Two-dimensional cure simulation of thick thermosetting composites," *Composite Materials*, vol. 25, pp. 239–273, 1991.

[98] J. Svanberg and J. Holmberg, "Prediction of shape distortions. part ii. experimental validation and analysis of boundary conditions," *Composites: Part A*, vol. 35, pp. 723–734, 2004.

[99] K. Zimmermann and B. V. D. Broucke, "Assessment of process-induced deformation and stress in ultra thick laminates using isoparametric 3d elements," *Reinforced Plastics and Composites*, vol. 31, pp. 163–178, 2012.

[100] S. R. White and H. T. Hahn, "Mechanical property and residual stress development during cure of a graphite/bmi composite," *Polymer Engineering and Science*, vol. 30, no. 2, pp. 1465–1473, 1990.

[101] S. White and H. Hahn, "Process modeling of composite materials: Residual stress development during cure. part ii. experimental validation," *Composite Materials*, vol. 26, no. 16, pp. 2423–2453, 1992.

[102] M. Hyer, C. Herakovich, S. Milkovich, and J. Short, "Temperature dependence of mechanical and thermal expansion properties of t300/5208 graphite/epoxy," *Composites*, vol. 14, no. 3, pp. 276–280, 1983.

[103] T. Hobbiebrunken, B. Fielder, M. Hojo, S. Ochiai, and K. Schulte, "Microscopic yielding of cf/epoxy composites and the effect on the formation of thermal residual stresses," *Composites Science and Technology*, vol. 65, pp. 1626–1635, 2005.

[104] E. Ruiz and F. Trochu, "Thermomechanical properties during cure of glass–polyester rtm composites: Elastic and viscoelastic modeling," *Composite Materials*, vol. 39, pp. 881–916, 2005.

[105] N. Ersoy, "Development of the properties of a carbon fibre reinforced thermosetting composite through cure," *Composites: Part A*, vol. 41, pp. 401–409, 2010.

[106] J. M. Whitney, "Elastic moduli of unidirectional composites with anisotropic filaments," *Composite Materials*, vol. 1, pp. 188–193, 1967.

[107] A. Armstrong, B. James, B. Wostenholm, J. Bourgoine, and J. Eastham, "Curing characteristics of a composite matrix," *Journal of Materials Science*, vol. 21, pp. 4289–4295, 1986.

[108] Y. Huang and C. Liang, "Volume shrinkage characteristics in the cure of low-shrink unsaturated polyester resins," *Polymer*, vol. 37, no. 3, pp. 401–412, 1996.

[109] C. Li, K. Potter, M. Wisnom, and G. Stringer, "In-situ measurement of chemical shrinkage of my750 epoxy resin by a novel gravimetric method," *Composites Science and Technology*, vol. 64, pp. 55–64, 2004.

[110] Y. Nawab, "Determination and modelling of the cure shrinkage of epoxy vinylester resin and associated composites by considering thermal gradients," *Composite Science and Technology*, vol. 73, pp. 81–87, 2012.

[111] L. Khoun and P. Hubert, "Cure shrinkage characterization of an epoxy resin system by two in situ measurement methods," *Polymer Composites*, vol. 31, pp. 1603–1610, 2010.

[112] Y. K. Kim and S. R. White, "Stress relaxation behavior of 3501-6 epoxy resin during cure," *Polymer Engineering and Science*, vol. 36, no. 23, pp. 2852–2862, 1996.

[113] S. White and Y. K. Kim, "Process-induced residual stress analysis of as4/3501-6 composite material," *Mechanics of Composite Materials and Structures*, vol. 5, no. 2, pp. 153–186, 1998.

[114] D. Obrien, P. Mather, and S. White, "Viscoelastic properties of an epoxy resin during cure," *Journal of Composite Materials*, vol. 35, pp. 883–904, 2001.

[115] D. Macon, "Effective adhesive modulus approach for evaluation of curing stresses," *Polymer*, vol. 42, pp. 5285–5291, 2001.

[116] Simon and McKenna, "Modeling the evolution of the dynamic mechanical properties of a commercial epoxy during cure after gelation," *Journal of Applied Polymer Science*, vol. 76, pp. 495–508, 2000.

[117] P. Prasatya, G. McKenna, and S. Simon, "A viscoelastic model for predicting isotropic residual stresses in thermosetting materials: Effects of processing parameters," *Journal of Composite Materials*, vol. 35, no. 10, pp. 826–848, 2001.

[118] N. Zobeiry, "Viscoelastic constitutive models for evaluation of residual stresses in thermoset composites during cure," Ph.D. dissertation, University of British Columbia, 2006.

[119] H. Wiersma, L. Peeters, and R. Akkerman, "Prediction of springforward in continuous-fibre/polymer l-shaped parts," *Composites: Part A*, vol. 29, pp. 1333–1342, 1998.

[120] J. Svanberg and J. Holmberg, "Prediction of shape distortions part i. fe-implementation of a path dependent constitutive model," *Composites: Part A*, vol. 35, pp. 711–721, 2004.

[121] N. Zobeiry, R. Vaziri, and A. Poursartip, "Computationally efficient pseudo-viscoelastic models for evaluation of residual stresses in thermoset polymer composites during cure," *Composites: Part A*, vol. 41, pp. 247–256, 2010.

[122] N. Zobeiry, S. Malek, R. Vaziri, and A. Poursartip, "A differential approach to finite element modelling of isotropic and transversely isotropic viscoelastic materials," *Mechanics of Materials*, vol. 97, pp. 76–91, 2016.

[123] Golestanian and El-Gizawy, "Cure dependent lamina stiffness matrices of resin transfer molded composite parts with woven fiber mats," *Journal of Composite Materials*, vol. 31, pp. 2402–2423, 1997.

[124] D. Radford, "Volume fraction gradient induced warpage in curved composite plates," *Composites Engineering*, vol. 5, no. 7, pp. 923–934, 1995.

[125] Q. Zhu and P. Geubelle, "Dimensional accuracy of thermoset composites: Simulation of process-induced residual stresses," *Journal of Composite Materials*, vol. 35, no. 24, pp. 2171–2205, 2001.

[126] D. Darrow and L. Smith, "Isolating components of processing induced warpage in laminated composites," *Journal of Composite Materials*, vol. 36, no. 21, pp. 2407–2419, 2002.

[127] Fernlund, "Finite element based prediction of process-induced deformatin of autoclaved composite structures using 2d process analysis and 3d structural analysis," *Composite Structures*, vol. 62, pp. 223–234, 2003.

[128] C. Albert and G. Fernlund, "Spring-in and warpage of angled composite laminates," *Composite Science and Technology*, vol. 62, pp. 1895–1912, 2002.

[129] S. Clifford, W. Jansson, V. Michaud, and J. Manson, "Thermoviscoelastic anisotropic analysis of process induced residual stresses and dimensional stability in real polymer matrix composite components," *Composites: Part A*, vol. 37, pp. 538–545, 2006.

[130] M. Wisnom, M. Gigliotti, N. Ersoy, M. Campbell, and K. Potter, "Mechanisms generating residual stresses and distortion during manufacture of polymer–matrix composite structures," *Composites: Part A*, vol. 37, pp. 552–529, 2006.

[131] Fernlund and Floyd, "Process analysis and tool compensation for a complex composite panel," in *American Society for Composites 22nd Annual technical Conference*, 2007.

[132] Fernlund and Floyd, "Process analysis and tool compensation for curved composite l-angles," in *Sixth Canadian-international composites Conference*, 2007.

[133] A. Arafath, "Closed-form solution for process-induced stress and deformation of a composite part cure on a solid tool: Part i - flat geometries," *Composites: Part A*, vol. 39, pp. 1106–1117, 2008.

[134] A. R. A. Arafath, "Closed-form solution for process-induced ststress and deformation of a composite part cure on a solid tool: Part ii - curved geometries," *Composites: Part A*, vol. 40, pp. 1545–1557, 2009.

[135] Dong, "Modeling the dimensional variations of composites using effective coefficients of thermal expansion," *Journal of Composite Materials*, vol. 34, pp. 2639–2652, 2009.

[136] C. Dong, "Modeling the process-induced dimensional variations of general curved composite components and assemblies," *Composites: Part A*, vol. 40, pp. 1210–1216, 2009.

[137] Zeng, "Role of tool-part interaction in process-induced warpage of autoclave-manufactured composite structures," *Composites: Part A*, vol. 41, pp. 1174–1183, 2010.

[138] D. W. Radford, "Balancing mechanisms of distortion to yield distortion-free/shape stable composites," *Journal of Reinforced Plastics and Composites*,

vol. 29, pp. 1875–1892, 2010.

[139] Kappel, "A semi-analytical simulation strategy and its application to warpage of autoclave-processed cfrp parts," *Composites: Part A*, vol. 42, pp. 1985–1994, 2011.

[140] Jahromi and Shojaei, "Prediction and optimization of cure cycle of thick fiber-reinforced composite parts using dynamic artificial neural networks," *Reinforced Plastics and Composites*, vol. 31, pp. 1201–1214, 2012.

[141] M. P. Hartmann, M. Strebinger, and R. M. Hinterhölzl, "An approach towards a basic materials characterization for the simulation of process induced deformations," in *19th International Conference on Composite materials*, 2013.

[142] J. M. Svanberg, "Predictions of manufacturing induced shape distortions," Ph.D. dissertation, Lulea University of Technology Sweden, 2002.

[143] H. Hahn and N. Pagano, "Curing stresses in composite laminates," *Journal of Composite Materials*, vol. 9, pp. 91–106, 1975.

[144] A. Griffin, "Three-dimensional curing stresses in symmetric cross-ply laminates with temperature-dependent properties," *Journal of Composite Materials*, vol. 17, pp. 449–463, 1983.

[145] H. Hahn, "Residual stresses in polymer matrix composite laminates," *Journal of Composite Materials*, vol. 10, pp. 266–278, 1976.

[146] E. Ruiz and F. Trochu, "Multi-criteria thermal optimization in liquid composite molding to reduce processing stresses and cycle time," *Composites: Part A*, vol. 37, pp. 913–924, 2006.

[147] P. Hubert and A. Poursartip, "Aspects of the compaction of composite angle laminates: An experimental investigation," *Journal of Composite Materials*, vol. 35, no. 01, pp. 2–26, 2001.

[148] M. Naji and V. Suong, "Curing of thick angle-bend thermoset composite part: Curing cycle effect on thickness variation and fiber volume fraction," *Journal of Reinforced Plastics and Composites*, vol. 18, no. 8, pp. 702–723, 1999.

[149] M. Naji and S. Hoa, "Curing of thick angle-bend thermoset composite part: Curing process modification for uniform thickness and uniform fiber volume fraction distribution," *Journal of Composite Materials*, vol. 34, no. 20, pp. 1710–1755, 2000.

[150] K. Potter, M. Campbell, C. Langer, and M. Wisnom, "The generation of geometrical deformations due to tool/part interaction in the manufacture

of composite components," *Composites: Part A*, vol. 36, pp. 301–308, 2005.

[151] D. W. Radford and T. Rennick, "Separating sources of manufacturing distortion in laminated composites," *Journal of Reinforced Plastics and Composites*, vol. 19, pp. 621–641, 2000.

[152] R. de Oliveira, S. Lavanchy, R. Charron, D. Constantini, V. Michaud, R. Salathe, and J. Manson, "Experimental investigation of the effect of the mould thermal expansion on the development of internal stresses during carbon fibre composite processing," *Composites: Part A*, vol. 39, pp. 1083–1090, 2008.

[153] Y. Wu, T. Takatoya, K. Chung, and J. Seferis, "Development of the transient simulated laminate(tsl) methodology for moisture ingression studies using unsymmetric laminates," *Journal of Composite Materials*, vol. 34, no. 23, pp. 1998–2015, 2000.

[154] Y. Kim and S. White, "Viscoelastic analysis of processing-induced residual stresses in thick composite laminates," *Mechanics of Composite Materials and Structures*, vol. 4, no. 4, pp. 361–387, 1997.

[155] E. Ruiz and F. Trochu, "Comprehensive thermal optimization of liquid composite molding to reduce cycle time and processing stresses," *Polymer Composites*, vol. 26, pp. 209–230, 2005.

[156] L. Sorrentina and L. Tersigni, "A method for cure process design of thick composite components manufactured by closed die technology," *Applied Composites Materials*, vol. 19, pp. 31–45, 2012.

[157] A. C. Loos and G. S. Springer, "Curing of epoxy matrix composites," *Journal of Composite Materials*, vol. 17, pp. 135–169, 1983.

[158] S. White and H. Hahn, "Process modeling of composite materials: Residual stress development during cure. part i. model formulation," *Composite Materials*, vol. 26, no. 16, pp. 2402–2422, 1992.

[159] R. P. Theriault and T. A. Osswald, "Processing induced residual stress in asymmetric laminate pane is," *Polymer Composites*, vol. 20, no. 3, pp. 493–509, 1999.

[160] A. Johnston, "A plane strain model for process-induced deformation of laminated composite structures," *Composite Materials*, vol. 35, no. 16, pp. 1435–1469, 2001.

[161] P. Hubert, A. Johnston, R. Vaziri, and A. Poursartip, "A two-dimensional finite element processing model for frp composite components," in *Proceedings of ICCM-10, Whistler, B. C., Canada*, 1995.

[162] P. Hubert, V. Reza, and A. Poursartip, "A two-dimensional flow model for the process simulation of complex shape composite laminates," *International journal for numerical methods in engineering*, vol. 44, pp. 1–26, 1999.

[163] *Convergent Manufacturing Technologies, Inc*, 2015.

[164] N. D. Ngo, R. Mohan, P. Chung, and K. K. Tamma, "Recent developments encompassing non-isothermal/isothermal liquid composite molding process modeling/analsys: Physically accurate, computationally effective, and affordable simulation and validations," *Journal of Thermoplastic Composite Materials*, vol. 11, pp. 493–532, 1998.

[165] D. Delaunay, N. Boyard, J.-L. Bailleul, M. Boutaous, Y. Nawab, F. Jacquemin, M. Quintard, V. Sobotka, G. Regnier, and S. LeCorre, *Heat Transfer in Polymer Composite Materials*, N. Boyard, Ed. ISTE Ltd and John Wiley & Sons, Inc., 2016.

[166] L. Lee, W. Young, and R. Lin, "Mold filling and cure modeling of rtm and srim processes," *Composite Structures*, vol. 27, pp. 109–120, 1994.

[167] W. Young, "Thermal behavior of the resin and mold in the process of resin transfer molding," *Journal of Reinforced Plastics and Composites*, vol. 14, pp. 310–332, 1995.

[168] P. Steinke, *Finite-Elemente-Methode*, 2nd ed. Springer, 2007.

[169] N. Ngo and K. Tamma, "Computational developments for simulation based design: Multi-scale physics and flow/thermal/cure/stress modeling, analysis, and validation for advanced manufacturing of composites with complex microstructures," *Archives of Computational Methods in Engineering*, vol. 41, pp. 3–206, 2003.

[170] L. Khoun and P. Hubert, "Investigation of the dimensional stability of carbon epoxy cylinders manufactured by resin transfer moulding," *Composites: Part A*, vol. 41, pp. 116–124, 2010.

[171] M. Duhovic, P. L'Eplattenier, I. Caldichoury, and J. Hausmann, "Advanced 3d finite element simulation of thermoplastic composite induction welding," in *Proceedings of the 20th International Conference on Composite Materials*, 2015.

[172] H. Schürmann, *Konstruieren mit Faser-Kunststoff-Verbunden*. Springer, 2007.

[173] G. Twigg, A. Poursartip, and G. Fernlund, "An experimental method for quantifying tool–part shear interaction during composites processing," *Composites Science and Technology*, vol. 63, pp. 1985–2002, 2003.

[174] G. Twigg, A. Poursartip, and G. Fernlund, "Tool–part interaction in composites processing. part ii: numerical modelling," *Composites: Part A*, vol. 35, pp. 135–141, 2004.

[175] Hsiao and Kikuchi, "Numerical analysis and optimal design of composites thermoforming process," *Computer methods in applied mechanics and engineering*, vol. 177, pp. 1–34, 1999.

[176] H. Golestanian and A. Sherif El-Gizawy, "Modeling of process induced residual stresses in resin transfer molded composites with woven fiber mats," *Journal of Composite Materials*, vol. 35, no. 17, pp. 1513–1528, 2001.

[177] V. Antonucci, A. Cusano, M. Giodano, J. Nasser, and L. Nicolais, "Cure-induced residual strain build-up in a thermoset resin," *Composites: Part A*, vol. 37, pp. 592–601, 2006.

[178] Rabearison, "A fem coupling model for properties prediction during the curing of an epoxy matrix," *Computational Materials Science*, vol. 45, pp. 715–724, 2009.

[179] C. Brauner, "Analysis of process-induced distorions and residual stresses of composite structures," Ph.D. dissertation, Universität Bremen, 2013.

[180] T. Servais, C. Lee, and C. Browning, "Intelligent processing of composite materials," in *SAMPE Journal*, vol. 22, 1986, pp. 14–18.

[181] J. Kim, J. Lee, H. Kim, H. Kim, and S. Lee, "Reduction of residual stresses in thick-walled composite cylinders by smart cure cycle with cooling and reheating," *Composite Structures*, vol. 75, pp. 261–266, 2006.

[182] A. Cebrian, M. Zogg, and P. Ermanni, "Methodology for optimization of the curing cycle of paste adhesives," *International Journal of Adhesion and Adhesives*, vol. 40, pp. 112–119, 2013.

[183] S. White and H. Hahn, "Cure cycle optimization for the reduction of processing-induced residual stresses in composite materials," *Journal of Composite Materials*, vol. 27, no. 14, pp. 1352–1378, 1993.

[184] P. Ciriscioli, Q. Wang, and G. Springer, "Autoclave curing - comparisons of model and test results," *Journal of Composite Materials*, vol. 26, no. 1, pp. 90–102, 1992.

[185] J. Kim and D. Lee, "Development of an autoclave cure cycle with cooling and reheating steps for thick thermoset composite laminates," *Journal of Composite Materials*, vol. 31, no. 22, pp. 2264–2284, 1997.

[186] R. Chen, C. Tu, and H. Tsai, "The effects of moisture upon the optimal temperature path of the viscoelastic symmetric composite laminates after post cure," *Journal of Composite Materials*, vol. 17, no. 16, pp. 1578–1597, 1993.

[187] D. Kranbuehl, P. Kingsley, S. Hart, G. Hasko, B. Dexter, and A. Loos, "ln situ sensor monitoring and intelligent control of the resin transfer molding process," *Polymer Composites*, vol. 15, no. 4, pp. 299–305, 1994.

[188] M. Jinno, S. Sakai, K. Osaka, and T. Fukuda, "Smart autoclave processing of thermoset resin matrix composites based on temperature and internal strain monitoring," *Advanced Composite Materials*, vol. 12, no. 01, pp. 57–72, 2003.

[189] S. Parthasarathy, S. Mantell, and K. Stelson, "Estimation, control and optimization of curing in thick-sectioned composite parts," *ASME Journal of Dynamic Systems, Measurement, and Control*, vol. 126, pp. 824–833, 2004.

[190] P. Ciriscioli and G. Springer, "An expert system for autoclave curing of composites," *Journal of Composite Materials*, vol. 25, pp. 1542–1587, 1991.

[191] J. Sheen, J. Hou, and T. Hou, "Optimal cure cycle design of a resin fiber composite laminate," Master's thesis, Old Dominion University, 1987.

[192] V. Pillai, A. Beri, and P. S. Dhurjati, "Heuristics guided optimization of a batch autoclave curing process," *Computers and Chemical Engineering*, vol. 20, no. 3, pp. 275–294, 1996.

[193] N. Rai and R. Pitchumani, "Optimal cure cycles for the fabrication of thermosetting-matrix composites," *Polymer Composites*, vol. 18, pp. 566–581, 1997.

[194] Colak, "Process modeling and optimization of resistance welding for thermoplastic composites," *Composite Materials*, vol. 36, pp. 721–742, 2002.

[195] M. Li and C. Tucker, "Optimal curing for thermoset matrix composites: Thermochemical and consolidation considerations," *Polymer Composites*, vol. 23, no. 5, pp. 739–757, 2002.

[196] J. Michaud, "Simulation-based design optimization and control of thick composite laminates manufactured by resin transfer molding," Ph.D. dissertation, University of Delaware, 2000.

[197] H. Yu and W. Young, "Optimal design of process parameters for resin transfer molding," *Journal of Composite Materials*, vol. 31, no. 11, pp. 1113–1140, 1997.

[198] M. Chang, C. Chen, and W. Young, "Optimal design of the cure cycle for consolidation of thick composite laminates," *Polymer Composites*, vol. 17, no. 5, pp. 743–750, 1996.

[199] N. Pantelelis, "Optimised cure cycles for resin transfer moulding," *Composite Science and Technology*, vol. 63, pp. 249–264, 2003.

[200] A. A. Skordos and I. K. Partridge, "inverse heat transfer for optimization and on-line thermal properties estimation in composites curing," *Inverse Problems in Science and Engineering*, vol. 12, pp. 157–172, 2004.

[201] K. Hsiao, R. Little, O. Restrepo, and B. Minaie, "A study of direct cure kinetics characterization during liquid composite molding," *Composites: Part A*, vol. 37, pp. 925–933, 2006.

[202] J. Spoerre, C. Zhang, B. Wang, and R. Parnas, "Integrated product and process design for resin transfer molded parts," *Journal of Composite Materials*, 1998.

[203] A. Gupta, "A surrogate model based evolutionary game-theoretic approach for optimizing non-isothermal compression rtm processes," *Composite Science and Technology*, vol. 84, pp. 92–100, 2013.

[204] B. Joseph, F. Hanratty, and J. Kardos, "Model based control of void and product thickness during autoclave curing of carbon/epoxy composite laminates," *Journal of Composite Materials*, vol. 29, no. 8, pp. 1000–1024, 1995.

[205] T. Weber, J. Arent, L. Münch, M. Duhovic, and J. Balvers, "A fast method for the generation of boundary conditions for thermal autoclave simulation," *Composites: Part A*, vol. 88, pp. 216–225, 2016.

[206] V. Sobotka, N. Lefevre, Y. Jarny, and D. Delaunay, "Inverse methodology to determine mold set-point temperature in resin transfer molding process," *International Journal fof Thermal Sciences*, vol. 49, pp. 2138–2147, 2009.

[207] A. Agazzi, V. Sobotka, R. LeGoff, and Y. Jarny, "Optimal cooling design in injection moulding process - a new approach based on morphological surfaces," *Applied Thermal Engineering*, vol. 52, pp. 170–178, 2012.

[208] *Safety data sheet of CYCOM 823 RTM resin*. Cytec, 2011.

[209] J. Lo, M. Anders, T. Centea, and S. Nutt, "The effect of process parameters on volatile release for a benzoxazine–epoxy rtm resin," *Composites: Part A*, vol. 84, pp. 326–335, 2016.

[210] M. Anders, J. Lo, T. Centea, and S. Nutt, "Eliminating volatile-induced surface porosity during resin transfer molding of a benzoxazine/epoxy

blend," *Composites: Part A*, vol. 84, pp. 442–454, 2016.

[211] M. Afendi, W. Banks, and D. Kirkwood, "Bubble free resin for infusion process," *Composites: Part A*, vol. 36, pp. 739–746, 2004.

[212] T. Lundström, "Measurement of void collapse during resin transfer moulding," *Composites: Part A*, vol. 28, pp. 201–214, 1997.

[213] M. P. Pham, "Theoretical studies of mechanisms of epoxy curing systems," Ph.D. dissertation, University of Utah, 2011.

[214] K. Yang, K. Yao, and W. Koh, "Kinetics analysis of the curing reaction of fast cure epoxy prepregs," *Journal of applied polymer science*, vol. 73, pp. 1501–1508, 1999.

[215] J. Barton, "The application of differential scanning calorimetry (dsc) to the study of epoxy resin curing reactions," *Advances in Polymer Science*, pp. 111–154, 1972.

[216] P. Hubert, A. Johnston, A. Poursartip, and K. Nelson, "Cure kinetics and viscosity models for hexcel 8552 epoxy resin," in *International SAMPE symposium and exhibition*, 2001.

[217] *Netzsch-Holding, Selb, Germany*, 2014.

[218] S. W. Hughes, "Measuring liquid density using archimedes' principle," *Physics Education*, vol. 41, no. 5, 2006.

[219] C. Tung and P. Dynes, "Relationship between viscoelastic properties and gelation in thermosetting systems," *Journal of applied polymer science*, vol. 27, pp. 569–574, 1982.

[220] H. Winter and F. Chambon, "Analysis of linear viscoelasticity of a crosslinking polymer at the gel point," *Journal of Rheology*, vol. 30, pp. 367–382, 1986.

[221] F. C. Nix and D. MacNair, "The thermal expansion of pure metals: Copper, gold, aluminum, nickel, iron," *Phyical Review*, vol. 60, pp. 597–605, 1941.

[222] H. Johnen, *Zink- Taschenbuch*, 3rd ed. Metall-Verlag GMBH, 1981.

[223] M. Wenzel, "Spannungsbildung und relaxationsverhalten bei der aushärtung von epoxidharzen," Ph.D. dissertation, TU Darmstadt, 2005.

[224] *Material data sheet of Araldite LY8616 resin*. Huntsman, 2008.

[225] *Material data sheet of Pyrofil TR30S 3K carbon fiber*. Grafil Inc., 2001.

[226] G. Kalogiannakis, A. Van Hemelrijck, and G. Van Assche, "Measurements of thermal properties of carbon/epoxy and glass/epoxy using modulated temperature differential scanning calorimetry," *Journal of Composite Mate-*

rials, vol. 38, no. 02, pp. 163–175, 2004.

[227] C. Zheng, T. Tan, J. Wen, and A. Maniatty, "Finite element model based temperature consensus control for material microstructure," in *American Control Conference (ACC)*. IEEE, 2015, pp. 619–624.

[228] R. Helmus, "Out-of-autoclave prepregs: Stochastic modelling of void formation," Ph.D. dissertation, Technische Universität München, 2015.

[229] T. Centea and P. Hubert, "Modelling the effect of material properties and process parameters on tow impregnation in out-of-autoclave prepregs," *Composites: Part A*, vol. 43, pp. 1505–1513, 2012.

[230] D. Arthur, "k-means++: The advantages of careful seeding," in *SODA '07 Proceedings of the eighteenth annual ACM-SIAM symposium on Discrete algorithms*, 2007.

[231] M. Özisik, *Heat Conduction*, 2nd ed. John Wiley & Sons, Inc., 1993.

[232] *MATLAB Documentation*, Mathworks, 2016. [Online]. Available: https://de.mathworks.com/help/matlab/

Publications

[P1] J.S. Weiland, P. Hubert, R. M. Hinterhölzl, "Thermal dimensioning of manufacturing moulds with multiple resistively heated zones for composite processing”, *Journal of Composite Materials*, 2017.

[P2] J.S. Weiland, M.P. Hartmann, R. M. Hinterhölzl, "Cure simulation with resistively in situ heated CFRP molds: Implementation and validation”, *Compos Part A. App Sci Manuf*, vol. 80, no. 0, pp. 171 – 181, 2016.

[P3] J.S. Weiland, M.P. Hartmann, R. M. Hinterhölzl, "Characterization and numerical investigation of an RTM cure process with CFRP molds and independent heat patches”, in *Proceedings of ICCM 20, 20th International Conference on Composite Materials*, 2015.

Supervised Student Theses

During my employment at the *Chair of Carbon Composites – Lehrstuhl für Carbon Composites* – I supervised the following student theses:

[S1] M. Juretko, ″Charakterisierung eines Harzsystems für die Simulation des Aushärtevorgangs von Rotorblättern im RTM-Prozess″, Student thesis, 2014.

[S2] A. Rauter, ″Auslegung eines innovativen CFK-Rotorblattwerkzeuges″, Bachelor′s thesis, 2014.

[S3] C. Thoma, ″Entwicklung eines experimentellen Verfahrens zur Bestimmung des Wärmeausdehnungskoeffizienten eines Harzsystems″, Bachelor′s thesis, 2014.

[S4] M. Eberlein, ″Experimental and simulative investigation in the influence of heat sinks on the curing of an RTM rotor blade″, Bachelor′s thesis, 2015.

[S5] W. Wölki, ″Analyse des Einflusses lokaler Laminateigenschaftsabweichungen auf prozessinduzierte Bauteildeformationen bei Faser-Kunststoff-Verbunden″, Master′s thesis, 2016.

The following student′s theses contributed to the presented doctoral thesis: [S1], [S2], [S3], [S4].